

**Spin-orbit driven transport:
Edelstein effect and chiral anomaly**

Dissertation

zur Erlangung des Doktorgrades der Naturwissenschaften
(Dr. rer. nat.)

der

Naturwissenschaftlichen Fakultät II
Chemie, Physik und Mathematik

der Martin-Luther-Universität
Halle-Wittenberg

vorgelegt von

Frau Annika Johansson
geb. am 02. Februar 1992 in Heidelberg

Erstgutachterin: Prof. Dr. Ingrid Mertig
Zweitgutachter: Prof. Dr. Steffen Trimper
Drittgutachter: Dr. Manuel Bibes

Datum der öffentlichen Verteidigung: 23.04.2019

Abstract

In this thesis, the spin-orbit driven transport phenomena Edelstein effect and chiral anomaly are considered within semiclassical Boltzmann transport theory.

The Edelstein effect, which is the generation of a homogeneous spin density by an electric field in systems with broken inversion symmetry, is discussed for Rashba systems as well as Dresselhaus systems and topological insulators. It is shown that anisotropies modify the orientation of the current-induced spin polarization as well as its magnitude. For Rashba systems with broken time-reversal symmetry an intrinsic Edelstein effect is predicted. Finally, Weyl semimetals are identified as candidates for providing an enormous Edelstein efficiency, mainly originating from their topological surface states.

The chiral anomaly is a quantum phenomenon and corresponds to the nonconservation of chiral charge due to external nonorthogonal magnetic and electric fields. It can be realized in Weyl semimetals and leads to a negative longitudinal magnetoresistance. In this work, transport phenomena in the presence of the classical Lorentz force as well as the chiral anomaly are discussed for anisotropic Weyl systems including energy- and momentum-dependent relaxation times.

In der vorliegenden Arbeit werden der Edelstein-Effekt und die chirale Anomalie untersucht, Transportphänomene, die durch Spin-Bahn-Wechselwirkung zustande kommen.

Der Edelstein-Effekt bezeichnet die Erzeugung einer homogenen Spindichte durch ein externes elektrisches Feld in Systemen mit Inversionsasymmetrie. Er wird hier für Rashba-Systeme, Dresselhaus-Systeme und topologische Isolatoren betrachtet. Es wird gezeigt, dass Anisotropien sowohl Richtung als auch Betrag der erzeugten Spindichte maßgeblich beeinflussen. Zudem wird für Rashba-Systeme mit gebrochener Zeitumkehrsymmetrie ein intrinsischer Edelstein-Effekt vorausgesagt. Weyl-Semimetalle werden als mögliche Kandidaten für einen sehr effizienten Edelstein-Effekt identifiziert.

Die chirale Anomalie ist ein Quantenphänomen und beschreibt die Nichterhaltung der chiralen Ladung durch externe, zueinander nicht orthogonale magnetische und elektrische Felder. Sie tritt in Weyl-Semimetallen auf und geht mit einem negativen longitudinalen Magnetwiderstand einher. In dieser Arbeit werden die Einflüsse der klassischen Lorentzkraft und der chiralen Anomalie auf die Transporteigenschaften von Weyl-Semimetallen mit anisotroper Bandstruktur untersucht, wobei ein Fokus auf der Energie- und Impulsabhängigkeit der Relaxationszeit liegt.

Contents

1	Introduction	7
2	Semiclassical transport theory	11
2.1	Concepts of Berry phases	11
2.2	Electron dynamics in electromagnetic fields	14
2.3	Boltzmann equation	17
2.4	Kubo theory	22
2.5	Scattering	22
3	Spin-orbit coupling	25
3.1	Relativistic correction to the Hamiltonian	25
3.2	Two-band model	26
3.3	Spin-orbit fields	27
3.4	Rashba effect	28
3.5	Dresselhaus effect	30
3.6	Topological insulators	30
3.7	Weyl semimetals	34
4	The Edelstein effect	39
4.1	Charge-to-spin conversion in a Rashba model	39
4.2	Intrinsic Edelstein effect	42
4.3	Inverse Edelstein effect	43
4.4	Experimental observation of the Edelstein effect	44
4.5	Edelstein effect in Rashba systems	45
4.6	Systems with Rashba and Dresselhaus SOC	62
4.7	Topological insulators	67
4.8	Weyl semimetals	69
5	Chiral anomaly in Weyl semimetals	77
5.1	Quantum anomalies in field theory	77
5.2	Ultraquantum limit	79
5.3	Semiclassical limit	86
5.4	Experimental evidence of the chiral anomaly	89
5.5	Chiral anomaly within a Fermi surface harmonics approach	90
6	Conclusion	101
A	Scattering at magnetic impurities	105
B	Fermi lines for a Rashba system with in-plane magnetic field	106
C	Rashba system with Zeeman splitting, $\mathbf{B} = B(1, 0, 1)$	107

Contents

D	Band structure and Fermi lines in systems with Rashba and Dresselhaus SOC	108
D.1	(001) surface	108
D.2	(110) surface	110
E	Fermi surface determination and integration	112
E.1	Two-dimensional triangular method	112
E.2	Three-dimensional tetrahedral method	113
	Bibliography	114
	List of publications	126
	Curriculum vitae	127

1. Introduction

Conventional semiconductor technology is based on transport of electric charge carried by electrons or holes. The main concept of the rapidly growing field of spintronics, which is short for spin-based electronics or spin transport electronics [1], is to additionally utilize the spin degree of freedom for storage, processing and transfer of data. Spintronic devices are expected to exhibit lower energy consumption, higher integration densities, faster processing and nonvolatility [1]. The most prominent phenomenon in the field of spintronics is the giant magnetoresistance (GMR) effect, whose discovery by Fert and Grünberg in 1988 is considered the starting point of spin-based technology [2, 3] and was awarded with the Nobel Prize in Physics in 2007 [4]. In multilayer systems of alternating magnetic and nonmagnetic layers, the resistivity of the heterostructure strongly depends on the orientation of the magnetization in adjacent ferromagnetic layers. If these are oriented antiparallel, the resistivity is remarkably increased in comparison to the parallel configuration, which can be explained by spin-dependent scattering.

On the basis of the GMR effect, a novel read head technology was developed by Parkin [5, 6]. Less than 10 years after its discovery, the GMR effect was utilized in spin-valve sensors, which are extremely sensitive magnetic field sensors, leading to reduced sizes and enhanced storage capacities of hard disk drives. This GMR-based technology rapidly became the standard in many electronic devices. Today, the GMR technology has been replaced by read heads using the tunnel magnetoresistance (TMR) effect, a spintronic effect which is also crucial for the magnetic random access memory (MRAM) technology.

Although the field of spintronics arose three decades ago, it is still a very active area of research, proposing and developing new electronic devices, such as the spin field-effect transistor [7] and the magnetic domain-wall racetrack memory [8].

Since the basic idea of spintronics is to use spin currents and spin-polarized currents instead of or in addition to purely electrical currents, one aim of research is to identify mechanisms and methods of efficiently generating and controlling spin(-polarized) currents as well as spin polarization. Ferromagnets naturally exhibit an imbalance of charge carriers with opposite spin orientation, thus, spin-polarized currents can be easily generated in these materials. However, injecting spin-polarized charge carriers from ferromagnets into semiconductors is often hard to realize and inefficient [1, 9]. Therefore, the focus of research is on creating spin polarization and spin currents directly in nonmagnetic materials.

The crucial interaction underlying this field of spintronics not based on ferromagnetic materials is the spin-orbit coupling (SOC), which is a relativistic effect relating the spin degree of freedom to the electronic structure and the orbital momentum. The emergence of SOC from relativistic wave equations as well as its influence on the electronic band structures in solids is introduced in chapter 3 of this thesis. Namely, the Rashba and Dresselhaus effect as well as topological nontrivial properties in topological insulators and Weyl semimetals are discussed, all strongly associated with spin-orbit interaction.

Due to SOC, various transport phenomena related to the spin degree of freedom arise. The most prominent example is the spin Hall effect: A transversal pure spin current (closed circuit geometry) and a pure spin voltage (open circuit), respectively, come along with a charge current [10–15]. The spin quantization axis, the direction of spin separation, and the electric charge current are mutually perpendicular. However, no transversal electric current or voltage occurs. The spin Hall effect results from asymmetric scattering at impurities and the intrinsic anomalous velocity.

A related phenomenon is the anomalous Hall effect (AHE). Here, in addition to a spin current or voltage, a transversal charge current/voltage occurs due to the imbalance of charge carriers with opposite spins resulting from a finite magnetization or broken time-reversal symmetry.

Another actively investigated spin-orbit effect is the Edelstein effect, first discussed in 1989 by

1. Introduction

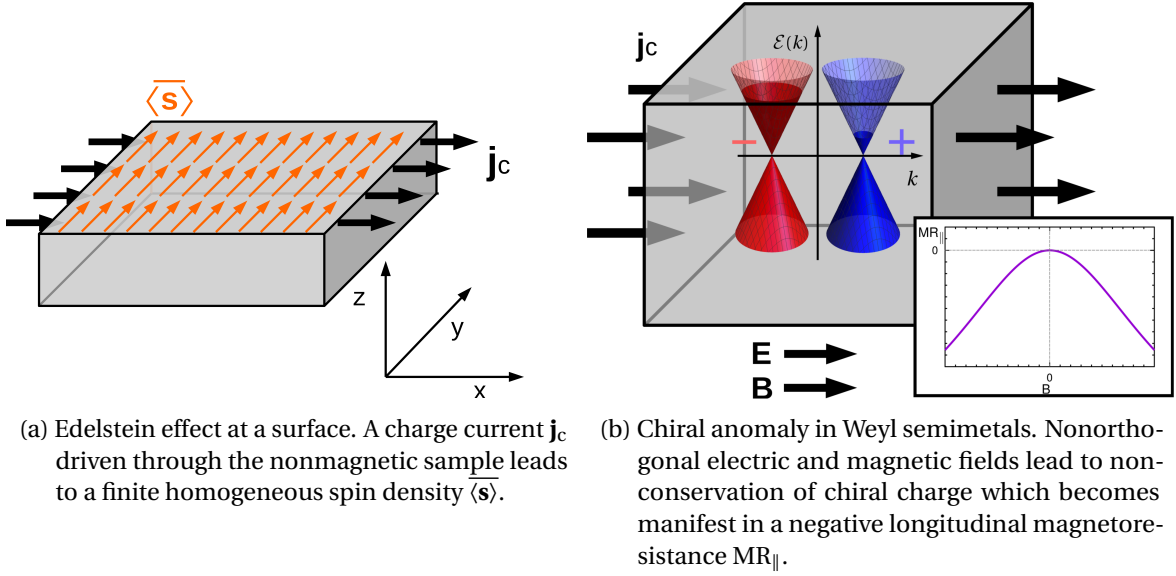


Figure 1.1.: Edelstein effect and chiral anomaly.

Aronov and Lyanda-Geller [16] as well as Edelstein [17]. It is a magnetoelectric phenomenon providing charge-current-to-spin conversion in systems with broken inversion symmetry. In nonmagnetic materials, a finite macroscopic spin polarization can be induced purely electrically by the application of an external electric field, as sketched in Fig. 1.1(a). In a two-dimensional isotropic Rashba system, which was the original model in the papers by Edelstein [17] as well as Aronov and Lyanda-Geller [16], the spin density is in-plane and perpendicular to the applied field. This electrically induced spin polarization can exert a spin-orbit torque on an adjacent ferromagnetic layer and lead to domain wall motion or magnetization switching [18]. Because of these promising properties, the Edelstein effect is considered an auspicious phenomenon for applications in spintronics.

Whereas for isotropic Rashba systems a large spin-orbit splitting is crucial for efficient charge-to-spin conversion [17], one focus of current research is on finding novel materials beyond conventional Rashba systems providing a large direct or inverse Edelstein effect, for example three-dimensional (3D) topological insulators [19–27] and oxide interfaces [28–30]. Therefore, this work aims at theoretically examining materials apart from isotropic Rashba systems in order to identify materials providing an efficient charge-to-spin conversion as potential candidates for practical applications of the Edelstein effect. In chapter 4 the Edelstein effect and the underlying physical mechanisms are introduced within a semiclassical theory. The charge-to-spin conversion is discussed in detail and calculated for Rashba and Dresselhaus systems with a focus on deviations from the conventional Edelstein geometry (induced spin density is in-plane and perpendicular to the electric field). Subsequently, the Edelstein effect is shown to be highly efficient in three-dimensional topological insulators. In addition, an enormous Edelstein effect is predicted for Weyl semimetals.

These topological semimetals have not been considered as Edelstein materials before. Rather, they are of interest for the solid state community due to the topologically nontrivial character of their three-dimensional bulk band structure and their topological surface states. Weyl semimetals are interpreted as the solid-state realization of Weyl fermions [31–35]. Although Weyl fermions were already theoretically introduced in 1929 as the solution of the Weyl equation [36], which is the massless version of the Dirac equation, they have not been observed as elementary particles in nature. However, in the last decade a novel topological semimetal phase was predicted [31], whose low-energy states around distinct degeneracy points can be described by the Weyl equation. Therefore, the corresponding materials were named *Weyl semimetals* [32].

Due to this interpretation of Weyl semimetals hosting Weyl fermions, concepts which were

originally developed for chiral Weyl fermions can be transferred to the field of solid states. Thus, the chiral anomaly, which is the violation of chiral gauge symmetry by an external magnetic field, initially discussed for fundamental Weyl particles [37, 38], is expected to occur in Weyl semimetals. The nonconservation of chiral charge due to the chiral anomaly is not experimentally accessible. However, it is accompanied by an unconventional negative longitudinal magnetoresistance (NLMR), schematically sketched in Fig. 1.1(b), which is considered a strong observable hint for the existence of Weyl fermions [39–41].

This atypical influence of an external magnetic field on the longitudinal charge conductivity due to nontrivial topology motivates chapter 5 of this work. The chiral anomaly is discussed in the ultraquantum as well as the semiclassical limit. In contrast to common literature, which usually discusses the chiral anomaly isolated from other charge transport contributions [39, 41], chapter 5 focuses on the interplay of chiral anomaly and classical Lorentz force, thereby providing a complete theory of magnetotransport in Weyl semimetals, which lacks in previous publications.

In this work, the relevant transport properties for examining the Edelstein effect as well as the chiral anomaly are calculated within a semiclassical Boltzmann theory, which is presented in chapter 2. This approach provides a clear, straightforward picture for discussing transport phenomena. The presented calculations base on effective model Hamiltonians. In comparison to realistic band structure calculations, this approach is less accurate. However, it provides the opportunity of gaining deep insights into the physics underlying the transport phenomena due to its transparent form. Therefore, the results presented in this work should be understood as qualitative contributions for understanding the Edelstein effect and the chiral anomaly, including qualitative predictions, rather than exact numerical ones.

2. Semiclassical transport theory

In the classical particle picture, transport in solids is caused by the motion of electrons. Under the influence of external electromagnetic fields, the dynamics of an electron between two scattering events is described by the classical equations of motion [42],

$$\dot{\mathbf{r}} = \frac{\mathbf{p}}{m}, \quad \dot{\mathbf{p}} = -e(\mathbf{E} + \mathbf{v} \times \mathbf{B}). \quad (2.1)$$

Here, \mathbf{r} is the real-space coordinate, \mathbf{p} is the momentum, $m = m_e$ is the electron mass, $e > 0$ is the elementary charge, \mathbf{E} is an electric field, \mathbf{v} the velocity and \mathbf{B} a magnetic field.

In quantum mechanics, the electronic states contributing to the transport are described by quantum mechanical wave equations, i.e. the Schrödinger or the Dirac equation. External fields enter these equations and modify the eigenstates of the system.

However, in solids, the influence of external fields can also be considered classically, whereas the electronic band structure is discussed quantum mechanically, which is known as *semiclassical approach*. The electronic states are constructed as wave packets from Bloch waves, which corresponds to a particle-like picture. Thus, the wave packet is not scattered at the periodic crystal potential but at impurities breaking the translational invariance. Between collisions, the wave packet dynamics is described by semiclassical equations of motion, in analogy to the classical equations of motion (2.1).

This chapter gives an introduction to semiclassical transport theory considering the electromagnetic fields classically and the electronic states quantum mechanically. The concepts of Berry phases are presented, leading to semiclassical equations of motion. Using the latter, the Boltzmann transport equation is introduced, which is probably the most important equation in this work and which will be used to calculate transport properties. An alternative way of considering transport is provided by the Kubo formalism, which is briefly sketched. Finally, the basic concepts of scattering theory used in this work are presented.

2.1. Concepts of Berry phases

In a seminal paper Berry considered the adiabatic evolution of a quantum state under the influence of slowly varying parameters [43]. A nondegenerate system performing a closed loop in parameter space comes back to its initial state but acquires a dynamical phase as well as an additional phase, which is today known as *Berry phase*. This new concept, also known as *Berryology*, has an enormous impact on different areas of physics. It explains transport phenomena such as the anomalous Hall effect and the quantum Hall effect and is strongly related to the concept of topological phases in solid state physics. In this section, the theory of Berry phases is introduced following the work of Berry [43] recapitulated by Niu [44] and Bernevig [45].

A system described by the Hamiltonian $\hat{H}(\mathbf{X})$, which does not depend explicitly on time but on a set of time-dependent parameters $\mathbf{X} = \mathbf{X}(t)$, is considered [44]. The eigenstates of $\hat{H}(\mathbf{X})$, $|n(\mathbf{X})\rangle$, form an instantaneous orthonormalized basis,

$$\hat{H}(\mathbf{X})|n(\mathbf{X})\rangle = \mathcal{E}^n(\mathbf{X})|n(\mathbf{X})\rangle \quad (2.2)$$

with the corresponding eigenvalues $\mathcal{E}^n(\mathbf{X})$. The eigenfunctions $|n(\mathbf{X})\rangle$ are defined by Eq. (2.2) up to an arbitrary phase factor. Here, a gauge is chosen which ensures this phase to be smooth and single-valued along a path in parameter space.

Now, the adiabatic evolution in time starting at $t = 0$ is considered, which means that the parameters $\mathbf{X}(t)$ vary slowly in comparison to the energy scale of the system. In accordance with

2. Semiclassical transport theory

the quantum adiabatic theorem [46], a system starting from the initial state $|n(\mathbf{X}(0))\rangle$ remains in the state $|n(\mathbf{X}(t))\rangle$ during the adiabatic evolution. The only degree of freedom is the phase $\theta(t)$, resulting in the state

$$|\Psi^n(t)\rangle = e^{-i\theta(t)} |n(\mathbf{X}(t))\rangle. \quad (2.3)$$

The time evolution of $|\Psi^n(t)\rangle$ is expressed by the Schrödinger equation

$$\hat{H}(\mathbf{X}) |\Psi^n(t)\rangle = i\hbar \frac{d}{dt} |\Psi^n(t)\rangle, \quad (2.4)$$

with i the imaginary unit and \hbar the Planck constant, resulting in

$$\hbar \frac{d}{dt} \theta(t) = \mathcal{E}^n(\mathbf{X}(t)) - i\hbar \left\langle n(\mathbf{X}(t)) \left| \frac{d}{dt} \right| n(\mathbf{X}(t)) \right\rangle. \quad (2.5)$$

From this differential equation, the phase $\theta(t)$ can be determined,

$$\theta(t) = \frac{1}{\hbar} \int_0^t \mathcal{E}^n(\mathbf{X}(t')) dt' - i \int_0^t \left\langle n(\mathbf{X}(t')) \left| \frac{d}{dt'} \right| n(\mathbf{X}(t')) \right\rangle dt'. \quad (2.6)$$

The first term on the right-hand side of Eq. (2.6) is the dynamical phase. The second term,

$$\gamma^n(t) = i \int_0^t \left\langle n(\mathbf{X}(t')) \left| \frac{d}{dt'} \right| n(\mathbf{X}(t')) \right\rangle dt' = i \int_{\mathcal{P}} \left\langle n(\mathbf{X}) \left| \frac{\partial}{\partial \mathbf{X}} \right| n(\mathbf{X}) \right\rangle d\mathbf{X} = \int_{\mathcal{P}} \mathcal{A}^n(\mathbf{X}) \cdot d\mathbf{X}, \quad (2.7)$$

is real valued and gives a phase factor to the wave function. Here, \mathcal{P} is a path from $\mathbf{X}(0)$ to $\mathbf{X}(t)$ in the parameter space. The vector $\mathcal{A}^n(\mathbf{X})$, defined as

$$\mathcal{A}^n(\mathbf{X}) = i \left\langle n(\mathbf{X}) \left| \frac{\partial}{\partial \mathbf{X}} \right| n(\mathbf{X}) \right\rangle, \quad (2.8)$$

is called *Berry connection* or *Berry vector potential* due to its analogy to the electromagnetic vector potential, as will be pointed out later.

If the eigenstate $|n(\mathbf{X}(t))\rangle$ is transformed by a gauge transformation, $|n(\mathbf{X})\rangle \rightarrow |n(\mathbf{X})\rangle e^{i\zeta(\mathbf{X})}$, the Berry connection transforms as $\mathcal{A}^n(\mathbf{X}) \rightarrow \mathcal{A}^n(\mathbf{X}) - \frac{\partial}{\partial \mathbf{X}} \zeta(\mathbf{X})$ and the phase as $\gamma^n \rightarrow \gamma^n - [\zeta(\mathbf{X}(t)) - \zeta(\mathbf{X}(0))]$. Before Berry's fundamental work in 1984 [43], no importance was attributed to the phase γ^n since it was assumed to be cancelable by an appropriate gauge choice. However, as Berry showed, this elimination cannot always be realized. For a closed path \mathcal{P} in parameter space, $\mathbf{X}(T) = \mathbf{X}(0)$. Since the gauge phase factor $e^{i\zeta(\mathbf{X})}$ must be single valued, $e^{i\zeta(\mathbf{X}(T))} = e^{i\zeta(\mathbf{X}(0))}$, the phase ζ can only change by an integer multiple of 2π on the closed path, $\zeta(\mathbf{X}(T)) - \zeta(\mathbf{X}(0)) = 2\pi m$ ($m \in \mathbb{Z}$). Thus, the phase γ^n cannot be eliminated by a gauge transformation but only be changed by $2\pi m$. For a closed path \mathcal{P} , γ^n is gauge-invariant (modulo 2π), depending only on the geometric aspects of the path, not on its specific form. It is called *Berry phase* or *geometric phase*.

Using Stokes' theorem, the Berry phase for a closed path \mathcal{P} is expressed as

$$\gamma^n = \oint_{\mathcal{P}} \mathcal{A}^n(\mathbf{X}) \cdot d\mathbf{X} = \int_S \frac{\partial \mathcal{A}_k^n(\mathbf{X})}{\partial X_i} dX_i \wedge dX_k = \frac{1}{2} \int_S \Omega_{ik}^n(\mathbf{X}) dX_i \wedge dX_k. \quad (2.9)$$

Here, i and k refer to the coordinates in parameter space, S is a surface enclosed by the path \mathcal{P} and the *Berry curvature* tensor reads

$$\Omega_{ik}^n(\mathbf{X}) = \frac{\partial \mathcal{A}_k^n(\mathbf{X})}{\partial X_i} - \frac{\partial \mathcal{A}_i^n(\mathbf{X})}{\partial X_k} = i \left[\left\langle \frac{\partial n(\mathbf{X})}{\partial X_i} \left| \frac{\partial n(\mathbf{X})}{\partial X_k} \right\rangle - \left\langle \frac{\partial n(\mathbf{X})}{\partial X_k} \left| \frac{\partial n(\mathbf{X})}{\partial X_i} \right\rangle \right]. \quad (2.10)$$

The Berry curvature is gauge-invariant. In 3D parameter space, the Berry curvature vector

$$\boldsymbol{\Omega}^n(\mathbf{X}) = \frac{\partial}{\partial \mathbf{X}} \times \mathcal{A}^n(\mathbf{X}) = i \left\langle \frac{\partial}{\partial \mathbf{X}} n(\mathbf{X}) \left| \times \right| \frac{\partial}{\partial \mathbf{X}} n(\mathbf{X}) \right\rangle \quad (2.11)$$

is defined and the Berry phase is given by

$$\gamma^n = \int_S \boldsymbol{\Omega}^n(\mathbf{X}) \cdot d\mathbf{S}. \quad (2.12)$$

Due to the structure of Berry connection and Berry curvature resembling the electromagnetic vector potential and magnetic field, respectively, the Berry connection can formally be interpreted as the equivalent of the electromagnetic vector potential in parameter space, the Berry curvature as the equivalent of the magnetic field.

The expressions (2.10) and (2.11) can be transformed to

$$\begin{aligned} \Omega_{ik}^n(\mathbf{X}) &= -\text{Im} \sum_{m \neq n} \frac{\left\langle n(\mathbf{X}) \left| \frac{\partial}{\partial X_i} \hat{H}(\mathbf{X}) \right| m(\mathbf{X}) \right\rangle \left\langle m(\mathbf{X}) \left| \frac{\partial}{\partial X_k} \hat{H}(\mathbf{X}) \right| n(\mathbf{X}) \right\rangle - (i \leftrightarrow k)}{(\mathcal{E}^n(\mathbf{X}) - \mathcal{E}^m(\mathbf{X}))^2}, \\ \boldsymbol{\Omega}^n(\mathbf{X}) &= -\text{Im} \sum_{m \neq n} \frac{\left\langle n(\mathbf{X}) \left| \frac{\partial}{\partial \mathbf{X}} \hat{H}(\mathbf{X}) \right| m(\mathbf{X}) \right\rangle \times \left\langle m(\mathbf{X}) \left| \frac{\partial}{\partial \mathbf{X}} \hat{H}(\mathbf{X}) \right| n(\mathbf{X}) \right\rangle}{(\mathcal{E}^n(\mathbf{X}) - \mathcal{E}^m(\mathbf{X}))^2}, \end{aligned} \quad (2.13)$$

which is a gauge-independent way of calculating the Berry curvature and has the advantage that the gradient of the Hamiltonian, and not the derivatives of the wave functions, have to be calculated. Thus, the Berry $\boldsymbol{\Omega}^n$ curvature accounts for the influence of all bands $m \neq n$ on a distinct band n and therefore represents interband transitions in a single-band model.

2.1.1. Berry phase of Bloch states

The Berry phase formalism introduced above is defined for a general Hamiltonian $\hat{H}(\mathbf{X})$ which depends on a set of parameters \mathbf{X} . In periodic solids, the states can be described by Bloch waves. The Berry phase, connection and curvature are conventionally defined within the parameter space \mathbf{q} , which is the canonical crystal momentum in the Brillouin zone.

However, a Hamiltonian describing electronic states initially does not include the crystal momentum \mathbf{q} as parameter, but contains the momentum operator $\hat{\mathbf{p}}$. In the approximation of noninteracting electrons, the band structure results from the single-electron Hamiltonian

$$\hat{H} = \frac{\hat{\mathbf{p}}^2}{2m} + V(\mathbf{r}). \quad (2.14)$$

For a periodic potential $V(\mathbf{r}) = V(\mathbf{r} + \mathbf{R})$, with \mathbf{R} a lattice vector, the eigenstates $|\Psi_{\mathbf{q}}^n\rangle$ fulfill the Bloch theorem,

$$|\Psi_{\mathbf{q}}^n(\mathbf{r} + \mathbf{R})\rangle = e^{i\mathbf{q}\mathbf{R}} |\Psi_{\mathbf{q}}^n(\mathbf{r})\rangle \quad (2.15)$$

leading to

$$|\Psi_{\mathbf{q}}^n(\mathbf{r})\rangle = e^{i\mathbf{q}\mathbf{r}} |u_{\mathbf{q}}^n(\mathbf{r})\rangle \quad (2.16)$$

with $|u_{\mathbf{q}}^n(\mathbf{r} + \mathbf{R})\rangle = |u_{\mathbf{q}}^n(\mathbf{r})\rangle$ being lattice-periodic. Using the Bloch boundary condition (2.15), the Hamiltonian \hat{H} can be transformed by unitary transformation to the crystal momentum representation,

$$\hat{H}(\mathbf{q}) = e^{-i\mathbf{q}\mathbf{r}} \hat{H} e^{i\mathbf{q}\mathbf{r}} = \frac{(\hat{\mathbf{p}} + \hbar\mathbf{q})^2}{2m} + V(\mathbf{r}). \quad (2.17)$$

2. Semiclassical transport theory

The correspondingly transformed eigenstates $|u_{\mathbf{q}}^n(\mathbf{r})\rangle = e^{-i\mathbf{q}\mathbf{r}} |\Psi_{\mathbf{q}}^n(\mathbf{r})\rangle$ “live” in the Hilbert space of lattice periodic functions. After this transformation, the Berry connection, curvature and phase can be defined with respect to the crystal momentum \mathbf{q} in the Brillouin zone as parameter space. However, Berry curvature and connection can be defined with respect to any parameter the Hamiltonian depends on. In order to distinguish between the Berry quantities derived from the crystal momentum and the Berry properties related to other parameters, the latter ones are called *mixed Berry* quantities [47], whereas *Berry* usually means the crystal momentum Berry properties.

2.2. Electron dynamics in electromagnetic fields

For the discussion of electronic transport properties, the influence of external fields on the electronic system has to be examined. The external fields are considered as perturbations which slowly vary in space and time and drive the dynamics of the system. They enter the Hamiltonian and can therefore influence the band structure as well as the eigenstates. However, the basic concept of the semiclassical transport theory is to describe the impact of external fields classically, i.e. their influence is expressed like in a classical single-particle system.

To analyze the effect of external fields on the quantum mechanical eigenstates of a Hamiltonian in the classical picture, the electronic states cannot be considered as free electron-like Bloch states any more. Rather, wave packets are considered [42, 44, 48],

$$|\Psi_{\mathbf{w}}^n(\mathbf{r}, t)\rangle = \int a(\mathbf{q}, t) |\Psi_{\mathbf{q}}^n(\mathbf{r}, t)\rangle d^d q, \quad (2.18)$$

which are constructed from Bloch waves (Eq. (2.16)) with the same band index n . Here, $a(\mathbf{q}, t)$ is a prefactor and d is the dimension of the system. A wave packet has a finite width in real and momentum space with $\Delta q \Delta r \geq 1$. The basic presumptions for a semiclassical approach are that Δq is small in comparison to the Brillouin zone and Δr is small with respect to the length scale of the fields as well as the mean free path, but large compared to the lattice constant [48]. In the semiclassical picture, a well-defined real-space coordinate \mathbf{r} and momentum \mathbf{q} , corresponding to the coordinates of the wave packet center, are attributed to the crystal electrons. This model corresponds to a particle-like picture of electrons, on which the external fields are acting. A crucial point of the semiclassical model is that the band index n remains constant, thus, no interband transitions can be induced by external fields.

In order to describe the influence of electric and magnetic fields in a classical way, the wave packet dynamics is considered in this section. Semiclassical equations of motion will be derived which form the basis for semiclassical transport theory. Using a time-dependent variational principle [49], it will be shown that the Berry curvature strongly influences the electron dynamics and the phase-space volume leading to a modified density of states.

The derivations follow the works of Sundaram and Niu [50] as well as Xiao *et al.* [44, 51].

2.2.1. Semiclassical equations of motion

In a crystal, the noninteracting electronic states are described by the lattice-periodic Hamiltonian (2.14), which is denoted by $\hat{H}_0 = \hat{H}_0(\hat{\mathbf{p}})$ in this section. The eigenstates are Bloch states, described by Eq. (2.16) with the crystal momentum \mathbf{q} , the periodic part of the eigenfunction $|u_{\mathbf{q}}(\mathbf{r})\rangle$ and the energy eigenvalue $\mathcal{E}_0(\mathbf{q})$. The band index n is omitted here.

External electromagnetic fields couple to the eigenstates of the system, which is respected in the Hamiltonian by the Peierls substitution [52–54],

$$\hat{H} = \hat{H}_0(\hat{\mathbf{p}} + e\mathbf{A}(\mathbf{r}, t)) - e\Phi(\mathbf{r}, t). \quad (2.19)$$

Here, \mathbf{r} is the position operator. The electric and magnetic fields are expressed by the electromag-

netic potentials $\mathbf{A}(\mathbf{r}, t)$ and $\Phi(\mathbf{r}, t)$,

$$\mathbf{B}(\mathbf{r}, t) = \frac{\partial}{\partial \mathbf{r}} \times \mathbf{A}(\mathbf{r}, t), \quad \mathbf{E}(\mathbf{r}, t) = -\frac{\partial}{\partial \mathbf{r}} \Phi(\mathbf{r}, t) - \frac{\partial}{\partial t} \mathbf{A}(\mathbf{r}, t). \quad (2.20)$$

In the Bloch basis, Eq. (2.19) reads

$$\hat{H} = \hat{H}_0 \left(\mathbf{q} + \frac{e}{\hbar} \mathbf{A}(\mathbf{r}, t) \right) - e\Phi(\mathbf{r}, t). \quad (2.21)$$

Now, a wave packet $|\Psi_W(\mathbf{r}_c, t)\rangle \equiv |\Psi\rangle$ centered at \mathbf{r}_c , given by Eq. (2.18), is considered. The perturbations due to the external fields are assumed to vary on a length scale which is very large in comparison to the width of the wave packet. Thus, the Hamiltonian can be linearized around the wave packet center \mathbf{r}_c ,

$$\hat{H} = \hat{H}_c + \Delta \hat{H} = \hat{H}_0 \left(\mathbf{q} + \frac{e}{\hbar} \mathbf{A}(\mathbf{r}_c, t) \right) - e\Phi(\mathbf{r}_c, t) + \frac{1}{2} \left\{ (\hat{\mathbf{r}} - \mathbf{r}_c), \frac{\partial \hat{H}}{\partial \mathbf{r}_c} \right\}, \quad (2.22)$$

with the local Hamiltonian at \mathbf{r}_c , $\hat{H}_c = \hat{H}_0 \left(\mathbf{q} + \frac{e}{\hbar} \mathbf{A}(\mathbf{r}_c, t) \right) - e\Phi(\mathbf{r}_c, t)$ and $\{, \}$ the anticommutator. The energy expectation value reads

$$\mathcal{E} = \langle \Psi | \hat{H}_c | \Psi \rangle + \langle \Psi | \Delta \hat{H} | \Psi \rangle = \mathcal{E}_c(\mathbf{r}_c, \mathbf{q}_c, t) - \text{Im} \left\langle \frac{\partial u}{\partial \mathbf{r}_c} \left| (\mathcal{E}_c - \hat{H}_c) \right| \frac{\partial u}{\partial \mathbf{q}} \right\rangle_{\mathbf{q}=\mathbf{q}_c}. \quad (2.23)$$

Here, $|u\rangle \equiv |u_{\mathbf{q}}(\mathbf{r}_c, t)\rangle$, \mathbf{q}_c is the center of the wave packet in \mathbf{q} -space and \mathcal{E}_c the eigenvalue of \hat{H}_c . The Lagrangian \mathcal{L} reads [49, 50]

$$\begin{aligned} \mathcal{L}(\mathbf{r}_c, \dot{\mathbf{r}}_c, \mathbf{q}_c, \dot{\mathbf{q}}_c, t) &= \left\langle \Psi \left| i\hbar \frac{d}{dt} - \hat{H} \right| \Psi \right\rangle \\ &= -\mathcal{E} + \hbar \left(\mathbf{q}_c \dot{\mathbf{r}}_c + \dot{\mathbf{q}}_c \cdot \left\langle u_c \left| i \frac{\partial u_c}{\partial \mathbf{q}_c} \right\rangle + \dot{\mathbf{r}}_c \cdot \left\langle u_c \left| i \frac{\partial u_c}{\partial \mathbf{r}_c} \right\rangle + \left\langle u_c \left| i \frac{\partial u_c}{\partial t} \right\rangle \right) \right), \end{aligned} \quad (2.24)$$

with $|u_c\rangle \equiv |u_{\mathbf{q}_c}(\mathbf{r}_c, t)\rangle$. Here, a total time derivative term was neglected since it has no influence on the semiclassical equations of motion.

Replacing the canonical crystal momentum \mathbf{q} by the gauge-invariant mechanical crystal momentum $\mathbf{k} = \mathbf{q} + \frac{e}{\hbar} \mathbf{A}(\mathbf{r}_c, t)$, the above equations can be further simplified. The periodic part of the Bloch states is now $|u_{\mathbf{k}}(\mathbf{r}_c, t)\rangle \equiv |u\rangle$. The eigenvalue of the local Hamiltonian reads

$$\mathcal{E}_c(\mathbf{r}_c, \mathbf{k}, t) = \mathcal{E}_0(\mathbf{k}) - e\Phi(\mathbf{r}_c, t), \quad (2.25)$$

with $\mathcal{E}_0(\mathbf{k})$ the eigenvalue of $\hat{H}_0(\mathbf{k})$. The energy correction $\Delta \mathcal{E} = \langle \Psi | \Delta \hat{H} | \Psi \rangle$ in Eq. (2.23) becomes

$$\Delta \mathcal{E} = -\frac{e}{2\hbar} \text{Im} \left\langle \frac{\partial u}{\partial \mathbf{k}} \left| \times (\mathcal{E}_0(\mathbf{k}) - \hat{H}_0(\mathbf{k})) \right| \frac{\partial u}{\partial \mathbf{k}} \right\rangle_{\mathbf{k}=\mathbf{k}_c} \cdot \mathbf{B} = -\mathcal{M} \cdot \mathbf{B}. \quad (2.26)$$

Here, \mathcal{M} is the orbital magnetic moment of the Bloch states [55]. Thus, the Lagrangian in terms of the gauge-invariant crystal momentum reads

$$\mathcal{L}(\mathbf{r}_c, \dot{\mathbf{r}}_c, \mathbf{k}_c, \dot{\mathbf{k}}_c, t) = -\mathcal{E}_0(\mathbf{k}_c) + \mathcal{M} \cdot \mathbf{B} + \hbar \dot{\mathbf{r}}_c \cdot \mathbf{k}_c - e \dot{\mathbf{r}}_c \cdot \mathbf{A}(\mathbf{r}_c, t) + \hbar \dot{\mathbf{k}}_c \cdot \left\langle u_c \left| i \frac{\partial u_c}{\partial \mathbf{k}_c} \right\rangle \right. \quad (2.27)$$

with $|u_c\rangle \equiv |u_{\mathbf{k}_c}\rangle$. Solving the Euler-Lagrange equations, the semiclassical equations of motion are obtained,

$$\dot{\mathbf{k}}_c = -\frac{e}{\hbar} \mathbf{E} - \frac{e}{\hbar} \dot{\mathbf{r}}_c \times \mathbf{B}, \quad (2.28a)$$

2. Semiclassical transport theory

$$\dot{\mathbf{r}}_c = \frac{1}{\hbar} \frac{\partial \mathcal{E}(\mathbf{k}_c)}{\partial \mathbf{k}_c} - \dot{\mathbf{k}}_c \times \boldsymbol{\Omega}_{\mathbf{k}_c}. \quad (2.28b)$$

Eq. (2.28a) is Newton's second axiom for the Lorentz force and Eq. (2.28b) corresponds to the electron velocity, which consists of the group velocity $\mathbf{v}_{\mathbf{k}} \equiv \frac{1}{\hbar} \frac{\partial \mathcal{E}(\mathbf{k}_c)}{\partial \mathbf{k}_c}$ and an additional Berry-curvature-related anomalous term. In the following, the index "c" is skipped and the coordinates \mathbf{k} and \mathbf{r} always refer to the center of the wave packet. Thus, the quantum mechanical wave packet is considered as a single particle located at \mathbf{r}_c with momentum \mathbf{k}_c . However, the group velocity of the wave packet is derived from the quantum mechanical band structure. Therefore, this approach is called *semiclassical*.

Decoupling Eqs. (2.28a) and (2.28b) leads to

$$\dot{\mathbf{k}} = \left(1 + \frac{e}{\hbar} \mathbf{B} \cdot \boldsymbol{\Omega}_{\mathbf{k}}\right)^{-1} \left[-\frac{e}{\hbar} \mathbf{E} - \frac{e}{\hbar} \mathbf{v}_{\mathbf{k}} \times \mathbf{B} - \frac{e^2}{\hbar^2} (\mathbf{E} \cdot \mathbf{B}) \boldsymbol{\Omega}_{\mathbf{k}}\right], \quad (2.29a)$$

$$\dot{\mathbf{r}} = \left(1 + \frac{e}{\hbar} \mathbf{B} \cdot \boldsymbol{\Omega}_{\mathbf{k}}\right)^{-1} \left[\mathbf{v}_{\mathbf{k}} + \frac{e}{\hbar} \mathbf{E} \times \boldsymbol{\Omega}_{\mathbf{k}} + \frac{e}{\hbar} (\boldsymbol{\Omega}_{\mathbf{k}} \cdot \mathbf{v}_{\mathbf{k}}) \mathbf{B}\right]. \quad (2.29b)$$

These semiclassical equations of motion are used for calculations of transport properties in the semiclassical limit. In the absence of a magnetic field, the anomalous velocity is perpendicular to the applied electric field. By the anomalous velocity, transport phenomena like the intrinsic anomalous Hall effect and the chiral anomaly can be explained.

2.2.2. Phase-space correction

In the presence of Berry curvature, the volume element $\Delta V = \Delta \mathbf{r} \Delta \mathbf{k}$ in the phase space spanned by \mathbf{r} and \mathbf{k} is not conserved in time, leading to a modified density of states due to violation of the Liouville theorem. If \mathbf{r} and \mathbf{k} change in time, the evolution of ΔV is [51]

$$\frac{1}{\Delta V} \frac{d\Delta V}{dt} = \frac{\partial}{\partial \mathbf{r}} \dot{\mathbf{r}} + \frac{\partial}{\partial \mathbf{k}} \dot{\mathbf{k}}. \quad (2.30)$$

Inserting the semiclassical equations of motion (2.28a) and (2.28b) and integrating over time yields

$$\Delta V(\mathbf{r}, \mathbf{k}) = \Delta V_0 \left(1 + \frac{e}{\hbar} \mathbf{B} \cdot \boldsymbol{\Omega}_{\mathbf{k}}\right)^{-1} \quad (2.31)$$

with ΔV_0 the initial phase-space volume element. Thus, in a system with vanishing Berry curvature or zero magnetic field, the phase-space element is constant during evolution in time whereas it is not conserved for nonzero \mathbf{B} and $\boldsymbol{\Omega}_{\mathbf{k}}$. This violation of the Liouville theorem is a consequence of the Berry phase leading to noncanonical equations of motion [51]. Importantly, the phase-space volume element is not mandatory conserved in a stationary system.

In order to consider the physical properties of a system within the semiclassical limit, this modified phase-space volume has to be compensated. Therefore, a corrected \mathbf{r} - and \mathbf{k} -dependent density of states is introduced,

$$\mathcal{N}(\mathbf{r}, \mathbf{k}) = \frac{1}{(2\pi)^d} \left(1 + \frac{e}{\hbar} \mathbf{B} \cdot \boldsymbol{\Omega}_{\mathbf{k}}\right)^{-1}. \quad (2.32)$$

The \mathbf{r} -dependence enters via the magnetic field, which can in general vary in space. The number of states in the volume element $\Delta V(\mathbf{r}, \mathbf{k}) \mathcal{N}(\mathbf{r}, \mathbf{k})$ is constant during time evolution.

2.3. Boltzmann equation

The occupation of states in a finite phase-space volume element is described by the distribution function $f_{\mathbf{k}}(\mathbf{r}, t)$. Its evolution under the influence of external fields, diffusion, and scattering processes can be expressed by the semiclassical Boltzmann transport equation,

$$\frac{\partial f_{\mathbf{k}}(\mathbf{r}, t)}{\partial t} + \left(\frac{\partial f_{\mathbf{k}}(\mathbf{r}, t)}{\partial t} \right)_{\text{field}} + \left(\frac{\partial f_{\mathbf{k}}(\mathbf{r}, t)}{\partial t} \right)_{\text{diff}} = \left(\frac{\partial f_{\mathbf{k}}(\mathbf{r}, t)}{\partial t} \right)_{\text{scatt}}, \quad (2.33)$$

with the field term

$$\left(\frac{\partial f_{\mathbf{k}}(\mathbf{r}, t)}{\partial t} \right)_{\text{field}} = \dot{\mathbf{k}} \cdot \frac{\partial f_{\mathbf{k}}(\mathbf{r}, t)}{\partial \mathbf{k}}, \quad (2.34)$$

the diffusion term

$$\left(\frac{\partial f_{\mathbf{k}}(\mathbf{r}, t)}{\partial t} \right)_{\text{diff}} = \dot{\mathbf{r}} \cdot \frac{\partial f_{\mathbf{k}}(\mathbf{r}, t)}{\partial \mathbf{r}}, \quad (2.35)$$

and the scattering term

$$\left(\frac{\partial f_{\mathbf{k}}(\mathbf{r}, t)}{\partial t} \right)_{\text{scatt}} = \sum_{\mathbf{k}'} [P_{\mathbf{k} \leftarrow \mathbf{k}'} g_{\mathbf{k}'}(\mathbf{r}, t) - P_{\mathbf{k}' \leftarrow \mathbf{k}} g_{\mathbf{k}}(\mathbf{r}, t)], \quad (2.36)$$

where $g_{\mathbf{k}}(\mathbf{r}, t) = f_{\mathbf{k}}(\mathbf{r}, t) - f_{\mathbf{k}}^0$ is the nonequilibrium part of the distribution function and $P_{\mathbf{k}' \leftarrow \mathbf{k}}$ is the microscopic transition probability rate for scattering from the state $|\mathbf{k}\rangle$ to the state $|\mathbf{k}'\rangle$. The first term on the right-hand side of Eq. (2.36) is the scattering-in term, the second term the scattering-out term describing the scattering processes into and out of the state $|\mathbf{k}\rangle$, respectively.

Considering a spatially homogeneous and stationary system, $f_{\mathbf{k}}(\mathbf{r}, t) = f_{\mathbf{k}}$, and using the semiclassical equations of motion, Eq. (2.29), the Boltzmann equation reads

$$-\frac{e}{\hbar} \left(1 + \frac{e}{\hbar} \mathbf{B} \cdot \boldsymbol{\Omega}_{\mathbf{k}} \right)^{-1} \left[\mathbf{E} + \mathbf{v}_{\mathbf{k}} \times \mathbf{B} + \frac{e}{\hbar} (\mathbf{E} \cdot \mathbf{B}) \boldsymbol{\Omega}_{\mathbf{k}} \right] \frac{\partial f_{\mathbf{k}}(\mathbf{r}, t)}{\partial \mathbf{k}} = \left(\frac{\partial f_{\mathbf{k}}(\mathbf{r}, t)}{\partial t} \right)_{\text{scatt}}. \quad (2.37)$$

For fermions, the equilibrium distribution function is the Fermi-Dirac distribution function,

$$f_{\mathbf{k}}^0 = \left[\exp \left(\frac{\mathcal{E}_{\mathbf{k}} - \mu}{k_{\text{B}} T} \right) + 1 \right]^{-1}, \quad (2.38)$$

where μ is the chemical potential, k_{B} the Boltzmann constant and T the temperature. In the following, zero temperature is considered, hence, μ is equivalent to the Fermi energy \mathcal{E}_{F} . For the nonequilibrium distribution function an ansatz of linear order in \mathbf{E} is used,

$$g_{\mathbf{k}} = \frac{\partial f_{\mathbf{k}}^0}{\partial \mathcal{E}} e \boldsymbol{\Lambda}_{\mathbf{k}} \cdot \mathbf{E} \quad (2.39)$$

with the mean free path $\boldsymbol{\Lambda}_{\mathbf{k}}$. Assuming only elastic scattering, Eqs. (2.36), (2.37) and (2.39) yield the linearized Boltzmann equation,

$$\begin{aligned} \boldsymbol{\Lambda}_{\mathbf{k}} - \frac{e}{\hbar} \tau_{\mathbf{k}} \left(1 + \frac{e}{\hbar} \mathbf{B} \cdot \boldsymbol{\Omega}_{\mathbf{k}} \right)^{-1} \left((\mathbf{v}_{\mathbf{k}} \times \mathbf{B}) \cdot \frac{\partial}{\partial \mathbf{k}} \right) \boldsymbol{\Lambda}_{\mathbf{k}} \\ = \tau_{\mathbf{k}} \left\{ \left(1 + \frac{e}{\hbar} \mathbf{B} \cdot \boldsymbol{\Omega}_{\mathbf{k}} \right)^{-1} \left[\mathbf{v}_{\mathbf{k}} + \frac{e}{\hbar} (\boldsymbol{\Omega}_{\mathbf{k}} \cdot \mathbf{v}_{\mathbf{k}}) \mathbf{B} \right] + \sum_{\mathbf{k}'} P_{\mathbf{k} \leftarrow \mathbf{k}'} \boldsymbol{\Lambda}_{\mathbf{k}'} \right\} \end{aligned} \quad (2.40)$$

with the momentum relaxation time

$$\tau_{\mathbf{k}} = \left(\sum_{\mathbf{k}'} P_{\mathbf{k}' \leftarrow \mathbf{k}} \right)^{-1}. \quad (2.41)$$

2. Semiclassical transport theory

The term $\propto \left(\mathbf{v}_{\mathbf{k}} \times \mathbf{B} \right) \cdot \frac{\partial}{\partial \mathbf{k}} \Lambda_{\mathbf{k}}$ represents the Lorentz force, the term $\propto \left[\mathbf{v}_{\mathbf{k}} + \frac{e}{\hbar} (\mathbf{\Omega}_{\mathbf{k}} \cdot \mathbf{v}_{\mathbf{k}}) \mathbf{B} \right]$ corresponds to the influence of the electric field and the term $\propto \sum_{\mathbf{k}'} P_{\mathbf{k} \leftarrow \mathbf{k}'} \Lambda_{\mathbf{k}'}$ accounts for the scattering-in processes. The scattering-out term is represented by the momentum relaxation time $\tau_{\mathbf{k}}$.

For the calculation of transport properties, the integro-differential equation (2.40) has to be solved. In general, an exact analytical solution cannot be found. In the following section, various approximations and methods for solving the linearized Boltzmann equation are introduced.

2.3.1. Relaxation time approximation

A simple phenomenological ansatz for solving the Boltzmann equation (2.37) is the relaxation time approximation

$$\left(\frac{\partial f_{\mathbf{k}}}{\partial t} \right)_{\text{scatt}} = -\frac{1}{\tau_{\mathbf{k}}^{\text{R}}} g_{\mathbf{k}}, \quad (2.42)$$

with the relaxation time $\tau_{\mathbf{k}}^{\text{R}}$, which is not necessarily equivalent to the momentum relaxation time defined in Eq. (2.41). The relaxation time ansatz yields the Boltzmann equation

$$\Lambda_{\mathbf{k}} - \frac{e}{\hbar} \tau_{\mathbf{k}}^{\text{R}} \left(1 + \frac{e}{\hbar} \mathbf{B} \cdot \mathbf{\Omega}_{\mathbf{k}} \right)^{-1} \left(\mathbf{v}_{\mathbf{k}} \times \mathbf{B} \right) \frac{\partial}{\partial \mathbf{k}} \Lambda_{\mathbf{k}} = \tau_{\mathbf{k}}^{\text{R}} \left(1 + \frac{e}{\hbar} \mathbf{B} \cdot \mathbf{\Omega}_{\mathbf{k}} \right)^{-1} \left[\mathbf{v}_{\mathbf{k}} + \frac{e}{\hbar} (\mathbf{\Omega}_{\mathbf{k}} \cdot \mathbf{v}_{\mathbf{k}}) \mathbf{B} \right]. \quad (2.43)$$

For $\mathbf{B} = 0$, the linearized Boltzmann equation in relaxation time approximation simplifies to

$$\Lambda_{\mathbf{k}} = \tau_{\mathbf{k}}^{\text{R}} \mathbf{v}_{\mathbf{k}}. \quad (2.44)$$

This ansatz is often interpreted as a shift of the Fermi surface in \mathbf{k} -space [56]. Obviously, the relaxation time approximation does not take into account the full scattering-in term. However, scattering-in processes from $|\mathbf{k}'\rangle$ to $|\mathbf{k}\rangle$ can be projected into the relaxation time $\tau_{\mathbf{k}}^{\text{R}}$, as in the transport lifetime discussed below.

Momentum relaxation time

A simple but often sufficient approach is using the momentum relaxation time defined by Eq. (2.41) in the relaxation time approximation, $\tau_{\mathbf{k}}^{\text{R}} = \tau_{\mathbf{k}}$, for $\mathbf{B} = 0$ leading to

$$\Lambda_{\mathbf{k}}^{\text{RTA}} = \tau_{\mathbf{k}} \mathbf{v}_{\mathbf{k}}. \quad (2.45)$$

In this approach, scattering-in processes are neglected. Mean free path and group velocity are parallel. In the presence of a finite magnetic field, $\mathbf{B} \neq 0$, the mean free path in relaxation time approximation is given by Eq. (2.43) with $\tau_{\mathbf{k}}^{\text{RTA}} = \tau_{\mathbf{k}}$. Here, the mean free path is not mandatory parallel to the group velocity. Neglecting the Lorentz force in Eq. (2.43) allows direct calculation of $\Lambda_{\mathbf{k}}^{\text{RTA}}$,

$$\Lambda_{\mathbf{k}}^{\text{RTA}} = \tau_{\mathbf{k}} \left(1 + \frac{e}{\hbar} \mathbf{B} \cdot \mathbf{\Omega}_{\mathbf{k}} \right)^{-1} \left[\mathbf{v}_{\mathbf{k}} + \frac{e}{\hbar} (\mathbf{\Omega}_{\mathbf{k}} \cdot \mathbf{v}_{\mathbf{k}}) \mathbf{B} \right]. \quad (2.46)$$

Although the Lorentz force term can be in general significant, neglecting this term is reasonable if transport along \mathbf{B} is considered.

Transport lifetime

The concept of transport lifetime includes scattering-out as well as scattering-in processes. Here, it is discussed only for $\mathbf{B} = 0$. The mean free path is assumed to be in the direction of the group velocity,

$$\Lambda_{\mathbf{k}}^{\text{tr}} = \tau_{\mathbf{k}}^{\text{tr}} \mathbf{v}_{\mathbf{k}}, \quad (2.47)$$

where $\tau_{\mathbf{k}}^{\text{tr}}$ is the transport lifetime including scattering-out as well as scattering-in processes. Using the ansatz (2.47), the linearized Boltzmann equation (2.40) transforms to

$$\mathbf{v}_{\mathbf{k}} = \sum_{\mathbf{k}'} (P_{\mathbf{k}' \leftarrow \mathbf{k}} \tau_{\mathbf{k}}^{\text{tr}} \mathbf{v}_{\mathbf{k}} - P_{\mathbf{k} \leftarrow \mathbf{k}'} \tau_{\mathbf{k}'}^{\text{tr}} \mathbf{v}_{\mathbf{k}'}) . \quad (2.48)$$

For an isotropic one-band system the transport lifetime is isotropic and can be calculated from Eq. (2.48) via

$$\tau_{\mathbf{k}}^{\text{tr}} = \left(\sum_{\mathbf{k}'} P_{\mathbf{k}' \leftarrow \mathbf{k}} - P_{\mathbf{k} \leftarrow \mathbf{k}'} \frac{v_{\mathbf{k}'}}{v_{\mathbf{k}}} \cos(\mathbf{v}_{\mathbf{k}'}, \mathbf{v}_{\mathbf{k}}) \right)^{-1} . \quad (2.49)$$

Here, the scattering-in processes are included by a projection on the direction of the group velocity. However, in general, $\tau_{\mathbf{k}}^{\text{tr}}$ depends on the wave vector \mathbf{k} and the band. In this case, the simplification (2.49) cannot be made and Eq. (2.48) has to be solved. For isotropic (multi-band) systems, it can be solved analytically, for more complex systems in general a numerical solution is necessary.

2.3.2. Iterative solution

Solving the linearized Boltzmann equation iteratively provides the opportunity of calculating the mean free path up to arbitrary accuracy while including the scattering-in processes and the Lorentz force,

$$\Lambda_{\mathbf{k}}^{(i)} = \tau_{\mathbf{k}} \left\{ \left(1 + \frac{e}{\hbar} \mathbf{B} \cdot \boldsymbol{\Omega}_{\mathbf{k}} \right)^{-1} \left[\left(\frac{e}{\hbar} (\mathbf{v}_{\mathbf{k}} \times \mathbf{B}) \cdot \frac{\partial}{\partial \mathbf{k}} \right) \Lambda_{\mathbf{k}}^{(i-1)} + \mathbf{v}_{\mathbf{k}} + \frac{e}{\hbar} (\boldsymbol{\Omega}_{\mathbf{k}} \cdot \mathbf{v}_{\mathbf{k}}) \mathbf{B} \right] + \sum_{\mathbf{k}'} P_{\mathbf{k} \leftarrow \mathbf{k}'} \Lambda_{\mathbf{k}'}^{(i-1)} \right\} , \quad (2.50)$$

$$\Lambda_{\mathbf{k}}^{(0)} = 0$$

with $i = 1, 2, 3, \dots$. Calculating the \mathbf{k} -derivative of $\Lambda_{\mathbf{k}}$ analytically becomes more demanding with increasing order of iteration. A numerical calculation of this derivative can be challenging since $\Lambda_{\mathbf{k}}$ is not known as a closed expression.

For $\mathbf{B} = 0$, the first order iteration $\Lambda_{\mathbf{k}}^{(1)} = \tau_{\mathbf{k}} \mathbf{v}_{\mathbf{k}}$ corresponds to the relaxation time approximation with momentum relaxation time. In the presence of a nonzero magnetic field, $\Lambda_{\mathbf{k}}^{(1)}$ is equivalent to the relaxation time approximation neglecting the Lorentz force (Eq. (2.46)). All iterations with $i \geq 2$ include scattering-in terms allowing nonparallel $\Lambda_{\mathbf{k}}$ and $\mathbf{v}_{\mathbf{k}}$ even for $\mathbf{B} = 0$. These contributions nonparallel to $\mathbf{v}_{\mathbf{k}}$ are also called *vertex corrections*.

2.3.3. Fermi surface harmonics

The method of Fermi surface harmonics (FSH), established in Refs. [57–60], provides a closed solution of the Boltzmann equation in the presence of magnetic and electric fields. By expanding the mean free path in terms of the Fermi surface harmonics $\Psi_M(\mathbf{k})$, its \mathbf{B} - and \mathbf{k} -dependence are separated,

$$\Lambda_{\mathbf{k}}(\mathbf{B}) = \sum_M \Lambda_M(\mathbf{B}) \Psi_M(\mathbf{k}) . \quad (2.51)$$

The FSHs are constructed from polynomials of the Cartesian components of the group velocity at the Fermi surface,

$$\Psi_M(\mathbf{k}) = \Psi_{n_x, n_y, n_z}(\mathbf{k}) = v_x^{n_x}(\mathbf{k}) v_y^{n_y}(\mathbf{k}) v_z^{n_z}(\mathbf{k}) \xi_{n_{\text{FS}}}(\mathbf{k}) . \quad (2.52)$$

The multi-index $M = (n_x, n_y, n_z, n_{\text{FS}})$ includes the integers $n_x, n_y, n_z \geq 0$ and the Fermi sheet index $n_{\text{FS}} = 1 \dots N_{\text{FS}}$, with N_{FS} the number of Fermi sheets. The FSHs are orthonormalized on the Fermi surface, or, in general, an iso-energy surface,

$$\sum_{\mathbf{k}} \delta(\mathcal{E}_{\mathbf{k}} - \mathcal{E}_{\text{F}}) \Psi_M(\mathbf{k}) \Psi_{M'}(\mathbf{k}) = \delta_{MM'} \sum_{\mathbf{k}} \delta(\mathcal{E}_{\mathbf{k}} - \mathcal{E}_{\text{F}}) . \quad (2.53)$$

2. Semiclassical transport theory

The order of the FSH is $N_{\text{FSH}} = n_x + n_y + n_z$. For a multi-sheeted Fermi surface the number of FSHs is increased likewise, which is expressed by the index n_{FS} . The weighting function $\xi_{n_{\text{FS}}}(\mathbf{k})$ ensures orthogonality of the FSHs with different n_{FS} . Conventionally, two different representations are used [58]: In the disjoint FSH representation, $\xi_{n_{\text{FS}}}$ provides a nonzero FSH only on one Fermi sheet. In the symmetric representation, however, each FSH is defined on all Fermi sheets.

Alternatively, using spherical harmonics or polynomials of the Cartesian components of the wave vector at the Fermi surface as a basis seems to be self-evident. The spherical harmonics are well-known, providing a complete set of orthonormalized functions. However, they do not reproduce the lattice-periodicity in reciprocal space and are not orthonormalized on anisotropic Fermi surfaces [58, 59]. Polynomials of the wave vector components provide cell-periodicity and orthogonality on the Fermi surface, but their derivatives are not continuous on the zone boundaries [58, 59]. The Fermi surface harmonics provide cell-periodicity as well as continuous derivatives. However, their completeness is not proven for general systems [58, 59]. For isotropic systems, all three sets of functions are equivalent in the first Brillouin zone.

The original FSH formalism introduced in Refs. [58, 59] does not contain Berry curvature effects. However, these effects can be directly included. Expanding the mean free path in Eq. (2.40) in terms of the FSHs yields the Boltzmann equation

$$\sum_M \left\{ \Psi_M(\mathbf{k}) + \tau_{\mathbf{k}} \left(1 + \frac{e}{\hbar} \mathbf{B} \cdot \boldsymbol{\Omega}_{\mathbf{k}} \right)^{-1} \left(-\frac{e}{\hbar} \mathbf{v}_{\mathbf{k}} \times \mathbf{B} \frac{\partial}{\partial \mathbf{k}} \Psi_M(\mathbf{k}) \right) - \tau_{\mathbf{k}} \sum_{\mathbf{k}'} P_{\mathbf{k} \rightarrow \mathbf{k}'} \Psi_M(\mathbf{k}') \right\} \boldsymbol{\Lambda}_M(\mathbf{B}) = \tau_{\mathbf{k}} \left(1 + \frac{e}{\hbar} \mathbf{B} \cdot \boldsymbol{\Omega}_{\mathbf{k}} \right)^{-1} \left[\mathbf{v}_{\mathbf{k}} + \frac{e}{\hbar} (\boldsymbol{\Omega}_{\mathbf{k}} \cdot \mathbf{v}_{\mathbf{k}}) \cdot \mathbf{B} \right]. \quad (2.54)$$

It can be transformed to

$$\sum_{M'} (\mathcal{B}_{MM'} + \mathcal{C}_{MM'}) \boldsymbol{\Lambda}_{M'}(\mathbf{B}) = \mathbf{D}_M \quad (2.55)$$

with the field term

$$\mathcal{B}_{MM'} = \frac{\sum_{\mathbf{k}} \delta(\mathcal{E}_{\mathbf{k}} - \mathcal{E}_F) \Psi_M(\mathbf{k}) \tau_{\mathbf{k}} \left(1 + \frac{e}{\hbar} \mathbf{B} \cdot \boldsymbol{\Omega}_{\mathbf{k}} \right)^{-1} \left(-\frac{e}{\hbar} (\mathbf{v}_{\mathbf{k}} \times \mathbf{B}) \frac{\partial}{\partial \mathbf{k}} \Psi_{M'}(\mathbf{k}) \right)}{\sum_{\mathbf{k}} \delta(\mathcal{E}_{\mathbf{k}} - \mathcal{E}_F)}, \quad (2.56)$$

containing the Lorentz force, the scattering term

$$\mathcal{C}_{MM'} = \delta_{MM'} - \frac{\sum_{\mathbf{k}, \mathbf{k}'} \delta(\mathcal{E}_{\mathbf{k}} - \mathcal{E}_F) \Psi_M(\mathbf{k}) \tau_{\mathbf{k}} P_{\mathbf{k} \rightarrow \mathbf{k}'} \Psi_{M'}(\mathbf{k}')}{\sum_{\mathbf{k}} \delta(\mathcal{E}_{\mathbf{k}} - \mathcal{E}_F)} \quad (2.57)$$

accounting for scattering-in processes, and the vector

$$\mathbf{D}_M = \frac{\sum_{\mathbf{k}} \delta(\mathcal{E}_{\mathbf{k}} - \mathcal{E}_F) \Psi_M(\mathbf{k}) \tau_{\mathbf{k}} \left\{ \left(1 + \frac{e}{\hbar} \mathbf{B} \cdot \boldsymbol{\Omega}_{\mathbf{k}} \right)^{-1} \left[\mathbf{v}_{\mathbf{k}} + \frac{e}{\hbar} (\boldsymbol{\Omega}_{\mathbf{k}} \cdot \mathbf{v}_{\mathbf{k}}) \cdot \mathbf{B} \right] \right\}}{\sum_{\mathbf{k}} \delta(\mathcal{E}_{\mathbf{k}} - \mathcal{E}_F)}. \quad (2.58)$$

Thus, the problem of solving the integro-differential Boltzmann equation reduces to solving the matrix equation (2.55). Depending on the maximum order N_{FSH} contained in this ansatz, the Boltzmann equation can be solved with arbitrary accuracy including all terms, especially the Lorentz force term and the scattering-in contributions. From the solution of the mean free path decomposed in terms of the Fermi velocity, insights into the effects of scattering and external fields on the electron paths can be gained.

Typically, the number of FSHs used to solve the Boltzmann equation ($\sim 10^1 \dots 10^2$) is considerably smaller than the number of \mathbf{k} -points on the Fermi surface used in the calculations ($\sim 10^4 \dots 10^5$) by

several orders of magnitude. Therefore, the dimension of the system of equations in Eq. (2.55) is remarkably reduced in comparison to Eq. (2.40), lowering the numerical effort.

2.3.4. Calculation of semiclassical transport properties

In the semiclassical limit, a macroscopic property \mathbf{O} is calculated as sum of the corresponding expectation values of all occupied states.

$$\mathbf{O} = \sum_{\mathbf{k}} \langle \hat{\mathbf{O}} \rangle_{\mathbf{k}} f_{\mathbf{k}}, \quad (2.59)$$

with $\langle \hat{\mathbf{O}} \rangle_{\mathbf{k}} = \langle \mathbf{k} | \hat{\mathbf{O}} | \mathbf{k} \rangle$ the \mathbf{k} -dependent expectation value of the operator $\hat{\mathbf{O}}$. The distribution function $f_{\mathbf{k}}$ is obtained by solving the Boltzmann equation. Usually, the electronic states are dense in \mathbf{k} -space, therefore, the transition

$$\sum_{\mathbf{k}} \rightarrow V^{(d)} \int \mathcal{N}(\mathbf{k}) d\mathbf{k}^d \quad (2.60)$$

is performed. Here, the density of states given by Eq. (2.32) is used, which is independent of \mathbf{r} since the external fields are homogeneous.

2.3.5. Limits of the Boltzmann theory

The semiclassical Boltzmann approach is predicated on various assumptions and approximations, therefore, its limits are briefly sketched here.

The semiclassical approach, especially the wave packet ansatz, bases on the assumption that the external fields vary on a large scale in comparison to the lattice constant [42]. Thus, it is valid only in the limit of slowly varying fields.

Interband contributions enter the Boltzmann equation via the Berry curvature. Further, scattering between different bands is considered. However, the wave packet ansatz does not fully include interband transitions since a wave packet $|\Psi_{\mathbf{W}}^n(\mathbf{r}, t)\rangle$ contains only Bloch states of a single band n . For regions in the Brillouin zone in which two (or even more) bands are close to each other or even intersect, these interband transitions can be important and affect the transport properties remarkably. Interband transition can occur if $\hbar\omega_{\text{EM}} \geq \Delta\mathcal{E}$, with ω_{EM} the frequency of the electromagnetic field and $\Delta\mathcal{E}$ the energy gap between neighboring bands. Further, these transitions can be induced by large magnitudes of the external fields, i.e. if $eEa \geq \Delta\mathcal{E}^2/\varepsilon_{\text{F}}$ or $\hbar\omega_c \geq \Delta\mathcal{E}^2/\varepsilon_{\text{F}}$ with a the lattice constant and ω_c the cyclotron frequency [42]. As long as the Fermi level is far from these (nearby) crossings and the fields are comparably small and slowly oscillating, the Boltzmann approach is applicable.

The importance of interband transitions can be estimated via the lifetime broadening: The finite lifetime of the electronic states is interpreted as a broadening of the energy bands. When two broadened bands overlap, the interband contributions cannot be neglected. By comparing this lifetime broadening $\Gamma \sim \hbar/\tau$ to the energy gap $\Delta\mathcal{E}$ between two neighboring bands, one of which is occupied, the other unoccupied, the validity of the Boltzmann approach can be estimated. If $\Gamma \geq \Delta\mathcal{E}$, interband transitions have a pronounced effect on the transport properties. For $\Gamma \ll \Delta\mathcal{E}$, the interband contributions can be safely neglected. The additional contributions to the transport properties due to interband transitions [61] can be considered within the Kubo theory introduced in the next section.

2. Semiclassical transport theory

2.4. Kubo theory

In addition to solving the semiclassical Boltzmann equation, another method of calculating the linear response to externally applied fields is the Kubo approach [62, 63]. The response of a macroscopic observable \mathbf{O} with the corresponding operator $\hat{\mathbf{O}}$ to an external perturbation is considered.

In equilibrium, the system is described by the Hamiltonian \hat{H}_0 . The equilibrium eigenstate and expectation value \mathbf{O}_0 are known. In the presence of an external perturbation switched on at $t = t_0$, the Hamiltonian is

$$\hat{H}(t) = \hat{H}_0 + \int \hat{\mathbf{F}}(\mathbf{r}) \cdot \mathbf{h}(\mathbf{r}, t) d\mathbf{r}^d \theta(t - t_0). \quad (2.61)$$

Here, the vector $\mathbf{h}(\mathbf{r}, t)$ represents an external force, $\hat{\mathbf{F}}(\mathbf{r})$ is the operator coupling the force to the system, and θ is the Heaviside step function. The change of the observable, $\delta\mathbf{O}$ is given by the Kubo formula [62],

$$\delta\mathbf{O}(t) = \int_{t_0}^t \hat{\chi}^{OF}(\mathbf{r}, t, \mathbf{r}', t') \mathbf{h}(\mathbf{r}', t') dt' d\mathbf{r}^d \quad (2.62)$$

with the response tensor

$$\chi_{ij}^{OF}(\mathbf{r}, t, \mathbf{r}', t') = -\frac{i}{\hbar} \theta(t - t') \left\langle \left[\hat{O}_i^I(\mathbf{r}, t), \hat{F}_j^I(\mathbf{r}', t') \right] \right\rangle_0. \quad (2.63)$$

Here, $\hat{\mathbf{O}}^I(\mathbf{r}, t) = e^{\frac{i}{\hbar} \hat{H}_0 t} \hat{\mathbf{O}}(\mathbf{r}) e^{-\frac{i}{\hbar} \hat{H}_0 t}$ in the interaction picture and $\langle \cdot \rangle_0$ is the canonical ensemble average. For an externally applied electric field, the Kubo formula can be transformed to [64, 65],

$$\begin{aligned} \delta\mathbf{O} = & -\frac{e\hbar}{\pi} \sum_{\mathbf{k}, n, m} \frac{\Gamma^2 \text{Re}(\langle \mathbf{k}^n | \hat{\mathbf{O}} | \mathbf{k}^m \rangle \langle \mathbf{k}^m | \hat{\mathbf{v}} \cdot \mathbf{E} | \mathbf{k}^n \rangle)}{[(\mathcal{E}_F - \mathcal{E}_n(\mathbf{k}))^2 + \Gamma^2] [(\mathcal{E}_F - \mathcal{E}_m(\mathbf{k}))^2 + \Gamma^2]} \\ & - 2\hbar e \sum_{\mathbf{k}, n \neq m} f_{\mathbf{k}}^n (1 - f_{\mathbf{k}}^m) \frac{\text{Im}(\langle \mathbf{k}^n | \hat{\mathbf{O}} | \mathbf{k}^m \rangle \langle \mathbf{k}^m | \hat{\mathbf{v}} \cdot \mathbf{E} | \mathbf{k}^n \rangle)}{(\mathcal{E}^n(\mathbf{k}) - \mathcal{E}^m(\mathbf{k}))^2}. \end{aligned} \quad (2.64)$$

Here, $\hat{\mathbf{v}} = i/\hbar [\hat{H}_0, \mathbf{r}]$ is the velocity operator, \mathcal{E}^n are eigenvalues of the unperturbed Hamiltonian \hat{H}_0 , and Γ is the lifetime broadening ($\Gamma \sim \hbar/\tau$). The first expression on the right-hand side of Eq. (2.64) represents extrinsic contributions. The terms with $n = m$ are approximately equivalent to the Boltzmann approach in a constant relaxation time approximation. For $\Gamma \geq |\mathcal{E}^n(\mathbf{k}) - \mathcal{E}^m(\mathbf{k})|$ the interband transitions ($n \neq m$) become significant and the Boltzmann approach is not sufficient to describe the transport properties. The second term on the right-hand side of Eq. (2.64) corresponds to intrinsic contributions and contains only interband transitions. These intrinsic contributions are independent of the scattering properties of the system. In general, interband transitions can occur due to the additional energy brought into the system by the external electric field. The extrinsic and intrinsic contributions in Eq. (2.64) transform oppositely under time reversal.

2.5. Scattering

The scattering term in the Boltzmann equation discussed in section 2.3 accounts for transitions from one state $|\mathbf{k}\rangle$ to states $|\mathbf{k}'\rangle$ due to scattering at impurities breaking the translational symmetry of the crystal. In absence of impurities, the Hamiltonian is \hat{H}_0 with the eigenfunctions $|\Psi_{\mathbf{k}}^0(\mathbf{r})\rangle$. Whereas in the main part of this work the unperturbed state is usually denoted by $|\mathbf{k}\rangle$, it is called $|\Psi_{\mathbf{k}}^0(\mathbf{r})\rangle$ in this section in order to avoid confusion with the scattered wave function, which is named $|\Psi_{\mathbf{k}}(\mathbf{r})\rangle$ here.

Now, a space-dependent scattering potential $\Delta U(\mathbf{r})$ is included, modifying the Hamiltonian to

$\hat{H}_0(\mathbf{r}) + \Delta U(\mathbf{r})$. A Bloch eigenstate of \hat{H}_0 is scattered at the impurity into the perturbed state $|\Psi_{\mathbf{k}}(\mathbf{r})\rangle$, which is an eigenstate of $\hat{H}_0(\mathbf{r}) + \Delta U(\mathbf{r})$. The scattered wave function can be expressed using the Green's function formalism [66],

$$\begin{aligned} |\Psi_{\mathbf{k}}(\mathbf{r})\rangle &= |\Psi_{\mathbf{k}}^0(\mathbf{r})\rangle + \int G^0(\mathbf{r}, \mathbf{r}', \mathcal{E}) \Delta U(\mathbf{r}') |\Psi_{\mathbf{k}}(\mathbf{r}')\rangle d\mathbf{r}'^d \\ &= |\Psi_{\mathbf{k}}^0(\mathbf{r})\rangle + \int G(\mathbf{r}, \mathbf{r}', \mathcal{E}) \Delta U(\mathbf{r}') |\Psi_{\mathbf{k}}^0(\mathbf{r}')\rangle d\mathbf{r}'^d . \end{aligned} \quad (2.65)$$

Here, $G^0(\mathbf{r}, \mathbf{r}', \mathcal{E})$ is the Green's function of the unperturbed system satisfying

$$[\mathcal{E} - \hat{H}_0(\mathbf{r})] G^0(\mathbf{r}, \mathbf{r}', \mathcal{E}) = \delta(\mathbf{r} - \mathbf{r}'), \quad (2.66)$$

and the perturbed system's Green's function $G(\mathbf{r}, \mathbf{r}', \mathcal{E})$ fulfills

$$[\mathcal{E} - \hat{H}_0(\mathbf{r}) - \Delta U(\mathbf{r})] G(\mathbf{r}, \mathbf{r}', \mathcal{E}) = \delta(\mathbf{r} - \mathbf{r}'). \quad (2.67)$$

The first line of Eq. (2.65) is called Lippmann-Schwinger equation and corresponds to the integral form of the Schrödinger equation [66]. It can be expanded into a Born series,

$$\begin{aligned} |\Psi_{\mathbf{k}}(\mathbf{r})\rangle &= |\Psi_{\mathbf{k}}^0(\mathbf{r})\rangle + \int G^0(\mathbf{r}, \mathbf{r}', \mathcal{E}) \Delta U(\mathbf{r}') \Psi_{\mathbf{k}}^0(\mathbf{r}') d\mathbf{r}'^d \\ &+ \int \int G^0(\mathbf{r}, \mathbf{r}', \mathcal{E}) \Delta U(\mathbf{r}') G^0(\mathbf{r}', \mathbf{r}'', \mathcal{E}) \Delta U(\mathbf{r}'') |\Psi_{\mathbf{k}}^0(\mathbf{r}'')\rangle d\mathbf{r}'^d d\mathbf{r}''^d + \dots . \end{aligned} \quad (2.68)$$

Here, the first term on the right-hand side is the zeroth order Born approximation, simply called *Born approximation*, the second term is the first order Born approximation, etc.

The transition matrix $T_{\mathbf{k}' \leftarrow \mathbf{k}}$ for scattering from $|\Psi_{\mathbf{k}}^0(\mathbf{r})\rangle$ to $|\Psi_{\mathbf{k}'}(\mathbf{r})\rangle$ is

$$T_{\mathbf{k}' \leftarrow \mathbf{k}} = \langle \Psi_{\mathbf{k}'}^0(\mathbf{r}) | \hat{T} | \Psi_{\mathbf{k}}^0(\mathbf{r}) \rangle = \langle \Psi_{\mathbf{k}'}^0(\mathbf{r}) | \Delta U(\mathbf{r}) | \Psi_{\mathbf{k}}(\mathbf{r}) \rangle \quad (2.69)$$

with the transition operator \hat{T} . In dilute limit the scattering potentials U_i of various impurities located at \mathbf{R}_i are considered non-overlapping yielding a total scattering potential

$$\Delta U(\mathbf{r}) = \sum_i U_i(\mathbf{r} - \mathbf{R}_i). \quad (2.70)$$

Assuming only one type of impurities ($U_i = U$) and Bloch-like undisturbed states, it is sufficient to consider scattering at a single impurity located at \mathbf{R}_i , expressed by the single transition matrix

$$T_{\mathbf{k}' \leftarrow \mathbf{k}}^i = \langle \Psi_{\mathbf{k}'}^0(\mathbf{r}) | U(\mathbf{r} - \mathbf{R}_i) | \Psi_{\mathbf{k}}(\mathbf{r}) \rangle = \tilde{T}_{\mathbf{k}' \leftarrow \mathbf{k}}. \quad (2.71)$$

The microscopic transition probability for elastic scattering is expressed by Fermi's golden rule,

$$P_{\mathbf{k}' \leftarrow \mathbf{k}} = \frac{2\pi}{\hbar} N_{\text{at}} c_i |\tilde{T}_{\mathbf{k}' \leftarrow \mathbf{k}}|^2 \delta(\mathcal{E}_{\mathbf{k}'} - \mathcal{E}_{\mathbf{k}}). \quad (2.72)$$

Here, N_{at} is the total number of atoms of the system, c_i is the atomic impurity concentration and $\delta(x)$ is the Dirac delta function. If the transition matrix elements depend on the impurity positions, for example in systems with localized surface states, $\tilde{T}_{\mathbf{k}' \leftarrow \mathbf{k}}$, which is the single transition matrix $T_{\mathbf{k}' \leftarrow \mathbf{k}}^i$ averaged over all impurity positions, is inserted instead of $\tilde{T}_{\mathbf{k}' \leftarrow \mathbf{k}}$.

In this work the scattered wave $|\Psi_{\mathbf{k}}(\mathbf{r})\rangle$ is approximated by the zeroth order Born approximation, $|\Psi_{\mathbf{k}}(\mathbf{r})\rangle \approx |\Psi_{\mathbf{k}}^0(\mathbf{r})\rangle$. The scattering potentials are assumed δ -shaped,

$$\Delta U(\mathbf{r}) = \sum_i U_0 \delta(\mathbf{r} - \mathbf{R}_i) V_{\text{at}}^{(d)} \quad (2.73)$$

2. Semiclassical transport theory

with U_0 the scattering strength and $V_{\text{at}}^{(d)}$ the volume per atom in d -dimensional space. In general, U_0 is a matrix and can be \mathbf{k} -dependent. However, in this work it is assumed \mathbf{k} -independent. U_0 is a scalar for nonmagnetic impurities and a matrix for magnetic impurities.

3. Spin-orbit coupling

Besides their electric charge, electrons carry a spin degree of freedom, which affects the electronic structure via spin-orbit interaction. Spin-orbit coupling (SOC) can split degenerate bands, leading to unique band structure properties, like Weyl points, topological surface states, and spin-momentum locking. Thereby, it induces transport phenomena like the spin Hall effect, the Edelstein effect or the chiral anomaly, from which the latter two will be considered in this work.

In this chapter SOC is introduced as a relativistic correction to the Hamiltonian. Subsequently, a minimal two-band model is presented which is sufficient to consider most of the phenomena discussed in this work. The spin-orbit field formalism, which is a useful tool for the analysis of spin-orbit effects, is introduced. Finally, several effects of SOC on the band structure are discussed: Rashba splitting, Dresselhaus splitting as well as topological insulators and semimetals.

3.1. Relativistic correction to the Hamiltonian

Spin-orbit interaction is a relativistic phenomenon. However, although it originates from special relativity, SOC can be included in a non-relativistic Hamiltonian as a correction term. Therefore, relativistic equations are employed in order to derive the spin-orbit coupling contribution in the non-relativistic Hamiltonian. The derivation of the SOC term in this section follows the textbook of Stepanow [67].

In the non-relativistic limit, a free-electron system is described by the Schrödinger equation

$$i\hbar \frac{\partial}{\partial t} \Psi(\mathbf{r}, t) = \frac{\hat{\mathbf{p}}^2}{2m} \Psi(\mathbf{r}, t) = \hat{H}_{\text{nr}} \Psi(\mathbf{r}, t) \quad (3.1)$$

with the electron mass $m = m_e$. This equation leads to the non-relativistic relation between energy and momentum $\mathcal{E} = \mathbf{p}^2/2m$. Due to the different order of derivatives in time and space, Eq. (3.1) is not Lorentz invariant. Thus, in order to describe relativistic systems and to obtain a relativistic energy-momentum relation, the Dirac equation for free particles was introduced [68, 69],

$$i\hbar \frac{\partial}{\partial t} \Psi(\mathbf{r}, t) = (c\hat{\boldsymbol{\alpha}} \cdot \hat{\mathbf{p}} + mc^2\hat{\beta}) \Psi(\mathbf{r}, t) = \hat{H}_{\text{D}} \Psi(\mathbf{r}, t), \quad (3.2)$$

which has the structure of a Schrödinger equation with the Hamiltonian \hat{H}_{D} . Here, c is the speed of light, $\Psi(\mathbf{r}, t)$ is a four-component spinor and the standard representation of the 4×4 matrices $\hat{\alpha}_i$ and $\hat{\beta}$ is

$$\hat{\alpha}_i = \hat{\sigma}_x \otimes \hat{\sigma}_i, \quad \hat{\beta} = \hat{\sigma}_z \otimes \hat{\sigma}_0 \quad (3.3)$$

with the 2×2 Pauli matrices $\hat{\sigma}_i$ ($i = x, y, z$) and the unity matrix $\hat{\sigma}_0 = \mathbb{1}_{2 \times 2}$. Eq. (3.2) is Lorentz invariant and results in the relativistic energy-momentum relation $\mathcal{E}^2 = c^2\mathbf{p}^2 + m^2c^4$. The angular momentum operator $\hat{\mathbf{L}} = \mathbf{r} \times \hat{\mathbf{p}}$ does not commute with the Hamiltonian \hat{H}_{D} but the total angular momentum $\hat{\mathbf{J}} = \hat{\mathbf{L}} + \hbar/2\hat{\boldsymbol{\Sigma}}$ does. Here, $\hbar/2\hat{\boldsymbol{\Sigma}}$ is the spin operator with $\hat{\boldsymbol{\Sigma}} = \hat{\sigma}_0 \otimes \hat{\boldsymbol{\sigma}}$.

In the presence of electromagnetic fields the Dirac equation reads

$$i\hbar \frac{\partial}{\partial t} \Psi(\mathbf{r}, t) = (c\hat{\boldsymbol{\alpha}} (\hat{\mathbf{p}} + e\mathbf{A}) + mc^2\hat{\beta} - e\Phi) \Psi(\mathbf{r}, t) \quad (3.4)$$

with the electromagnetic potentials \mathbf{A} and Φ . In the following, the Dirac equation (3.4) is analyzed in the non-relativistic limit. The electric field is assumed stationary and the magnetic field is zero.

Using the ansatz $\Psi(\mathbf{r}, t) = e^{-i\frac{\mathcal{E}+mc^2}{\hbar}t} \Psi'(\mathbf{r})$ with $\Psi' = \begin{pmatrix} \Psi'_1 \\ \Psi'_2 \end{pmatrix}$, in which Ψ'_1 and Ψ'_2 are two-component

3. Spin-orbit coupling

spinors, the four-component Dirac equation (3.4) is split into two coupled equations,

$$\begin{aligned} (\mathcal{E} + e\Phi) \Psi'_1 &= c\hat{\sigma} \cdot \hat{\mathbf{p}} \Psi'_2 \\ (\mathcal{E} + e\Phi + 2mc^2) \Psi'_2 &= c\hat{\sigma} \cdot \hat{\mathbf{p}} \Psi'_1. \end{aligned} \quad (3.5)$$

Obviously, $\Psi'_2 \ll \Psi'_1$. These equations are decoupled in order to obtain a wave equation for the large part Ψ'_1 . Analyzing the decoupled two-component Dirac equation for Ψ'_1 up to terms $\sim 1/c^2$ and considering only the Hermitian contribution, this equation can be interpreted as a stationary Schrödinger equation for the two-component wave function Ψ'_1 with the Hamiltonian

$$\hat{H}_{\text{rel}} = \frac{\hat{\mathbf{p}}^2}{2m} + V - \frac{(\hat{\mathbf{p}}^2)^2}{8m^3c^2} + \frac{\hbar}{4m^2c^2} \left(\frac{\partial V}{\partial \mathbf{r}} \times \hat{\mathbf{p}} \right) \cdot \hat{\sigma} + \frac{\hbar^2}{8m^2c^2} \frac{\partial^2}{\partial \mathbf{r}^2} V \quad (3.6)$$

with $V = -e\Phi$. Here, the term $-\frac{(\hat{\mathbf{p}}^2)^2}{8m^3c^2}$ is the relativistic energy correction, $\frac{\hbar^2}{8m^2c^2} \frac{\partial^2}{\partial \mathbf{r}^2} V$ is the Darwin term and

$$\hat{H}^{\text{SO}} = \frac{\hbar}{4m^2c^2} \left(\frac{\partial V}{\partial \mathbf{r}} \times \hat{\mathbf{p}} \right) \cdot \hat{\sigma} \quad (3.7)$$

is the spin-orbit coupling term leading to various band structure and transport properties. Although spin-orbit coupling is a relativistic phenomenon, it can be discussed in the non-relativistic limit by adding the spin-orbit coupling term \hat{H}^{SO} to the non-relativistic Hamiltonian, which will be done in this work.

For a centrosymmetric potential $\partial V/\partial \mathbf{r} = \partial V/\partial r \hat{\mathbf{e}}_{\mathbf{r}}$ (e.g. the atomic potential) the SOC Hamiltonian simplifies to

$$\hat{H}^{\text{SO}} = \frac{1}{2m^2c^2r} \frac{\partial V}{\partial r} \hat{\mathbf{L}} \cdot \hat{\mathbf{S}} \quad (3.8)$$

with $\hat{\mathbf{S}} = \hbar/2\hat{\sigma}$. This term represents the coupling of orbital angular momentum and spin, leading e.g. to the fine structure of the hydrogen orbitals. It is abbreviated as $\mathbf{L} \cdot \mathbf{S}$ coupling in the following.

In addition, spin-orbit coupling can arise due to broken symmetries, e.g. structural inversion asymmetry at interfaces or broken inversion symmetry in the bulk.

3.2. Two-band model

In the presence of spin-orbit coupling the minimum number of bands of an electronic system is two due to the two spin orientations represented by the 2×2 Pauli matrices in Eq. (3.6). Throughout most of this work two-band models are used to describe the physical properties of different systems in a comprehensive approach. Therefore, a general two-band system is introduced with the corresponding scattering properties.

In a perfect crystal with translational symmetry the eigenstates of the Hamiltonian \hat{H} are Bloch waves and the momentum operator $\hat{\mathbf{p}}$ can be replaced by its eigenvalue, the crystal momentum $\hbar\mathbf{k}$. A general two-band Hermitian Hamiltonian can be expressed in the basis of the Pauli matrices,

$$\hat{H}(\mathbf{k}) = \sum_{i=0}^3 d_i(\mathbf{k}) \hat{\sigma}_i. \quad (3.9)$$

Here, $d_i(\mathbf{k})$ are real functions and $i = 1, 2, 3$ corresponds to the coordinates x, y, z , respectively. The energy dispersion is

$$\mathcal{E}^n(\mathbf{k}) = d_0(\mathbf{k}) + n\sqrt{\mathbf{d}(\mathbf{k}) \cdot \mathbf{d}(\mathbf{k})}, \quad \mathbf{d}(\mathbf{k}) = (d_1(\mathbf{k}), d_2(\mathbf{k}), d_3(\mathbf{k})) \quad (3.10)$$

with $n = \pm 1$. The two-component normalized eigenstates read

$$|\mathbf{k}^n\rangle = \begin{pmatrix} \frac{n(d_1(\mathbf{k}) - id_2(\mathbf{k}))}{d(\mathbf{k}) - nd_3(\mathbf{k})} \\ 1 \end{pmatrix} \sqrt{\frac{d(\mathbf{k}) - nd_3(\mathbf{k})}{2d(\mathbf{k})V^{(d)}}}, \quad (3.11)$$

with, $d(\mathbf{k}) = |\mathbf{d}(\mathbf{k})|$ and $V^{(d)}$ the volume of the d -dimensional system. The group velocity is given by the \mathbf{k} -gradient of the energy dispersion,

$$\mathbf{v}_{\mathbf{k}}^n = \frac{1}{\hbar} \frac{\partial \mathcal{E}^n(\mathbf{k})}{\partial \mathbf{k}} = \frac{1}{\hbar} \left[\frac{\partial d_0(\mathbf{k})}{\partial \mathbf{k}} + \frac{n}{d(\mathbf{k})} \sum_{i=1}^3 d_i(\mathbf{k}) \frac{\partial d_i(\mathbf{k})}{\partial \mathbf{k}} \right]. \quad (3.12)$$

The Berry curvature calculated from Eq. (2.13) reads [70],

$$\Omega_i^n(\mathbf{k}) = \frac{n}{4d(\mathbf{k})^3} \epsilon_{ijkl} \mathbf{d}(\mathbf{k}) \cdot \left(\frac{\partial \mathbf{d}(\mathbf{k})}{\partial k_l} \times \frac{\partial \mathbf{d}(\mathbf{k})}{\partial k_j} \right) = \frac{n}{4d(\mathbf{k})^3} \epsilon_{ijkl} \epsilon_{uvw} d_u(\mathbf{k}) \frac{\partial d_v(\mathbf{k})}{\partial k_l} \frac{\partial d_w(\mathbf{k})}{\partial k_j}. \quad (3.13)$$

Here, ϵ_{ijkl} is the Levi-Civita symbol and the indices i, j, l, u, v, w run from 1 to 3.

In general, the Pauli matrices correspond to the pseudospin of the two bands, i.e. conduction and valence bands. For the special case that they also represent the spin degree of freedom, the spin expectation values are given by

$$\langle \boldsymbol{\sigma} \rangle_{\mathbf{k}}^n = \langle \mathbf{k}^n | \hat{\boldsymbol{\sigma}} | \mathbf{k}^n \rangle = n \frac{\mathbf{d}(\mathbf{k})}{d(\mathbf{k})}, \quad (3.14)$$

where the factor $\hbar/2$ was set to 1.

For the scalar δ -shaped scattering potential introduced in Eq. (2.73), the microscopic transition probabilities are obtained from Fermi's golden rule (2.72),

$$P_{\mathbf{k}' \leftarrow \mathbf{k}}^{n' \leftarrow n} = \frac{\pi |U_0|^2 c_i}{\hbar N_{\text{at}}} \left[1 + \frac{nn'}{d(\mathbf{k})d(\mathbf{k}')} \mathbf{d}(\mathbf{k}) \cdot \mathbf{d}(\mathbf{k}') \right]. \quad (3.15)$$

Thus, when the Pauli matrices correspond to the spin degree of freedom, the angle between the spin expectation values of the initial and final states determines the scattering probability. Scattering into the same spin state is preferred whereas scattering with a complete reversal of the spin (spin-flip) is suppressed ($P = 0$).

3.3. Spin-orbit fields

The influence of the SOC term in the Hamiltonian can be analyzed using the picture of spin-orbit fields. By this formalism, the band splitting as well as the spin texture can be evaluated.

In the following a two-band Hamiltonian with the general structure given by Eq. (3.9) is considered. Now, the Pauli spin matrices represent explicitly the spin degree of freedom. If $\mathbf{d}(\mathbf{k}) = 0$, the states are doubly degenerate. For nonzero $\mathbf{d}(\mathbf{k})$, Kramers degeneracy is lifted and the band is split into two branches with nonzero spin texture. The band gap is closed if $\mathbf{d}(\mathbf{k}) = 0$. The spin-orbit term $\mathbf{d}(\mathbf{k})$ can be interpreted as an effective \mathbf{k} -dependent field acting like a Zeeman or exchange field on the electronic states. The energy of states with spin aligned with $\mathbf{d}(\mathbf{k})$ is raised, the energy of states with opposite spin is lowered. Therefore, $\mathbf{d}(\mathbf{k})$ is called *spin-orbit field*. Its orientation represents the spin texture, its absolute value corresponds to the energy splitting of the two bands.

Especially for systems in which various SOC terms coexist, for example in systems with Rashba and Dresselhaus SOC (introduced in sections 3.4 and 3.5), the corresponding spin-orbit fields provide an intuitive way of analyzing the interplay of the different SOC terms, often more comprehensible than investigating only the band structure.

3. Spin-orbit coupling

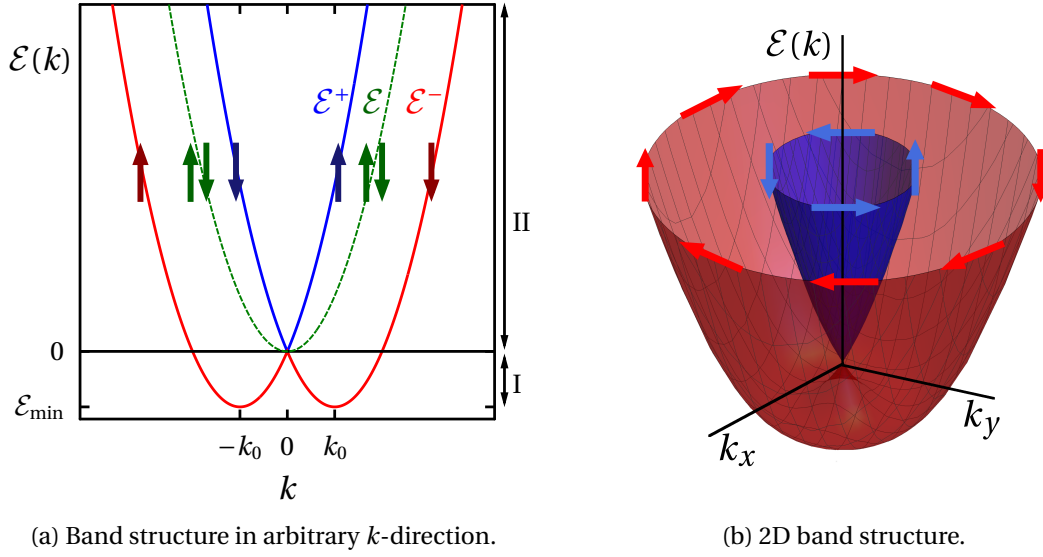


Figure 3.1.: Band structure of a 2D free electron gas without (green dashed line) and with (red/blue solid lines) Rashba SOC for arbitrary direction in \mathbf{k} -space (a). The full 2D band structure is obtained by rotation around the \mathcal{E} -axis (b). The arrows represent the spin expectation values along an in-plane quantization axis perpendicular to \mathbf{k} . Fig. (a) is adapted from [J4].

3.4. Rashba effect

At a surface or interface of a crystal, inversion symmetry is naturally broken by the macroscopic structure. The two sides of the surface or interface are not equivalent. Due to this structural inversion asymmetry a potential gradient $\partial V/\partial \hat{\mathbf{n}}$ occurs with $\hat{\mathbf{n}}$ the local surface normal. In the case of a planar surface, $\hat{\mathbf{n}}$ is constant and the spin-orbit coupling Hamiltonian reads

$$\hat{H}_R^{\text{SO}} = \frac{\alpha_R}{\hbar} [\hat{\mathbf{n}} \times \hat{\mathbf{p}}] \cdot \hat{\boldsymbol{\sigma}}. \quad (3.16)$$

Here, the Pauli vector $\hat{\boldsymbol{\sigma}}$ represents the spin degree of freedom. The Rashba parameter α_R is a measure for the potential gradient and the strength of the SOC [71] and is defined by the SOC Hamiltonian (3.7),

$$\alpha_R = \frac{\hbar^2}{4m^2 c^2} \int d^3 r |\Phi(\hat{\mathbf{n}})|^2 \frac{\partial V(\hat{\mathbf{n}})}{\partial n} \quad (3.17)$$

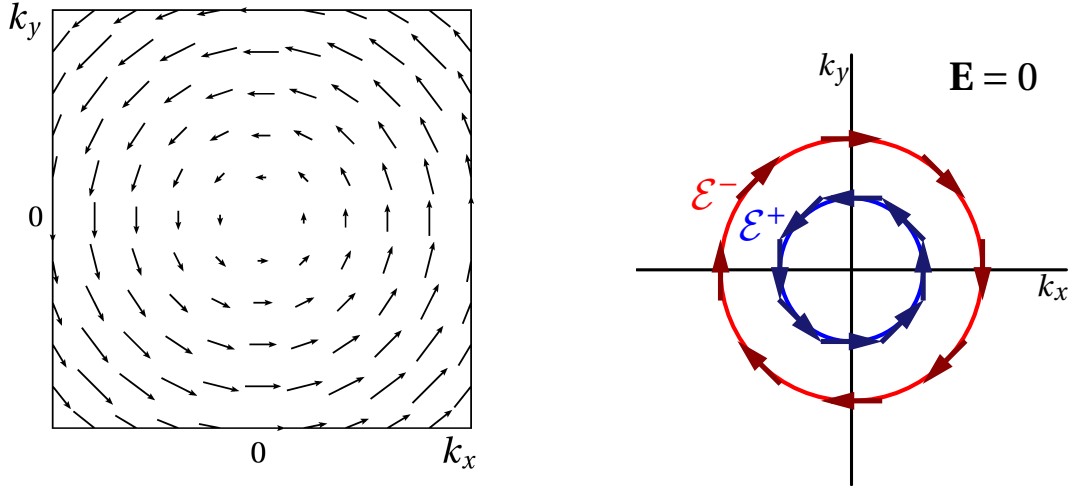
with $\Phi(\hat{\mathbf{n}})$ the component of the wave function varying in the direction of the surface normal $\hat{\mathbf{n}}$. Due to the broken inversion symmetry, Kramers spin degeneracy is lifted. At the interfaces or surfaces of 3D materials, e.g. the Au(111) surface or the Bi/Ag(111) surface alloy, quasi-2D electron gases exist which are well approximated by a 2D free-electron model with additional Rashba SOC.

α_R is material dependent and typically takes values between 0.01 and 3eVÅ [72]. At an interface of regions with different dopant concentrations, the Rashba interaction can be tuned by varying the doping asymmetry [72]. Alternatively, α_R can be modified by external fields [73]. For an infinite two-dimensional system with translational symmetry, the momentum operator $\hat{\mathbf{p}}$ is transformed into (2D) \mathbf{k} -space. Thus, the Hamiltonian reads

$$\hat{H}_R = \frac{\hbar^2 \mathbf{k}^2}{2m} + \alpha_R [\hat{\mathbf{n}} \times \mathbf{k}] \cdot \hat{\boldsymbol{\sigma}}, \quad (3.18)$$

leading to the energy dispersion

$$\mathcal{E}^n(\mathbf{k}) = \frac{\hbar^2 k^2}{2m} + n \alpha_R k, \quad n = \pm 1. \quad (3.19)$$



(a) Spin-orbit field of the Rashba Hamiltonian. (b) Fermi lines in an equilibrium Rashba system.

Figure 3.2.: Spin-orbit field and Fermi lines with spin expectation values of a 2DEG with Rashba SOC. Due to the spin-orbit field (a), the spin-degenerate band is split, resulting in the band structure shown in Fig. 3.1. (b): The Fermi level is above the diabolic point (energy region II). Blue and red colors represent the $n = +1$ and $n = -1$ branches, respectively. The spins (arrows) are aligned ($n = +1$) and antiparallel ($n = -1$) with the spin-orbit field. Fig. (b) is adapted from [J4].

with $k = |\mathbf{k}|$. In Fig. 3.1, the band structure of a free two-dimensional electron gas (2DEG) without and with the Rashba SOC term, respectively, is shown. Here and in the following the Rashba system is in the xy -plane with the surface normal in z -direction. Due to the Rashba SOC, in each direction in \mathbf{k} -space the formerly twofold degenerate free-electron parabola is split into two parabolas shifted in \mathbf{k} -space and energy. The degeneracy point, here at $k = 0$, $\mathcal{E} = 0$, is sometimes called *Dirac point* due to the linear dispersion in its vicinity [74]. This notation will be omitted here in order to avoid confusion with the Dirac Hamiltonian describing e.g. the band structure around Dirac points in topological semimetals. The Rashba system is topologically trivial and here, the degeneracy point will be called *diabolic point*, named after the juggling prop diablo [75].

Two energy regions are distinguished. Between the band edge at $\mathcal{E}_{\min} = -\alpha_{\text{R}}^2 m / 2\hbar^2$ and the diabolic point (region I), only the $n = -1$ branch is occupied, giving two concentric Fermi circles. The inner Fermi circle hosts hole-like states, the outer electron-like states. For $\mathcal{E} > 0$ (region II), both branches are occupied with two concentric electron-like Fermi circle. The density of states is free-electron-like for energies above the diabolic point and diverges at the band edge,

$$\mathcal{N}(\mathcal{E}) = \frac{m}{\hbar^2 \pi} \begin{cases} \alpha_{\text{R}} \sqrt{\frac{m}{\alpha_{\text{R}}^2 m + 2\mathcal{E}\hbar^2}}, & \mathcal{E} \leq 0 \\ 1, & \mathcal{E} \geq 0 \end{cases}. \quad (3.20)$$

The corresponding eigenfunctions are two-component spinors,

$$|\mathbf{k}^n\rangle = \begin{pmatrix} \Psi_{\uparrow}^n(\mathbf{k}) \\ \Psi_{\downarrow}^n(\mathbf{k}) \end{pmatrix} = \frac{1}{\sqrt{2A}} \begin{pmatrix} 1 \\ i n e^{i\varphi_{\mathbf{k}}} \end{pmatrix}, \quad (3.21)$$

with $\varphi_{\mathbf{k}}$ the azimuth of \mathbf{k} , $\cos \varphi_{\mathbf{k}} = k_x/k$ and A the area of the system. Due to the Rashba spin-orbit field, sketched in Fig. 3.2(a), spin and momentum are locked with opposite orientation of the spin expectation values on both branches,

$$\langle \boldsymbol{\sigma} \rangle_{\mathbf{k}}^n = n \frac{1}{k} (\hat{\mathbf{n}} \times \mathbf{k}), \quad (3.22)$$

3. Spin-orbit coupling

which are in-plane and perpendicular to \mathbf{k} . Here and in the following, the factor $\hbar/2$ is skipped, thus, the spin is a dimensionless quantity. Fig. 3.2(b) depicts the Fermi lines with \mathbf{k} -dependent spin expectation values in the energy region II.

The Rashba model was the first system for which the Edelstein effect was predicted [16, 17], which is introduced and discussed in chapter 4.

3.5. Dresselhaus effect

In non-centrosymmetric bulk systems, the inversion symmetry of the crystal structure is broken, which is called *bulk inversion asymmetry*. The paradigm system of a non-centrosymmetric three-dimensional crystal is the zincblende structure, which consists of an fcc lattice with two nonequivalent atoms in the basis. The broken inversion symmetry leads to an additional SOC contribution, called *Dresselhaus term* [76]. Within a $\mathbf{k}\cdot\mathbf{p}$ theory, the zincblende Dresselhaus term up to third order in k is

$$\hat{H}_D^{\text{SO}} = \gamma_D \sum_i \hat{\sigma}_i k_i (k_{i+1}^2 - k_{i+2}^2) = \gamma_D \left[k_x (k_y^2 - k_z^2) \hat{\sigma}_x + k_y (k_z^2 - k_x^2) \hat{\sigma}_y + k_z (k_x^2 - k_y^2) \hat{\sigma}_z \right], \quad (3.23)$$

where $i = x, y, z$ cyclic and $\hat{\sigma}$ corresponds to the spin degree of freedom. The Dresselhaus effect leads to a spin splitting of the bulk bands. However, when a two-dimensional system at a surface or interface is considered, the Dresselhaus term is projected onto the corresponding plane leading to a surface Dresselhaus SOC term which depends on the surface plane ([001], [110], [111], etc.). At surfaces and interfaces, the Rashba and Dresselhaus terms coexist. Depending on the point group of the system and the ratio of Rashba and Dresselhaus SOC, unconventional spin textures show up, for example systems with a single spin component [77] or showing a persistent spin helix [72].

The Dresselhaus parameter γ_D is a material-dependent bulk property. For GaAs, which is the paradigm of a zincblende crystal, values from 6.5 to 30 eVÅ³ have been reported [78, 79]. Dresselhaus systems are also expected to host an Edelstein effect, which is considered in section 4.6 for various surfaces with Rashba and Dresselhaus SOC.

3.6. Topological insulators

Besides the Rashba and Dresselhaus effects introduced in the previous sections, the $\mathbf{L}\cdot\mathbf{S}$ spin-orbit coupling can also give rise to unique band structure properties.

In ordinary insulators and semiconductors, the conduction and valence bands usually differ by their orbital character: the conduction band is typically *s*-like, whereas the valence band has *p*-like character [80]. In systems with spin-orbit coupling, the relativistic corrections to the Hamiltonian (3.6) split and shift the orbital energy levels in comparison to the non-relativistic case, which can have remarkable effects on the band structure. In case of strong SOC, the orbital ordering of the conduction and valence bands can be inverted in distinct regions of the Brillouin zone, which means that the valence band is shifted above the conduction band. However, due to hybridization of the states, these inverted bands do not cross but open up a band gap. The band inversion with such an avoided crossing is shown schematically in Fig. 3.3.

The non-inverted and especially the inverted band structures can be characterized by topological invariants, which are integer numbers that remain invariant as long as the band gap is not closed and the symmetries of the system are conserved. A Hamiltonian producing a gapped band structure is classified by its topological invariant. Common insulators with non-inverted bands are (*topologically*) *trivial*. Hamiltonians with the same topological invariant can be continuously transformed into one another without closing the band gap. When they differ with respect to their topological invariant, the band gap has to close to make such a transformation possible [81].

Bringing two materials with different topological invariants into contact (e.g. a topologically nontrivial insulator and vacuum, which is topologically trivial) gives rise to topological surface

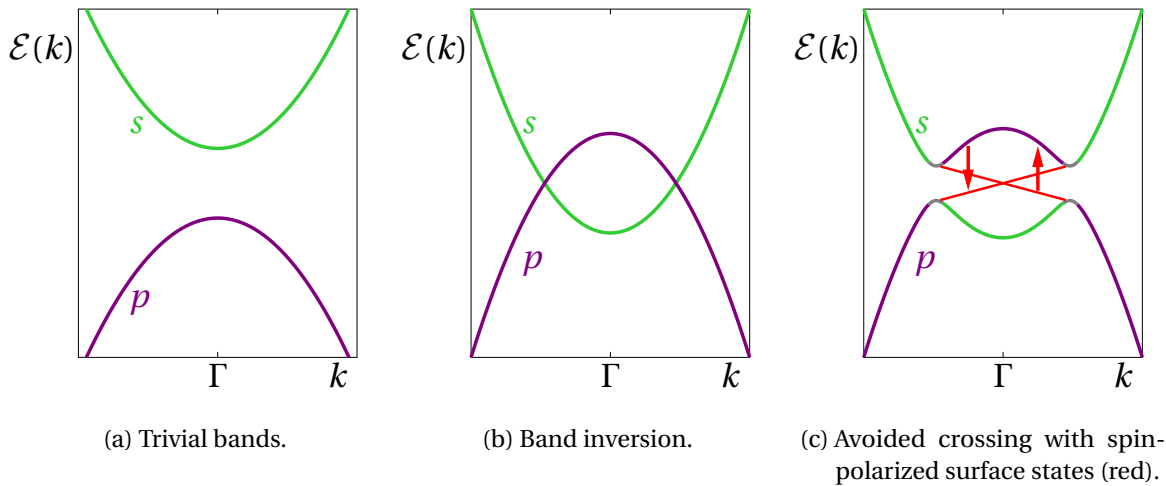


Figure 3.3.: Topological transition from trivial (a) to topologically nontrivial bands (c). Due to the relativistic corrections to the Hamiltonian (3.6), the s - and p -bands are shifted and their order is inverted. A gap opens around the crossing points. The helical edge states (red, c) correspond to a time-reversal invariant topological insulator. For a Chern insulator, only one linear chiral mode would exist at each edge.

states at the interface which are protected by symmetry and thus cannot be annihilated by a symmetry-preserving perturbation. The emergence of topological surface states can be directly understood from the analysis of the topological invariants, which is known as *bulk-boundary correspondence*. In real space, the topological invariant has to change across the interface. However, this is only possible if the band gap is closed [45, 82]. Therefore, in the interface region between two topologically different regions the band gap is closed by surface states.

In the following, two- and three-dimensional topological insulators as well as the corresponding topological invariants and the emergent surface states will be introduced.

3.6.1. Chern insulators

Chern insulators were first predicted by Haldane [83] as systems in which an integer quantum Hall effect exists even in the absence of a magnetic field. In these two-dimensional insulators time-reversal symmetry is broken. The characteristic invariant is the integer *Chern number* for band n , which is defined as the integral of the Berry curvature over the 2D Brillouin zone (BZ) [81],

$$C_n = \frac{1}{2\pi} \int_{\mathbf{k} \in \text{BZ}} \Omega_z^n(\mathbf{k}) d^2k. \quad (3.24)$$

Here, the 2D Brillouin zone is in the $k_x k_y$ -plane. The (total) Chern number C for topological classification is the sum over the Chern numbers of all occupied bands.

The corresponding surface states in the 2D bulk energy gap are 1D chiral edge states propagating into one direction along the edge and counterpropagating at opposite edges, giving rise to the quantum Hall effect. The Fermi surface is a single \mathbf{k} -point at each edge. Thus, the edge states are insensitive to disorder since they cannot be scattered [82].

The simplest model Hamiltonian for a Chern insulator is a 2D massive two-band Dirac Hamiltonian,

$$\hat{H}(\mathbf{k}) = \hbar v_0 (k_x \hat{\sigma}_x + k_y \hat{\sigma}_y) + m \hat{\sigma}_z, \quad (3.25)$$

yielding the gapped bulk band structure $\mathcal{E}(\mathbf{k}) = \pm \sqrt{\hbar v_0 k^2 + m^2}$. The topological character of the system depends on the mass term m . For $m = 0$ the bands gap is closed; this gap closing marks

3. Spin-orbit coupling

the topological transition point between two different topological phases with $m < 0$ and $m > 0$, respectively.

In order to demonstrate the emergence of topological surface states at the boundary between two topologically different regions, the translational symmetry of the system is broken in y -direction by assuming $m = m(y) = -m_0 \text{sgn}(y)$. Thus, at the boundary $y = 0$ the surface states closing the bulk band gap decay exponentially into the bulk,

$$\Psi^s(\mathbf{r}) = \frac{1}{\sqrt{2}} \begin{pmatrix} 1 \\ 1 \end{pmatrix} e^{ik_x x + \lambda(y)y}, \quad (3.26)$$

with $\lambda(y) = -\text{sgn}(y) \sqrt{m_0^2 + \hbar v_0^2 k_x^2 - \mathcal{E}^2} / \hbar v_0$. These 1D chiral edge states disperse linearly in energy at the edge in x -direction, $\mathcal{E} = \text{sgn}(m_0) \hbar v_0 k_x$. However, the integral (3.24) $\tilde{C} = -1/2 \text{sgn}(m_0 y)$ is not an integer and therefore not a Chern number. This apparent inconsistency comes from the fact that the model Hamiltonian (3.25) is not a lattice Hamiltonian but describes the low-energy states around the Γ -point. Thus, modifying the gapped Dirac Hamiltonian (3.25) to a lattice-periodic form, an integer Chern number is obtained. In any case, the difference of \tilde{C} obtained from Eq. (3.24) between the two regions $y < 0$ and $y > 0$ is integer, which is crucial for the emergence of chiral topological edge states.

3.6.2. Time-reversal symmetric topological insulators

In time-reversal invariant systems the Chern number cannot be used for topological classification, since it vanishes for symmetry reasons. The corresponding topological invariant is a Z_2 number which is either 0 (trivial) or 1 (nontrivial) [84]. A 2D time-reversal invariant topological insulator can be interpreted as two copies of a Chern insulator which are related by time reversal.

The Z_2 invariant for time-reversal symmetric topological insulators was first defined by Kane and Mele [84] in terms of eigenfunctions. The probably most intuitive way of calculating the Z_2 invariant is strongly related to the definition of the Chern number (3.24). The set of eigenstates of the time-reversal invariant system is decomposed into two subspaces (I/II) which are related by time-reversal and have the Chern numbers C_I and C_{II} , respectively. The Z_2 invariant ν is then given by [85]

$$\nu = \frac{1}{2} (C_I - C_{II}) \pmod{2}. \quad (3.27)$$

The topological surface states are two counterpropagating helical modes with opposite spin polarization, as shown in Fig. 3.3(c). They give rise to the quantum spin Hall effect. Although the Fermi surface consists of two \mathbf{k} -points, the surface states Ψ^I and Ψ^{II} are also robust against backscattering since they are related by time-reversal and therefore orthogonal: $\langle \Psi^I | \Psi^{II} \rangle = \langle \Psi^I | \hat{T} \Psi^I \rangle = \langle \hat{T}^2 \Psi^I | \hat{T} \Psi^I \rangle = -\langle \Psi^I | \hat{T} \Psi^I \rangle = 0$. Here, \hat{T} is the time-reversal operator with $\hat{T}^2 = -1$ for spin-1/2 particles [86]. The first theoretically predicted and experimentally realized topological insulator was a HgTe quantum well [87, 88]. Here, the Hg s -band is shifted below the Te p -band giving an inverted band structure, if the well is thicker than a critical thickness. Bringing HgTe in contact with CdTe, whose band structure is not inverted due to weaker spin-orbit coupling, topological surface states occur at the boundaries.

Topological insulators exist also in three dimensions. Here, Z_2 invariants are defined for distinct time-reversal invariant 2D planes in the 3D Brillouin zone [89]. The corresponding surface states are 2D helical states with a cone-like dispersion and helical spin-momentum locking. They are sometimes called *Dirac cones* since their band structure resembles 2D Dirac fermions. In these 2D helical states scattering can occur since the Fermi surface is a circle and for each state $|\mathbf{k}\rangle$ various scattering paths with nonzero transition probability are present.

The existence of topological surface states of a 3D topological insulator is demonstrated employing a minimal model Hamiltonian based on the Dirac Hamiltonian [90, 91]. In [90] the model

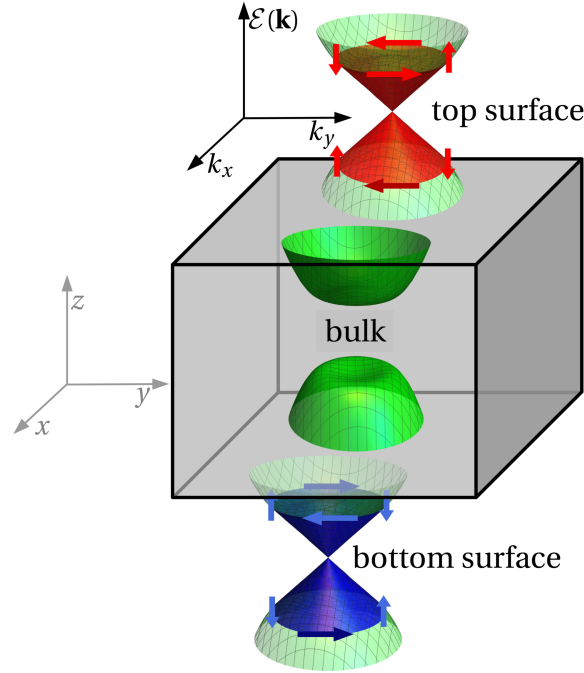


Figure 3.4.: Bulk (green) and surface states (blue/red) of a 3D topological insulator described by the effective Hamiltonian (3.28). The 3D bulk spectrum is projected to the ($k_z = 0$)-plane. The black coordinate system corresponds to the band structure. The bulk spectrum is gapped whereas the surfaces host topological helical surface states with spin-momentum locking. Here, the sample is assumed finite only in z -direction (the real-space coordinates are indicated by the gray coordinate axes), but in general surface states can occur on any surface in this model.

was introduced to describe the low-energy states around the Γ -point of the 3D topological insulators Bi_2Se_3 , Bi_2Te_3 and Sb_2Te_3 including the four low-energy orbitals which form the basis ($|p1_z^+, \uparrow\rangle$, $|p1_z^+, \downarrow\rangle$, $|p2_z^-, \uparrow\rangle$, $|p2_z^-, \downarrow\rangle$),

$$\hat{H} = \mathcal{E}_0(\mathbf{k}) + M(\mathbf{k})\hat{\sigma}_0 \otimes \hat{\tau}_z + \hat{\sigma}_x \otimes \sum_i v_0 \hat{p}_i \hat{\tau}_i. \quad (3.28)$$

Here, the Pauli matrices $\hat{\sigma}_i$ and $\hat{\tau}_i$ ($i = x, y, z$) correspond to the spin and orbital degrees of freedom, respectively. The term $\mathcal{E}_0(\mathbf{k})$ does not affect the topological properties of the system and is set to $\mathcal{E}_0(\mathbf{k}) = 0$. Thus, the model Hamiltonian (3.28) is a Dirac Hamiltonian with a \mathbf{k} -dependent mass term $M(\mathbf{k}) = M_0 - \sum_i Bk_i^2$ inducing a band gap in the 3D bulk bands. It can be shown that the bulk bands have a topological nontrivial character if $M_0B > 0$ and are trivial otherwise. Therefore, in the following $M_0B > 0$ is assumed.

Now, the system is assumed infinite in x - and y -direction and confined to the half space $z < 0$. Therefore, $\hbar k_{x/y}$, the eigenvalues of $\hat{p}_{x/y}$, are good quantum numbers. In order to obtain the eigenstates of Eq. (3.28), two independent zero-energy solutions for $k_x = k_y = 0$ and open boundary conditions at $z = 0$ are found,

$$|\Psi_0^\uparrow(z)\rangle = \frac{1}{\sqrt{N}} \begin{pmatrix} i \\ \text{sgn}(B) \\ 0 \\ 0 \end{pmatrix} (e^{\lambda_+ z} - e^{\lambda_- z}), \quad |\Psi_0^\downarrow(z)\rangle = \frac{1}{\sqrt{N}} \begin{pmatrix} 0 \\ 0 \\ -i \\ \text{sgn}(B) \end{pmatrix} (e^{\lambda_+ z} - e^{\lambda_- z}). \quad (3.29)$$

Here, $1/\sqrt{N}$ is a normalization factor and $\lambda_\pm = 1/(2|B|\hbar) \left(v_0 \pm \sqrt{v_0^2 - 4M_0B} \right)$. These zero energy solutions are used as basis of the surface states. They correspond to the \uparrow and \downarrow states, respectively.

3. Spin-orbit coupling

Projecting the Hamiltonian (3.28) into this new basis yields

$$\hat{H}_{\text{eff}}^{\text{surf}} = \hbar \text{sgn}(B) v_F (k_x \hat{\sigma}_y - k_y \hat{\sigma}_x) = \chi \hbar v_F (k_x \hat{\sigma}_y - k_y \hat{\sigma}_x) . \quad (3.30)$$

The Pauli matrices $\hat{\sigma}_{x/y}$ correspond to the spin degree of freedom in the surface basis ($|\Psi_0^\uparrow\rangle, |\Psi_0^\downarrow\rangle$) and $\chi = \text{sgn}(B)$ is the chirality of the surface states. Thus, Eq. (3.30) describes two-dimensional surface states which are linearly dispersing with a cone-like band structure. Spin and momentum are locked perpendicularly. Here, *chirality* corresponds to the sense of rotation of the spin expectation values and does not refer to chiral edge states of Chern insulators. At the opposite surface (topological insulator for $z > 0$, vacuum for $z < 0$) the sense of rotation of the spin expectation values along the Fermi line is opposite, corresponding to an opposite chirality. Fig. 3.4 schematically shows the gapped bulk and the helical surface band structure of a 3D topological insulator described by Eq. (3.28).

The band structure of the surface states resembles the Rashba model near the diabolic point. Due to the spin-momentum locking, they are expected to provide an efficient charge-to-spin conversion, which is discussed in section 4.7.

3.7. Weyl semimetals

Besides the above introduced topological insulators, metals and semimetals can also exhibit a topologically nontrivial character. In contrast to topological insulators, the bulk states of topological (semi)metals are not gapped at the Fermi level and provide a finite density of states in the whole energy range of interest (except of singular points). Due to the topological character of the gapless bulk band structure, unique topological surface states exist.

One type of topological semimetals are *Weyl semimetals* [31–35], that exhibit characteristic 3D bulk band structure properties. In a Weyl semimetal, at least one of time-reversal or inversion symmetry is broken, which lifts the Kramers degeneracy and leads to nondegenerate bands. At special singular twofold degenerate points \mathbf{k}_W^χ in the bulk spectrum, called Weyl points, the conduction and valence bands touch with a cone-like band structure linearly dispersing in all three directions in \mathbf{k} -space. The density of states vanishes at the Weyl point energy and is finite otherwise. The states around these points are described by the Weyl Hamiltonian

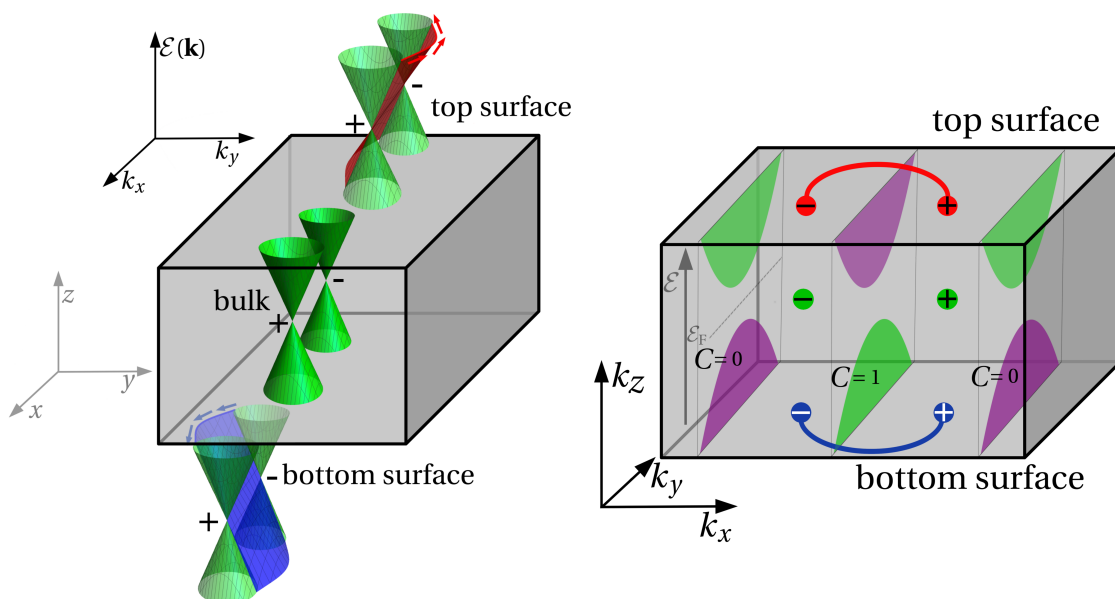
$$\hat{H}_W^\chi(\mathbf{k}) = \chi \hbar v_0 (\mathbf{k} - \mathbf{k}_W^\chi) \cdot \hat{\boldsymbol{\sigma}} , \quad (3.31)$$

yielding the energy dispersion

$$\mathcal{E}^n = n \hbar v_0 |\mathbf{k} - \mathbf{k}_W^\chi| , \quad n = \pm 1 . \quad (3.32)$$

Here, χ is the chirality of the Weyl fermion, which is ± 1 for first-order Weyl semimetals, $\hat{\boldsymbol{\sigma}}$ represents in general the pseudospin of conduction and valence bands and v_0 characterizes the group velocity. The low-energy states near the Weyl points are interpreted as the solid-state realization of relativistic Weyl fermions, which are the solutions of the massless Dirac equation, called *Weyl equation* [36]. Although Weyl fermions have been discussed since the 1920s, Weyl semimetals were the first and up to now only known materials hosting Weyl fermions. Weyl points always occur in pairs of opposite chirality, which is stated by the Nielsen-Ninomiya no-go theorem [92–94]. The bulk energy dispersion of a pair of Weyl cones is shown schematically in Fig. 3.5(a). Due to the Weyl points, the band structure features a topological nontrivial character. Corresponding to Eq. (2.13), the Berry curvature around the Weyl points is

$$\boldsymbol{\Omega}_{\mathbf{k}}^{\chi, n} = -n \chi \frac{1}{2|\mathbf{k} - \mathbf{k}_W^\chi|^3} (\mathbf{k} - \mathbf{k}_W^\chi) . \quad (3.33)$$



(a) Band structure of bulk (green) and surface states (red/blue) of a Weyl point pair. The signs + and – represent the chiralities of the Weyl points, the arrows correspond to the spin polarization along the Fermi arcs.

(b) Topological surface states with Fermi arcs (red/blue lines). The 3D Brillouin zone is decomposed into 2D planes with trivial ($C=0$) and nontrivial ($C=1$) Chern number. Inverted colors of the 2D band structures represent the band inversion.

Figure 3.5.: Schematic bulk and surface bands of a Weyl semimetal. (a): bulk and surface states and their occurrence in real space. (b): Emergence of topological surface states in the reciprocal space. The coordinates are rotated with respect to (a).

Depending on the chirality, a Weyl point is either a monopole or an antimonopole of the Berry curvature field of each band. Integration over a closed surface $\mathbf{S}_{\mathbf{k}}$ around a Weyl point yields

$$-n\chi = \frac{1}{2\pi} \oint_{\chi} \boldsymbol{\Omega}_{\mathbf{k}}^{\chi,n} \cdot d\mathbf{S}_{\mathbf{k}}. \quad (3.34)$$

This integer-valued integral is independent of the specific shape of $\mathbf{S}_{\mathbf{k}}$ and only depends on the chirality of the enclosed Weyl point. Therefore, the chirality χ corresponds to a topological charge, which is defined as integral of the Berry curvature in the valence band. The topological charge is inherent of the specific band structure as long as a Weyl point exists. Integrating over a surface which encloses two Weyl points of opposite chirality would give zero topological charge. Due to this topological property, a Weyl point can only be “destroyed” (which means the a gap is opened) if it annihilates with a Weyl point with opposite chirality.

The existence of Weyl points gives rise to topological surface states that connect the surface projections of the Weyl points. The corresponding Fermi lines in the two-dimensional Brillouin zone are open contours, called *Fermi arcs* [32]. The occurrence of these topological surface states can be understood by interpreting the 3D Brillouin zone of a Weyl semimetal as a stack of (insulating) slices in 2D \mathbf{k} -space [33], as sketched in Fig. 3.5(b). For each slice not intersecting the Weyl points, the band structure is gapped and a Chern number is defined. In the planes including the Weyl points the band gap is closed and the Chern number changes by χ . Thus, when the 2D system is trivial in the outer parts of the Brillouin zone, it is nontrivial in between the Weyl points leading to the existence of in-gap surface states [33, 82]. These surface states exist in the whole \mathbf{k} -region in which the 2D bands exhibit nontrivial character, giving rise to the topological Fermi arcs connecting

3. Spin-orbit coupling

the Weyl points' projections [32, 33].

The chirality of a Weyl point is invariant under time reversal and is reversed under spatial inversion. Therefore, a system with inversion symmetry hosts at least two Weyl points. When time-reversal symmetry is present, the band structure contains at least four Weyl points.

Due to their topological properties, Weyl semimetals provide various promising transport phenomena, such as a large anomalous Hall effect [32, 95, 96], a current-induced spin polarization [J4], and the chiral anomaly [37–39], the latter two effects are discussed in section 4.8 and chapter 5 of this work.

3.7.1. Model Hamiltonian

In realistic systems, the Weyl points are embedded in the bulk band structure and connected at higher energies. Therefore, a minimal model Hamiltonian for simulating realistic band structure properties has to produce at least two Weyl points. In this work the Hamiltonian proposed by Okugawa and Murakami [97, 98] is slightly modified to describe a Weyl pair in the vicinity of the point \mathbf{k}_p^0 ,

$$\hat{H}_W^p(\mathbf{k}) = \varrho_p \gamma_W (k_{p,x}^2 - m_W) \hat{\sigma}_y + \hbar (v_z k_{p,z} \hat{\sigma}_z - v_y k_{p,y} \hat{\sigma}_x), \quad (3.35)$$

where $\hat{\sigma}$ corresponds to the spin degree of freedom and γ_W , m_W , and $v_{x,y,z}$ are model parameters. p is the pseudospin index of a Weyl point pair, $\varrho_p = \pm 1$ determines the orientation of the Weyl pair in \mathbf{k} -space (Weyl dipole [99]) and $\mathbf{k}_p = \mathbf{k} - \mathbf{k}_p^0$. In contrast to the original model [97, 98], in which $\hat{\sigma}$ is a pseudospin generating a two-band system, in Eq. (3.35) a real spin degree of freedom is explicitly imposed in order to simulate realistic spin textures that have been calculated [100] and observed in experiments [101]. For a system of four Weyl points two copies of the Hamiltonian (3.35) are required with $\varrho_{1/2} = \pm 1$ and $\mathbf{k}_1^0 = -\mathbf{k}_2^0$.

In this reinterpreted model, the Weyl pairs around different points \mathbf{k}_p^0 (e.g. \mathbf{k}_1^0 and $-\mathbf{k}_1^0$) are not coupled. Therefore, the Hamiltonians (3.35) for different indices p can be considered separately. The bulk band structure reads

$$\mathcal{E}_p^n(\mathbf{k}) = n \sqrt{\gamma_W^2 (k_{p,x}^2 - m_W)^2 + \hbar^2 (v_y^2 k_{p,y}^2 + v_z^2 k_{p,z}^2)}, \quad n = \pm 1. \quad (3.36)$$

By the parameter m_W the material properties can be tuned from insulating ($m_W < 0$) to Weyl semimetal ($m_W > 0$). At the topological phase transition point $m_W = 0$, Weyl points of opposite chirality χ are created (or annihilated) at \mathbf{k}_p^0 .

In the Weyl semimetal phase the Weyl points are located at $\mathbf{k}_{W,p}^\chi = \mathbf{k}_p^0 + (\varrho_p \chi \sqrt{m_0}, 0, 0)$ with $m = m_0 > 0$. The bulk band structure of a pair of Weyl points around \mathbf{k}_0 as well as the corresponding surfaces of constant energy are shown in Fig. 3.6. In the vicinity of the Weyl points the band structure is conical. At the saddle points at $\mathcal{E}_S^\pm = \pm \gamma_W m_0$ the two Weyl cones are connected and the system goes through a Lifshitz transition.

The bulk eigenstates of the model Hamiltonian (3.35) are

$$|\mathbf{k}_p^{\text{bk}}\rangle = \begin{pmatrix} -\hbar v_y k_{p,y} - i \varrho_p \gamma_W (k_{p,x}^2 - m_0) \\ \mathcal{E}_p^n(\mathbf{k}) - \hbar v_z k_{p,z} \\ 1 \end{pmatrix} \frac{1}{\sqrt{M_{p,\mathbf{k}}}}, \quad M_{p,\mathbf{k}} = \frac{2\mathcal{E}_p^n(\mathbf{k})}{\mathcal{E}_p^n(\mathbf{k}) - \hbar v_z k_{p,z}} V, \quad (3.37)$$

with the \mathbf{k} -dependent spin expectation values

$$\langle \boldsymbol{\sigma} \rangle_{p,\mathbf{k}}^{\text{bk}} = \left(\frac{-\hbar v_y k_{p,y}}{\mathcal{E}_p^n(\mathbf{k})}, \frac{\varrho_p \gamma_W (k_{p,x}^2 - m_0)}{\mathcal{E}_p^n(\mathbf{k})}, \frac{\hbar v_z k_{p,z}}{\mathcal{E}_p^n(\mathbf{k})} \right). \quad (3.38)$$

For the calculation of the surface states, the system is assumed infinite in x - and y -direction but finite in z -direction with the thickness L_z . The ($z = 0$)-plane is labeled as top (T), the ($z = -L_z$)-

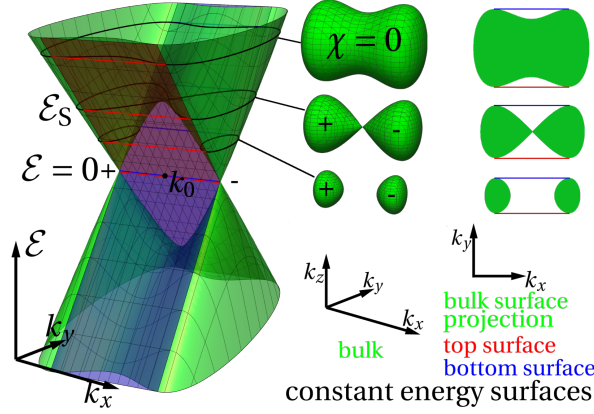


Figure 3.6.: Band structure and constant energy surfaces of the Hamiltonian (3.35) around \mathbf{k}_0 . The bulk states are drawn green, the top (bottom) surface states red (blue), respectively. The chirality of the Weyl points is marked by + and -. The figure is adapted from [J5].

plane as bottom surface (B). To simulate the surface properties, m_W is assumed z -dependent,

$$m_W(z) = \begin{cases} m_1 < 0, & z < -L_z \\ m_0 > 0, & -L_z \leq z \leq 0 \\ m_1 < 0, & z > 0 \end{cases} \quad (3.39)$$

with $|m_1| \gg m_0$. The wave functions and energy dispersions of the surface states at the top surfaces of the Weyl semimetal ($-L_z \leq z \leq 0$) are

$$|\mathbf{k}_p^T\rangle = \begin{pmatrix} \varrho_p \\ 1 \end{pmatrix} e^{-\frac{\gamma_W}{v_z \hbar} (k_{p,x}^2 - m_0)z} \frac{1}{\sqrt{N_{p,\mathbf{k}}}}, \quad \mathcal{E}_p^T = -\varrho_p v_y \hbar k_{p,y} \quad (3.40)$$

and at the bottom surface

$$|\mathbf{k}_p^B\rangle = \begin{pmatrix} -\varrho_p \\ 1 \end{pmatrix} e^{\frac{\gamma_W}{v_z \hbar} (k_{p,x}^2 - m_0)(z+L_z)} \frac{1}{\sqrt{N_{p,\mathbf{k}}}}, \quad \mathcal{E}_p^B = \varrho_p v_y \hbar k_{p,y}. \quad (3.41)$$

The normalization factor reads

$$N_{p,\mathbf{k}} = \frac{L_x L_y \hbar v_z}{\gamma_W (m_0 - k_{p,x}^2)} \left(1 - \exp \frac{2\gamma_W (k_{p,x}^2 - m_0) L_z}{\hbar v_z} \right). \quad (3.42)$$

The surface states exist in between two Weyl nodes, that is $-\sqrt{m_0} \leq k_{p,x} \leq \sqrt{m_0}$. In real space they decay exponentially from the surface to the bulk with a $k_{p,x}$ -dependent decay length $\lambda_z = \frac{v_z \hbar}{\gamma_W (m_0 - k_{p,x}^2)}$. At the ends of the arcs, $k_{p,x} = \pm \sqrt{m_0}$, the surface states are equivalent to the bulk states. The surface states at the center of the arc, $k_{p,x} = 0$, have the shortest decay length. Since $|m_1| \gg m_0$, the wave functions decrease rapidly in the vacuum regions outside the Weyl semimetal ($z > 0$ and $z < -L_z$) and are excluded from further considerations.

The \mathbf{k} -dependent surface spin expectation values are constant on each Fermi arc, point along the arc and are (mutually) oppositely aligned on the top and bottom surface,

$$\langle \boldsymbol{\sigma} \rangle_{p,\mathbf{k}}^T = (\varrho_p, 0, 0), \quad \langle \boldsymbol{\sigma} \rangle_{p,\mathbf{k}}^B = (-\varrho_p, 0, 0). \quad (3.43)$$

In Fig. 3.6 in addition to the bulk bands, the surface band structure of the Hamiltonian (3.35) is shown. The surface band dispersion is linear and touches the bulk bands tangentially. In addition,

3. Spin-orbit coupling

constant-energy surfaces are depicted for the bulk states (center); on the right-hand side constant-energy cuts show both surface states and the projection of the bulk states onto the z -surface.

The paradigm Weyl semimetals with broken inversion symmetry are NbP, TaP, NbAs and TaAs [102, 103], which belong to a non-centrosymmetric space group.

The model Hamiltonian (3.35) will be used in sections 4.8.2 and 5.5 to approximate the band structure of the Weyl semimetal TaAs in order to calculate the Edelstein effect as well as the chiral anomaly.

Besides the above introduced *type-I* Weyl semimetals, which provide point-like Fermi surfaces and a vanishing density of states at the Weyl point energy, a second class of Weyl semimetals, called *type-II*, exists [104]. In these materials, the Weyl cones are tilted in \mathbf{k} -space and the corresponding Fermi surfaces at the energy of the Weyl points are electron and hole pockets with a nonzero density of states. Like type-I Weyl points, type-II Weyl points are monopoles of the Berry curvature field of each band and give rise to topological surface states. Candidates for type-II Weyl semimetals are for example MoTe₂ and WTe₂ [104, 105]. However, the focus of this work is on type-I Weyl semimetals. Thus, when Weyl semimetals are discussed, this usually refers to type-I.

In systems with time-reversal and inversion symmetry, the bands are twofold degenerate. Here, similar band structure features as Weyl points can arise, described by the massless Dirac Hamiltonian, which is interpreted as two copies of the Weyl Hamiltonian. The band crossing points are therefore called *Dirac points* and the materials are *Dirac semimetals*. The band structure is cone-like around the Dirac points, but the Berry curvature vanishes. However, Z_2 invariants can be defined and topological surface states also exist. By applying a magnetic field to a Dirac semimetal, the time-reversal symmetry is lifted and two Weyl points are created from one Dirac point.

4. The Edelstein effect

The Edelstein effect, also known as Rashba-Edelstein effect [106], inverse spin-galvanic effect [107], Aronov-Lyanda-Geller-Edelstein (ALGE) effect [J4] or, less specific, as current-induced spin polarization, provides the opportunity of purely electrically inducing a spin polarization in nonmagnetic materials. At surfaces or interfaces hosting Rashba states or topological surface states, or in bulk Dresselhaus systems, the spin degeneracy of the electronic states is lifted by spin-orbit coupling (SOC) [108–110]. Due to the broken inversion symmetry and the spin polarization of the states, the application of an external electric field induces a macroscopic spin polarization. Thus, the Edelstein effect is promising for spintronic applications since it allows for generating and controlling a spin polarization electrically, which can be used to exert a spin-orbit torque on a ferromagnetic layer and thereby move domain walls and even switch magnetization. It has been subject of various theoretical [16, 17, 107, 111–116] as well as experimental [25, 106, 117–123] papers.

In this chapter, the Edelstein effect is introduced within a straightforward picture using the semiclassical Boltzmann transport theory. An isotropic Rashba system is used as a paradigm model, like in the original papers [16, 17]. In addition, the inverse Edelstein effect, which is the generation of a charge current from a nonequilibrium spin density, is introduced. Further, a magnetoelectric effect coupling electric field and spin polarization, which can be classified as intrinsic Edelstein effect, is discussed within Kubo theory. A short overview of the experimental effort and progress on detecting the Edelstein effect is given. Further, the current-induced spin polarization is calculated and discussed for Rashba systems with anisotropies and nonmagnetic as well as magnetic impurities, Dresselhaus systems, Rashba systems with a Zeeman field, topological insulators and Weyl semimetals. Materials providing an efficient charge-to-spin conversion are identified. It is demonstrated that the current-induced spin polarization is not mandatory perpendicular to the applied electric field. Parts of this chapter were published in [J4, J5].

4.1. Charge-to-spin conversion in a Rashba model

The isotropic Rashba system, introduced in section 3.4, is the paradigm model system for the theoretical discussion of the Edelstein effect [16, 17, 108–110]. Due to its free-electron-like band structure, it is employed here to give a coherent and intuitive explanation for the current-induced spin density. Originally, the Edelstein effect was discussed for energies above the diabolic point (region II, defined in section 3.4), in which both branches ($n = \pm 1$) are occupied, whereas it is calculated in the entire energy region in this work [J4].

The total spin polarization of the system is calculated by summing the spin expectation values of all occupied states,

$$\langle \mathbf{s} \rangle = \sum_{\mathbf{k}, n} f_{\mathbf{k}}^n \langle \boldsymbol{\sigma} \rangle_{\mathbf{k}}^n. \quad (4.1)$$

This macroscopic spin expectation value corresponds to a magnetic moment of $\mathbf{m} = -\mu_B \langle \mathbf{s} \rangle$, with μ_B the Bohr magneton. In equilibrium $\langle \mathbf{s} \rangle$ vanishes because of time-reversal symmetry. Within semiclassical Boltzmann transport theory (section 2.3), the influence of an external electric field \mathbf{E} can be interpreted as a shift of the Fermi lines in \mathbf{k} -space, as shown in Fig. 4.1. In this nonequilibrium configuration, a nonzero total spin expectation value results,

$$\langle \mathbf{s} \rangle = - \sum_{\mathbf{k}, n} e (\boldsymbol{\Lambda}_{\mathbf{k}}^n \cdot \mathbf{E}) \delta(\mathcal{E}_{\mathbf{k}}^n - \mathcal{E}_F) \langle \boldsymbol{\sigma} \rangle_{\mathbf{k}}^n = - \sum_{\mathbf{k}, n} e \tau_{\mathbf{k}}^{R, n} (\mathbf{v}_{\mathbf{k}}^n \cdot \mathbf{E}) \delta(\mathcal{E}_{\mathbf{k}}^n - \mathcal{E}_F) \langle \boldsymbol{\sigma} \rangle_{\mathbf{k}}^n, \quad (4.2)$$

in which the mean free path $\boldsymbol{\Lambda}_{\mathbf{k}}$ was approximated by $\tau_{\mathbf{k}}^R \mathbf{v}_{\mathbf{k}}$ (relaxation time approximation), as discussed in section 2.3.1. Here, either the momentum relaxation time $\tau_{\mathbf{k}}$ defined by Eq. (2.41) or

4. The Edelstein effect

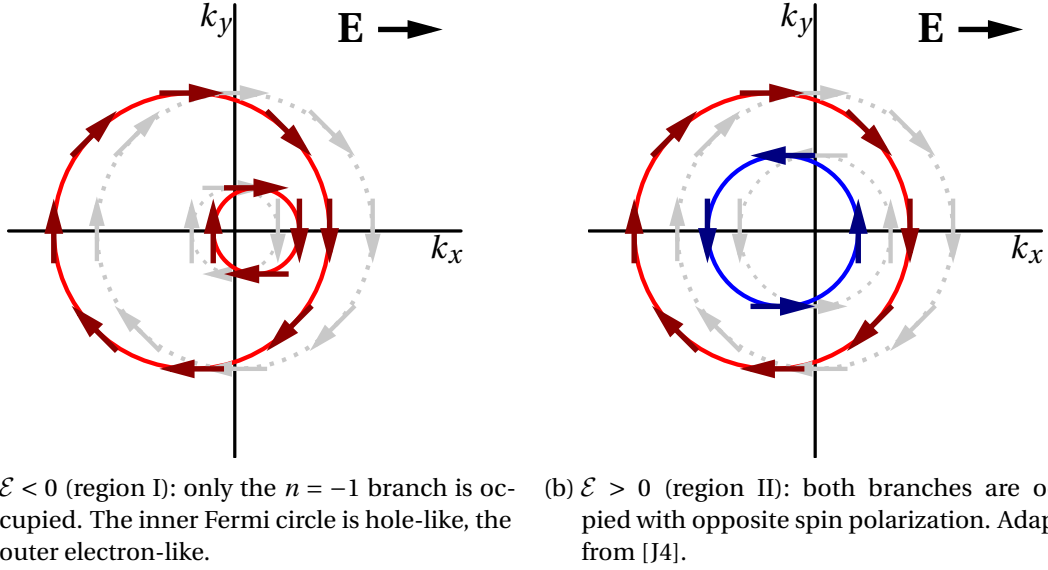


Figure 4.1.: Fermi lines and spin expectation values (arrows) of a 2DEG with Rashba SOC in the presence of an external electric field \mathbf{E} . The influence of the electric field is interpreted as a “shift” of the Fermi lines with the direction of the shift depending on the electron/hole character of the states. The gray lines correspond to the equilibrium. The colors blue and red represent the $n = +1$ and $n = -1$ branches, respectively. In both energy regions I and II the spin density contributions of the two Fermi lines partially compensate and a nonzero spin polarization pointing in y -direction shows up.

the transport lifetime $\tau_{\mathbf{k}}^{\text{tr}}$ given by Eq. (2.48) can be used.

For a scalar scattering potential U_0 , the transition probability $P_{\mathbf{k}' \leftarrow \mathbf{k}}^{n' \leftarrow n}$ calculated from Eqs. (2.72) and (3.15), respectively, depends only on the scattering angle between \mathbf{k} and \mathbf{k}' ,

$$P_{\mathbf{k}' \leftarrow \mathbf{k}}^{n' \leftarrow n} = \frac{c_i |U_0|^2 \pi}{\hbar N_{\text{at}}} [1 + n n' \cos(\varphi_{\mathbf{k}'} - \varphi_{\mathbf{k}})] \delta(\mathcal{E}_{\mathbf{k}}^n - \mathcal{E}_{\mathbf{k}'}^{n'}), \quad (4.3)$$

with $\varphi_{\mathbf{k}}$ the azimuth of \mathbf{k} . In the isotropic model system, both momentum relaxation time $\tau_{\mathbf{k}}$ as well as transport lifetime $\tau_{\mathbf{k}}^{\text{tr}}$ are isotropic and can be calculated analytically,

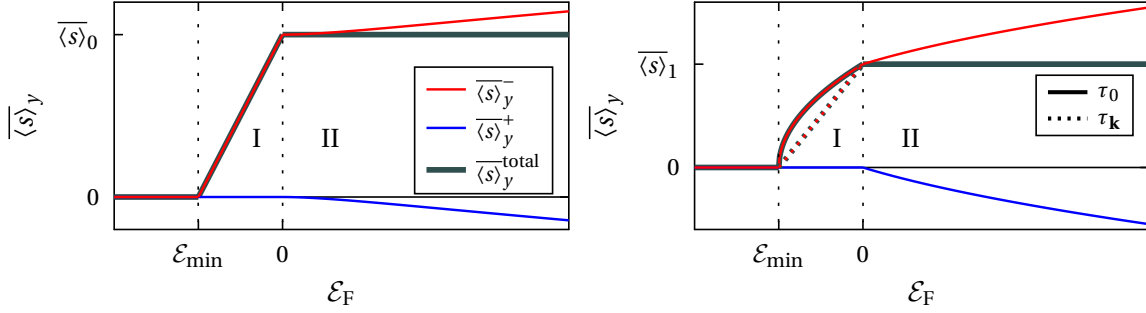
$$\tau_{\mathbf{k}}^n = \tau_0(\mathcal{E}) = \frac{1}{c_i |U_0|^2 A_{\text{at}} m} \begin{cases} \frac{\hbar^4 v(\mathcal{E})}{\alpha_{\text{R}}}, & \mathcal{E} \leq 0 \\ \hbar^3, & \mathcal{E} \geq 0 \end{cases} \quad (4.4a)$$

$$\tau_{\mathbf{k}}^{\text{tr}, n} = \tau_0^{\text{tr}, n}(\mathcal{E}) = \frac{1}{c_i |U_0|^2 A_{\text{at}} m^2} \begin{cases} \frac{\hbar^6 v(\mathcal{E}) k^n(\mathcal{E})}{\alpha_{\text{R}}}, & \mathcal{E} \leq 0 \\ \frac{\hbar^4 k^n(\mathcal{E})}{v(\mathcal{E})}, & \mathcal{E} \geq 0. \end{cases} \quad (4.4b)$$

Here, the band index is $n = \pm 1$ for $\mathcal{E} > 0$ referring to the two energy branches and $n = (-1, e/\hbar)$ for $\mathcal{E} < 0$ labeling the electron- and hole-like states, respectively. $A_{\text{at}} = A/N_{\text{at}}$ is the average area per atom, $\mathbf{v}_{\mathbf{k}}(\mathcal{E})$ the group velocity, whose absolute value, $v(\mathcal{E}) = \left(\frac{\alpha_{\text{R}}^2}{\hbar^2} + \frac{2\mathcal{E}}{m}\right)^{1/2}$ is constant on an iso-energy line. Both $\tau_{\mathbf{k}}$ and $\tau_{\mathbf{k}}^{\text{tr}}$ are continuous at $\mathcal{E} = 0$. The momentum relaxation time $\tau_{\mathbf{k}}$, which includes only scattering-out processes, has the same value on both iso-energy circles, whereas the transport lifetime $\tau_{\mathbf{k}}^{\text{tr}}$, which also takes account of the scattering-in processes, has different values. Thus, the choice of the relaxation time can influence the results of the transport properties drastically.

In this chapter, the transport lifetime $\tau_{\mathbf{k}}^{\text{tr}}$ is used in the majority of cases because it provides a more accurate way of discussing the scattering properties of the system. Within this approach, the

4.1. Charge-to-spin conversion in a Rashba model



(a) Branch-resolved spin density for the transport lifetime $\tau_{\mathbf{k}}^{\text{tr}}$. Adapted from [J4]. (b) Constant relaxation time τ_0 and momentum relaxation time $\tau_{\mathbf{k}}$, respectively. The curves are equivalent in region II.

Figure 4.2.: Energy-dependent spin density for an isotropic Rashba system in the presence of an electric field $\mathbf{E} \parallel x$. The contributions from the $n = \pm 1$ branches are shown in blue and red, respectively. Using the momentum relaxation time instead of the transport lifetime influences the value of the spin density by a factor of $1/2$: $\overline{\langle s \rangle}_1 = \overline{\langle s \rangle}_0/2$. The constant relaxation time approach (assuming $\tau_0 = \tau_{\mathbf{k}}(\mathcal{E} > 0)$) modifies the energy dependence qualitatively in region I.

spin density, which is defined as total spin expectation value per two-dimensional unit cell, reads

$$\overline{\langle \mathbf{s} \rangle} = \frac{\langle \mathbf{s} \rangle}{\text{u.c.}} = \frac{eN_{\text{u.c.}}}{\pi c_1 |U_0|^2} [\mathbf{e}_z \times \mathbf{E}] \begin{cases} 0, & \mathcal{E}_F \leq \mathcal{E}_{\min} \\ \left(\alpha_R + \frac{2\hbar^2}{\alpha_R m} \mathcal{E}_F \right), & 0 \geq \mathcal{E}_F \geq \mathcal{E}_{\min} \text{ (region I) } \\ \alpha_R, & \mathcal{E}_F \geq 0 \text{ (region II) } \end{cases}, \quad (4.5)$$

as shown in Fig. 4.2(a). Here, $N_{\text{u.c.}}$ is the number of atoms in the unit cell. Shifting the Fermi level can be achieved experimentally by applying a gate voltage or doping the Rashba system. However, the dopants would also affect the scattering properties.

The qualitative energy dependence of $\overline{\langle \mathbf{s} \rangle}$ can be directly explained from the band structure and the Fermi lines of the system (Figs. 3.1 and 4.1). For $\mathcal{E}_{\min} \leq \mathcal{E}_F < 0$, only the branch $n = -1$ is occupied. The spin textures on the two Fermi circles have the same orientation. Due to the opposite character of charge carriers (electrons/holes), their contributions to the total spin partially compensate. With increasing Fermi energy the difference in radii is enlarged, reducing the compensation and thus enhancing the net spin density of the system. In addition, the transport lifetime also exhibits an energy dependence leading to the linear increase of $\overline{\langle s \rangle}_y$. Above the diabolic point ($\mathcal{E} > 0$), both branches $n = \pm 1$ are occupied. Due to the opposite spin orientation and electron-like character of both bands, their contributions also partially compensate. Here, the difference in radii of the Fermi lines does not change with \mathcal{E}_F giving a spin density constant in energy.

For comparison, Fig. 4.2(b) shows the energy-dependent induced spin density for a constant, energy-independent relaxation time τ_0 and the momentum relaxation time $\tau_{\mathbf{k}}$, given by Eq. (4.4a), respectively. Whereas all three τ -approaches provide a constant total spin expectation value above the diabolic point (region II), the results differ with respect to the absolute values as well as the contributions of the bands. Using the momentum relaxation time results in a spin density reduced by a factor of $1/2$ in comparison to the transport lifetime approach. The constant τ_0 approach leads to a modified energy dependence in region I representing the difference of the two Fermi circles' radii.

At the opposite surface of the material, the current-induced spin density would point in the opposite direction since the sign of the Rashba parameter would change.

Analogously to the charge conductivity defined by Ohm's law, the Edelstein tensor $\hat{\kappa}$ is defined,

4. The Edelstein effect

linearly connecting the spin density and the electric field,

$$\overline{\langle s \rangle}_i = \kappa_{ij} E_j, \quad (4.6)$$

with $i = x, y, z$ and $j = x, y$. For the isotropic Rashba system $\hat{\kappa}$ is

$$\kappa_{yx} = -\kappa_{xy} = \frac{eN_{\text{u.c.}}}{\pi c_i |U_0|^2} \begin{cases} 0, & \mathcal{E}_F \leq \mathcal{E}_{\text{min}} \\ \left(\alpha_R + \frac{2\hbar^2}{\alpha_R m} \mathcal{E}_F \right), & 0 \geq \mathcal{E}_F \geq \mathcal{E}_{\text{min}} \\ \alpha_R, & \mathcal{E}_F \geq 0. \end{cases} \quad (4.7)$$

All other tensor elements vanish because of symmetry.

Alternatively to the E-dependent formulation, the spin density can also be expressed in terms of the charge current \mathbf{j}^c . Using the Mott two-current model [124], the charge current in the Rashba system is

$$\mathbf{j}^c = \frac{e^2}{4\pi} \nu(\mathcal{E}_F) \sum_n k^n(\mathcal{E}_F) \tau^{\text{tr}n}(\mathcal{E}_F) \mathbf{E}. \quad (4.8)$$

The spin density induced by the same electric field \mathbf{E} is represented as a function of the charge current,

$$\overline{\langle \mathbf{s} \rangle} = \frac{\alpha_R m \hbar A_0}{e(\alpha_R^2 m + \hbar^2 \mathcal{E}_F)} [\mathbf{e}_z \times \mathbf{j}^c], \quad (4.9)$$

A_0 is the area of the unit cell. In Ref. [107], the expression $\langle \mathbf{s} \rangle / A \approx \alpha_R m / e \hbar \mathcal{E}_F [\mathbf{e}_z \times \mathbf{j}^c]$ is derived which corresponds to Eq. (4.9) in the limit $\hbar^2 \mathcal{E}_F \gg 2|\mathcal{E}_{\text{min}}|$. Expressing the current-induced spin density in terms of the charge current instead of the electric field has the advantage that the result does not depend on details of the scattering properties. The scattering potential U_0 and the impurity concentration c_i enter the transport properties as parameters via the relaxation time. The values of U_0 and c_i can vary between different samples of the same material and are often not known. When the nonequilibrium spin density is calculated as a function of the electric field, these parameters are set to arbitrary values. Expressing the spin density as a function of the charge current density, the influence of U_0 and c_i is eliminated. Here, also an Ohm's law-like relation can be defined,

$$\overline{\langle s \rangle}_i = \zeta_{ij} j_j^c \quad (4.10)$$

with the tensor $\hat{\zeta}$ for an isotropic Rashba system ,

$$\zeta_{yx} = -\zeta_{xy} = \frac{\alpha_R m \hbar A_0}{e(\alpha_R^2 m + \hbar^2 \mathcal{E}_F)}. \quad (4.11)$$

Expressing the induced spin as a function of the charge current is not appropriate for systems with metallic bulk states. Here, applying an electric field to the sample induces a spin density as well as a charge current at the surface or interface, but in addition also a charge current in the bulk. Therefore, the total current in the sample is larger than the charge current originating from the surface states. Consequently, the current-to-spin efficiency is overestimated by Eq. (4.11).

The general expression Eq. (4.2) for calculating the spin density induced by an external electric field is not restricted to isotropic Rashba systems, but can be in general used for 2D and even 3D systems. In the following sections, it will be applied to more complex systems.

4.2. Intrinsic Edelstein effect

The Edelstein effect introduced in the previous section within semiclassical Boltzmann transport theory includes only extrinsic transport effects due to scattering. However, within Kubo theory [62],

intrinsic effects can also give rise to a nonzero spin density induced by an external electric field. Using the Kubo formula for intrinsic interband contributions [64, 65] given by Eq. (2.64), the expectation value of the intrinsic spin density is

$$\overline{\langle \mathbf{s} \rangle}^i = -\frac{2\hbar e N_{\text{u.c.}}}{N_{\text{at}}} \sum_{\mathbf{k}, n \neq m} f_{\mathbf{k}}^n (1 - f_{\mathbf{k}}^m) \frac{\text{Im}(\langle \mathbf{k}^n | \hat{\boldsymbol{\sigma}} | \mathbf{k}^m \rangle \langle \mathbf{k}^m | \hat{\mathbf{v}} \cdot \mathbf{E} | \mathbf{k}^n \rangle)}{(\mathcal{E}_{\mathbf{k}}^n - \mathcal{E}_{\mathbf{k}}^m)^2}, \quad (4.12)$$

where n and m are band indices and $\hat{\mathbf{v}} = -i/\hbar [\hat{H}, \hat{\mathbf{r}}]$ is the velocity operator. In a time-reversal invariant system, the imaginary parts of $\langle \mathbf{k}^n | \hat{\boldsymbol{\sigma}} | \mathbf{k}^m \rangle$ and $\langle \mathbf{k}^n | \hat{\mathbf{v}} | \mathbf{k}^m \rangle$ transform odd under time reversal whereas the real parts transform even. In a pure Rashba system, the term $\langle \mathbf{k}^n | \hat{\boldsymbol{\sigma}} | \mathbf{k}^m \rangle \langle \mathbf{k}^m | \hat{\mathbf{v}} \cdot \mathbf{E} | \mathbf{k}^n \rangle$ is real for all \mathbf{k} . Thus, in systems with TRS, the intrinsic interband contributions to the Edelstein effect vanish for symmetry reasons.

In systems with broken TRS, however, an intrinsic Edelstein effect may exist. In magnetic materials, the current-induced spin density is usually not called *Edelstein effect* but *magnetoelectric effect*. Since the physical origin of the magnetoelectric coupling is similar to the Edelstein effect, it is discussed within this work for Rashba systems with Zeeman coupling (section 4.5.4) and will also be called *Edelstein effect* for reasons of consistency.

4.3. Inverse Edelstein effect

Besides the direct Edelstein effect, its Onsager reciprocal [114], which is generation of a charge current by an injected nonequilibrium spin density, exists. This *inverse Edelstein effect* has been experimentally observed in various materials [25, 28, 30, 106].

The mechanism of the inverse Edelstein effect is understood by the same physical picture as the direct Edelstein effect. In equilibrium, the total spin of the system as well as the charge current vanishes, as depicted in Fig. 3.2(b). Injecting a nonequilibrium spin density can be interpreted as a shift of the Fermi lines, similar to Fig. 4.1, but with the two Fermi circles shifted in opposite directions. A nonequilibrium spin polarization in y -direction corresponds to a higher occupation of states with negative k_x -value leading to a charge current in x -direction.

A more elaborate explanation is given by Shen *et al.* [114]. A nonequilibrium spin density injected at an arbitrary momentum into a Rashba system gains an additional spin component by the Rashba spin-orbit field. Due to the inverse spin Hall effect, this spin current is converted into a perpendicular charge current [125] which manifests itself as the inverse Edelstein signal.

Further, Ref. [114] shows the connection between direct and inverse Edelstein effect using Kubo theory. The direct Edelstein effect is the spin density response to an external electric field, Eq. (4.6), while the inverse Edelstein effect is defined as the charge current response to a linearly time-dependent magnetic field \mathbf{B} injecting a nonequilibrium spin density,

$$j_i^{\text{c},2\text{D}} = \sigma_{ij}^{\text{IEE}} \frac{g\mu_B}{A} \dot{B}_j \quad (4.13)$$

with $g \approx 2$ the Landé g -factor. Kubo theory leads to $\kappa_{ij} = A_0 \sigma_{ji}^{\text{IEE}}$ [114] because in the time-reversal invariant systems discussed here, κ_{ij} and σ_{ji}^{IEE} are Onsager reciprocals.

In experiments, a 3D spin current $\mathbf{j}^{\text{s},3\text{D}}$ is injected into the 2D system (e.g. Rashba system) by spin pumping using ferromagnetic resonance (FMR) [25, 106]. The Edelstein system cannot be considered isolated but is covered by layers of other materials, i.e. a ferromagnetic layer for the FMR. The nonequilibrium spin density injected as 3D spin current is converted into a 2D charge current $\mathbf{j}^{\text{c},2\text{D}}$ due to the inverse Edelstein effect. The spin-to-charge current conversion efficiency is characterized by the tensor

$$\lambda_{ij}^{\text{IEE}} = \frac{j_i^{\text{c},2\text{D}}}{j_j^{\text{s},3\text{D}}}. \quad (4.14)$$

4. The Edelstein effect

Here, the spin current has the same unit as a charge current. Thus, $\lambda_{ij}^{\text{IEE}}$ has the dimension of a length. The spin-to-current conversion tensor $\hat{\lambda}^{\text{IEE}}$ is approximately proportional to the transposed Edelstein tensor $\hat{\kappa}^{\text{T}}$. However, for calculating $\hat{\lambda}^{\text{IEE}}$ in a spin-pumping setup, the system cannot be considered purely two-dimensional. Rather, scattering and transport through the adjacent layers has to be considered, as discussed in Refs. [126, 127].

4.4. Experimental observation of the Edelstein effect

Since the first theoretical prediction of the Edelstein effect in 1989, experimental effort was put into detecting the current-induced spin density using various techniques. Here, the most promising and established techniques and the corresponding systems providing an Edelstein effect are introduced.

Optical methods

For the detection of magnetoelectric effects, optical methods are self-evident. Exploiting the Faraday effect, which is the rotation of the polarization plane when linearly polarized light penetrates a medium magnetized in the direction of light propagation, the bulk magnetization of a 3D material can be measured. Kato *et al.* detected the current-induced spin polarization in a strained n -GaAs/In_{0.07}Ga_{0.93} heterostructure using static and time-resolved Faraday rotation [117, 118]. Due to the zincblende structure of GaAs, its bulk inversion symmetry is broken, which gives rise to a bulk Dresselhaus SOC term introduced in section 3.5. In addition, anisotropic strain leads to Rashba-like spin-orbit coupling of the bulk bands.

The magneto-optic Kerr effect (MOKE) is used to detect the surface spin polarization and can provide even spatially resolved signals. Polarized light reflected at a magnetic surface changes its polarization plane as well as ellipticity and intensity. Different geometries are distinguished which are sensitive to different magnetization orientations. In the polar geometry (PMOKE), an out-of-plane magnetization can be detected. An in-plane surface magnetization can be detected in the longitudinal geometry (LMOKE) with a signal which is typically smaller by approximately one order of magnitude in comparison to PMOKE. Due to the different amplitudes of the signals, the out-of-plane magnetization is experimentally better accessible than the in-plane magnetization.

Sih *et al.* used PMOKE to detect signatures of the spin Hall effect as well as a current-induced spin polarization in a 2DEG confined in (110) AlGaAs quantum wells [119]. They observed spatially resolved images of the out-of-plane magnetization in the presence of an in-plane electric field. The homogeneous contribution is explained as current-induced spin polarization due to the Dresselhaus SOC. Further, the in-plane Edelstein component was also detected.

Resistivity measurements

A nonzero spin polarization due to the Edelstein effect or due to a finite magnetization in a ferromagnetic material corresponds to an imbalance of charge carriers with opposite spin orientations. The spin-dependent conductivities depend on the magnetization direction, which allows to detect the spin polarization induced in a 2DEG brought into contact with a ferromagnet. By switching the magnetization of either the ferromagnet or the 2DEG, the resistivity of the heterostructure changes and the current-induced spin polarization can be determined [128]. The method was used by Hammar and Johnson to investigate the Rashba spin splitting of an InAs quantum well [129].

In a similar way, the spin polarization can be detected nonlocally by a ferromagnetic tunnel contact. This method has been employed to detect the current-induced spin polarization in the surface states of topological insulators, e.g. Bi_{1.5}Sb_{0.5}Te_{1.7}Se_{1.3} [22], Bi₂Se₃ [23] and Bi₂Te₂Se [24].

System	m (m_e)	α_R (eVÅ)	\mathcal{E}_F (eV)	κ_{yx} (10^{-9}mV^{-1})	ζ_{yx} (10^{-8}mA^{-1})	Ref.
Au(111) sf	0.27	0.33	0.475	1.05	7.22	[134, 135]
Ag(111) sf	0.37	0.03	0.178	0.10	2.43	[135, 136]
InGaAs/InAlAs (001) hs	0.05	0.07	0.092	0.46	3.53	[73]
Bi/Ag(111) sfal	-0.35	3.05	-0.180	29.13	205.50	[121, 137]

Table 4.1.: Field-to-spin conversion efficiency κ_{yx} and charge-to-spin conversion efficiency ζ_{yx} for isotropic Rashba systems, sf=surface state, hs=heterostructure, sfal=surface alloy. The parameters m , α_R and \mathcal{E}_F are taken from the cited references. Here and in the following the scattering potential is set to $U_0 = 1\text{eV}$ with an impurity concentration of $c_i = 1\%$. Similar data was published in [J4].

Ferromagnetic resonance

Spin pumping by ferromagnetic resonance (FMR) is an established method for studying the inverse Edelstein effect. In comparison to the direct Edelstein effect, its inverse provides the advantage that the signal is a charge current, which can directly be detected. The first experimental evidence of the inverse Edelstein effect was given by Rojas Sánchez *et al.* at an Ag/Bi interface [106]. The Ag/Bi heterostructure (Bi covered by Ag) is covered by a magnetic NiFe layer. By ferromagnetic resonance, a 3D spin current density is injected from the magnetic NiFe layer into the Ag layer [130] and penetrates through the Ag layer into the Ag/Bi interface. Here, the injected nonequilibrium spin density induces a charge current density in the two-dimensional Ag/Bi layer via the inverse Edelstein effect which can be detected electrically.

Further, Rojas Sánchez *et al.* measured the inverse Edelstein effect in the surface states of the topological insulator α -Sn [25]. The experimental method has also been used to observe the inverse Edelstein effect in the Rashba-like spin-split 2DEG between SrTiO₃ and LaAlO₃ [28, 30].

Similarly, the direct Edelstein effect can be detected using spin torque ferromagnetic resonance (ST-FMR) [131]. Here, the spin density created by the Edelstein effect in the 2DEG (e.g. Rashba system) diffuses as a spin current into the ferromagnetic layer and exerts a torque on the magnetization, which manifests in a change of the FMR signal [131, 132]. This method was used to detect the charge-to-spin current conversion in the topological insulator (Bi_{1-x}Sb_x)₂Te₃ [132].

4.5. Edelstein effect in Rashba systems

The theory developed in section 4.1 is used to calculate the Edelstein effect in paradigm Rashba systems which can be approximated by the isotropic Rashba Hamiltonian (3.18). Further, the model is extended by introducing anisotropies in order to better simulate systems with C_{2v} and C_{3v} symmetry. Subsequently, the Edelstein effect is calculated for systems with magnetic impurities. The results are presented in two different ways, (I) as a response to the external electric field \mathbf{E} and (II) to the charge current \mathbf{j}^c through the 2DEG. The anisotropic Fermi lines are calculated within an adaptive triangular method, which is briefly sketched in appendix E.1.

4.5.1. Isotropic Rashba systems

The analytical expressions derived in section 4.1 are used to calculate the field- or current- induced spin density for the Au(111) and Ag(111) surface states, the InGaAs/InAlAs(001) heterostructure and the ordered ($\sqrt{3} \times \sqrt{3}$)R30° Bi/Ag(111) surface alloy. These systems provide spin-split surface states which are approximated by an isotropic Rashba Hamiltonian here. The microscopic origin of the surface states' band splitting is discussed in more detail in Ref. [133].

The tensor components κ_{yx} and ζ_{yx} are shown in Table 4.1, relating the induced spin density in y -direction to the electric field and the charge current in x -direction, respectively. The Au(111)

4. The Edelstein effect

surface is often discussed as paradigm of a Rashba system [134, 138]. The surface states provide a comparably large Rashba splitting leading to an efficient spin generation factor κ_{yx} . In contrast, the Edelstein effect is less pronounced in the Ag(111) surface states as well as in the InGaAs/InAlAs heterostructure due to the smaller SOC expressed by a reduced Rashba parameter.

The Bi/Ag(111) surface alloy provides a ‘‘giant’’ Rashba SOC enhanced particularly by the additional in-plane potential gradient that comes with the ordered alloy [137]. However, since the Fermi level is outside the band with the large Rashba SOC [137], the system in its pristine form is not appropriate for calculating the Edelstein effect within the Boltzmann approach. Therefore, the Fermi level is shifted artificially into the strongly spin-split band and a very high efficiency of spin generation is obtained.

As discussed above, the current-to-spin conversion factor ζ_{yx} does not give much information about the relation between induced spin density and the charge current in the whole sample but relates only the spin density to the charge current in the 2D Rashba system. Nevertheless, calculating both κ_{yx} and ζ_{yx} illustrates that an apparently high charge-to-spin conversion efficiency can be obtained by normalizing the spin density with respect to the charge current, even if the spin splitting is not very pronounced. As long as the charge current is low, the factor ζ_{yx} is comparably large even for a small Rashba SOC. As an example, the Au(111) and Ag(111) surfaces are compared. Although the Rashba parameter of the Ag(111) surface is remarkably smaller than α_R of Au(111) and so is the tensor element κ_{yx} , the difference of the current-to-spin conversion factors ζ_{yx} is less pronounced due to the low charge conductivity in Ag(111).

In general, $\hat{\kappa}$ connects the electric field \mathbf{E} as origin of the nonequilibrium distribution, and the response $\overline{\langle \mathbf{s} \rangle}$. It represents the ability of the system to create a nonzero spin density as a response to an electric field and should therefore be chosen as the quantity in order to evaluate the magnitude of the Edelstein effect.

4.5.2. Anisotropic Rashba systems

More realistic systems are not isotropic but exhibit anisotropies due to the crystal structure. Therefore, using a $\mathbf{k} \cdot \mathbf{p}$ approach [139], the isotropic Rashba model is modified. Two examples of anisotropic Rashba systems will be discussed here, systems with C_{2v} and C_{3v} symmetry, respectively. In the first case, the parameters m and α_R are anisotropic. In the latter case, a contribution to the Rashba Hamiltonian is added in order to account for the reduced symmetry. The surface normal is always assumed in z -direction.

C_{2v} symmetry

Rashba systems with C_{2v} symmetry can be found e.g. at the (110) surface of fcc crystals. In order to express the nonequivalence of the two symmetry axes (x and y , respectively), an anisotropy of the Rashba parameters, $\alpha_{Rx} \neq \alpha_{Ry}$, and the effective masses, $m_x \neq m_y$, is introduced. The Rashba Hamiltonian becomes [71, 139]

$$\hat{H}_R^{C_{2v}} = \frac{\hbar^2 k_x^2}{2m_x} + \frac{\hbar^2 k_y^2}{2m_y} + \alpha_{Rx} k_x \hat{\sigma}_y - \alpha_{Ry} k_y \hat{\sigma}_x \quad (4.15)$$

with the energy eigenvalues

$$\mathcal{E}^n(\mathbf{k}) = \frac{\hbar^2 k_x^2}{2m_x} + \frac{\hbar^2 k_y^2}{2m_y} + n \sqrt{\alpha_{Rx}^2 k_x^2 + \alpha_{Ry}^2 k_y^2}. \quad (4.16)$$

Here, the anisotropic Rashba parameters α_{Rx} and α_{Ry} can be decomposed into an isotropic contribution originating from the surface gradient, which is constant with respect to the in-plane direction [Eq. (3.17)], and an additional anisotropic contribution originating from the admixture of

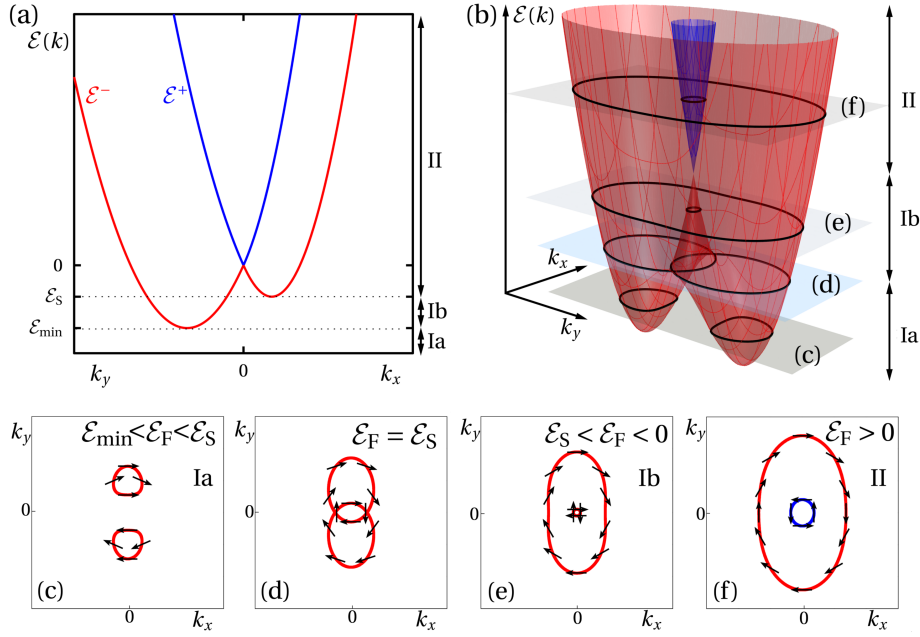


Figure 4.3.: Band structure and iso-energy lines of a Rashba system with C_{2v} symmetry. The model parameters read $m_x = 0.5m_y$, $\alpha_{Rx} = \alpha_{Ry}$. Adapted from [J4].

$p_{x,y}$ bulk states [71].

In Fig. 4.3 the band structure and iso-energy lines for a model with ($m_x = 0.5m_y$, $\alpha_{Rx} = \alpha_{Ry}$) are shown. Due to the C_{2v} symmetry, the position of the band edge and the band curvature are anisotropic. Figs. 4.3(c)-(f) display the contours of constant energy with the \mathbf{k} -dependent spin polarization for selected energy values. The spin is not tangential to the Fermi lines due to the anisotropy of the system.

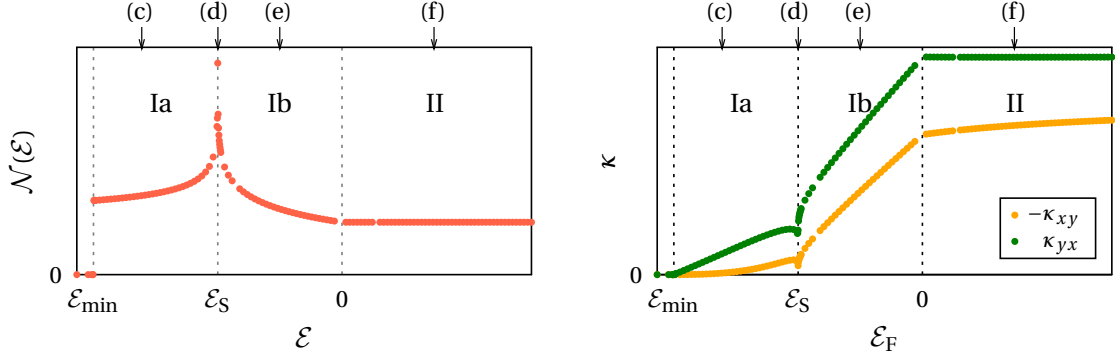
In the band structure, the density of states [Fig. 4.4(a)] as well as the energy-dependent Edelstein effect [Fig. 4.4(b)], three energy regions can be identified. Above the diabolic point (region II), both branches $n = \pm 1$ are occupied. Here, the total spin density is nearly constant in energy, as in the isotropic Rashba system. For $\mathcal{E}_F < 0$ (regions Ia and Ib), only the branch $n = -1$ is occupied. At $\mathcal{E}_S = -\frac{1}{2\hbar^2} \min(\alpha_{Rx}^2 m_x, \alpha_{Ry}^2 m_y)$ the band edge is reached in the direction of one of the symmetry axes (here: k_x). Here, the band structure exhibits a saddle point, the lines of constant energy intersect, depicted in Fig. 4.3(d). As shown by the evolution of the constant-energy lines in Figs 4.3(c)-(e), a Lifshitz transition occurs, leading to a van Hove singularity in the density of states [140], shown in Fig. 4.4(a). The iso-energy line changes its topology from two concentric closed contours (energy region Ib) to two separated closed lines (energy region Ia).

Around the energy of the Lifshitz transition, the spin density is reduced down to 0 at \mathcal{E}_S , shown in Fig. 4.4(b). This drastic reduction is explained by the behavior of the mean free path on the Fermi line, $\Lambda_{\mathbf{k}} = \mathbf{v}_{\mathbf{k}} \tau_{\mathbf{k}}^{\text{tr}}$. At the intersection points [saddle points, Fig. 4.3(d)], the group velocity and also the mean free path are zero. Solving the linearized Boltzmann equation (2.48) leads to $\tau_{\mathbf{k}}^{\text{tr}} = 0$ for all other points on the Fermi line, also resulting in $\Lambda_{\mathbf{k}} = 0$. In Fig. 4.4(b) the spin density is not exactly zero for numerical reasons.

At $\mathcal{E}_{\min} = -\frac{1}{2\hbar^2} \max(\alpha_{Rx}^2 m_x, \alpha_{Ry}^2 m_y)$ the global band minimum is reached which corresponds to two single points in \mathbf{k} -space (here: on the k_y -axis). Within the regions Ia and Ib the induced spin density exhibits a nearly linear energy dependence, as for the isotropic Rashba system. However, the slope of the curve differs between the both regions due to the different Fermi line topology. The shape of the Fermi line in energy range Ib is similar to the isotropic system, but distorted. In energy region Ia, not all directions in \mathbf{k} -space are occupied which leads to a smaller slope than in region Ib.

Although the Edelstein tensor elements κ_{xy} and κ_{yx} exhibit a qualitatively similar energy-de-

4. The Edelstein effect



(a) Density of states with van Hove singularity at \mathcal{E}_S . (b) Spin density as response to an electric field. A similar figure was published in [J4].

Figure 4.4.: Density of states and field-induced spin density as a function of the energy for a system with the model parameters ($m_x = 0.5m_y$, $\alpha_{Rx} = \alpha_{Ry}$). At \mathcal{E}_S a Lifshitz transition occurs leading to a logarithmic van Hove singularity in the density of states and a reduction of the spin density to 0. The letters (c)-(f) correspond to the selected energies in Fig. 4.3.

m_x (m_e)	m_y (m_e)	α_{Rx} (eVÅ)	α_{Ry} (eVÅ)	\mathcal{E}_F (eV)	κ_{xy} (10^{-9} m/V)	κ_{yx} (10^{-9} m/V)	ζ_{xy} (10^{-8} m/A)	ζ_{yx} (10^{-8} m/A)
0.11	0.32	0.80	0.17	0.370	-0.72	1.72	-12.14	10.01

Table 4.2.: Current-induced spin density of Au(110) surface states. The model parameters are taken from Ref. [71]. The spin per surface unit cell is shown as a function of an electric field ($\hat{\kappa}$) as well as as function of the charge current ($\hat{\zeta}$) induced by the electric field. Similar results were published in [J4].

pendence, they differ with respect to their absolute values due to the anisotropy of the system. As a consequence, the induced spin polarization is not always perpendicular to the direction of the applied electric field but includes an angle θ with the field,

$$\cos\theta(\langle \mathbf{s} \rangle, \mathbf{E}) = \frac{(\kappa_{xy} + \kappa_{yx}) \cos\phi \sin\phi}{\sqrt{\kappa_{xy}^2 \sin^2\phi + \kappa_{yx}^2 \cos^2\phi}}, \quad (4.17)$$

with ϕ the angle of the electric field with respect to the x -direction. Thus, when \mathbf{E} is aligned with the symmetry axes, spin density and electric field are perpendicular whereas the angle can deviate for different orientations of \mathbf{E} and $\kappa_{xy} \neq -\kappa_{yx}$. Further, the absolute value of the induced spin density also oscillates with the angle ϕ ,

$$|\langle \mathbf{s} \rangle| = \sqrt{\kappa_{xy}^2 \sin^2\phi + \kappa_{yx}^2 \cos^2\phi} |\mathbf{E}|. \quad (4.18)$$

As an example of a system approximated by the C_{2v} Rashba Hamiltonian (4.15), the Au(110) surface states are discussed. Here, the directions x and y in the model Hamiltonian (4.15) correspond to the crystallographic axes [001] and $[\bar{1}10]$, respectively [71]. The model parameters taken from Ref. [71] as well as the tensors $\hat{\kappa}$ and $\hat{\zeta}$ are presented in Table 4.2. Obviously, $\kappa_{xy} \neq -\kappa_{yx}$ and $\zeta_{xy} \neq -\zeta_{yx}$ due to the nonequivalence of the axes [001] and $[\bar{1}10]$. Thus, by an appropriate choice of the direction of the applied electric field, the magnitude of the Edelstein effect can be influenced remarkably. For the Au(110) surface, an electric field $\mathbf{E} \parallel [001]$ induces a spin density which is enhanced by more than 100% in comparison to the spin density resulting from $\mathbf{E} \parallel [\bar{1}10]$.

Further, Table 4.2 demonstrates that the occurrence of a “large” Edelstein effect also depends on the choice of quantity that is used to characterize the effect. Although the response to an electric

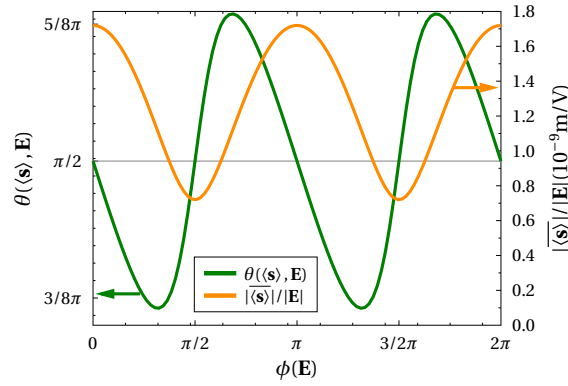


Figure 4.5.: Angle θ between the induced spin density and the applied electric field and absolute value of the spin density for the Au(110) surface states. The electric field is rotated in-plane including the angle ϕ with the [001]-direction.

field is larger for $\mathbf{E} \parallel [001]$ ($|\kappa_{yx}| > |\kappa_{xy}|$), the induced spin density as a function of the charge current seems to be larger for $\mathbf{E} \parallel [\bar{1}10]$ ($|\zeta_{xy}| > |\zeta_{yx}|$) because the Fermi surface properties lead to an enhanced spin as well as charge current density, as discussed below.

In Fig. 4.5 the angle between the induced spin density and the electric field is shown as a function of the orientation of the electric field in the (110) surface plane, calculated using Eq. (4.17) and the values κ_{xy} and κ_{yx} shown in Table 4.2. Due to the strong anisotropy of the Fermi surface, the angle θ included by $\langle \mathbf{s} \rangle$ and \mathbf{E} considerably oscillates when \mathbf{E} is rotated in-plane. For \mathbf{E} not aligned with the symmetry axes, the deviation from orthogonality can become as large as $\pi/8$. As expected from the anisotropy of the system, the absolute value of the \mathbf{E} -induced spin density also strongly oscillates when \mathbf{E} is rotated in-plane, as also displayed in Fig. 4.5.

For possible applications of the Edelstein effect, a high efficiency of spin generation is preferable. Therefore, some general remarks on the most efficient direction of \mathbf{E} in a C_{2v} system are of interest. For a more illustrative understanding, the influence of anisotropies of m and α_R are examined separately here. For $\alpha_{Rx} = \alpha_{Ry}$ and $m_x \neq m_y$, as in the paradigm system whose band structure and Fermi lines are shown in Fig. 4.3, the anisotropy of effective masses results in anisotropic Fermi lines, which are elongated in the direction of the axis with the larger effective mass, for Au(110) this is the $[\bar{1}10]$ -direction. The spin-orbit field is not modified by the mass anisotropy and identical to the isotropic Rashba spin-orbit field depicted in Fig. 3.2(a).

An electric field applied in the direction of elongation shifts the Fermi lines in such a way that mostly the states at the less extended side of the Fermi line contribute to the Edelstein effect, which is comparably small, shown in Fig. 4.6(a). If the field is applied in the direction of the axis with the smaller effective mass, for Au(110) this is [001], the main contribution to the Edelstein effect originates from the states at the elongated sides of the Fermi line, the spin density is comparably large, illustrated in Fig. 4.6(b).

Thus, in general an enhanced spin density is expected if the electric field is in the direction of the smaller effective mass. By the same Fermi surface geometry properties the magnitude of the charge conductivity is similarly influenced. However, the anisotropy of charge conductivity is even more pronounced because here the contributions from both Fermi lines do not cancel but add up. Therefore, applying a charge current in the direction of the smaller effective mass ($x \parallel [001]$ for Au(110)) reduces the corresponding tensor element of $\hat{\zeta}$ (here: ζ_{yx}) giving the impression of a less efficient charge-to-spin conversion.

The influence of the Rashba parameter anisotropy is examined assuming $m_x = m_y$ and $\alpha_{Rx} \neq \alpha_{Ry}$. Due to this asymmetry the Fermi lines also become anisotropic with the elongated side in the direction of the smaller Rashba parameter for the $n = +1$ branch (for Au(110) this is $[\bar{1}10]$) and in

4. The Edelstein effect

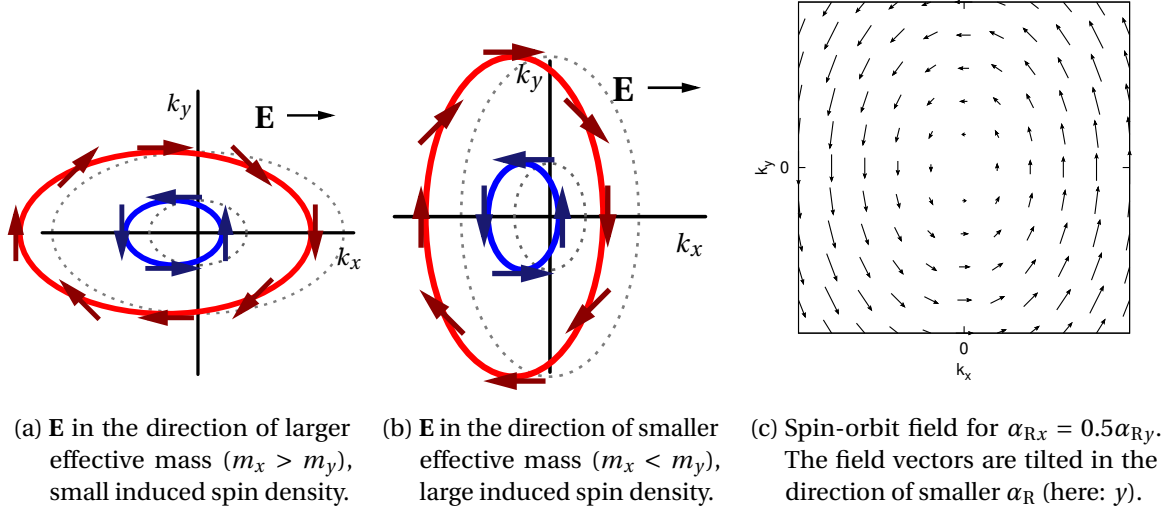


Figure 4.6.: (a), (b): Fermi lines of a system with anisotropic effective masses in equilibrium (dashed lines) and in the presence of an electric field \mathbf{E} (solid lines). The direction of the electric field influences the magnitude of the Edelstein effect. (c): Spin-orbit field of a system with anisotropic Rashba parameters.

the direction of the larger Rashba parameter for the $n = -1$ branch (for Au(110): [001]), respectively. Further, the \mathbf{k} -dependent spin expectation values are tilted in the direction of the smaller Rashba parameter, illustrated by the spin-orbit field shown in Fig. 4.6(c) for the model system $\alpha_{Rx} = 0.5\alpha_{Ry}$: The spin-orbit field vectors have in general a larger component in the y -direction.

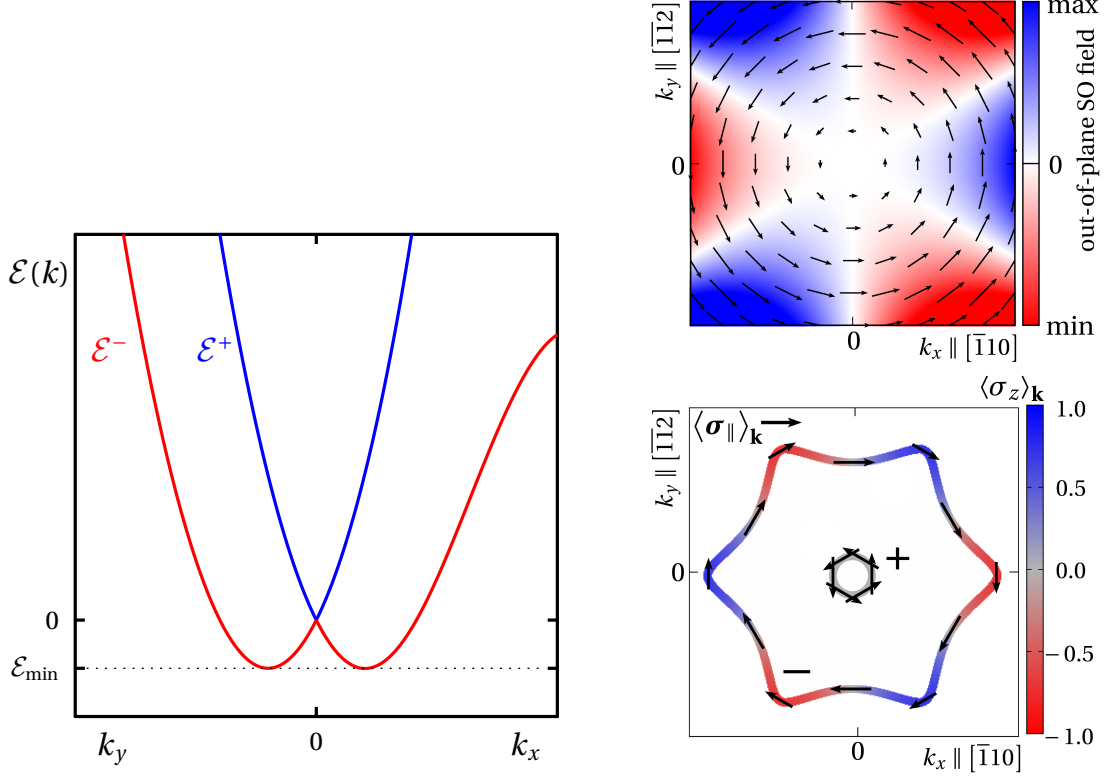
If the electric field is applied in the direction of the larger Rashba parameter (for Au(110): [001]-direction), the states contributing to the Edelstein effect have a comparably large spin component perpendicular to that field and provide an effective charge-to-spin conversion. On the other hand, an electric field applied in the direction of smaller α_R induces a smaller spin density because the contributing states carry a lower spin component perpendicular to the field. Further, the Fermi surface geometry also enhances the effect if \mathbf{E} is applied in the direction of larger Rashba parameter, similar to the case $m_x \neq m_y$ discussed above.

By these considerations, the enormous enhancement of the Edelstein effect in Au(110) when \mathbf{E} is tilted from the [001] to the $[\bar{1}10]$ -direction can be explained. In general, the rule that applying the field in the direction of the smaller m and the larger α_R enhances the Edelstein effect can be formulated.

Besides the Au(110) surface, not many Rashba systems with C_{2v} symmetry have been identified until now. However, recently a highly anisotropic Rashba spin splitting at the Bi/InAs(110)-(2 × 1) surface has been reported [141]. For this system, the surface states exhibit a quasi-one-dimensional character. The Fermi lines are elongated in the [001]-direction and open in the first Brillouin zone. The band structure in the $[\bar{1}10]$ -direction can be approximated by a one-dimensional Rashba model with $\alpha_R \approx 5.5\text{eV}\text{\AA}$, which is even larger than in the Bi/Ag(111) surface alloy. Thus, a very efficient charge-to-spin conversion can be expected for this system. However, due to the strong anisotropy with open Fermi lines, this system cannot be described by the model Hamiltonian (4.15) and is therefore not discussed further here.

C_{3v} symmetry

The (111) surfaces of fcc crystals and ordered (111) surface alloys, which were presented as examples of isotropic Rashba systems, are only approximately isotropic and possess C_{3v} symmetry. Ast *et al.* [137] and Premper *et al.* [142] have shown that a large in-plane potential gradient, as in the



(a) Energy dispersion in the direction of a mirror plane (k_y) and perpendicular to a mirror plane (k_x). Due to the k^3 -dependence, the warping term mainly affects the band structure of the $n = -1$ branch at higher k -values.

(b) Upper panel: Spin-orbit field. Lower panel: Iso-energy lines with spin expectation values. The arrows indicate the in-plane field/spin polarization, the color is the out-of-plane component.

Figure 4.7.: Energy dispersion, spin-orbit field and Fermi surface with spin polarization of a system with C_{3v} symmetry (schematic). One mirror plane is in k_y -direction.

Bi/Ag($\sqrt{3} \times \sqrt{3}$) $R30^\circ$ surface alloy, leads to an enhanced spin splitting which results in a large Edelstein effect, as discussed above. Thus, these systems are of special interest for possible applications due to their efficient charge-to-spin conversion. Considering a more detailed model Hamiltonian for these systems provides the opportunity to make more reliable statements about the magnitude of the Edelstein effect.

In order to take account of the broken isotropy, the Hamiltonian is extended by a C_{3v} symmetric term [143],

$$\hat{H}_R^{C_{3v}} = \frac{\hbar^2 \mathbf{k}^2}{2m} + \alpha_R (k_x \hat{\sigma}_y - k_y \hat{\sigma}_x) + \frac{\lambda_w}{2} (k_+^3 + k_-^3) \hat{\sigma}_z. \quad (4.19)$$

Here, the k_x -direction corresponds to the ΓK -direction ($[\bar{1}10]$ -direction) in the (111) surface Brillouin zone and the k_y -direction corresponds to the ΓM -direction ($[\bar{1}12]$). Thus, the y -direction is chosen to be aligned with one of the mirror planes. The parameter λ_w characterizes the strength of the in-plane gradient, and $k_\pm \equiv k_x \pm ik_y$. The energy spectrum has a sixfold rotational symmetry,

$$\mathcal{E}^n(\mathbf{k}) = \frac{\hbar^2 k^2}{2m} + n \sqrt{\alpha_R^2 k^2 + \lambda_w^2 k^6 \cos^2(3\varphi_{\mathbf{k}})}. \quad (4.20)$$

In the direction of the three mirror planes (e.g. k_y -direction), the spin expectation value is completely in-plane and the band structure corresponds to the isotropic model. The additional third-order Hamiltonian proportional to $\hat{H}_3 = \frac{\lambda_w}{2} (k_+^3 + k_-^3) \hat{\sigma}_z$, called *warping term*, is maximum in the directions perpendicular to the mirror planes (e.g. k_x -direction) [144] and modifies the band struc-

4. The Edelstein effect

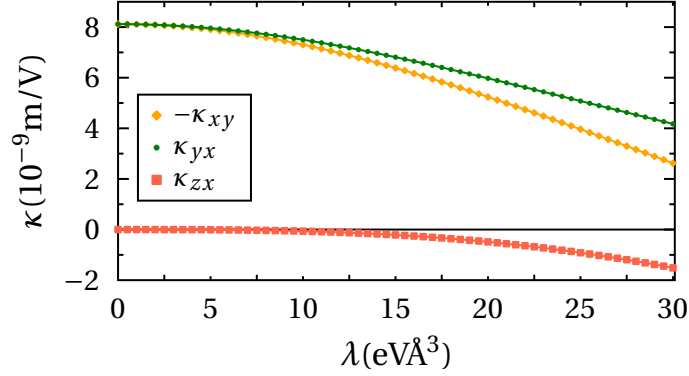


Figure 4.8.: Influence of the warping parameter λ_w on the tensor elements of $\hat{\kappa}$. The model parameters read $m = -0.29m_e$, $\alpha_R = 0.85\text{eV}\text{\AA}$, $\mathcal{E}_F = -0.215\text{eV}$, corresponding to the Bi/Cu(111) surface alloy [144–146].

system	m (m_e)	α_R ($\text{eV}\text{\AA}$)	λ_w ($\text{eV}\text{\AA}^3$)	\mathcal{E}_F (meV)	κ_{xy} (10^{-9}mV^{-1})	κ_{yx} (10^{-9}mV^{-1})	κ_{zx}	ζ_{xy} (10^{-8}mA^{-1})	ζ_{yx} (10^{-8}mA^{-1})	ζ_{zx}
Bi/Cu	-0.29	0.85	0	-215	-8.12	8.12	0.00	-93.06	93.06	0.00
			12		-6.97	7.25	-0.11	-84.51	83.69	-1.27
Bi/Ag	-0.32	2.95	0	-180	-28.17	28.17	0.00	-202.30	202.30	0.00
			18		-12.95	17.43	-2.46	-191.20	146.65	-20.71

Table 4.3.: Charge-to-spin conversion factors $\hat{\kappa}$ and $\hat{\zeta}$ for Bi/Cu(111) and Bi/Ag(111) ($\sqrt{3} \times \sqrt{3}$) $R30^\circ$ surface alloys. The conversion factors are calculated without ($\lambda_w = 0$) and with ($\lambda_w \neq 0$) the warping term. As in Table 4.1, the Fermi energy of the Bi/Ag surface alloy was assumed within the band with strong Rashba SOC. The model parameters are taken from Refs. [144–146] (Bi/Cu) and [121, 137, 144, 145, 147] (Bi/Ag), respectively.

ture in these directions, as shown in Fig. 4.7(a). Due to the k^3 -dependence of \hat{H}_3 , its influence is more pronounced on the $n = -1$ branch because of the larger k -values. The Fermi line of the $n = -1$ branch has a hexagonal shape, the $n = 1$ Fermi line is nearly circular, as shown in Fig. 4.7(b).

Due to the in-plane potential gradient, the \mathbf{k} -dependent spin expectation values have an out-of-plane component, which is shown by the spin-orbit field and the Fermi line with spin expectation values in Fig. 4.7(b). Although the energy spectrum has sixfold rotation symmetry, the spin texture reveals the C_{3v} symmetry of the system.

Because of the reduced symmetry, the tensor elements κ_{xy} , κ_{yx} and κ_{zx} are nonzero, and in general $\kappa_{xy} \neq -\kappa_{yx}$. Fig. 4.8 shows the dependence of these tensor elements on the warping parameter λ_w for a model system whose parameters resemble the Bi/Cu(111) surface alloy. In general, the additional warping term in the Hamiltonian reduces the magnitude of the in-plane spin expectation values and therefore also diminishes the in-plane induced spin density (κ_{xy} and κ_{yx}). The enhanced out-of-plane spin expectation values gives rise to a finite out-of-plane spin density (κ_{zx}) if the electric field is applied in x -direction. Further, the modified shape of the Fermi lines leads to a reduced absolute value of the current-induced spin density.

Thus, the orientation of \mathbf{E} with respect to the crystallographic axes can affect the direction and absolute value of the induced spin density, although this angular dependence is typically not as pronounced as for systems with C_{2v} symmetry.

In Table 4.3 the nonzero elements of $\hat{\kappa}$ and $\hat{\zeta}$ of the the Bi/Cu(111) and Bi/Ag(111) ($\sqrt{3} \times \sqrt{3}$) $R30^\circ$ surface alloys are shown. In order to examine the influence of the warping term, the results are

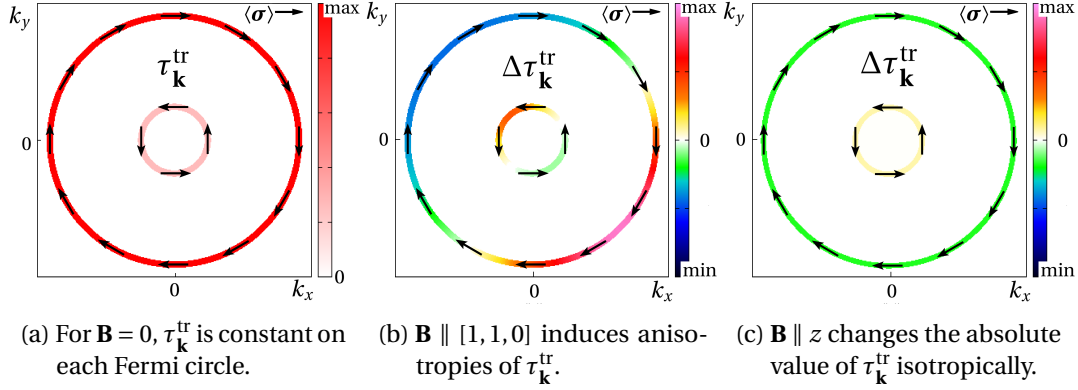


Figure 4.9.: Transport lifetime of an isotropic Rashba system with nonmagnetic and magnetic impurities, respectively. Panels (b) and (c) show the deviation from the case $\mathbf{B} = 0$ (panel (a)).

calculated without ($\lambda_w = 0$) and with ($\lambda_w \neq 0$) warping, respectively. Especially κ_{yx} describing the spin polarization as a function of the applied electric field is decreased by the warping term whereas ζ_{yx} , the charge-to-spin conversion factor, is only weakly influenced because the charge conductivity is affected by the warping term in a similar way as the spin polarization due to the modified Fermi lines.

4.5.3. Magnetic impurities

Until now, the scattering potentials used in Eq. (2.73) were assumed to be scalar, corresponding to nonmagnetic impurities. However, an impurity with a finite magnetic moment induces a local magnetic field, the single-impurity scattering strength is expressed as

$$U_0 = u_0 + \frac{g\mu_B}{2} \hat{\sigma} \cdot \mathbf{B}_{\text{imp}}. \quad (4.21)$$

Here, u_0 is the scalar potential, g is the g -factor, μ_B the Bohr magneton and \mathbf{B}_{imp} is the local magnetic field induced by the magnetic moment of an impurity. By applying a small external magnetic field, the magnetic moments of the impurities can be aligned.

The microscopic transition probabilities $P_{\mathbf{k}' \leftarrow \mathbf{k}}$ do not only depend on the scattering angle between \mathbf{k} and \mathbf{k}' , but are influenced also by the angle between \mathbf{B}^{imp} and \mathbf{k} as well as \mathbf{k}' , respectively,

$$P_{\mathbf{k}' \leftarrow \mathbf{k}}^{n' \leftarrow n} = \frac{c_i \pi}{\hbar N_{\text{at}}} \left\{ u_0^2 [1 + nn' \cos(\tilde{\varphi}' - \tilde{\varphi})] + \frac{g^2 \mu_B^2}{4} \left[B_x^2 (1 - nn' \cos(\tilde{\varphi}' + \tilde{\varphi})) \right. \right. \\ \left. \left. + B_y^2 (1 + nn' \cos(\tilde{\varphi}' + \tilde{\varphi})) + B_z^2 (1 - nn' \cos(\tilde{\varphi}' - \tilde{\varphi})) - 2nn' B_x B_y \sin(\tilde{\varphi}' + \tilde{\varphi}) \right] \right. \\ \left. + \frac{g\mu_B}{2} [-2n' B_x u_0 (\sin \tilde{\varphi}' + nn' \sin \tilde{\varphi}) + 2n' B_y u_0 (\cos \tilde{\varphi}' + nn' \cos \tilde{\varphi}) \right] \right\}, \quad (4.22)$$

where $\mathbf{B} = \mathbf{B}_{\text{imp}}$. In the presence of a scalar scattering potential, $P_{\mathbf{k}' \leftarrow \mathbf{k}}$ corresponds to the overlap of the wave functions $|\mathbf{k}\rangle$ and $|\mathbf{k}'\rangle$. The magnetic moment of the impurity modifies this overlap, therefore, the electrons can now scatter between originally orthogonal states. As an example, the microscopic transition probability for magnetic impurities with $\mathbf{B} \parallel [1, 1, 0]$ is shown for different values of \mathbf{k} in the appendix A. The phase space for scattering is enhanced for initial states which are spin-polarized parallel to \mathbf{B} and reduced for initial states with opposite spin polarization leading to a reduced and respectively enhanced momentum relaxation time as well as transport life time.

Due to the in-plane spin polarization of the Rashba states, the in-plane component of the magnetic field \mathbf{B} causes anisotropies of $\tau_{\mathbf{k}}^{\text{tr}}$, whereas the out-of-plane component acts on all states

4. The Edelstein effect

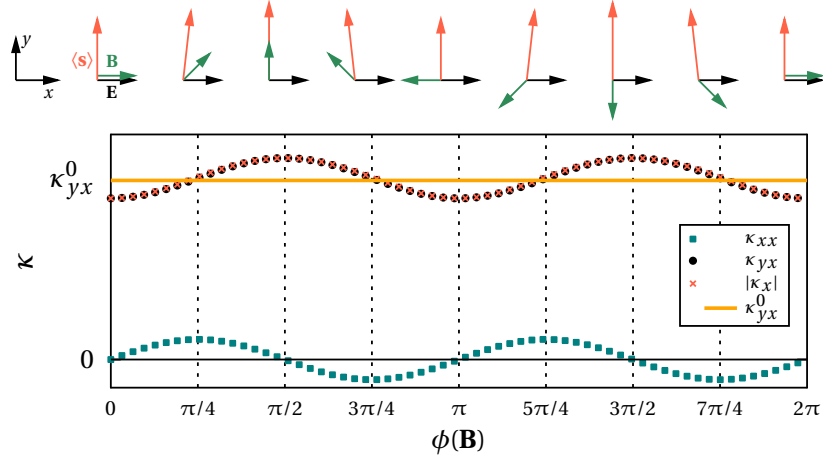


Figure 4.10.: Spin density induced by an electric field in a Rashba system with magnetic impurities. Here, $\frac{g\mu_B|B|}{2} = 0.3|u_0|$ is chosen. The small external magnetic field that orients the magnetic moments of the impurities is rotated in the xy -plane, thus, the local magnetic field at the impurity positions is also rotated. The angle between \mathbf{B} and the x -axis is denoted by $\phi(\mathbf{B})$. The tensor components κ_{xx} and κ_{yx} as well as $(|\kappa_x|)$, which corresponds to the absolute spin density induced by an electric field in x -direction, are shown. For comparison, the spin density in a system with nonmagnetic impurities represented by κ_{yx}^0 is marked. In the upper row, the directions of $\langle \mathbf{s} \rangle$ for $\mathbf{E} \parallel x$ and \mathbf{B} rotated in-plane are shown.

$|\mathbf{k}\rangle$ similarly and accounts only for a global change of the transport lifetime. Consequently, if \mathbf{B} has a finite in-plane component, $\tau_{\mathbf{k}}^{\text{tr}}$ is anisotropic and \mathbf{B} -dependent even for an isotropic Rashba system because the magnetic moments of the impurities break both time-reversal symmetry and in-plane rotation symmetry.

As an example, the transport lifetime on the Fermi line of an isotropic Rashba system is shown in Fig. 4.9 for a system with nonmagnetic impurities [Fig. 4.9(a)], as well as for magnetic impurities with $\mathbf{B} \parallel [110]$ [Fig. 4.9(b)] and with $\mathbf{B} \parallel z$ [Fig. 4.9(c)]. Due to the Rashba SOC and the in-plane spin polarization of the states, the transport lifetime is maximum for states with the spin polarization antiparallel to the magnetic field of the impurities. For the example shown in Fig. 4.9(b), the state with maximum $\tau_{\mathbf{k}}^{\text{tr}}$ is at in $[1, -1, 0]$ -direction in \mathbf{k} -space with a spin polarization in $[-1, -1, 0]$ -direction.

Because of the broken time-reversal symmetry leading to an anisotropic transport lifetime, an anisotropy of the spin density induced by an external electric field is expected. In Fig. 4.10 the components of the Edelstein tensor κ_{xx} and κ_{yx} in a Rashba system are shown as a function of the orientation of the local magnetic field \mathbf{B} of the impurities. For comparison, κ_{yx} in an isotropic system with nonmagnetic impurities is shown.

In the presence of in-plane magnetic moments of the impurities, the induced spin density is not always perpendicular to the applied electric field but can have a nonzero component parallel to \mathbf{E} , depending on the angle $\phi(\mathbf{B}, \mathbf{E})$ between \mathbf{B} and \mathbf{E} . Both parallel (κ_{xx}) and perpendicular (κ_{yx}) components are oscillating with the period π and a mutual phase shift of $\pi/4$. The absolute value of the spin density is dominated by the spin component perpendicular to \mathbf{E} , but the parallel component can lead to an in-plane tilt of $\langle \mathbf{s} \rangle$.

As discussed above, the transport lifetime has its maximum in the direction perpendicular to the magnetic field. The spin polarization of the corresponding state is opposite to the orientation of \mathbf{B} . Thus, the magnetic field leads to an additional \mathbf{k} -dependent weighting factor via $\tau_{\mathbf{k}}^{\text{tr}}$, allowing a spin polarization not perpendicular to \mathbf{E} .

As can be seen in Eq. (4.2), the projection $\mathbf{v}_{\mathbf{k}} \cdot \mathbf{E}$ also enters the total spin density as a weighting factor. Therefore, the total spin density is not always tilted in the direction of $-\mathbf{B}$. The periodicity of

π results from the superposition of the periodicities of $\langle \boldsymbol{\sigma} \rangle_{\mathbf{k}}$ and $\mathbf{v}_{\mathbf{k}} \cdot \mathbf{E}$ which oscillate both with 2π with respect to the azimuth on the Fermi line.

4.5.4. Rashba system with Zeeman splitting

An external magnetic field \mathbf{B} breaks the time-reversal symmetry of the Rashba system and therefore modifies the eigenfunctions as well as the band structure. For strong external magnetic fields, Landau quantization occurs and the semiclassical transport theory becomes invalid. The influence of a small magnetic field \mathbf{B} is expressed by an additional Zeeman term in the Hamiltonian,

$$\hat{H}_R^Z = \frac{\hbar^2 k^2}{2m} + \alpha_R(k_x \hat{\sigma}_y - k_y \hat{\sigma}_x) + \mu_B \mathbf{B} \cdot \hat{\boldsymbol{\sigma}}, \quad (4.23)$$

resulting in the energy spectrum

$$\mathcal{E}^n(\mathbf{k}) = \frac{\hbar^2 k^2}{2m} + n \sqrt{\mu_B^2 B^2 + \alpha_R^2 k^2 + 2\mu_B \alpha_R (B_y k_x - B_x k_y)} = \frac{\hbar^2 k^2}{2m} + n d_{\mathbf{k}}, \quad n = \pm 1 \quad (4.24)$$

with $d_{\mathbf{k}} = \sqrt{\mu_B^2 B^2 + \alpha_R^2 k^2 + 2\mu_B \alpha_R (B_y k_x - B_x k_y)}$. The impact of an external out-of-plane and in-plane magnetic field on the Rashba band structure is shown in Figs. 4.11(a)(I) and 4.11(b)(I), respectively. However, the influence of external magnetic fields on the band structure is typically small.

A magnetic field perpendicular to the Rashba 2DEG lifts the degeneracy at the diabolic point and opens a local band gap. For small magnetic fields, $|B| < \alpha_R^2 m / \hbar^2 \mu_B$, the band structure is Rashba-like with a gap around the diabolic point, as shown in Fig. 4.11(a)(I). For larger fields ($|B| > \alpha_R^2 m / \hbar^2 \mu_B$), the Zeeman term is dominant, the bands are parabola-like and separated in energy with their global minima at $\mathbf{k} = 0$, not shown in Fig. 4.11.

A field of 1T induces an energy gap of $\Delta \mathcal{E} = 2\mu_B |B| \approx 0.12 \text{meV}$. In order to discuss the effects of the Zeeman term qualitatively, the energy splitting in Fig. 4.11(a) is chosen as $\Delta \mathcal{E} = 40 \text{meV}$, which corresponds to an unrealistically large external magnetic field of $|B| \approx 345 \text{T}$. An energy splitting of this magnitude can be realized in systems with a finite magnetization due to ferromagnetic order, magnetic impurities or an adjacent ferromagnetic layer. Here, the exchange interaction yields a Zeeman-like Hamiltonian $\hat{H}_{\text{ex}} = -J_{\text{ex}} \hat{\mathbf{M}} \cdot \hat{\boldsymbol{\sigma}}$ with $\hat{\mathbf{M}}$ the direction of the magnetization and J_{ex} the exchange coupling strength between the electron spins and the magnetization [148]. The exchange interaction typically induces an energy splitting of a few 100meV [149]. However, in the following \mathbf{B} is used as a parameter to characterize the Zeeman as well as the exchange splitting, thus, $J_{\text{ex}} \hat{\mathbf{M}} \rightarrow -\mu_B \mathbf{B}$.

A coexistence of Rashba and exchange splitting is realized in three-dimensional multiferroic Rashba semiconductors (e.g. $\text{Ge}_{1-x}\text{Mn}_x\text{Te}$), which are ferroelectric materials with magnetic dopants. The finite ferroelectric polarization breaks the structural inversion symmetry and leads to a Rashba SOC, whereas the magnetic moments of the dopants induce magnetic exchange coupling [149–151].

An in-plane magnetic field or magnetization shifts the diabolic point in the \mathbf{k} -direction perpendicular to the field as well as in energy, as shown in Fig. 4.11(b)(I). The degeneracy is not lifted. A saddle point \mathcal{E}_S^- exists in the band structure and a Lifshitz transition occurs between a single Fermi line ($\mathcal{E} < \mathcal{E}_S^-$) and two Fermi lines ($\mathcal{E} > \mathcal{E}_S^-$). The corresponding iso-energy lines are depicted in appendix B. If the magnetic field has in-plane as well as out-of-plane components, the diabolic point is shifted in \mathbf{k} -space and the degeneracy is lifted, as shown in appendix C.

The modified band structure leads to an altered density of states, depicted in Figs. 4.11(a)(II) and 4.11(b)(II). For $\mathbf{B} \parallel z$, the DOS is similar to an ordinary Rashba system with additional finite steps at the local band gap. The in-plane magnetic field induces a qualitative change of the DOS. Due to the asymmetry of the band structure [Fig. 4.11(b)(I)], the band edge $\mathcal{E}_{\text{min}}^-$ is a single point leading to a

4. The Edelstein effect

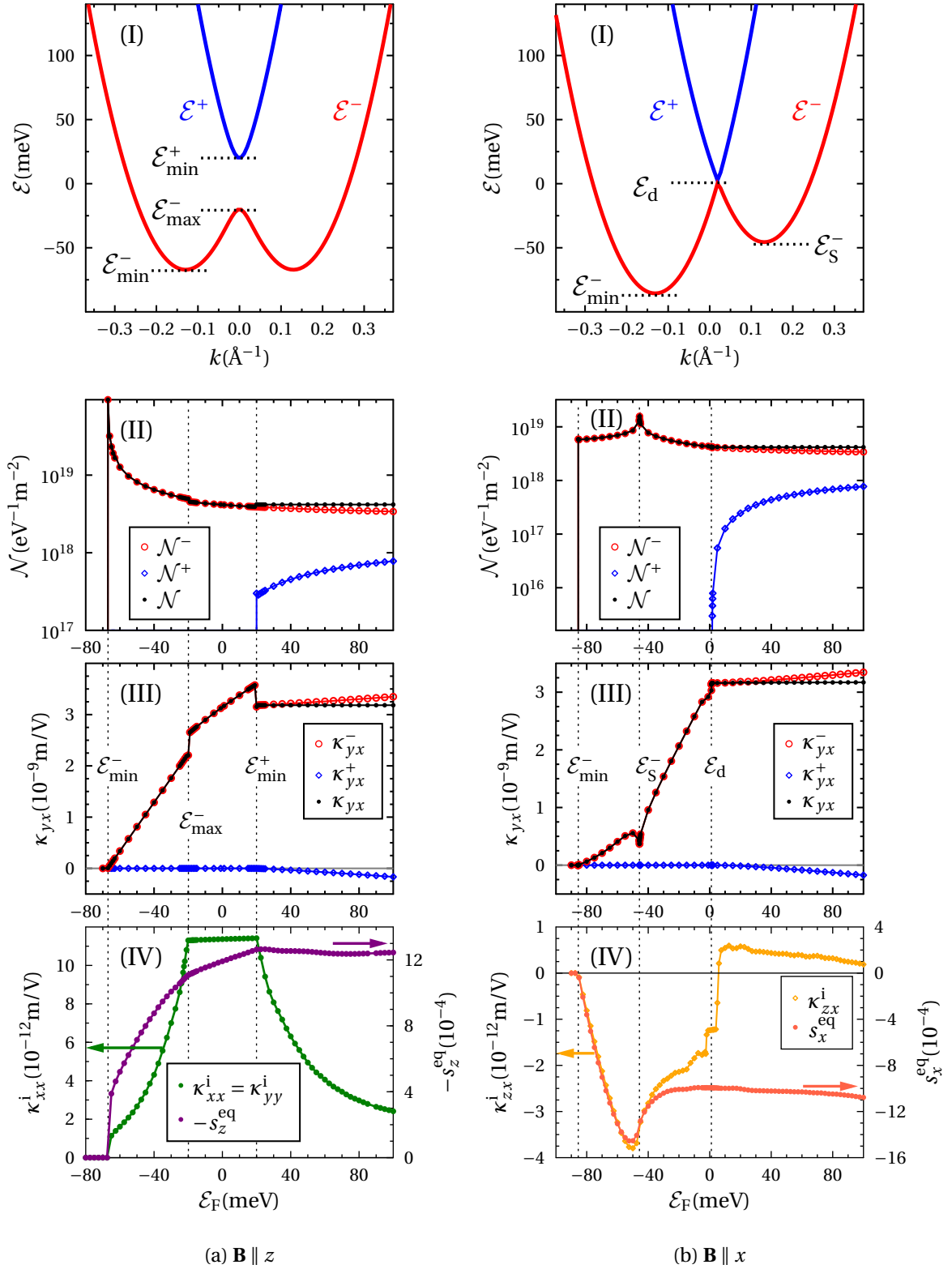


Figure 4.11.: Band structure, density of states and Edelstein effect in a Rashba system with out-of-plane (left column) and in-plane (right column) magnetic field, respectively. The model parameters are $\alpha_R = 1\text{eV}\text{\AA}$, $m = m_e$ and $\Delta\mathcal{E} = 2\mu_B|B| = 40\text{meV}$. Experimentally, such a strong splitting could only be achieved by an intrinsic magnetization, not by an external magnetic field.

finite step of the DOS, whereas the saddle point \mathcal{E}_S^- induces a logarithmic van Hove singularity.

The \mathbf{k} -dependent spin expectation values achieve additional components in the direction of \mathbf{B} ,

$$\langle \boldsymbol{\sigma} \rangle_{\mathbf{k}}^n = n \left(\frac{-\alpha_R k_y + \mu_B B_x}{d_{\mathbf{k}}}, \frac{\alpha_R k_x + \mu_B B_y}{d_{\mathbf{k}}}, \frac{\mu_B B_z}{d_{\mathbf{k}}} \right). \quad (4.25)$$

Thus, even in equilibrium, the system has a non-vanishing spin density due to the magnetic field. An electric field can induce an additional nonzero contribution to the total spin expectation value. Due to the broken time-reversal and inversion symmetries, intrinsic as well as extrinsic effects exist.

A symmetry analysis shows which tensor elements of $\hat{\kappa}$ are in general nonzero. If $\mathbf{B} \parallel z$, the system is invariant with respect to rotations around the z -axis, but no mirror symmetry in the $k_x k_y$ -plane exists. Thus, nonzero tensor elements $\kappa_{xx}, \kappa_{xy}, \kappa_{yx}, \kappa_{yy}$ are allowed. If $\mathbf{B} \parallel x$, in-plane rotational symmetry is broken, but a mirror plane in k_y -direction exists. Therefore, the tensor elements κ_{xy}, κ_{yx} and κ_{zx} can be nonzero. If \mathbf{B} has in-plane as well as out-of-plane components, in general all of these tensor elements may be finite.

Extrinsic Edelstein effect

The external magnetic field enters the Boltzmann equation (2.40) via the Lorentz force term, which is neglected here. If the magnetic field has an out-of-plane component, the Rashba system achieves a Berry curvature,

$$\Omega_z^n(\mathbf{k}) = -n \frac{\alpha_R^2 \mu_B B_z}{2d(\mathbf{k})^3}, \quad (4.26)$$

which enters the Boltzmann equation via the phase-space correction factor $(1 + \frac{e}{\hbar} \mathbf{B} \cdot \boldsymbol{\Omega}_{\mathbf{k}})$. However, this term can be neglected because $\frac{e}{\hbar} \mathbf{B} \cdot \boldsymbol{\Omega}_{\mathbf{k}} \ll 1$ in the \mathbf{k} - and \mathcal{E} -range considered here. Therefore the extrinsic contribution to the Edelstein effect is calculated as in the previous sections following Eq. (4.2).

Figs. 4.11(a)(III) and 4.11(b)(III) display the spin induced extrinsically by an external electric field in Rashba systems with out-of-plane and in-plane magnetic field, respectively. The extrinsic Edelstein contribution is in-plane. For an out-of-plane magnetic field (Fig. 4.11(a)(III)) the energy-dependent spin density is similar to the isotropic Rashba case: It increases approximately linearly from the band edge and reaches a constant value when both bands are occupied. However, at the edges of the local band gap region (\mathcal{E}_{\max}^- and \mathcal{E}_{\min}^+), the tensor element κ_{yx} exhibits a finite step because of Lifshitz transitions between the two Fermi lines (outside the gap region) and one Fermi line (between \mathcal{E}_{\max}^- and \mathcal{E}_{\min}^+). For symmetry reasons, $\kappa_{xy} = -\kappa_{yx}$, hence, the extrinsically induced spin density is perpendicular to the applied electric field.

If the magnetic field is in-plane (Fig. 4.11(b)(III)), the energy-dependent κ_{yx} resembles the result for the C_{2v} symmetric Rashba system discussed in section 4.5.2. Although the band structures of both systems are quite different (the in-plane magnetic field breaks C_{2v} symmetry), both systems exhibit a characteristic saddle point with a Lifshitz transition, which reduces the spin density down to zero. Due to the in-plane symmetry breaking, $\kappa_{xy} \neq -\kappa_{yx}$ (not shown in Fig. 4.11(b)(III)). Hence, the extrinsically induced spin density is not mandatory perpendicular to the electric field.

In a ferromagnetic system, the current-induced spin polarization exerts a torque on the magnetization [107, 148]. Thus, the Edelstein effect could be used to electrically manipulate the magnetization of ferromagnetic systems.

Intrinsic Edelstein effect

Due to the time-reversal breaking magnetic field, additional intrinsic contributions to the Edelstein effect occur, which are forbidden by time-reversal symmetry in conventional Rashba systems. These interband terms can be interpreted as additional contributions to the transport properties due to transitions between the bands induced by the external electric field.

4. The Edelstein effect

For a two-band model, the Kubo formula (4.12) can be split into two contributions,

$$\overline{\langle \mathbf{s} \rangle}^i = -\frac{2e\hbar N_{\text{u.c.}}}{N_{\text{at}}} \sum_{\mathbf{k}} \frac{f_{\mathbf{k}}^- (1 - f_{\mathbf{k}}^+)}{(\mathcal{E}_{\mathbf{k}}^- - \mathcal{E}_{\mathbf{k}}^+)^2} [\text{Im} \langle -|\hat{\boldsymbol{\sigma}}|+ \rangle \text{Re} \langle +|\hat{\mathbf{v}}|- \rangle \cdot \mathbf{E} + \text{Re} \langle -|\hat{\boldsymbol{\sigma}}|+ \rangle \text{Im} \langle +|\hat{\mathbf{v}}|- \rangle \cdot \mathbf{E}] , \quad (4.27)$$

in which $|\pm\rangle$ is short for $|\mathbf{k}^\pm\rangle$. The terms $\langle -|\hat{\boldsymbol{\sigma}}|+ \rangle$ and $\langle +|\hat{\mathbf{v}}|- \rangle$ are denoted as interband spin expectation value and velocity, respectively;

$$\langle -|\hat{\boldsymbol{\sigma}}|+ \rangle = \frac{1}{d\sqrt{d_x^2 + d_y^2}} (d_x d_z - i d_y d, d_y d_z + i d_x d, -d_x^2 - d_y^2) \quad (4.28a)$$

$$\langle +|\hat{\mathbf{v}}|- \rangle = \frac{\alpha_{\text{R}}}{\hbar d\sqrt{d_x^2 + d_y^2}} (d_y d_z - i d_x d, -d_x d_z - i d_y d) \quad (4.28b)$$

Here, \mathbf{d} is the spin-orbit field, whose \mathbf{k} -dependence is not explicitly written. The real and imaginary parts of the interband spin polarization as well as the spin-orbit field are mutually perpendicular. Eq. (4.28a), is valid for general two-band models whereas Eq. (4.28b) is obtained using the Rashba-Zeeman Hamiltonian with $\mathbf{d} = (-\alpha_{\text{R}} k_y + \mu_{\text{B}} B_x, \alpha_{\text{R}} k_x + \mu_{\text{B}} B_y, \mu_{\text{B}} B_z)$. Thus, the following analysis of the intrinsic Edelstein effect is valid only for Rashba systems with Zeeman splitting.

The intrinsic Edelstein tensor reads

$$\kappa_{xx}^i = \kappa_{yy}^i = \frac{e N_{\text{u.c.}}}{\alpha_{\text{R}} N_{\text{at}}} \sum_{\mathbf{k}} \Omega_z^-(\mathbf{k}) \theta(\mathcal{E}_{\text{F}} - \mathcal{E}_{\mathbf{k}}^-) \theta(\mathcal{E}_{\mathbf{k}}^+ - \mathcal{E}_{\text{F}}) , \quad (4.29a)$$

$$\kappa_{zx}^i = \frac{e \alpha_{\text{R}} N_{\text{u.c.}}}{2 N_{\text{at}}} \sum_{\mathbf{k}} \frac{\theta(\mathcal{E}_{\text{F}} - \mathcal{E}_{\mathbf{k}}^-) \theta(\mathcal{E}_{\mathbf{k}}^+ - \mathcal{E}_{\text{F}})}{d_{\mathbf{k}}^3} (\alpha_{\text{R}} k_y - \mu_{\text{B}} B_x) , \quad (4.29b)$$

$$\kappa_{zy}^i = -\frac{e \alpha_{\text{R}} N_{\text{u.c.}}}{2 N_{\text{at}}} \sum_{\mathbf{k}} \frac{\theta(\mathcal{E}_{\text{F}} - \mathcal{E}_{\mathbf{k}}^-) \theta(\mathcal{E}_{\mathbf{k}}^+ - \mathcal{E}_{\text{F}})}{d_{\mathbf{k}}^3} (\alpha_{\text{R}} k_x + \mu_{\text{B}} B_y) . \quad (4.29c)$$

Here, $\theta(x)$ is the Heaviside step function. Thus, an in-plane electric field can generate a spin polarization in the direction of the electric field if $B_z \neq 0$, whereas an in-plane \mathbf{B} allows the generation of an out-of-plane spin polarization even if $B_z = 0$. These are exactly the elements of $\hat{\kappa}$ which are allowed by symmetry but not provided by the extrinsic Edelstein effect.

This non-intuitive phenomenon – for instance an out-of-plane spin is created although no state has an out-of-plane spin expectation value – is explained by a closer analysis of the intrinsic Edelstein effect.

For the following phenomenological discussion the electric field is assumed in x -direction. Thus, each state contributes to the transport corresponding to the negative projection of its interband velocity onto the external electric field, which is $[-\langle +|\hat{v}_x|- \rangle]$.

Both contributions in Eq. (4.27) are analyzed separately. First, the magnetic field is assumed to be out-of-plane. Fig. 4.12(a) visualizes the term $[-\text{Im} \langle -|\hat{\boldsymbol{\sigma}}|+ \rangle \text{Re} \langle +|\hat{v}_x|- \rangle / \Delta \mathcal{E}^2]$, in which $\Delta \mathcal{E} = \mathcal{E}_{\mathbf{k}}^+ - \mathcal{E}_{\mathbf{k}}^-$. The blue/red color scale represents the real part of the (negative) interband velocity divided by $\Delta \mathcal{E}^2$. In order to show which states contribute, only the occupied states of the lower ($n = -1$) band are shown. The real part of the interband velocity is parallel to the group velocity, but differs with respect to the absolute value. The imaginary part of the interband spin (black arrows) is completely in-plane and perpendicular to the spin-orbit field (gray arrows). Thus, the interband spin expectation value can be interpreted as an in-plane torque acting on the electron spins.

A close inspection of Fig. 4.12(a) shows that the \mathbf{k} -points with $k_x > 0$ ($k_x < 0$) contribute negatively (positively) with an additional spin component in $-x$ ($+x$)-direction, respectively. Thus, a finite spin density in $(+x)$ -direction remains, the Zeeman field in z -direction leads to a nonzero κ_{xx}^i -component of the Edelstein tensor.

In Fig. 4.12(b) the second term of Eq. (4.27) , $[-\text{Re} \langle -|\hat{\boldsymbol{\sigma}}|+ \rangle \text{Im} \langle +|\hat{v}_x|- \rangle / \Delta \mathcal{E}^2]$, is shown. The

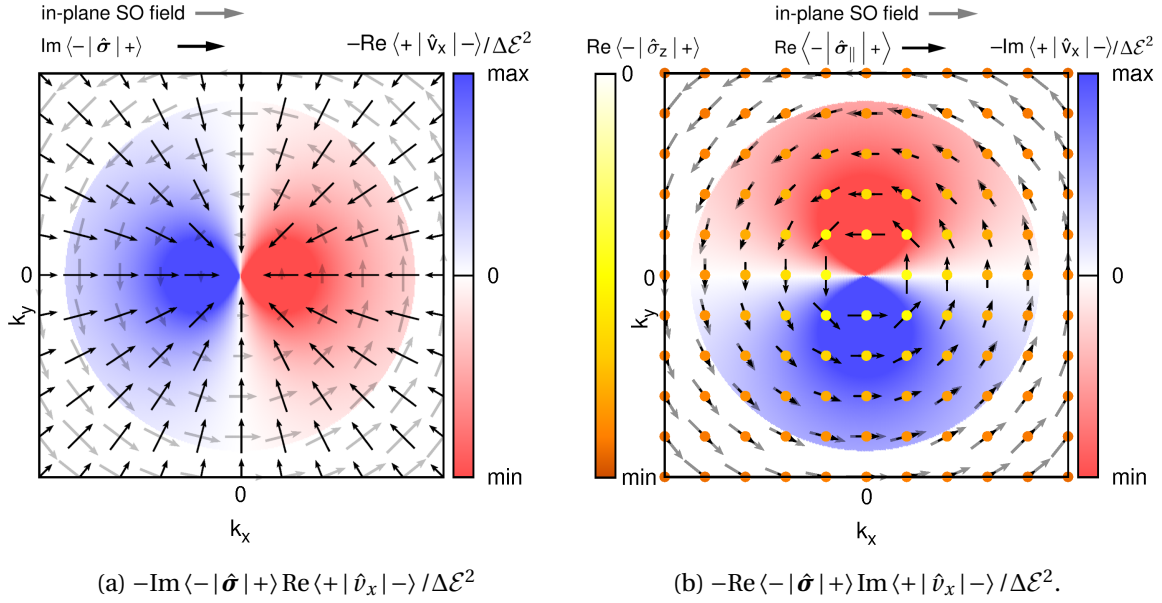


Figure 4.12.: Visualization of the intrinsic Edelstein contributions provided by each \mathbf{k} for $\mathbf{B} \parallel z$, $\mathbf{E} \parallel x$. The blue/red color plot shows the x -component of the interband velocity (divided by $\Delta\mathcal{E}^2$), the black arrows correspond to the in-plane interband spin expectation values and the yellow/orange dots to the out-of-plane interband spin components. The in-plane spin-orbit field is represented by gray arrows; it does not directly contribute to the intrinsic Edelstein effect.

imaginary part of the interband velocity is perpendicular to the group velocity. The real part of the interband spin polarization (in-plane component: black arrows, out-of-plane component: yellow/orange dots) is also perpendicular to the spin-orbit field with a finite out-of-plane component. Thus, the real part of the interband spin polarization can be interpreted as a torque with an out-of-plane component acting on the electron spins. For $\mathbf{B} \parallel z$, the \mathbf{k} -points with $k_y > 0$ ($k_y < 0$) contribute negatively (positively) with an additional spin component in $(-1, 0, -1)$ ($(1, 0, -1)$)-direction. The z -contributions compensate each other for symmetry reasons and also a nonzero spin density $\parallel x$ remains.

Now, a Rashba system with $\mathbf{B} \parallel x$ is considered. $\text{Re}\langle +|\hat{v}|-\rangle$ vanishes, thus, the first term of Eq. (4.27) does not contribute to the intrinsic Edelstein effect. Fig. 4.13 visualizes the second term of Eq. (4.27). The imaginary interband velocity is asymmetric with respect to the k_y -direction due to the broken C_{2v} symmetry. The interband spin polarization is completely out-of-plane and constant for all \mathbf{k} -points. Thus, nearly all occupied states contribute with a spin component in the $(-z)$ -direction, and a spin expectation value in $(-z)$ -direction is induced intrinsically, represented by a finite tensor element κ_{zx}^i although in equilibrium none of the states has an out-of-plane spin component.

In simple words, the intrinsic Edelstein effect can be attributed to an intrinsic torque acting on the electron spins. In the presence of an external electric field, an imbalance of states is created giving rise to a finite spin density.

In all discussed examples, it was assumed that only the lower band ($n = -1$) is occupied and the second band ($n = +1$) is unoccupied for all \mathbf{k} -values. For \mathbf{k} -points and energies at which both bands are occupied, the previously discussed contributions are completely compensated. Thus, only \mathbf{k} -points at which only one band is occupied contribute to the intrinsic Edelstein effect.

In Figs. 4.11(a)(IV) and 4.11(b)(IV) on page 56 the intrinsically induced spin density is shown as a function of the Fermi level for out-of-plane and in-plane magnetic fields, respectively. In addition, the equilibrium spin density of these magnetic systems is depicted. For $\mathbf{B} \parallel z$, an intrinsic spin density parallel to the electric field, $\kappa_{xx}^i = \kappa_{yy}^i$, is induced with a maximum value in the gap energy

4. The Edelstein effect

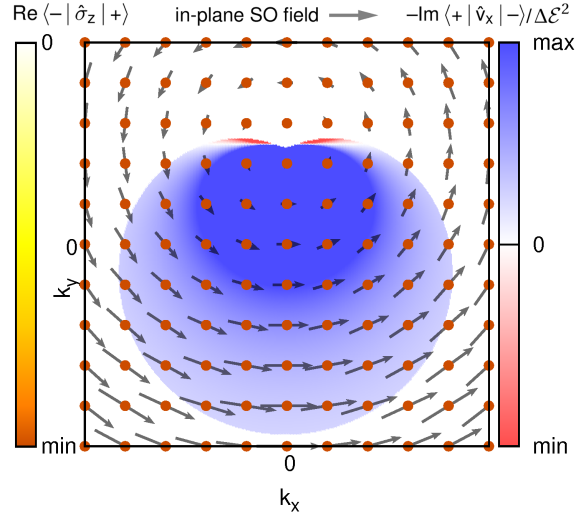


Figure 4.13.: Visualization of the term $[-\text{Re}(-|\hat{\sigma}|+)\text{Im}(+|\hat{v}_x|-)]$ in Eq. (4.27) for $\mathbf{B} \parallel x$, $\mathbf{E} \parallel x$. The spin-orbit field is sketched by gray arrows, the imaginary part of the interband velocity (divided by $\Delta\mathcal{E}^2$) is shown by the blue/red color scale and the real part of the out-of-plane interband spin polarization is represented by orange dots. The in-plane real part of the interband spin polarization is zero.

region. Here only one ($n = -1$) band is occupied, thus, no compensation occurs, as discussed above. The (negative) equilibrium spin expectation value increases with \mathcal{E}_F and obtains a constant value when both bands are occupied.

If the magnetic field is in-plane, an out-of-plane spin density is induced intrinsically (κ_{zx}^i in Fig. 4.11(b)(IV)). Its energy dependence is more complex than for $\mathbf{B} \parallel z$ because of the strongly anisotropic Fermi lines. It provides a (negative) maximum near the saddle point and even changes its sign when both branches are occupied. A small plateau exists around the diabolic point because of the approximately linear band dispersion. The (negative) in-plane equilibrium spin density increases with \mathcal{E}_F and takes a constant value above the saddle point.

To conclude the previous findings, three components of the spin density in a Rashba system in an external magnetic field or with a finite magnetization can be determined: (I) the equilibrium spin density in the (opposite) direction of the magnetic field, (II) the spin density due to the extrinsic Edelstein effect, which is in-plane and approximately perpendicular to the electric field, and (III) the intrinsically induced spin polarization perpendicular to the magnetic field.

The nonequilibrium contributions scale linearly with the electric field whereas the equilibrium spin expectation value is independent of \mathbf{E} . Thus, the ratio of the contributions can be modified by the field strength. However, as Figs. 4.11(a) and 4.11(b) illustrate, the magnitudes of the contributions differ strongly. By applying an electric field of 10^5V m^{-1} , the extrinsic Edelstein contribution would be of the same magnitude as the equilibrium contribution. Alternatively, the extrinsic contribution could be increased by modifying the scattering parameters, e.g. lowering the impurity potential. For the results shown in Figs. 4.11(a)(III) and 4.11(b)(III) the scattering potential is set to $U_0 = 1 \text{eV}$ which is comparably large. Assuming a smaller scattering potential of $U_0 = 0.1 \text{eV}$ would increase the charge-to-spin efficiency by a factor of 100. Further, applying a weaker magnetic field would reduce the equilibrium contribution. Hence, extrinsic contributions of the same order as the equilibrium spin density are in general realizable.

The intrinsic contribution shown in Fig. 4.11 is reduced by nearly three orders of magnitudes in comparison to the extrinsic contribution. It cannot be influenced by manipulating the scattering properties. Like the equilibrium contribution, it exists only in the presence of a magnetic field. In

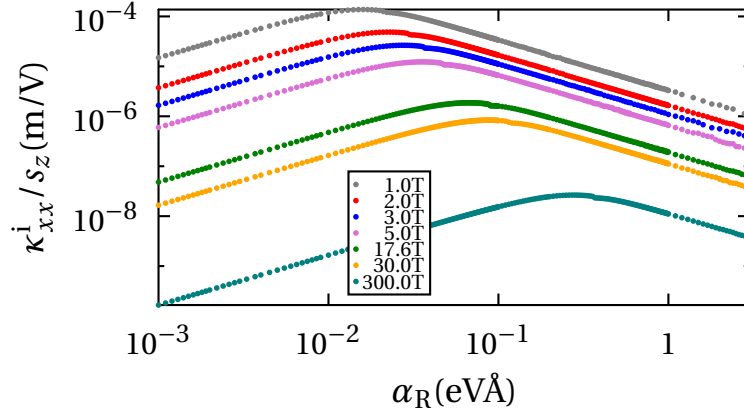


Figure 4.14.: Ratio of intrinsic Edelstein effect and equilibrium spin density for $\mathbf{B} \parallel z$. The model parameters are $m = m_e$, $\mathcal{E}_F = 0$.

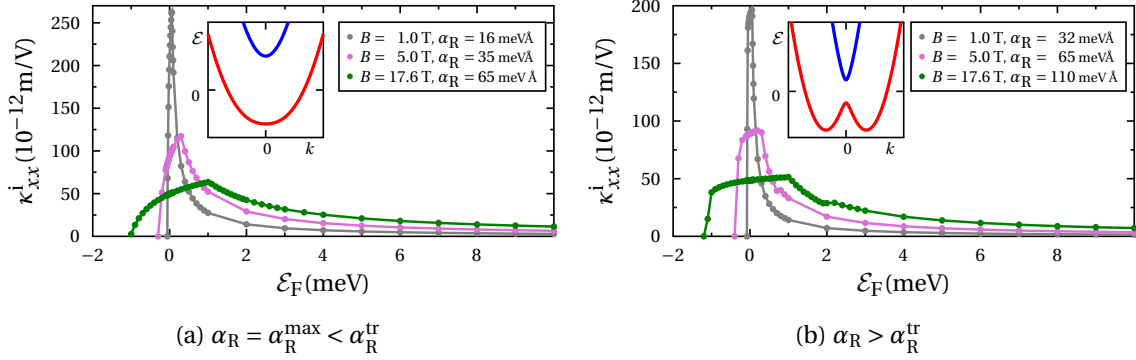


Figure 4.15.: Energy-dependent intrinsic Edelstein effect ($\mathbf{B} \parallel z$) for various parameters α_R and B . The band structure is dominated by the Zeeman term (a) and the Rashba term (b), respectively.

order to identify systems in which the intrinsic Edelstein effect could be experimentally observable, the ratio κ_{xx}^i/s_z is systematically analyzed for $\mathcal{E}_F = 0$ and various parameters α_R and $\mathbf{B} \parallel z$, shown in Fig. 4.14. In general, the ratio κ_{xx}^i/s_z strongly decreases with B . For fixed B , the ratio has a maximum at α_R^{\max} , slightly below $\alpha_R^{\text{tr}} = \sqrt{\mu_B B \hbar^2 / m}$, which marks the transition point between the Zeeman-dominated (large B) and Rashba-dominated band structure. At α_R^{tr} the curves in Fig. 4.14 have a slight step due to this transition.

The intrinsic Edelstein effect could be of similar strength as the equilibrium spin polarization for low magnetic fields $B < 5\text{T}$, electric fields of $\approx 10^4 \text{V m}^{-1}$ and Rashba parameters of $\alpha_R \approx 10^{-2} \text{eV\AA}$.

Fig. 4.15 shows the tensor element κ_{xx}^i as a function of the Fermi level for various parameter combinations of α_R and B . In Fig. 4.15(a) the Rashba parameter α_R^{\max} was chosen, which corresponds to the maximum ratio κ_{xx}^i/s_z and is below the transition value α_R^{tr} . Therefore, the band structure is dominated by the Zeeman term and consists of two parabola-like bands with their minima at $\mathbf{k} = 0$. The Edelstein tensor element κ_{xx}^i has a peak with its maximum at the band edge energy of the $n = +1$ band. The height of the peak decreases with B whereas its width increases, corresponding to the energy gap at $\mathbf{k} = 0$.

Fig. 4.15(b) shows similar results for systems with a Rashba-dominated band structure. Here, the signal is maximum in the gap region. As in Fig. 4.15(a), the peak height decreases with B , but the width increases. For small fields B , the intrinsic Edelstein signal is large enough for experimental observation. However, this large signal could be observed only in a very narrow energy range. Thus, the experimental detection remains a challenging task.

4. The Edelstein effect

Anomalous Hall effect

Since the Zeeman term breaks time-reversal symmetry, a finite intrinsic anomalous Hall effect (AHE) can exist in Rashba systems with Zeeman splitting. Here, a transversal charge current or voltage is generated in the absence of an external magnetic field, which corresponds to nonzero transversal tensor elements σ_{xy} and σ_{yx} of the conductivity tensor. Using the Kubo formula, the anomalous Hall conductivity reads

$$\begin{aligned}\sigma_{xy}^{\text{AHE}} = -\sigma_{yx}^{\text{AHE}} &= \frac{2\hbar e^2}{A} \sum_{\mathbf{k}} f_{\mathbf{k}}^- (1 - f_{\mathbf{k}}^+) \frac{\text{Im}(\langle -|\hat{v}_x|+\rangle \langle +|\hat{v}_y|-\rangle)}{(\mathcal{E}_{\mathbf{k}}^+ - \mathcal{E}_{\mathbf{k}}^-)^2} \\ &= -\frac{e^2}{A\hbar} \sum_{\mathbf{k}} \Omega_z^-(\mathbf{k}) \theta(\mathcal{E}_{\mathbf{k}} - \mathcal{E}_{\mathbf{k}}^-) \theta(\mathcal{E}_{\mathbf{k}}^+ - \mathcal{E}_{\mathbf{k}}) = -\frac{e\alpha_{\text{R}} N_{\text{u.c.}}}{\hbar A N_{\text{at}}} \kappa_{xx}^i.\end{aligned}\quad (4.30)$$

The same formula is obtained by calculating the intrinsic contribution to the charge conductivity via the Boltzmann equation,

$$\mathbf{j}_{\text{c}}^{\text{AHE}} = -\frac{e}{A} \sum_{\mathbf{k},n} f_{\mathbf{k},n}^0 \mathbf{r}_{\mathbf{k},n}, \quad \sigma_{xy}^{\text{AHE}} = -\frac{e^2}{A\hbar} \sum_{\mathbf{k},n} f_{\mathbf{k},n}^0 \Omega_z^n(\mathbf{k}), \quad (4.31)$$

in which only the anomalous velocity contributes to the charge current for symmetry reasons. The qualitative energy dependence of the anomalous Hall conductivity is equivalent to κ_{xx}^i , which is shown in Fig. 4.11(a)(IV) on page 56.

4.6. Systems with Rashba and Dresselhaus SOC

As discussed in section 3.5, at surfaces or interfaces of crystals with broken bulk inversion symmetry, Rashba and Dresselhaus SOC terms coexist. Due to this symmetry breaking, a current-induced spin polarization is expected [152, 153] even in the absence of Rashba SOC.

In the following, different surfaces of a zincblende crystal are considered. In the surface-projected Hamiltonian, Dresselhaus terms which scale linearly and cubically with k , respectively, are distinguished. The interplay of Rashba and Dresselhaus terms is visualized by the individual spin-orbit fields which are superposed. The influence of a Dresselhaus SOC term in addition to the Rashba SOC is considered by calculating the Edelstein effect for a GaAs system, which has a comparably small Rashba parameter.

By group theoretical systematical symmetry considerations, Cartoixà *et al.* have shown that additional higher-order terms can exist in systems with structural and/or bulk inversion asymmetry which are not covered by the conventional Rashba and Dresselhaus Hamiltonians [154]. These additional terms are not considered here in order to demonstrate clearly the influence of the Dresselhaus term. However, they could be easily included in the calculations using the general two-band formalism presented in section 3.2.

4.6.1. (001) surface

Projecting the Dresselhaus Hamiltonian onto the (001) surface, the averaged k_z -component vanishes and k_z^2 averages to a finite value, $\langle k_z^2 \rangle = \pi^2/d^2$ [72]. The Dresselhaus Hamiltonian simplifies to [107, 154–156]

$$\hat{H}_{\text{D}}^{\text{SO}} = \hat{H}_{\text{D}}^{(1)} + \hat{H}_{\text{D}}^{(3)} = \beta_{\text{D}} (k_y \hat{\sigma}_y - k_x \hat{\sigma}_x) + \gamma_{\text{D}} (k_x k_y^2 \hat{\sigma}_x - k_y k_x^2 \hat{\sigma}_y) \quad (4.32)$$

with $\beta_{\text{D}} = \gamma_{\text{D}} \langle k_z^2 \rangle$. Here, $x \parallel [100]$, $y \parallel [010]$ and $z \parallel [001]$. Eq. (4.32) contains a linear ($\hat{H}_{\text{D}}^{(1)}$) and a cubic ($\hat{H}_{\text{D}}^{(3)}$) term and is C_{2v} symmetric because of the bulk inversion asymmetry. The linear

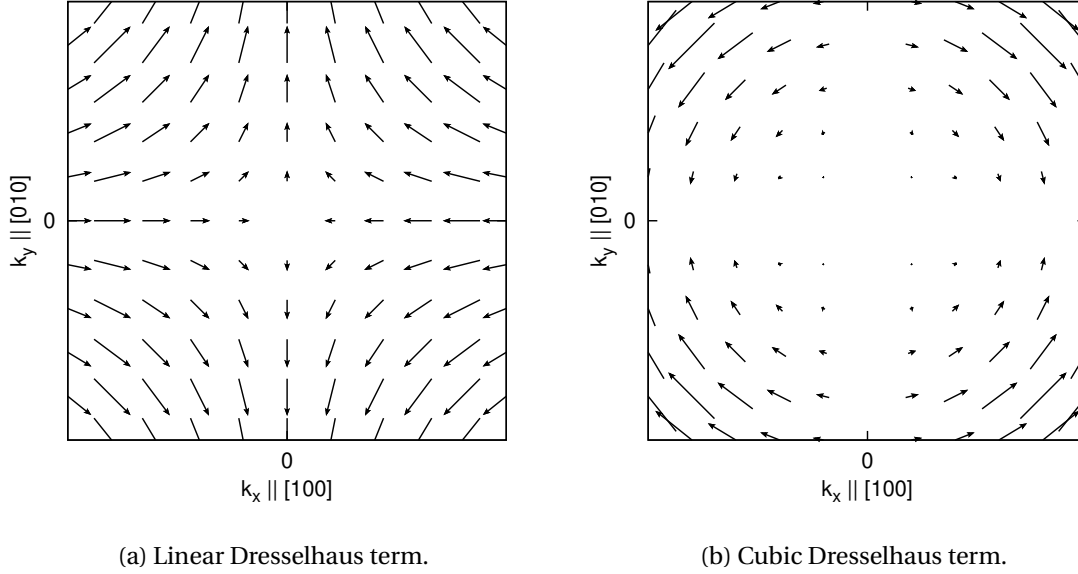


Figure 4.16.: Spin-orbit fields of the linear and the cubic (001) Dresselhaus term.

Dresselhaus coupling can be tuned by the sample thickness d . In realistic samples with a thickness of a few nm, β_D is typically of the same order of magnitude as the Rashba parameter α_R [72].

In Fig. 4.16 the spin-orbit fields of the linear and the cubic Dresselhaus term, respectively, are shown. Although the structure of $\hat{H}_D^{(1)}$ resembles the isotropic Rashba Hamiltonian, its spin-orbit field is remarkably different: rotational symmetry is broken. The spin texture is not perpendicular to \mathbf{k} , the angle between \mathbf{k} and the spin-orbit field strongly depends on the direction in \mathbf{k} -space. The cubic Dresselhaus term is pronounced for large \mathbf{k} -values and can be neglected near the Γ -point. The spin-orbit field is perpendicular to \mathbf{k} , its sign as well as the amplitude also strongly depend on the direction in \mathbf{k} -space.

For the discussion of a surface with Dresselhaus SOC, the Rashba SOC also has to be taken into account which is approximately isotropic [107]. The effective spin-orbit field is a superposition of the Rashba and Dresselhaus spin-orbit fields.

In a first approximation, the cubic Dresselhaus term is neglected. The corresponding band structure, $\mathcal{E}^n(\mathbf{k}) = \frac{\hbar^2 k^2}{2m} + n\sqrt{(\alpha_R^2 + \beta_D^2)k^2 + 4\alpha_R\beta_D k_x k_y}$ resembles the band structure of a C_{2v} symmetric Rashba system (discussed in section 4.5.2) with a characteristic Lifshitz transition at the saddle point. The band structure and iso-energy lines for various ratios β_D/α_R are schematically shown in appendix D.1. However, since the Dresselhaus spin-orbit field is not perpendicular to \mathbf{k} , the spin texture differs from that of a pure Rashba system.. The energy dependence of the current-induced spin density is similar to a C_{2v} symmetric Rashba system (Fig. 4.4(b)) and not explicitly discussed here.

Fig. 4.17(a) shows the Edelstein efficiency tensor $\hat{\kappa}$ of a (001) surface including Rashba as well as linear Dresselhaus SOC. The model parameters were chosen to approximate the AlGaAs surface experimentally examined in Ref. [119]; the linear Dresselhaus parameter is varied. Such a variation of β_D could be achieved by considering samples of different thicknesses.

The induced spin density is not always perpendicular to the electric field but strongly depends on the parameter configuration as well as the direction of \mathbf{E} . In the presence of a nonzero linear Dresselhaus SOC term, diagonal tensor elements κ_{xx} and κ_{yy} exist which are forbidden by symmetry in a pure Rashba system.

The Edelstein tensor elements possess the symmetries $\kappa_{xx} = -\kappa_{yy}$ and $\kappa_{xy} = -\kappa_{yx}$. Assuming the \mathbf{E} -field rotated in the plane by an angle ϕ with respect to the $x \parallel [100]$ -axis, the angle θ between

4. The Edelstein effect

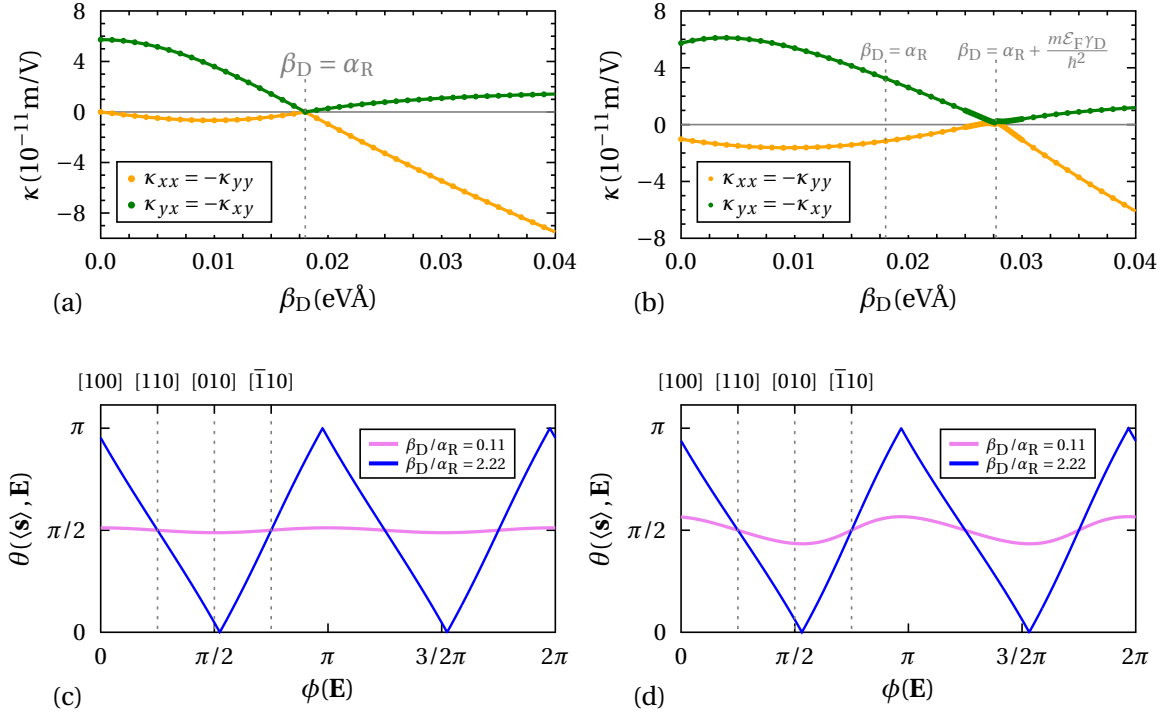


Figure 4.17.: Current-induced spin density in the presence of Rashba and Dresselhaus SOC at the (001) interface. The model parameters are $m = 0.074m_e$, $\alpha_R = 0.018\text{eV\AA}$, $\mathcal{E}_F = 100\text{meV}$ and $\gamma_D = 0$ [(a) and (c)], $\gamma_D = 10\text{eV\AA}^3$ [(b) and (d)]. Panels (a) and (b) show the Edelstein tensor elements as a function of the linear Dresselhaus parameter β_D , panels (c) and (d) depict the orientation of the induced spin density with respect to the electric field for different ratios β_D/α_R .

the current-induced spin polarization and the electric field reads

$$\cos\theta(\langle \mathbf{s} \rangle, \mathbf{E}) = \frac{\kappa_{xx}(\cos^2\phi - \sin^2\phi)}{\sqrt{\kappa_{xx}^2 + \kappa_{yx}^2 + 4\kappa_{xx}\kappa_{xy}\cos\phi\sin\phi}}. \quad (4.33)$$

For $|\alpha_R| > |\beta_D|$, the Rashba SOC is dominant and $\theta \approx \pi/2$: the spin density is approximately perpendicular to \mathbf{E} since $|\kappa_{yx}| > |\kappa_{xx}|$. This is illustrated in Fig. 4.17(c) for $\beta_D/\alpha_R = 0.11$. However, if $|\beta_D| > |\alpha_R|$, the Dresselhaus SOC is more pronounced and $|\kappa_{xx}| > |\kappa_{yx}|$. Due to the anisotropic spin texture shown in Fig. 4.16(a), the orientation of the spin density with respect to the field can be modified from nearly (anti)parallel ($\mathbf{E} \parallel [100]$ or $\parallel [010]$) to perpendicular ($\mathbf{E} \parallel [110]$ or $\parallel [\bar{1}10]$) by rotating \mathbf{E} in-plane, as depicted in Fig. 4.17(c) for $\beta_D/\alpha_R = 2.22$.

A special parameter configuration is $|\beta_D| = |\alpha_R|$. The corresponding Fermi lines are two circles intersecting at two twofold degenerate points, shown in Fig. D.1(d) on page 108. All spin expectation values at the Fermi level are oriented parallel or antiparallel to the [110]-direction. This configuration corresponds to a persistent spin helix in real space [157]. In such a system, SU(2) symmetry is present despite of the SOC. Consequently, the spin polarization is conserved with an infinite spin lifetime [157]. Exciting the system at a characteristic wave length, a persistent spin helix can be induced [72]. The field-induced spin density is zero in this configuration because the spin expectation values on the Fermi lines are parallel but point in opposite directions within one energy branch [107]. Therefore, all contributions to the Edelstein effect completely compensate. Thus, although the persistent spin helix provides a real-space-dependent spin polarization, the net spin density of the system vanishes for any electric field.

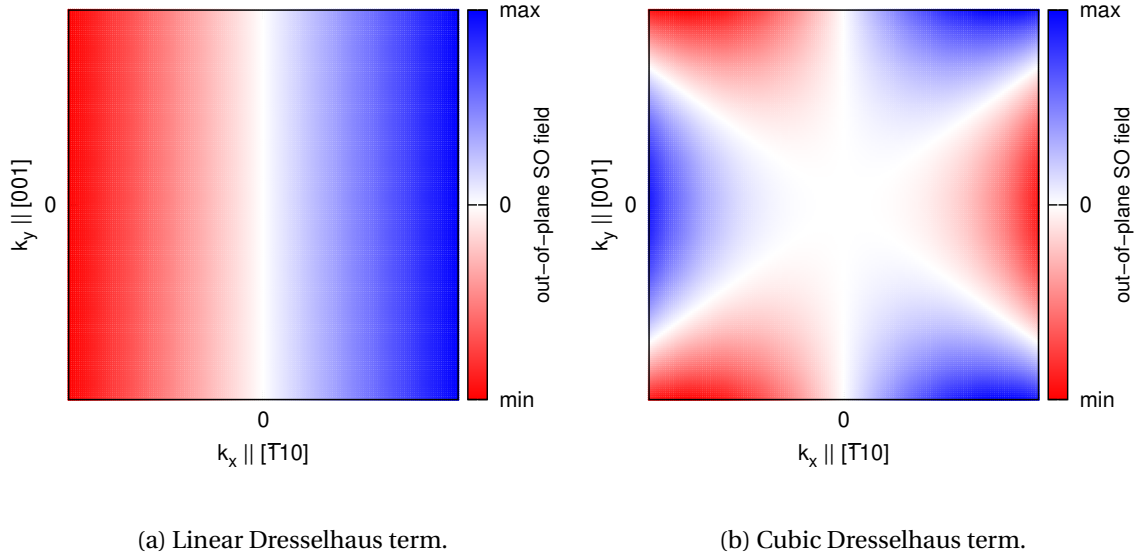


Figure 4.18.: Spin-orbit fields of the linear and the cubic (110) Dresselhaus term. The color scale corresponds to the out-of-plane SO field.

In Fig. 4.17(b) the influence of the cubic Dresselhaus term with $\gamma_D = 10\text{eV}\text{\AA}^3$ is illustrated. The cubic term slightly modifies the band structure, as shown in appendix D.1 on page 108. The most significant effect of the cubic term is a shift of the β_D -value at which no net spin density is induced to $\beta_D = \text{sgn}(\alpha_R \beta_D) \alpha_R + m \varepsilon_F \gamma_D / \hbar^2$. For this parameter combination, a persistent spin helix can occur [72]. As discussed above for $\gamma_D = 0$, the Fermi lines are two intersecting circles with opposite spin texture, thus, the Edelstein effect vanishes.

The additional cubic Dresselhaus contribution increases the longitudinal tensor elements of $\hat{\kappa}$ and therefore leads to larger deviations from orthogonality of $\langle \mathbf{s} \rangle$ and \mathbf{E} , especially for a small ratio β_D / α_R , as shown in Fig. 4.17(d).

4.6.2. (110) surface/interface

At the (110) surface the projected Dresselhaus term reads [77, 107, 154–156]

$$\hat{H}_D^{\text{SO}} = k_x \hat{\sigma}_z \left[\lambda_D + \frac{\gamma_D}{2} (2k_y^2 - k_x^2) \right]. \quad (4.34)$$

Here, $x \parallel [\bar{1}10]$, $y \parallel [001]$, $z \parallel [110]$ and $\lambda_D = \gamma_D \langle k_z^2 \rangle / 2$ [77, 107, 154, 158]. The corresponding spin-orbit field is completely out of plane and shown in Fig. 4.18. The cubic Dresselhaus term resembles the Rashba warping term [Eq. (4.19)], but is not equivalent. Both terms correspond to different surfaces (the Rashba warping term was derived for the (111) surface) and have different physical origins, namely bulk inversion asymmetry and structural asymmetry, respectively. The Rashba Hamiltonian for the (110) surface has the C_{2v} symmetric form introduced in section 4.5.2. The band structure of the superposed Hamiltonian which contains Rashba as well as Dresselhaus SOC is shown for various parameter combinations in appendix D.2 on page 110.

The current-induced spin polarization as well as the spin Hall effect in a (110) AlGaAs quantum well have been experimentally observed using Kerr microscopy [119]. Due to the out-of-plane spin-orbit field, a nonzero out-of-plane spin polarization is induced by an electric field which provides usually a larger MOKE signal than an in-plane spin polarization.

In Fig. 4.19 the calculated spin density induced by an external electric field at the (110) surface

4. The Edelstein effect

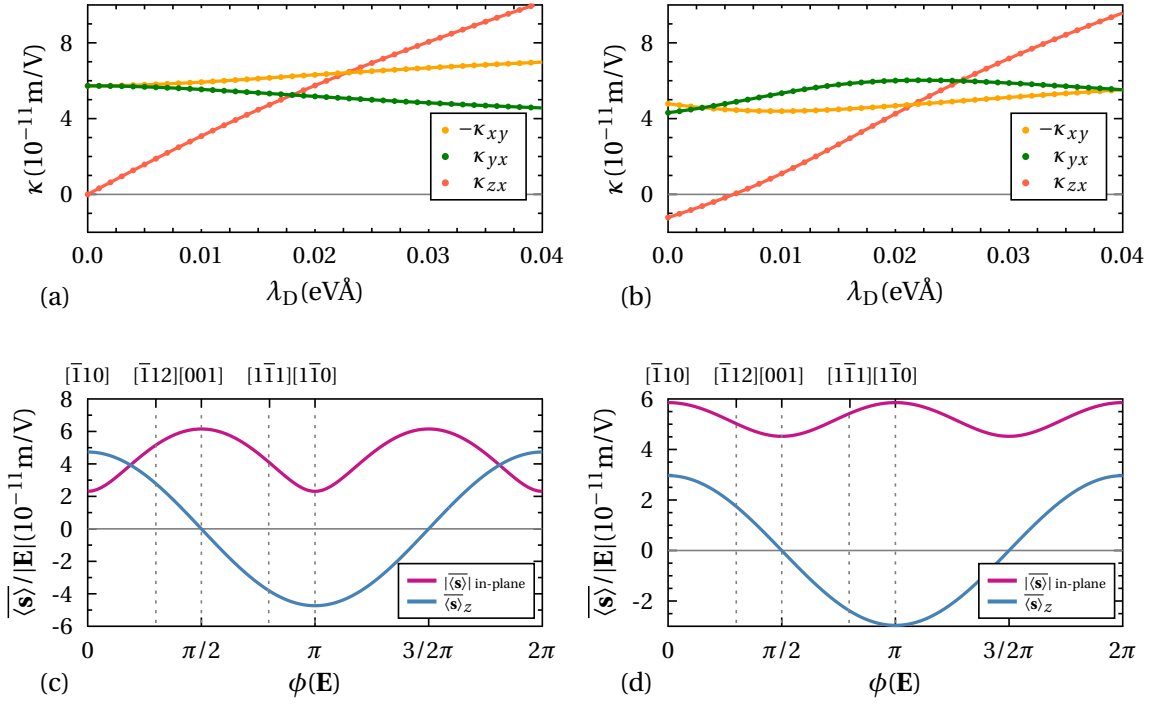
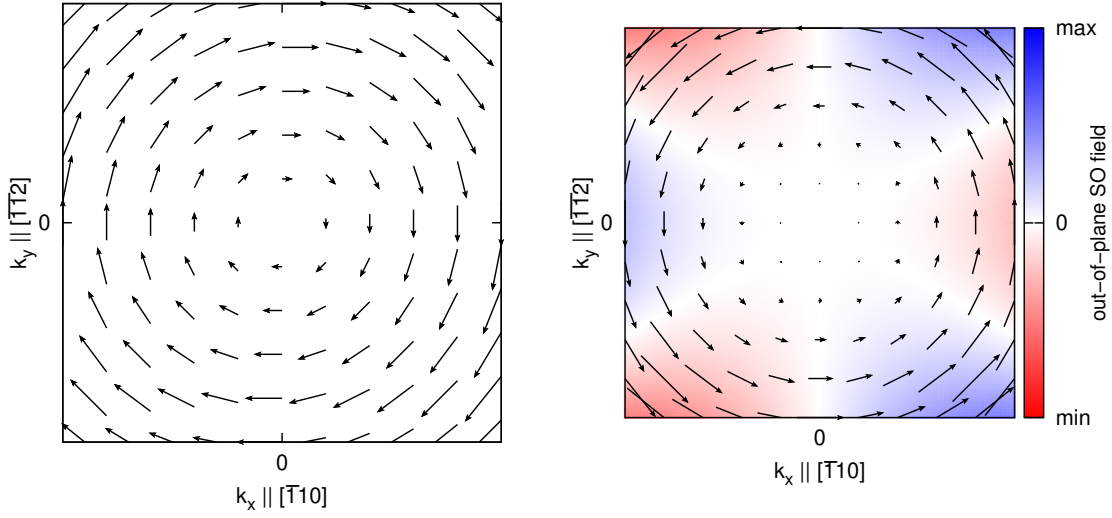


Figure 4.19.: Current-induced spin density at the (110) surface with Rashba and Dresselhaus SOC. The model parameters are as in Fig. 4.17. Panels (a) and (b) show the tensor elements of $\hat{\kappa}$ as a function of the linear Dresselhaus parameter λ_D without (a) and with (b) a cubic Dresselhaus term ($\gamma_D = 10 \text{ eV\AA}^3$). Panels (c) and (d) depict in-plane and out-of-plane components of the spin density with respect to the direction of \mathbf{E} for $\lambda_D = 0.016 \text{ eV\AA}$ with and without the cubic term, respectively. Specific directions of \mathbf{E} examined in [119] are marked.

of a zincblende structure is shown without [panels (a) and (c)] and with [panels (b) and (d)] the cubic Dresselhaus term, respectively. Here, the same model parameters as above were chosen to approximate the AlGaAs structure experimentally examined in Ref. [119]. Although already the Rashba term exhibits anisotropies at the (110) surface, the corresponding parameters are assumed isotropic, $m_x = m_y$ and $\alpha_{R_x} = \alpha_{R_y}$, in order to clearly demonstrate the anisotropy effects induced by the Dresselhaus terms.

The Dresselhaus terms lead to a nonzero out-of-plane spin density when the applied electric field has a nonzero $x \parallel [001]$ -component. The corresponding tensor element κ_{zx} increases with λ_D [Figs. 4.19(a) and 4.19(b)]. If \mathbf{E} points in $y \parallel [001]$ -direction, no out-of-plane spin density is induced ($\kappa_{zy} = 0$), as also observed in Ref. [119]. The individual in-plane spin expectation values $\langle \sigma_{\parallel} \rangle_{\mathbf{k}}$ are reduced in the presence of the Dresselhaus term. However, the Dresselhaus SOC also affects the shape of the Fermi lines and induces additional anisotropies. Therefore, the tensor elements κ_{xy} and κ_{yx} exhibit a qualitatively different λ_D -dependence. Due to the nonequivalence of κ_{xy} and $-\kappa_{yx}$, the spin density is not always perpendicular to \mathbf{E} , as discussed in section 4.5.2 for a C_{2v} symmetric Rashba system.

In Ref. [119] the out-of-plane component of the induced spin density has been detected for various in-plane orientations of the applied electric field: $\mathbf{E} \parallel [1\bar{1}0]$, $[\bar{1}\bar{1}1]$, $[001]$ and $[\bar{1}\bar{1}2]$. The MOKE signal was found to differ with respect to amplitude as well as sign. Figs. 4.19(c) and 4.19(d) depict the in-plane and out-of-plane components of the calculated spin density without and with the cubic term, respectively, for various in-plane orientations of \mathbf{E} . The parameter λ_D was set to 0.016 eV\AA , corresponding to $\gamma_D = 10 \text{ eV\AA}^3$ and a slab thickness $d = 9.6 \text{ nm}$ [119]. Although the calculated out-of-plane signal changes sign and amplitude, the numerical results are not completely



(a) Linear Dresselhaus term.

(b) Cubic Dresselhaus term.

Figure 4.20.: Spin-orbit fields of the linear and the cubic (111) Dresselhaus term. The arrows represent the in-plane SO field, the color scale corresponds to the out-of-plane component.

consistent with the data measured in [119]: For an field applied in $[\bar{1}10]$ -direction an opposite sign than in experiment was calculated. In Figs. 4.19(c) and 4.19(d) the results mainly reflect the symmetry of the linear Dresselhaus term whereas in the experimental results the out-of-plane spin density seems to be dominated by the cubic Dresselhaus term. Thus, the magnitude of the linear Dresselhaus term might be overestimated in the calculations. Further, anisotropies of the Rashba Hamiltonian, which are not considered here, can influence the results.

4.6.3. (111) surface/interface

The Dresselhaus term at the (111) surface resembles the Rashba term [107, 154–156],

$$\hat{H}_D = \delta_D (k_y \hat{\sigma}_x - k_x \hat{\sigma}_y) + \frac{\gamma_D}{2\sqrt{3}} \left[(-k_x^2 k_y - k_y^3) \hat{\sigma}_x + (k_x^3 + k_x k_y^2) \hat{\sigma}_y + \sqrt{2} k_x (3k_y^2 - k_x^2) \hat{\sigma}_z \right]. \quad (4.35)$$

Here, $x \parallel [\bar{1}10]$, $y \parallel [\bar{1}\bar{1}2]$, $z \parallel [111]$ and $\delta_D = 2\gamma_D \langle k_z^2 \rangle / \sqrt{3}$. The influence of the linear Dresselhaus term can be considered by using an effective Rashba parameter, $\alpha' = \alpha - \delta_D$ in the Rashba Hamiltonian (3.18). Similarly, the cubic Dresselhaus term $\sim \hat{\sigma}_z$ is equivalent to the hexagonal warping term discussed in section 4.5.2 and can be included by an effective warping parameter $\lambda'_w = \lambda_w - \gamma_D / \sqrt{6}$. However, the cubic Dresselhaus term contains an additional in-plane spin-orbit field perpendicular to \mathbf{k} , whose amplitude scales with k^3 and which points oppositely to the linear Dresselhaus field. Thus, this in-plane component of the cubic Dresselhaus term diminishes the influence of the linear Dresselhaus term.

4.7. Topological insulators

The surface states of three-dimensional topological insulators, introduced in section 3.6, often provide a cone-like band structure with spin-momentum locking [82, 84, 87], similar to Rashba systems. However, whereas in Rashba systems the Fermi lines consist of two curves whose contributions to the Edelstein effect compensate partially, the surface states of topological insulators provide a single Fermi line. Due to the lack of partial compensation, the charge-to-spin conversion

4. The Edelstein effect

efficiency is expected to be comparably large in topological insulators [19–21]. The Edelstein effect in the surface states of topological insulators was predicted theoretically and detected in various experiments [22–25, 27].

The surface states of 3D topological insulators are approximated by the Hamiltonian (3.30) with linearly dispersing bands,

$$\mathcal{E}^n(\mathbf{k}) = n\hbar v_F k. \quad (4.36)$$

Here, v_F is the Fermi velocity and $n = \pm 1$ corresponds to the branches above and below the diabolic point ($\mathcal{E} = 0$), which is the only degenerate point in this model band structure.

The Edelstein conversion tensor reads

$$\kappa_{yx} = -\kappa_{xy} = -\frac{\chi e A_0}{4\pi\hbar^2 v_F} \tau_F^{\text{tr}} |\mathcal{E}_F| = -\frac{\chi e \hbar v_F N_{\text{u.c.}}}{\pi c_1 |U_0|^2}, \quad \tau_F^{\text{tr}} = \frac{4\hbar^2 v_F}{A_{\text{at}} k_F c_1 |U_0|^2} \quad (4.37)$$

with $k_F = |\mathcal{E}_F|/\hbar v_F$. The chirality $\chi = \pm 1$ determines the sense of rotation of the spin expectation values along the Fermi circle. At opposite surfaces, χ changes sign. The total spin density is constant within the whole energy range, except for the diabolic point at which the Boltzmann model is not applicable, as discussed in section 2.3.5. By measuring the sign of the spin density generated by the Edelstein effect the chirality χ of the surface states can be determined directly.

Eq. (4.37) differs from the expression for isotropic Rashba systems with $\mathcal{E}_F > 0$ [Eq. (4.7)] only by the chirality determining the sign of the effect and a factor of $\hbar v_F$ instead of α_R . This seems to be inconsistent with the above mentioned enhancement of the effect due to the lack of compensation from a second Fermi circle, which has also been the motivation of examining the Edelstein effect in the surface states of topological insulators. However, the simple picture of reduced compensation usually approximates the relaxation time as a parameter and does not take into account its explicit dependence on the system's properties.

The Fermi velocity v_F is typically in the order of 10^5 m s^{-1} . Thus, the product $\hbar v_F$ is in the range of a few $\text{eV}\text{\AA}$. In Rashba systems the Rashba parameter is typically below $1 \text{ eV}\text{\AA}$ and takes values of a few $\text{eV}\text{\AA}$ for special systems with extraordinary large Rashba splitting, as for example the Bi/Ag surface alloy. Therefore, the Edelstein effect calculated for the surface states of topological insulators is in general large in comparison to that in Rashba systems. By this comparison between the analytical expressions for Rashba systems and topological insulators, it seems that the enhanced Edelstein effect is caused mainly by the large factor of $\hbar v_F$ in comparison to α_R . However, the models discussed here describe qualitatively different physical systems. For a comparison of Rashba systems and topological insulators a more detailed consideration is needed.

For small k the Rashba Hamiltonian (3.18) is approximated in first order in k by the topological insulator surface Hamiltonian (3.30). Within this approximation, the Fermi circle of a topological insulator corresponds to the inner Fermi circle of a Rashba system. Though, the current-induced spin density in a topological insulator is not equivalent to the contribution of the inner Fermi circle of a Rashba system, since in topological insulators only scattering events within the only Fermi circle contribute to the transport lifetime whereas in Rashba systems also inter-circle scattering takes place. Therefore, the spin density in topological insulators does not depend on the Fermi energy while the Edelstein contribution of the inner Fermi line of Rashba systems does. Hence, the similarity of the analytical expressions (4.7) and (4.37) is rather by chance than of physical origin.

The bulk states of 3D topological insulators exhibit a band gap in which the topological surface states exist. Thus, for Fermi energies in the bulk band gap, an electric charge current driven through the sample is carried only by the surface states and not by the bulk states. Therefore, calculating the current-induced spin density as a response to the electric charge current is more reasonable here than for the surface states of bulk metals. The electric charge current density is

$$\mathbf{j}^c = \frac{e^2 \tau_F^{\text{tr}} |\mathcal{E}_F|}{4\pi\hbar^2} \mathbf{E}. \quad (4.38)$$

system	v_F ($\frac{10^5 \text{m}}{\text{s}}$)	λ_w ($\text{eV}\text{\AA}^3$)	\mathcal{E}_F (eV)	κ_{yx} (10^{-9}mV^{-1})	ζ_{yx} (10^{-8}mA^{-1})	Ref.
α -Sn	6.0	0	0.03	-12.57	-142.41	[25]
Bi_2Se_3	6.2	0	-0.01	-13.00	-74.71	[90]
Bi_2Se_3 , Cu-doped	2.9	140	0.45	-6.11	-16.66	[144]
Bi_2Te_3 , Sn-doped	3.9	250	0.28	-8.33	-59.72	[143]

Table 4.4.: Charge-to-spin conversion factors $\hat{\kappa}$ and $\hat{\zeta}$ for the surface states of selected topological insulators. Here, results for isotropic systems and for systems with hexagonal warping are presented. Similar results were published in [J4].

Thus, the tensor $\hat{\zeta}$ is

$$\zeta_{yx} = -\zeta_{xy} = -\chi \frac{A_0}{e v_F}. \quad (4.39)$$

Although the spin density increases with v_F for a fixed applied electric field, it scales with v_F^{-1} when the current is kept constant. Interestingly, also for this definition of charge-current-to-spin conversion efficiency, the effect is constant in energy. Since the surface states of topological insulators provide an approximately constant and comparably large spin density independent of the Fermi energy they seem to be a promising class of materials for possible applications of the Edelstein effect, e.g. for inducing spin-orbit torque in a ferromagnetic material adjacent to the surface. The charge-to-spin-current conversion efficiency was examined experimentally in $(\text{Bi}_{1-x}\text{Sb}_x)_2\text{Te}_3$ as a function of the Fermi level [132]. The induced spin polarization was found to be approximately constant with respect to the Fermi level except for a small region around the diabolic point, and its sign was constant in the whole energy region, which fits well with the theory presented here.

Like in Rashba systems, the isotropic model Hamiltonian can be extended by higher-order terms respecting the symmetry of the surface. At a topological insulator surface with C_{3v} symmetry, Fermi surfaces with a hexagonal snowflake-like shape were observed in angle-resolved photoemission spectroscopy (ARPES) experiments [143]. A corresponding additional contribution to the Hamiltonian was derived by Fu using a perturbative $\mathbf{k} \cdot \mathbf{p}$ approach [143]. It is equivalent to the third-order warping term introduced in Eq. (4.19), $\hat{H}^{(3)} = \frac{\lambda_w}{2} (k_+^3 + k_-^3) \hat{\sigma}_z$.

In Table 4.4 the spin density generated by an electric field and 2D charge current, respectively, in the surface states of selected topological insulators is expressed by the tensors $\hat{\kappa}$ and $\hat{\zeta}$. The α -Sn and Bi_2Se_3 surface states are approximated within the isotropic model, for the surface states of Cu-doped Bi_2Se_3 and Sn-doped Bi_2Te_3 the warping term of the Hamiltonian is included. In general, the absolute values of the spin density are larger than for most of the isotropic Rashba systems presented in Table 4.1, except of the Bi/Ag surface alloy. For the topological insulators considered here the product $\hbar v_F$ is in the range from 1.91 to 4.08 eV \AA , which is large in comparison to the Rashba parameter α_R of the Rashba systems in Table 4.1. The additional warping term reduces the effect, as discussed above for Rashba systems, due to the out-of-plane component of the spin expectation values on the Fermi line. However, the influence of the warping term is less pronounced here: The in-plane anisotropy $\kappa_{xy} \neq -\kappa_{yx}$ and the out-of-plane element κ_{zx} can be neglected.

4.8. Weyl semimetals

For experimental observations and potential technical applications of the Edelstein effect, a large spin density induced by an electric field is preferable. The identification of materials with large efficiency of “converting” the electric current into spin polarization is therefore highly desirable. In the previous sections, several system properties favoring an efficient charge-to-spin conversion were identified. In section 4.5.2 it was shown that elongated Fermi contours give rise to an enhanced

4. The Edelstein effect

Edelstein effect if the electric field is perpendicular to that elongated region. A strong uniform spin polarization of the states also enhances the effect. Further, in section 4.7 it was discussed that a large Edelstein effect is expected in systems with a single Fermi line in which no contributions from Fermi lines with opposite spin polarization occur, compensating the effect.

These desirable properties are provided by the topological surface states of Weyl semimetals, introduced in section 3.7. They disperse roughly linearly giving rise to Fermi arcs with an elongated linear shape. They are strongly spin polarized and usually occur as single Fermi lines. Therefore, in the following the current-induced spin polarization in type-I Weyl semimetals with broken inversion symmetry is considered, particularly the contribution provided by the surface states. The focus lies on TaAs for which the layer-resolved spin density induced by a uniform electric field is calculated. In contrast to the previously discussed purely two-dimensional model systems (2DEGs with Rashba SOC and surface states of topological insulators), the Weyl semimetals' bulk as well as surface states will be discussed since Weyl semimetals provide also a finite bulk density of states. Due to their topologically nontrivial character and the closed band gap, the Weyl semimetal bulk states' influence on the transport properties cannot be neglected. The bulk bands are nondegenerate, except of the Weyl points, and also spin polarized. Therefore, in the presence of an external electric field, a nonzero total spin polarization originating from the bulk states is also expected and needs to be discussed.

As for the two-dimensional systems discussed above, the transport properties are considered within the semiclassical Boltzmann transport theory [159]. However, the general expression for the Edelstein effect, Eq. (4.2), contains now three-dimensional \mathbf{k} and $\Lambda_{\mathbf{k}}$. By contrast to the previous sections 4.5-4.7, the mean free path is approximated by the relaxation time approximation $\Lambda_{\mathbf{k}} = \tau_{\mathbf{k}} \mathbf{v}_{\mathbf{k}}$, with $\tau_{\mathbf{k}}$ the momentum relaxation time including only scattering-out processes. By using the transport lifetime instead of the momentum relaxation time, the results would gain more accuracy. However, the order of magnitude of the transport properties would not be changed remarkably. Since the models used in this section are quite simple, the predictive power of the results for the Edelstein effect is limited to statements on the order of magnitude. Therefore, including the transport lifetime could slightly modify the quantitative results but would not change the main messages of this section. The main part of this section was published in [J5].

4.8.1. Edelstein effect from the Fermi arcs

A sample finite in z -direction but infinite in x - and in y -direction (slab geometry) is considered, whose band structure contains a pair of Weyl points of opposite chirality separated in \mathbf{k} -space by $\Delta \mathbf{k}_W$. At the top (T) and bottom (B) surfaces, Fermi arcs connect the surface projections of the Weyl points [32]. In the simplest case the Fermi arcs can be approximated as straight lines. For a rough estimation of the current-induced total spin expectation value provided by these surface states it is assumed that the Fermi velocity, the spin expectation value, and the momentum relaxation time are constant along the Fermi arcs: $\mathbf{v}_F^T = -\mathbf{v}_F^B \equiv \mathbf{v}_0$, $\langle \boldsymbol{\sigma} \rangle_{\mathbf{k}}^T = -\langle \boldsymbol{\sigma} \rangle_{\mathbf{k}}^B \equiv \langle \boldsymbol{\sigma}_0 \rangle$, and $\tau_{\mathbf{k}}^B = \tau_{\mathbf{k}}^T \equiv \tau_0$. Using Eq. (4.2), the current-induced spin density at both surfaces reads

$$\frac{\langle \mathbf{s} \rangle^T}{A} = \frac{\langle \mathbf{s} \rangle^B}{A} = -\frac{|e|}{4\pi^2 \hbar \nu_0} \tau_0 \langle \boldsymbol{\sigma} \rangle_0 (\mathbf{v}_0 \cdot \mathbf{E}) \Delta k_W, \quad (4.40)$$

where A is the area of the surface and $\Delta k_W = |\Delta \mathbf{k}_W|$. The surface spin polarization is maximum if $\mathbf{E} \parallel \mathbf{v}_0$ (which means \mathbf{E} is perpendicular to the Fermi arcs) and vanishes for $\mathbf{E} \perp \mathbf{v}_0$. It has the same sign on both surfaces, whereas it points in opposite directions at opposing surfaces of a system with Rashba surface states. Thus, the total system would not be invariant under a rotation of π around the current axis, which is reasonable because of the broken rotation symmetry of the Weyl semimetal. The additional spin polarization from the bulk states will be discussed for the type-I Weyl semimetal TaAs in the next section.

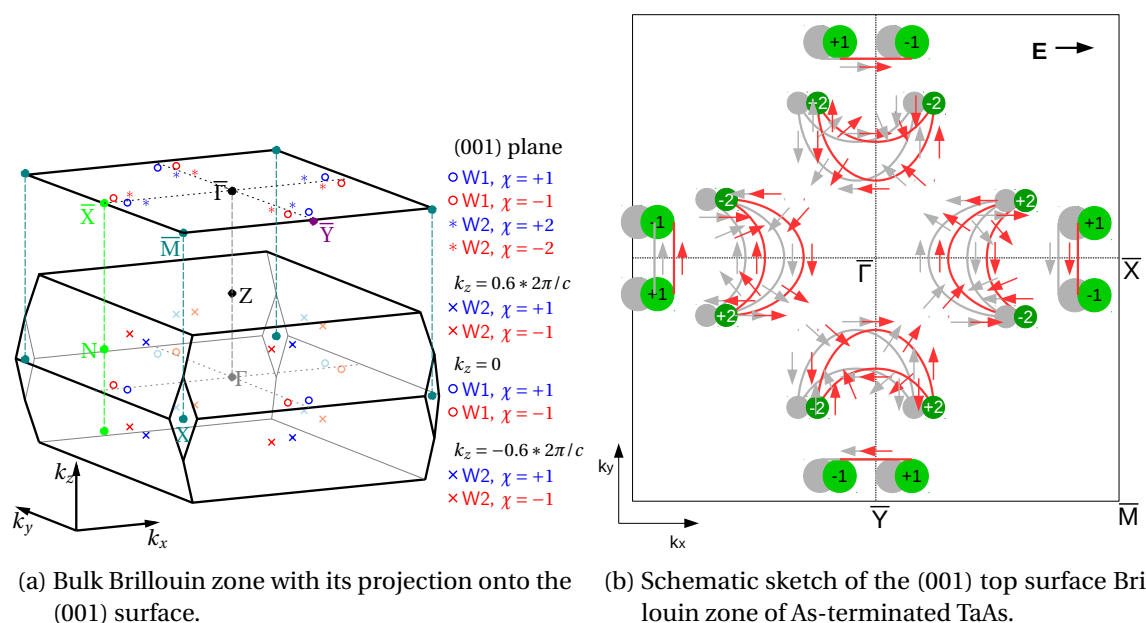


Figure 4.21.: Bulk Brillouin zone of TaAs and its projection onto the (001) surface. The 24 Weyl points near the Fermi level [102] are separated into 8 Weyl points of type W1 and 16 Weyl points of type W2; the latter are surface-projected onto 8 W2 points of chirality $\chi = \pm 2$. (a): The positions of the 24 Weyl points in the bulk and 16 Weyl points in the surface Brillouin zone are marked by red and blue symbols, respectively. (b): The 16 projected Weyl points (green) are connected by Fermi arcs (red). Arrows indicate the \mathbf{k} -dependent spin polarization. The “shift” of the Fermi surface due to an external electric field E is sketched as gray lines. Both figures were published in [J5] [(a) was slightly modified].

4.8.2. Current-induced spin polarization in the type-I Weyl semimetal TaAs

Using Eq. (4.2) and the Hamiltonian (3.35), the macroscopic spin polarization of a type-I Weyl semimetal is estimated. The minimal number of Weyl points is two in systems with inversion symmetry and four in time-reversal symmetric systems that are considered here. In a system with a larger number of Weyl points which can be approximated by this Hamiltonian as well, more bulk and surface states contribute to the total spin polarization. However, considering elastic scattering, the consequently increased number of scattering events reduces the momentum relaxation time. Thus, the total spin polarization is not affected by the larger number of Weyl points.

As an application of the above theory, the Weyl semimetal TaAs [103, 160, 161] is considered which has a body-centered tetragonal crystal structure with lattice constants $a = 3.437\text{\AA}$ and $c = 11.656\text{\AA}$ [103]. Each primitive unit cell contains 2 Ta and 2 As atoms; inversion symmetry is broken [103].

The band structure exhibits 24 Weyl points near the Fermi level. A sketch of the three-dimensional Brillouin zone with the Weyl points is shown in Fig. 4.21(a). Two different types of Weyl points exist in TaAs: 8 points called W1, located in the ($k_z = 0$)-plane, and 16 points called W2 located in the planes $k_z = \pm 0.6 \frac{2\pi}{c}$. They differ with respect to their position in energy and \mathbf{k} , their Fermi velocity \mathbf{v}_F , and the saddle point energies $\pm \mathcal{E}_S$. The details of the band structure, given in Ref. [162], were used to fit the bulk band structure near the W1 and W2 Weyl points by the Hamiltonian (3.35). Numbers are given in Table 4.5. The \mathbf{k} -points at the Fermi level are determined using an adaptive tetrahedral method, introduced in section E.2 in the appendix.

In what follows, the As-terminated (001) surface of TaAs [100] is considered. In the projection onto the two-dimensional Brillouin zone, two W2 nodes of the same chirality are projected onto each other; thus, the 16 W2 nodes are mapped onto 8 nodes of chirality $\chi = \pm 2$ [103, 160, 161], which

4. The Edelstein effect

	number	\mathcal{E}_{FW} (meV)	\mathcal{E}_{S} (meV)	Δk_{W} (\AA^{-1})	v_x (10^5ms^{-1})	v_y	v_z	m_0 (10^{-4}\AA^{-2})	γ_{W} ($\text{eV}\text{\AA}^2$)
W1	8	22.1	22.5	0.026	5.2	2.2	0.2	1.73	130
W2	16	8.9	47.9	0.068	4.3	2.6	3.1	11.4	42

Table 4.5.: Properties of the TaAs bulk band structure around the W1 and W2 Weyl points. \mathcal{E}_{FW} is the energy distance between \mathcal{E}_{F} and the Weyl points, \mathcal{E}_{S} is the saddle point energy with respect to the Weyl points, v_x is the group velocity in the direction $\Delta \mathbf{k}_{\text{W}}$ at the Weyl point energy. The values for \mathcal{E}_{FW} , Δk_{W} , v_x , v_y , and v_z are taken from Ref. [162] and were used to determine the parameters m_0 and γ_{W} that enter the Hamiltonian (3.35). The data was published in [J5].

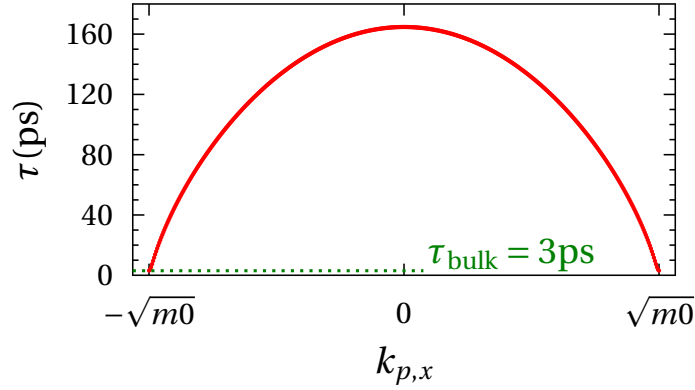


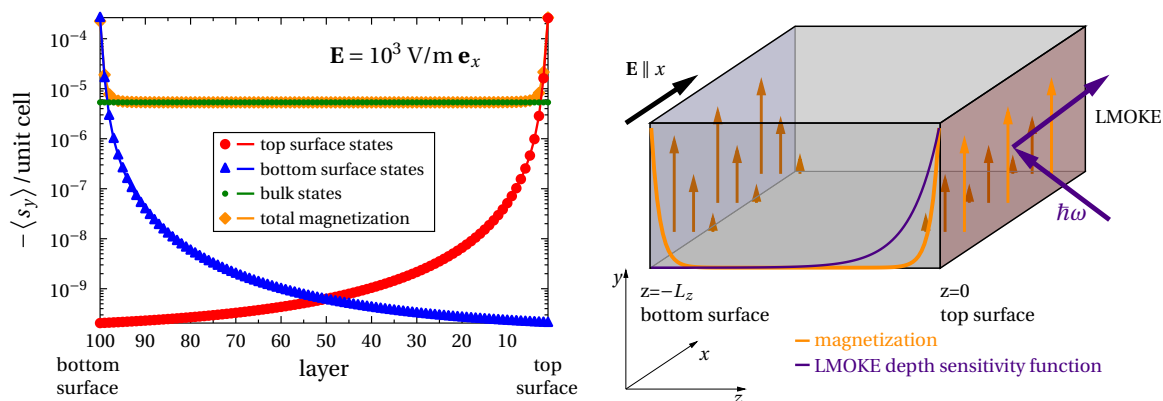
Figure 4.22.: Momentum relaxation time along the Fermi arc between the W1 Weyl points for δ -shaped impurities with $U_0 = 1 \text{ eV}$ and $c_i = 1\%$. The states are maximally localized at the surface at $k_{p,x} = 0$ and continuously evolve into bulk states for $k_{p,x} = \pm\sqrt{m_0}$, which is the connecting point with the bulk states. The figure is adapted from [J5].

is sketched in Fig. 4.21(b). The Weyl points are not exactly at the Fermi energy. The Fermi arcs connect the projections of the Weyl cones, the number of Fermi arcs terminating at a projected Weyl cone corresponds to the (modulus of the) chirality of the respective projected Weyl point [102]. However, since the model Hamiltonian (3.35) describes only projected Weyl points with $\chi = \pm 1$, it does not reproduce properly the Fermi arcs connecting the W2 nodes.

Experiments [35, 101, 160, 163] and calculations [100, 102, 103] have shown that the Fermi arcs between two W2 nodes of opposite chirality are two crescent-shaped lines with opposite spin polarization but same sign of the Fermi velocity on each surface. The Fermi arcs with the spin polarization are also sketched in Fig. 4.21(b). Roughly estimating the total spin density provided by the surface states of the W2 nodes by Eq. (4.2), these states do not contribute considerably to the total spin polarization of the system because their contributions compensate nearly completely.

The W1 surface states provide single-line Fermi arcs between the W1 nodes which can be approximated as straight lines with constant spin polarization along the arc, which is consistent with the Hamiltonian (3.35) [100, 103]. Therefore, only the contribution of the bulk states of all 24 nodes and the W1 surface states are considered here. However, the W2 surface states are taken into account in the scattering probabilities.

The impurities are assumed δ -shaped with a scattering potential of $U_0 = 1 \text{ eV}$, whose concentration is set to $c_i = 1\%$. For bulk-bulk scattering processes, the single-impurity transition matrices $T_{\mathbf{k}' \leftarrow \mathbf{k}}^i$ are independent of the impurity position. However, if at least one of the involved states is a surface state, the transition matrix depends on the coordinates of the impurity due to the z -dependence of the surface-state wave functions given by Eqs. (3.40) and (3.41). In the calculation of the momentum relaxation time the transition matrix elements are averaged over all z -positions of the impurity across the sample, as discussed in section 2.5.



(a) Induced spin per unit cell as a function of the layer index in z -direction. The top surface is at layer 1 (right), the bottom surface at layer 100 (left). The electric field is $E_x = 10^3 \text{ V/m}$. The figure is adapted from [J5].

(b) Sketch of a proposed experiment for detecting the Edelstein effect in TaAs. The MOKE signal is the integrated signal originating from the layers at the surface and from the adjacent layers, depending on the penetration profile of the light.

Figure 4.23.: Layer-resolved current-induced spin density in TaAs calculated within the Boltzmann approach and proposal of an experiment for detecting the surface spin density.

In Fig. 4.22 the momentum relaxation time $\tau_{\mathbf{k}}$ of the W1 bulk states as well as surface states along the Fermi arc is shown. The bulk momentum relaxation time is constant at the Fermi surface because of time-reversal symmetry. It is comparably large due to the low bulk density of states near the Weyl points which reduces the phase space for scattering. The relaxation time is even enhanced for the surface states because of their localization. The surface states in the centers of the Fermi arcs are maximally localized at the surface and are scattered preferably at impurities near the surface. In contrast, the surface states near the ends of the Fermi arcs, which are attached to the bulk states, are extended across the sample; in other words, they exhibit bulk-like scattering. Due to their spatial extension, bulk states have more scattering possibilities than surface states; thus, the bulk relaxation time τ_{bulk} is in general smaller than the surface relaxation times. Therefore, $\tau_{\mathbf{k}}$ shown in Fig. 4.22 has its maximum at the center of the Fermi arc and decreases to τ_{bulk} at the ends.

In Fig. 4.23(a) the current-induced total spin per bulk unit cell is shown as a function of the layer index in z -direction. The size of the sample is taken as $1 \mu\text{m} \times 1 \mu\text{m} \times 1.164 \mu\text{m}$, the latter corresponding to 100 layers in z -direction. An electric field of 10^3 V/m is applied in x -direction, which is a voltage of 10^{-3} V across the sample. The current-induced spin polarization is in-plane and perpendicular to the electric field. The bulk states give rise to a spin density constant in z , since they are Bloch-like and spread over the whole sample. The localized top (bottom) surface states produce a spin polarization with a maximum at the corresponding surface which decreases toward the interior of the sample.

The main contribution to the total spin expectation value stems from the surface states due to their large momentum relaxation time and the uniform spin polarization along the Fermi arcs. A Fermi arc contributes most if the electric field is applied perpendicular to the arc, that is parallel to the Fermi velocity. Due to the opposite spin polarizations and opposite group velocities of the top and bottom surface states, the spin polarization points in the same direction at both surfaces. This is a major difference in comparison to the Edelstein effect in Rashba systems and in topological insulators for which the spin polarization points in opposite directions at opposite surfaces.

Due to the maximum spin polarization at the surfaces, surface-sensitive experimental methods, i.e. MOKE measurements, could be used to detect the Edelstein effect. Since the spin polarization is in-plane, the MOKE experiment would have to be performed in longitudinal geometry (LMOKE), sketched in Fig. 4.23(b). The light beam enters the sample e.g. at the top surface and is attenuated on

4. The Edelstein effect

System	α_R (eVÅ)	\bar{v}_F (10^5ms^{-1})	τ (ps)	κ_{yx} ($10^{-9}/\text{Vm}$)
Au(111)	0.33	–	0.26	1.1
Bi/Ag(111)	3.05	–	0.31	29.1
α -Sn(001)	–	6.00	0.39	–12.6
TaAs	–	3.00	3...165	–290

Table 4.6.: Edelstein tensor κ_{yx} , model parameters and momentum relaxation time for the Rashba systems Au(111) and Bi/Ag(111) (taken from Table 4.1), for the (001) surface of the topological insulator α -Sn (taken from Table 4.4), and the Weyl semimetal TaAs. The data was published in [J5].

its way through the sample. The MOKE signal originates from the magnetization at the surface but also from the subjacent bulk layers, depending on the penetration depth of the incident light. Due to the magnetization profile – decreasing from the surface toward the bulk – a MOKE measurement is similar to experiments at thin magnetic layers.

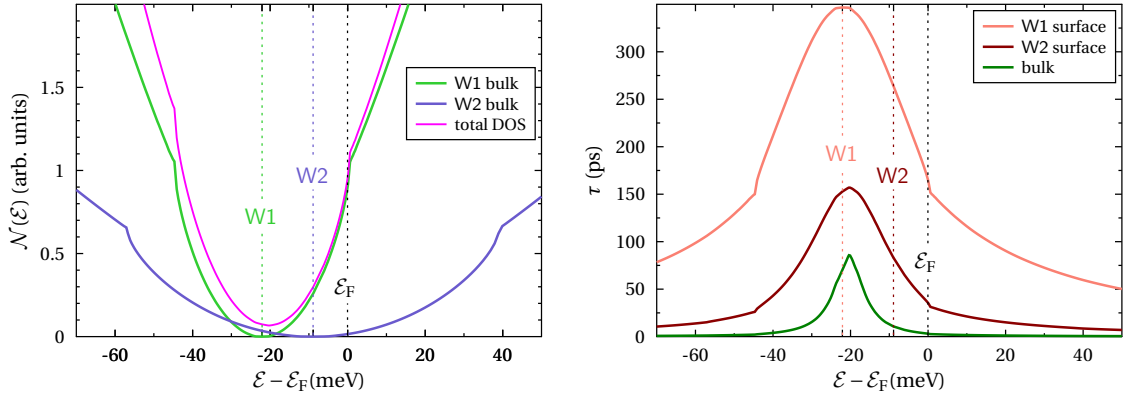
To estimate the strength of the MOKE signal of a TaAs sample, the light is assumed s -polarized with a wavelength of $\lambda = 650 \text{nm}$. The complex refractive index of TaAs is $n_R = 1.98 + 6.07i$ [164]. The contribution of the magnetization at a position z_i to the complex Kerr signal is multiplied by a factor of $\exp(-4\pi i n_R z_i / \lambda)$ [165–167]. By integrating over the attenuated Kerr signal of all layers a Kerr rotation signal which corresponds to a current-induced magnetic moment of $2.9 \cdot 10^{-4} \mu_B$ per surface unit cell is obtained, equivalent to an Edelstein tensor of $\kappa_{yx} = -2.9 \cdot 10^{-7}$.

Comparison to Rashba systems and topological insulators

To demonstrate the relevance of the above results, the current-induced spin density in TaAs is compared to the previous results for Rashba systems and topological insulators [J4] discussed in sections 4.5.1 and 4.7. In Table 4.6 the Rashba constants and Fermi velocities, respectively, relaxation times, and Edelstein tensor elements κ_{yx} are given for the paradigmatic Rashba systems Au(111) and Bi/Ag(111) as well as the topological insulator α -Sn. Assuming the same impurity concentration, scattering potential, and electric-field strength as for TaAs (see the previous section), the results for the current-induced spin expectation value are considerably smaller; more precisely, the TaAs result is increased by several orders of magnitude.

To understand these results, the general formula (4.2) for the field-induced spin polarization and the analytical expressions (4.7), (4.37), and (4.40) are recalled. The total spin polarization can be approximated as product of average momentum relaxation time τ and DOS at the Fermi level weighted with the \mathbf{k} -dependent spin expectation value $\langle \sigma \rangle_{\mathbf{k}}$ and Fermi velocity v_F . The latter two quantities are of the same order of magnitude for all systems compared here. Thus, the enhanced Edelstein effect in TaAs must result from an extraordinary large product $\mathcal{N}(\mathcal{E}) \times \tau$. Usually, this product is approximately constant in energy, since a low DOS means a reduced phase space available for each state to scatter into and an increased relaxation time. This argument holds for Rashba systems, the surface states of topological insulators and for the bulk states of Weyl semimetals.

However, the situation is different for the TaAs system. In TaAs the Fermi energy is close to the energy of the Weyl points, the bulk DOS at the Fermi level is low (semimetal). The DOS of the W1 and W2 Weyl points reduce to zero at the corresponding Weyl point energies, but since the Weyl points are located at different energies, the total DOS is always nonzero, as shown in Fig. 4.24(a). Here, only the energy region between the Lifshitz transitions, where the band structure is approximated sufficiently by the model Hamiltonian (3.35), is considered. Further, the surface state DOS does not vanish at the Weyl point energies; in the model used here it is constant in energy. Both bulk and surface states can scatter into bulk as well as surface states. Thus, the scattering rate from bulk/surface to surface states is not affected by changes in energy, whereas approaching one of the Weyl point energies considerably reduces the phase space for scattering from bulk/surface to



(a) Density of states of the bulk states and the total DOS of all states. (b) Momentum relaxation time τ for the W1 and W2 surface states (in the center of the Fermi arcs) and the bulk states.

Figure 4.24.: Density of states and momentum relaxation time versus energy. (a): The W1 and W2 bulk DOS vanishes at the corresponding Weyl point energies (vertical dotted lines). The kinks are attributed to the van Hove-singularities at the Lifshitz transition. The surface states DOS is constant in energy and not shown here, but is included in the total DOS; the latter is never zero. (b): The maximum of τ is located at the energy at which the total DOS reaches its minimum. Both figures are adapted from [J5].

bulk states. Therefore, the relaxation time of the bulk states as well as the surface states is enhanced for energies near the Weyl points, as shown in Fig. 4.24(b). For the bulk states, the enhancement of τ is compensated by the reduced DOS, but for the surface states the product of DOS and τ is large for energies near the Weyl points, which leads to the enormous Edelstein effect. Hence, one can expect an even larger Edelstein effect if the Weyl points were closer to the Fermi energy, as shown in Fig. 4.25(a).

Limits of the Boltzmann approach

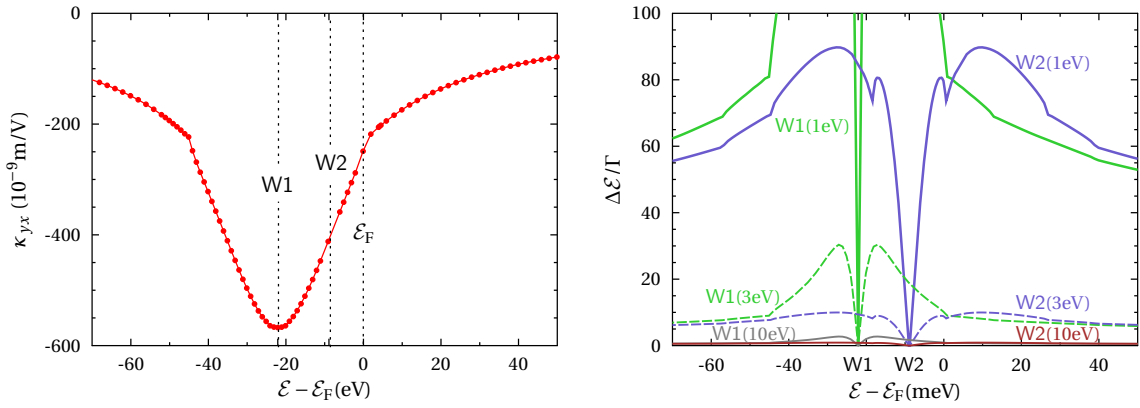
As discussed in section 2.3.5, the Boltzmann approach is not appropriate when the Fermi surface contains \mathbf{k} -values near small band gaps, which means energies close to the Weyl point energies. Around the Weyl points, the interband transitions strongly affect the transport properties and cannot be neglected. The intrinsic contribution of the Kubo formula, Eq. (4.12), vanishes for the TaAs system because of time-reversal symmetry. A detailed discussion of the extrinsic contributions to the charge conductivity for the model Hamiltonian (3.35) using Kubo linear response theory is given in Ref. [168]. Although elastic interband scattering is considered in the semiclassical Boltzmann theory, inelastic transitions are neglected, which leads to an overestimated relaxation time. Further, interband transitions would give additional contributions to Eq. (4.2), as discussed in Ref. [61], which are comprised in the constant Γ approach [64, 65],

$$\langle \sigma \rangle^{\text{ext}} = -\frac{e\hbar}{\pi} \sum_{\mathbf{k}, n, m} \frac{\Gamma^2 \text{Re}(\langle \mathbf{k}^n | \hat{\sigma} | \mathbf{k}^m \rangle \langle \mathbf{k}^m | \hat{\mathbf{v}} \cdot \mathbf{E} | \mathbf{k}^n \rangle)}{[(\mathcal{E}_F - \mathcal{E}_n(\mathbf{k}))^2 + \Gamma^2][(\mathcal{E}_F - \mathcal{E}_m(\mathbf{k}))^2 + \Gamma^2]}, \quad (4.41)$$

where Γ is the lifetime broadening ($\Gamma = \frac{\hbar}{\tau}$). The terms $n = m$ are approximately equivalent to a Boltzmann approach with constant relaxation time. If $\Gamma \ll |\mathcal{E}^m - \mathcal{E}^n|$, the influence of the interband transitions is insignificant.

In Fig. 4.25(b) the ratio of the bulk interband energy difference $\Delta\mathcal{E} = |\mathcal{E}^+ - \mathcal{E}^-|$ and lifetime broadening $\Gamma = \Gamma^+ + \Gamma^-$ is shown for energies near the Fermi level. For the scattering potential

4. The Edelstein effect



(a) Energy dependence of the Edelstein signal. It has its maximum (absolute value) near the W1 point energy, where the momentum relaxation time is also maximum. (b) Ratio of energy difference $\Delta\mathcal{E}$ and lifetime broadening Γ of the bulk bands near the Weyl points versus energy for various scattering potentials. Adapted from [J5].

Figure 4.25.: Energy dependence of the Edelstein effect (a) and estimate of regions in which the Boltzmann approach is not applicable (b).

$U_0 = 1\text{eV}$ and the impurity concentration $c_i = 1\%$ used in the previous calculations, $\Gamma \ll \Delta\mathcal{E}$ holds at the Fermi level and nearly within the entire energy range. For $5\Gamma < \Delta\mathcal{E}$ the interband contributions can safely be neglected. Only energies close to the Weyl points, $W_{1/2} \pm 1 \text{ meV}$ are critical: there, interband transitions have to be included. The momentum relaxation time strongly depends on the scattering potential and the impurity concentration, $\tau \propto U_0^{-2} c_i^{-1}$. Thus, $\Gamma \propto U_0^2 c_i$. For larger U_0 and c_i ($U_0 = 3\text{eV}$ in the figure), $\Gamma > |\mathcal{E}^+ - \mathcal{E}^-|$ holds in a wider energy range. For very large scattering potentials ($U_0 = 10\text{eV}$ in the figure), $\Gamma \gtrsim \Delta\mathcal{E}$ in the whole energy region, and the semiclassical Boltzmann approach is not sufficient and should be used only for weak scatterers.

5. Chiral anomaly in Weyl semimetals

Since Weyl semimetals host low-energy states which are described by the Weyl equation [36], they are considered as solid-state equivalent of Weyl fermions. Therefore, quantum anomalies originally introduced in the framework of fundamental Weyl particles can also be discussed in solid states. Especially the Adler-Bell-Jackiw anomaly [37–39], also known as chiral anomaly, is of interest because it is related to anomalous transport signatures which can actually be detected experimentally. In the presence of nonorthogonal electric and magnetic fields, the number of particles of a distinct chirality is not conserved. This nonconservation of the chiral charge violates the chiral gauge symmetry of the system [169], thus, it is called an anomaly.

In Weyl semimetals, chiral Weyl fermions exist in the vicinity of Weyl points with a distinct chirality χ . Whereas the chirality of a Weyl point is defined by the Weyl Hamiltonian (3.31), the number of states carrying this chirality is related to the occupation of states around the Weyl point. In Weyl semimetals, each Weyl point has its counterpart with the opposite chirality $-\chi$. The total chirality vanishes according to the Nielsen-Ninomiya no-go theorem [92]. Therefore, the chiral anomaly can be interpreted as transfer of states from one chirality (e.g. $-\chi$) to the other (χ) in the presence of nonorthogonal magnetic and electric fields. However, no electric charge is created or annihilated when the chiral character of a state is reversed. Therefore, the total electric charge and the related charge current are conserved and can be described by a continuity equation.

The chiral charge of a Weyl semimetal and nonconservation of chiral charge are not experimentally accessible quantities. However, the chiral anomaly remarkably affects the transport properties of the system by increasing the longitudinal charge conductivity in the direction of the magnetic field, leading to a negative longitudinal magnetoresistance (NLMR). This unconventional magnetic field dependence – usually, the longitudinal charge conductivity parallel to the magnetic field is reduced since the electrons are forced to move on orbits perpendicular to the magnetic field by the Lorentz force – has been detected in various Weyl and Dirac semimetals [26, 170–172].

Although the detection of a NLMR is a strong hint for the existence of Weyl points near the Fermi level, the chiral anomaly is not the only phenomenon causing a NLMR [26]. Thus, when a NLMR signal is detected experimentally, origins different from the chiral anomaly have to be eliminated in order to clearly identify the chiral anomaly.

The chiral anomaly and the resulting anomalous transport properties can be discussed in the ultraquantum limit, which implies large magnetic fields and Fermi energies close to the Weyl point energies, as well as in the semiclassical limit, which is appropriate for weak magnetic fields and Fermi energies not too close to the Weyl point energies. Although both approaches can explain the phenomenon qualitatively, they differ with respect to the magnetic field dependence of the charge conductivity.

In this chapter, a short introduction of the underlying concept of anomalies in field theory is given. Subsequently, the phenomenon of the chiral anomaly and the resulting transport properties are derived in the ultraquantum as well as the semiclassical limit. A short overview on the present experimental observations of the chiral-anomaly-related transport signatures in various Weyl and Dirac semimetals is given. Finally, the transport properties in model systems of two (broken time-reversal symmetry) and four (broken inversion symmetry) Weyl points as well as the realistic Weyl semimetal TaAs are calculated using the semiclassical Fermi surface harmonics method introduced in section 2.3.3 and with a focus on energy-dependent and transversal transport properties.

5.1. Quantum anomalies in field theory

In this section the concept of quantum field anomalies will be briefly introduced following the works of Jackiw [169] and Adler [173]. The Noether theorem [174] states that each continuous

5. Chiral anomaly in Weyl semimetals

symmetry is connected to a conservation law. Prominent examples from classical physics are time invariance leading to energy conservation, translational invariance related to momentum conservation and rotational invariance which leads to conservation of angular momentum. Each of these conservation laws can be expressed by an associated continuity equation.

Anomalies in quantum field theory correspond to breaking classical symmetries and the related conservation laws by quantum effects. Symmetries which exist for unquantized and commuting variables can be broken as soon as the dynamics of the system is quantized with noncommuting variables [169].

The basic concept of a quantum anomaly will be demonstrated for a massless four-component Dirac-Fermi field $\Psi(\mathbf{x})$ described by the massless Dirac equation

$$i\hbar\hat{\gamma}^\mu \frac{\partial}{\partial x^\mu} \Psi(\mathbf{x}) = 0. \quad (5.1)$$

Here $\mu = 0, 1, 2, 3$ with $x^0 = ct$, whereas the other components of \mathbf{x} are the spatial components x, y, z . The explicit form of the set of 4×4 matrices $\hat{\gamma}^\mu$ can be freely chosen as long as they satisfy the Clifford algebra $\hat{\gamma}^\mu \hat{\gamma}^\nu + \hat{\gamma}^\nu \hat{\gamma}^\mu = 2g^{\mu\nu} \mathbb{1}_{4 \times 4}$ with the Lorentz signature $\hat{g} = \text{diag}(1, -1, -1, -1)$. First, $\Psi(\mathbf{x})$ is assumed a classical unquantized field. Eq. (5.1) is invariant under the global gauge transformation

$$\Psi(\mathbf{x}) \rightarrow e^{i\theta} \Psi(\mathbf{x}), \quad (5.2)$$

with constant θ . The Noether theorem states that this gauge symmetry leads to a conservation law, namely the conservation of the charge Q associated with the field $\Psi(\mathbf{x})$, which is defined as

$$Q \equiv \int \Psi(\mathbf{x})^\dagger \Psi(\mathbf{x}) d^3 r, \quad \mathbf{r} = (x, y, z). \quad (5.3)$$

The charge conservation can also be expressed by the corresponding continuity equation

$$\frac{\partial}{\partial x^\mu} J^\mu(\mathbf{x}) = 0 \quad (5.4)$$

with the charge current 4-vector

$$J^\mu(\mathbf{x}) \equiv \Psi^\dagger(\mathbf{x}) \hat{\gamma}^0 \hat{\gamma}^\mu \Psi(\mathbf{x}). \quad (5.5)$$

Applying the chiral projection operator $\hat{P}_\chi = \frac{1}{2}(\mathbb{1}_{4 \times 4} + \chi \hat{\gamma}_5)$ with $\hat{\gamma}_5 = i\hat{\gamma}^0 \hat{\gamma}^1 \hat{\gamma}^2 \hat{\gamma}^3$ and the chirality $\chi = \pm 1$ to $\Psi(\mathbf{x})$, its chiral components are projected, which are eigenfunctions of $\hat{\gamma}_5$,

$$\Psi_\chi(\mathbf{x}) \equiv \hat{P}_\chi \Psi(\mathbf{x}), \quad \hat{\gamma}_5 \Psi_\chi(\mathbf{x}) = \chi \Psi_\chi(\mathbf{x}). \quad (5.6)$$

The chiral components $\Psi_\chi(\mathbf{x})$ separately fulfill Eq. (5.1) which is invariant under the global gauge transformation

$$\Psi(\mathbf{x}) \rightarrow e^{i\hat{\gamma}_5 \theta} \Psi(\mathbf{x}), \quad \Psi_\chi(\mathbf{x}) \rightarrow e^{i\chi \theta} \Psi_\chi(\mathbf{x}). \quad (5.7)$$

Due to this symmetry, the corresponding charges Q_+ and Q_- , defined according to Eq. (5.3), are conserved and the charge currents $J_+^\mu(\mathbf{x})$ and $J_-^\mu(\mathbf{x})$, constructed analogously to Eq. (5.5), satisfy separate continuity equations. Consequently, the chiral charge $Q_5 \equiv \int d^3 r \Psi^\dagger(\mathbf{x}) \hat{\gamma}_5 \Psi(\mathbf{x}) = Q_+ - Q_-$ is also constant and the chiral charge current $J_5^\mu(\mathbf{x}) \equiv \Psi^\dagger(\mathbf{x}) \hat{\gamma}^0 \hat{\gamma}^\mu \hat{\gamma}_5 \Psi(\mathbf{x}) = J_+^\mu(\mathbf{x}) - J_-^\mu(\mathbf{x})$ satisfies the continuity equation

$$\frac{\partial}{\partial x^\mu} J_5^\mu(\mathbf{x}) = 0. \quad (5.8)$$

Now, a vector gauge field $A_\mu(\mathbf{x})$ is coupled to the Dirac field and Eq. (5.1) is transformed to

$$i\hat{\gamma}^\mu \left(\frac{\partial}{\partial x^\mu} + iA_\mu(\mathbf{x}) \right) \Psi(\mathbf{x}) = 0, \quad (5.9a)$$

$$i\hat{\gamma}^\mu \left(\frac{\partial}{\partial x^\mu} + iA_\mu(\mathbf{x}) \right) \Psi_\chi(\mathbf{x}) = 0. \quad (5.9b)$$

The global gauge transformations given by Eqs. (5.2) and (5.7) can be generalized to a local gauge with $\theta = \theta(\mathbf{x})$. To preserve gauge invariance of Eq. (5.9), the field $A_\mu(\mathbf{x})$ has to transform like $A_\mu(\mathbf{x}) \rightarrow A_\mu(\mathbf{x}) - \frac{\partial}{\partial x^\mu} \theta(\mathbf{x})$ [to fulfill Eq. (5.9a)] and $A_\mu(\mathbf{x}) \rightarrow A_\mu(\mathbf{x}) - \chi \frac{\partial}{\partial x^\mu} \theta(\mathbf{x})$ [to fulfill the chiral Eq. (5.9b)], respectively. This gauge symmetry leads to (chiral) charge conservation, as discussed above.

From these considerations one could conclude that the charge as well as the chiral charge remain conserved quantities and the corresponding charge currents fulfill continuity equations. This holds as long as $\Psi(\mathbf{x})$ is a classical field. However, if $\Psi(\mathbf{x})$ is a quantum field operator, the (chiral) charge and the (chiral) charge current are not well defined by Eqs. (5.3), (5.5) (and their chiral counterparts) because the fundamental quantization condition

$$\Psi_m^\dagger(t, \mathbf{r}) \Psi_n(t, \mathbf{r}') + \Psi_n(t, \mathbf{r}') \Psi_m^\dagger(t, \mathbf{r}) = \delta_{mn} \delta(\mathbf{r} - \mathbf{r}'), \quad (5.10)$$

in which m and n are the components of the field, yields singularities in the above definitions. Therefore, regularization and renormalization is necessary in order to provide a definition of the (chiral) charges and currents [169]. However, in the presence of a nonzero vector gauge field $A_\mu(\mathbf{x})$, no renormalization can be found that preserves both gauge symmetries (5.2) and (5.7). It is possible to find a renormalization that conserves either the charge or the chiral charge, but not both. Thus, assuming charge conservation, under quantization, the chiral charge Q_5 is not conserved in the presence of a vector gauge field $A_\mu(\mathbf{x})$, which is called a chiral anomaly.

5.2. Ultraquantum limit

The Landau quantization of Weyl fermions and the resulting chiral anomaly is derived, the main steps following the work of Nielsen and Ninomiya [39]. They performed the transition from the chiral anomaly in high energy physics to quasiparticles in solids.

In the following, the states in the vicinity of a pair of Weyl points with chirality $\chi = \pm 1$ centered around \mathbf{k}_W^χ are considered, described by the Weyl Hamiltonian (3.31). Now, an external magnetic field, here pointing in z -direction, $\mathbf{B} = (0, 0, B)$, is applied (here $B \geq 0$). The magnetic field couples to the electronic states via the magnetic vector potential, which is expressed using the Landau gauge, $\mathbf{A}(x) = (0, Bx, 0)$. Thus, the Hamiltonian reads

$$\hat{H} = \chi v_0 (\hat{\mathbf{p}} - \hbar \mathbf{k}_W^\chi + ex \mathbf{B} \mathbf{e}_y) \cdot \hat{\boldsymbol{\sigma}}. \quad (5.11)$$

Here, the vector potential breaks translational invariance in x -direction and k_x is not a good quantum number. The eigenfunction Ψ^χ with the eigenvalue \mathcal{E}^χ fulfills the eigenequation

$$\chi v_0 \left(\hat{\mathbf{p}} \cdot \hat{\boldsymbol{\sigma}} - \hbar \mathbf{k}_W^\chi \cdot \hat{\boldsymbol{\sigma}} + exB \hat{\sigma}_y - \chi \frac{\mathcal{E}^\chi}{v_0} \right) \Psi^\chi = 0. \quad (5.12)$$

To solve the eigenequation, the auxiliary function Φ^χ is introduced,

$$\Psi^\chi = \left(\hat{\mathbf{p}} \cdot \hat{\boldsymbol{\sigma}} - \hbar \mathbf{k}_W^\chi \cdot \hat{\boldsymbol{\sigma}} + exB \hat{\sigma}_y + \chi \frac{\mathcal{E}^\chi}{v_0} \right) \Phi^\chi. \quad (5.13)$$

Φ^χ satisfies

$$\left(\frac{(\mathcal{E}^\chi)^2}{\hbar^2 v_0^2} - \left(-i \frac{\partial}{\partial x} - k_W^\chi \right)^2 - \left(k_y - k_{W,y}^\chi + \frac{eBx}{\hbar} \right)^2 - (k_z - k_{W,z}^\chi)^2 - \frac{eB}{\hbar} \hat{\sigma}_z \right) \Phi^\chi = 0. \quad (5.14)$$

5. Chiral anomaly in Weyl semimetals

Here $\hbar k_{y,z}$, the eigenvalues of $\hat{p}_{y,z}$, are good quantum numbers and were inserted. k_z can be interpreted as the crystal momentum in z -direction, but k_y is only a good quantum number because of the chosen Landau gauge of the vector potential. Thus, k_y should not be interpreted as the crystal momentum. The \mathbf{k} -space is not well defined for three dimensions but is reduced to the k_z -direction, which is parallel to the magnetic field.

Eq. (5.14) is similar to the harmonic oscillator equation. The energy eigenvalues are

$$\mathcal{E}_{n,s_z}^{\chi,\alpha} = \alpha \sqrt{(2n+1+s_z)eB\hbar v_0^2 + v_0^2 \hbar^2 (k_z - k_{Wz}^\chi)^2} \quad (5.15)$$

with $\alpha = \pm 1$, $n = 0, 1, 2, \dots$ and $s_z = \pm 1$. The eigenfunctions Φ^χ can be found from the harmonic oscillator solutions,

$$\Phi_{n,s_z}^\chi(\mathbf{r}) = e^{ik_y y + ik_z z + ik_{Wx}^\chi x} e^{-\tilde{x}^2/2} H_n(\tilde{x}) \Upsilon(s_z) \quad (5.16)$$

with $\tilde{x} = \sqrt{\frac{eB}{\hbar}} \left(x + \frac{(k_y - k_{Wy}^\chi) \hbar}{eB} \right)$, H_n is the n th Hermite polynomial and $\Upsilon(s_z)$ is a two-component spinor eigenfunctions of $\hat{\sigma}_z$ with the eigenvalue s_z . Using Eq. (5.13), the eigenfunctions of the Weyl Hamiltonian (5.11) read

$$\begin{aligned} \Psi_{n,s_z=1}^{\chi,\alpha}(\mathbf{r}) &= e^{ik_y y + ik_z z + ik_{Wx}^\chi x} e^{-\tilde{x}^2/2} \begin{pmatrix} \left(\frac{\mathcal{E}_{n,1}^{\chi,\alpha}}{\hbar v_0 \chi} + (k_z - k_{Wz}^\chi) \right) H_n(\tilde{x}) \\ i \sqrt{\frac{eB}{\hbar}} H_{n+1}(\tilde{x}) \end{pmatrix} \frac{1}{\sqrt{N_{n,s_z=1}^{\chi,\alpha}}}, \\ \Psi_{n,s_z=-1}^{\chi,\alpha}(\mathbf{r}) &= e^{ik_y y + ik_z z + ik_{Wx}^\chi x} e^{-\tilde{x}^2/2} \begin{pmatrix} -2in H_{n-1}(\tilde{x}) \sqrt{\frac{eB}{\hbar}} \\ \left(\frac{\mathcal{E}_{n,-1}^{\chi,\alpha}}{\hbar v_0 \chi} - (k_z - k_{Wz}^\chi) \right) H_n(\tilde{x}) \end{pmatrix} \frac{1}{\sqrt{N_{n,s_z=-1}^{\chi,\alpha}}}, \end{aligned} \quad (5.17)$$

with

$$\begin{aligned} N_{n,s_z=1}^{\chi,\alpha} &= \sqrt{\frac{\hbar\pi}{eB}} \frac{2^{n+1} n! \mathcal{E}_{n,1}^{\chi,\alpha}}{\hbar^2 v_0^2} \left(\mathcal{E}_{n,1}^{\chi,\alpha} + \chi(k_z - k_{Wz}^\chi) \hbar v_0 \right), \\ N_{n,s_z=-1}^{\chi,\alpha} &= \sqrt{\frac{\hbar\pi}{eB}} \frac{2^{n+1} n! \mathcal{E}_{n,-1}^{\chi,\alpha}}{\hbar^2 v_0^2} \left(\mathcal{E}_{n,-1}^{\chi,\alpha} - \chi(k_z - k_{Wz}^\chi) \hbar v_0 \right). \end{aligned} \quad (5.18)$$

Since $\Psi_{n,s_z=1}^{\chi,\alpha} = \Psi_{n+1,s_z=-1}^{\chi,\alpha}$, only the solutions $\Psi_{n,s_z=-1}^{\chi,\alpha}$ are considered. For $(n=0, s_z=-1)$ only the energy branch $\mathcal{E}_{0,-1}^{\chi,\alpha=-\chi} = -\chi \hbar v_0 (k_z - k_{Wz}^\chi)$ exists because $\mathcal{E}_{0,-1}^{\chi,\alpha=\chi} = \chi \hbar v_0 (k_z - k_{Wz}^\chi)$ gives a vanishing wave function. Thus, each Weyl point provides a linearly dispersing chiral Landau level with the slope $-\chi \hbar v_0$.

In Fig. 5.1 the Landau levels of a pair of Weyl fermions in the presence of a magnetic field pointing in z -direction are shown. Only the chiral Landau levels intersect the former Weyl point energy $\mathcal{E} = 0$. The higher Landau levels ($n \neq 0$) provide separated electron and hole bands with an approximately linear dispersion for large k_z . The lowest (electronic) Landau level besides the chiral one ($n=1$) has its minimum at $\mathcal{E}_{n=1}^{\min} = \sqrt{2eB\hbar v_0^2}$. Thus, for Fermi energies in the energy range $-\mathcal{E}_{n=1}^{\min} < \mathcal{E}_F < \mathcal{E}_{n=1}^{\min}$, in which only the chiral Landau levels intersect the Fermi level, the transport properties have to be discussed within the ultraquantum limit.

Similarly to the Landau quantization for a free electron gas discussed in standard textbooks [48], the density of states of Landau quantized Weyl fermions is

$$\mathcal{N}(\mathcal{E}) = \frac{eB}{4\pi^2 \hbar^2 v_0} \left(1 + 2|\mathcal{E}| \sum_{n=1}^{n_{\max}} (\mathcal{E}^2 - 2\hbar v_0^2 n eB)^{-\frac{1}{2}} \right). \quad (5.19)$$

Here, the first term stems from the chiral mode and the second term corresponds to the other levels up to the highest occupied Landau level $n_{\max} = \lfloor \mathcal{E}^2 / 2eB\hbar v_0^2 \rfloor$ with $\lfloor \cdot \rfloor$ is the floor function. The density

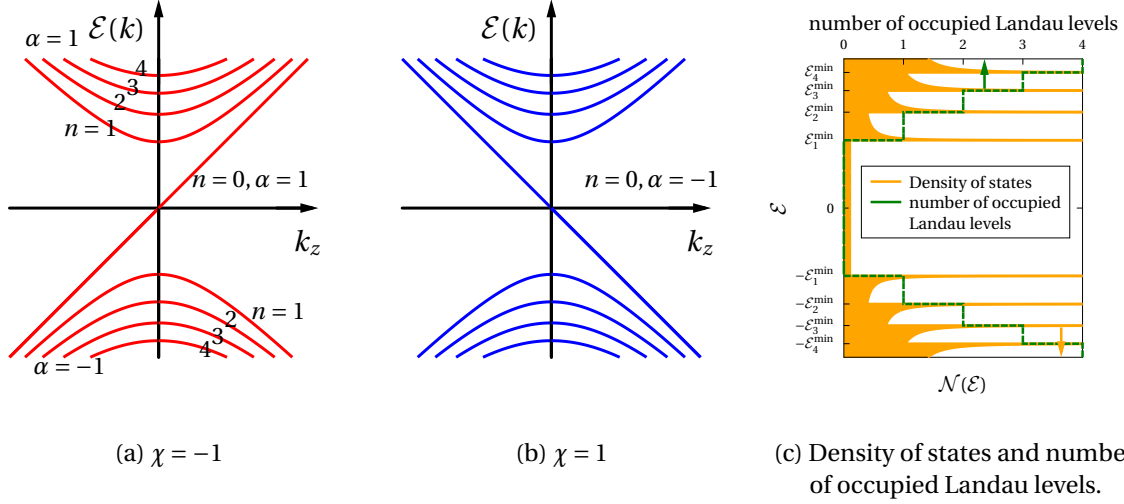


Figure 5.1.: Landau quantization of Weyl fermions with chirality $\chi = \pm 1$, $\mathbf{B} \parallel z$. The band structure (a,b) as well as the density of states (c) is shown. In addition, the number of occupied Landau levels is presented. Here, no occupied Landau levels means that only the chiral level is occupied.

of states and the number of occupied Landau levels are illustrated in Fig. 5.1(c). At the band edge of each Landau level, the DOS diverges, as in the Landau quantized free electron gas. Differently from a pure one-dimensional Weyl fermion, the “background” DOS underlying the divergences is not constant in \mathcal{E} but increases with \mathcal{E} because of the more complex band structure of the Landau levels with $n > 0$.

If an electric field $\mathbf{E} = (0, 0, E)$ is applied parallel to \mathbf{B} , the number of states with the chirality χ is changed by [39]

$$\dot{N}^\chi = \sum_{n,\alpha,k_z} \frac{\dot{f}^{\chi,\alpha,n}(k_z)}{V} = \sum_{n,\alpha,k_z} \frac{\partial f^{\chi,\alpha,n}}{\partial \mathcal{E}} \frac{\partial \mathcal{E}_n^{\chi,\alpha}(k_z)}{\partial k_z} \frac{\dot{k}_z}{V} = \frac{e^2 B}{4\pi^2 \hbar^2} \sum_{n,\alpha,k_z=k_F} \frac{v_z^{\chi,\alpha,n}(k_z)}{|v_z^{\chi,\alpha,n}(k_z)|} E \quad (5.20)$$

in which the last equation was derived using the classical equation of motion $\dot{k}_z = -e/\hbar E_z$. The contributions from the two Fermi points of the $n > 0$ levels compensate. Therefore, only the chiral Landau level contributes to \dot{N}^χ ,

$$\dot{N}^\chi = -\chi \frac{e^2 B E}{4\pi^2 \hbar^2}. \quad (5.21)$$

Thus, in a system of two Weyl points of opposite chirality, the chiral charge $Q_5 \propto N^{\chi=1} - N^{\chi=-1}$ is not conserved in the presence of nonorthogonal fields \mathbf{B} and \mathbf{E} whereas the total charge (here: number of states) $Q \propto N^{\chi=1} + N^{\chi=-1}$ is conserved. Hence, Eq. (5.21) expresses the chiral anomaly for a pair of Weyl points.

The electric charge current density generated by the electric field in the presence of a nonorthogonal magnetic field is

$$\begin{aligned} j_z^c &= \frac{e^2}{V} \sum_{\chi,n,\alpha,k_z} (v_z^{\chi,\alpha,n}(k_z))^2 \tau_{k_z}^{\chi,\alpha,n} \delta(\mathcal{E}_n^{\chi,\alpha}(k_z) - \mathcal{E}_F) E_z \\ &= \frac{e^3 B v_0}{2\pi^2 \hbar^2} \left(\tau_{k_z}^{n=0} + \frac{2}{\mathcal{E}_F} \sum_{n=1}^{n_{\max}} \tau_{k_z}^n \sqrt{\mathcal{E}_F^2 - 2neB\hbar v_0^2} \right) E_z. \end{aligned} \quad (5.22)$$

This expression can be derived using Boltzmann transport theory, as done by Nielsen and Ninomiya, [39], or via the time derivative of the expectation value of the electric polarization operator [99, 175]. In [39] the charge current is calculated for systems in which only the chiral mode is occupied. Eq. (5.22) is equivalent to the result given in [39] but also includes contributions from all other

5. Chiral anomaly in Weyl semimetals

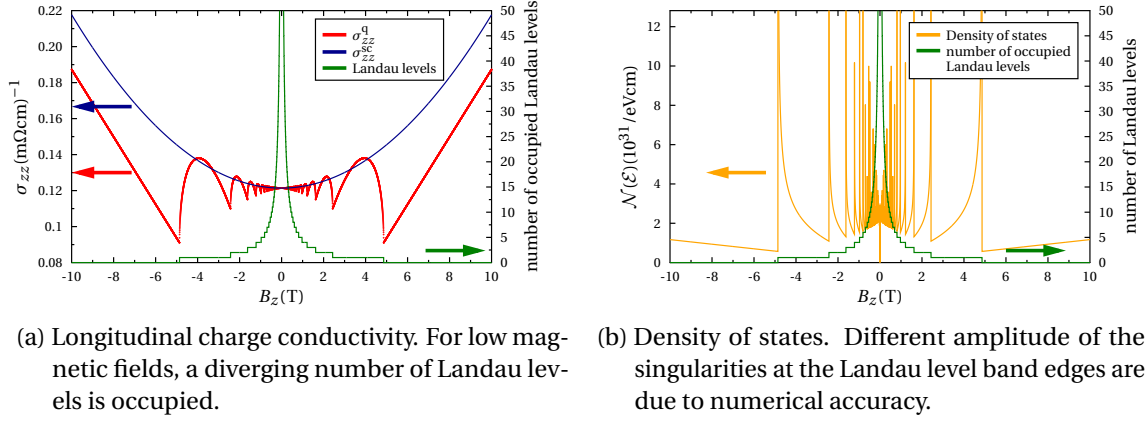


Figure 5.2.: Longitudinal charge conductivity, density of states and number of occupied Landau levels of a system of two Weyl points as a function of the magnetic field. Here $\mathcal{E}_F = 8\text{meV}$, $\nu_0 = 10^5\text{ms}^{-1}$ and $\tau_0 = 1\text{ps}$. For comparison, the conductivity in the semiclassical limit is shown.

occupied Landau levels.

In the following, only the diagonal element σ_{zz}^q of the conductivity tensor, which is in the direction of the magnetic field and therefore called *longitudinal charge conductivity*, will be discussed since this component is remarkably changed by the presence of the magnetic field $\mathbf{B} = (0, 0, B)$ and is considered an experimentally observable signature of the chiral anomaly. The index “q” stands for “quantum limit”. The magnetic field and energy dependence of the longitudinal charge conductivity can be discussed assuming a constant momentum relaxation time, $\tau_{k_z}^{\chi, \alpha, n} = \tau_0$ or as a (χ, α, n, k_z) -dependent quantity according to the formalism introduced in section 2.5. The results for both approaches will be presented in the following.

5.2.1. Constant relaxation time

The chiral anomaly is often discussed within a constant relaxation time approximation. Although the intra- and inter-cone momentum relaxation times are considered different, both enter the expressions for the conductivity as parameters [39]. In this section, the longitudinal charge conductivity is calculated assuming a single momentum relaxation time τ for both intra- and inter-cone scattering.

In Fig. 5.2(a) the B -dependent longitudinal charge conductivity σ_{zz}^q is shown for a system of two Weyl cones. For comparison, σ_{zz}^{sc} calculated in the semiclassical limit (discussed in section 5.3, Eq. (5.34)) is presented. In addition, the number of occupied Landau levels is depicted.

For low magnetic fields, the Landau levels are close to each other, many bands are occupied and the longitudinal charge conductivity is well approximated by σ_{zz}^{sc} , which scales $\propto B^2$. If the magnetic field is increased, the distance between neighboring Landau levels gets larger. Less bands intersect the Fermi level and contribute to the transport. When the band edge of a Landau level passes the Fermi energy, the density of states, which is shown in Fig. 5.2(b), has a singularity. The conductivity is sharply reduced due to the low electron velocity near the band edges. When the band edge of the n th level has passed the Fermi level, the conductivity is enhanced due to the filling factor of the remaining bands, $g = \frac{eBL_x L_y}{2\pi\hbar}$ increasing linearly with B . Thus, the oscillations of the charge conductivity shown in Fig. 5.2 are explained by the varying number of levels intersecting the Fermi energy, the B -dependent electron dynamics, i.e. the group velocity, as well as the filling factor. The amplitude of these oscillations scales approximately with B^2 , which is consistent with the semiclassical limit. For magnetic fields $B > B_1^{\text{min}} = \frac{\mathcal{E}_F^2}{2e\hbar\nu_0}$ the $n = 1$ Landau level is raised above the Fermi level and only the chiral modes are occupied and contribute to the charge conductivity which increases linearly with B .

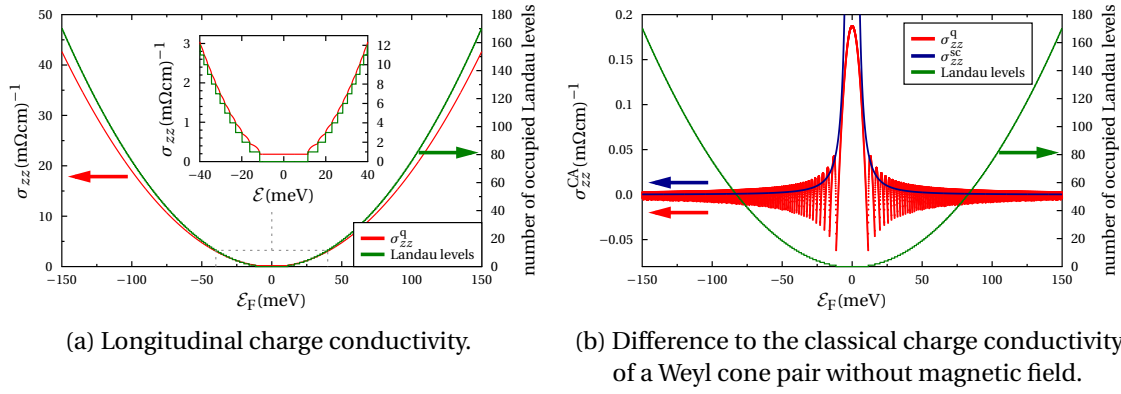


Figure 5.3.: Charge conductivity of a Weyl cone pair in the presence of a magnetic field $B = 10\text{T}$, $v_0 = 10^5\text{m s}^{-1}$ and $\tau_0 = 1\text{ps}$. The right panel shows the difference to the classical charge conductivity without a magnetic field.

In Fig. 5.3 the longitudinal charge conductivity is shown as a function of the Fermi level for constant B . As displayed in the inset of Fig. 5.3(a), for low Fermi energies only the chiral Landau level is occupied and the charge conductivity is constant in energy. With increasing Fermi level more Landau levels are occupied, leading to a stepwise increase of the charge conductivity. The energy dependence becomes smoother at higher energies since the Landau level separation is reduced.

For large Fermi energies the system can also be described in the semiclassical limit, as discussed in section 5.3. Here, the charge conductivity exhibits a dependence $\propto \mathcal{E}_F^2$, as for a pair of Weyl cones without any magnetic field, $\sigma_{zz}^{\text{cl}}(B=0) = \frac{e^2 \tau \mathcal{E}_F^2}{3\pi^2 \hbar^3 v_0}$, because the conventional charge conductivity, which is the charge conductivity not originating from the chiral anomaly, dominates here.

In order to demonstrate the influence of the magnetic field, the additional chiral-anomaly-related contribution $\sigma_{zz}^{\text{CA}} = \sigma_{zz}^{\text{q}}(B) - \sigma_{zz}^{\text{cl}}(B=0)$, called *chiral conductivity*, which is the difference between the charge conductivity from Eq. (5.22) and the classical charge conductivity for $B=0$, is shown in in Fig. 5.3(b). The oscillations due to the discretely increasing number of Landau levels are clearly visible. The amplitude of the oscillations decreases with the Fermi energy, as expected in the semiclassical limit. For comparison, the chiral conductivity in the semiclassical limit is sketched which scales with $\propto \mathcal{E}_F^{-2}$ and approximates the conductivity in the Landau quantized system well for high energies.

For low energies at which only the $n=0$ level is occupied, the chiral conductivity decreases with \mathcal{E} although the total charge conductivity is constant with respect to \mathcal{E} . The reason for this counterintuitive energy dependence is the classical zero-field conductivity $\sigma_{zz}^{\text{cl}}(B=0)$ scaling with $\propto \mathcal{E}_F^2$ and therefore σ_{zz}^{CA} decreasing with $\propto -\mathcal{E}_F^2$.

In Fig. 5.4(a) the chiral conductivity is shown as a function of B and \mathcal{E}_F . If the Fermi energy is below the $n=1$ Landau level, $\mathcal{E}_F < \mathcal{E}_1^{\text{min}} = \sqrt{2eB\hbar v_0^2}$, the system is in the ultraquantum limit. Only the chiral mode is occupied and contributes to the transport. The chiral conductivity increases linearly with B and decreases with \mathcal{E}_F , as discussed above.

For large Fermi energies and low magnetic fields, many Landau levels are occupied and the system can be considered semiclassically. In general, the conductivity increases with B and decreases with \mathcal{E}_F , what is not clearly visible in Fig. 5.4(a) because of the large conductivity scale.

In this intermediate regime with a medium number of occupied Landau levels, the longitudinal charge conductivity is not always enhanced due to the magnetic field, but changes sign due to the oscillations induced by the discrete number of occupied Landau levels.

Usually, when the chiral anomaly is discussed, not the longitudinal charge conductivity but the longitudinal magnetoresistance MR_{\parallel} is considered and examined experimentally. Here, *longitu-*

5. Chiral anomaly in Weyl semimetals

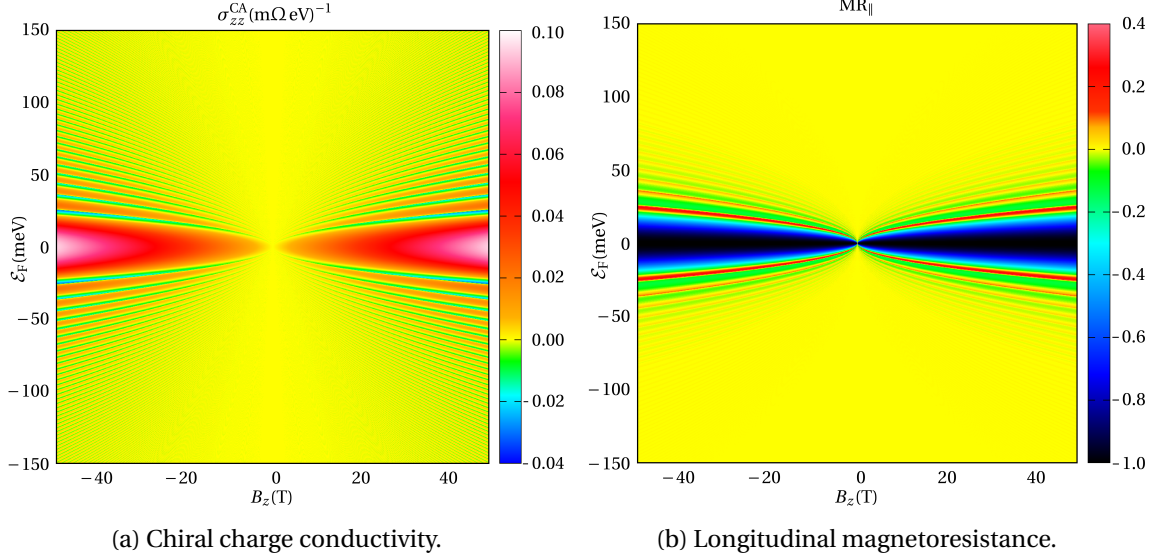


Figure 5.4.: Chiral charge conductivity and longitudinal magnetoresistance as a function of \mathcal{E}_F and B . The model parameters are the same as above.

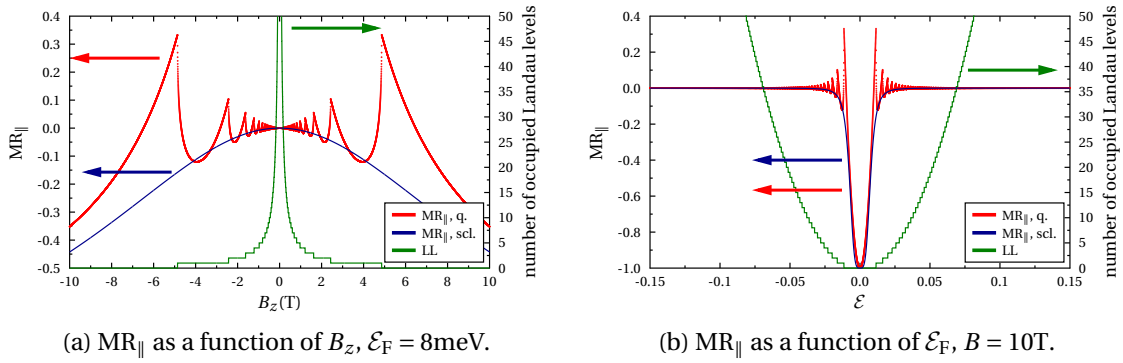


Figure 5.5.: Longitudinal magnetoresistance $MR_{||}$ calculated in the quantum limit (red) as well as the semiclassical limit (scl., blue). In addition, the number of occupied Landau levels (LL) is shown. The model parameters are the same as above for the discussion of the charge conductivity.

dinal refers to the magnetoresistance with respect to the direction of the magnetic field. In the quasi-one-dimensional Landau system, it reads

$$MR_{||} = \frac{\rho_{zz}(B) - \rho_{zz}(B=0)}{\rho_{zz}(B=0)} = \frac{\sigma_{zz}^{cl}(0) - \sigma_{zz}^q(B)}{\sigma_{zz}^q(B)} = -\frac{\sigma_{zz}^{CA}(B)}{\sigma_{zz}^q(B)}. \quad (5.23)$$

Its discussion has the advantage that $MR_{||}$ is independent of specific material parameters which enter $\sigma_{zz}^{CA}(B)$ and $\sigma_{zz}^q(B)$ the same way, e.g. the momentum relaxation time.

In Fig. 5.4(b) the longitudinal magnetoresistance is shown as a function of B and \mathcal{E}_F . As for the chiral conductivity shown in Fig. 5.4(a), different regions corresponding to the ultraquantum and semiclassical limit as well as an intermediate region can be identified.

Fig. 5.5 depicts the longitudinal magnetoresistance as a function of the magnetic field and the Fermi level, respectively. In the limit of low magnetic field and large Fermi level, the amplitudes of the oscillating curves are well approximated by $MR_{||}$ calculated in the semiclassical limit (discussed in section 5.3). In the ultraquantum limit, the magnetoresistance is clearly negative yielding the NLMR as significant property of a Weyl semimetal. However, when a larger finite number of Landau levels is occupied, the longitudinal magnetoresistance is not in general negative but oscillates and

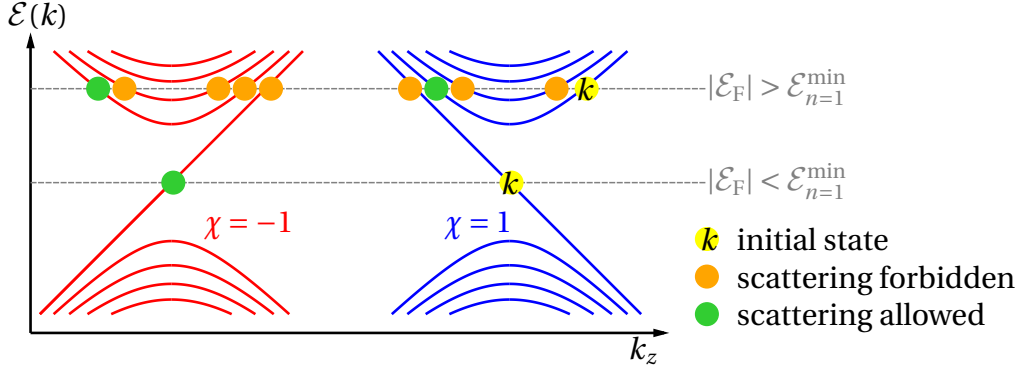


Figure 5.6.: Allowed and forbidden elastic scattering processes within a pair of Landau quantized Weyl cones for two exemplarily chosen initial state, which are shown as yellow circles at different energies. The impurity potential is assumed δ -shaped. Scattering is allowed only between Landau levels with the same index n . Further, no scattering occurs between states with $\chi' = -\chi \wedge \Delta k'_z = \Delta k_z$. The possible scattering processes for both energies are sketched. If $|\mathcal{E}_F| < \mathcal{E}_{n=1}^{\min}$, only the chiral modes ($n = 0$) are occupied and scattering is allowed between the states with different chirality, the approach of δ -shaped impurities is reasonable here. For $|\mathcal{E}_F| \geq \mathcal{E}_{n=1}^{\min}$, only a very limited number of scattering events is allowed due to the δ -shape of the impurity potentials.

changes its sign, similarly to the chiral charge conductivity.

5.2.2. \mathcal{E} -, \mathbf{B} - and \mathbf{k} -dependent momentum relaxation time

In the previous section, the momentum relaxation time was assumed independent of the crystal momentum, the energy and the magnetic field. However, a \mathbf{k} -dependent momentum relaxation time can remarkably affect the macroscopic transport properties. Therefore, the momentum relaxation time of Landau quantized Weyl cones is calculated using the scattering theory introduced in section 2.5, which includes \mathbf{k} -, \mathcal{E} - and \mathbf{B} -dependencies.

Since the eigenstates given by Eq. (5.17) are no Bloch waves and the chosen Landau gauge leads to a specific spatial dependence of the eigenstates, the transition matrix $T_{\mathbf{k}' \leftarrow \mathbf{k}}^i$, corresponding to an impurity located at \mathbf{r}_i , also sustains a dependence on the impurity's real-space coordinates. Therefore, an averaged $\bar{T}_{\mathbf{k}' \leftarrow \mathbf{k}}$ is calculated, including all impurity positions.

Assuming δ -shaped impurity potentials, using the averaged transition matrices $\bar{T}_{\mathbf{k}' \leftarrow \mathbf{k}}$, and Fermi's golden rule (2.72), the microscopic transition probabilities read

$$P_{k'_z \leftarrow k_z}^{n' \leftarrow n} = \frac{2\pi c_1 U_0^2}{\hbar N_{\text{at}}} \delta_{nn'} \delta(\mathcal{E}_n^\chi(k_z) - \mathcal{E}_{n'}^{\chi'}(k'_z)) \begin{cases} 1, & \chi' = \chi \wedge \Delta k'_z = \Delta k_z \\ \frac{2neB\hbar v_0^2}{\mathcal{E}^2}, & \chi' = \chi \wedge \Delta k'_z = -\Delta k_z \\ 0, & \chi' = -\chi \wedge \Delta k'_z = \Delta k_z \\ \frac{\Delta k_z^2 \hbar^2 v_0^2}{\mathcal{E}^2}, & \chi' = -\chi' \wedge \Delta k'_z = -\Delta k_z \end{cases} \quad (5.24)$$

with $\Delta k_z = k_z - k_{\text{Wz}}^\chi$. Thus, only scattering processes between Landau levels with identical quantum number n provide a nonzero transition probability, (Fig. 5.6) because the wave functions are Hermitian polynomials and therefore orthogonal if $n' \neq n$. Further, scattering is also suppressed between states with $\chi = -\chi' \wedge \Delta k'_z = \Delta k_z$ since these states are also orthogonal. The momentum relaxation time reads

$$\tau^n(\mathcal{E}, B) = \frac{\hbar^3 \pi v_0 \sqrt{\mathcal{E}^2 - 2neB\hbar v_0^2}}{eBV_0 c_1 |U_0|^2 |\mathcal{E}|}. \quad (5.25)$$

For $|\mathcal{E}_F| < \mathcal{E}_{n=1}^{\min} = \sqrt{2eB\hbar v_0^2}$, only the $n = 0$ level is occupied, scattering processes can occur only

5. Chiral anomaly in Weyl semimetals

between the linear modes of opposite chirality, the δ -impurity approximation is a reasonable approach. Here, $\tau \propto B^{-1}$. The longitudinal charge conductivity parallel to the magnetic field is

$$\sigma_{zz} = \frac{e^2 v_0^2 \hbar}{4\pi V_0 c_i |U_0|^2}, \quad |\mathcal{E}_F| < \mathcal{E}_{n=1}^{\min}. \quad (5.26)$$

Thus, in the limit of low energies, the charge conductivity is independent of the magnetic field. This finding agrees with that of Nielsen and Ninomiya [39], although in their work the impurities are approximated as screened Coulomb potentials. The B -dependence of the momentum relaxation time is often not considered in the discussion of the chiral anomaly in the ultraquantum limit. The often discussed linear B -dependence of the charge conductivity is valid only in the limit of constant momentum relaxation time, which was considered in the previous section.

If $|\mathcal{E}_F| \geq \mathcal{E}_{n=1}^{\min}$, the number of allowed scattering processes is strongly limited due to the δ -impurity potentials suppressing scattering between Landau levels with different quantum number n . This behavior does not approach the semiclassical limit, in which elastic scattering processes can occur between nearly all states on an iso-energy surface. For extended scattering potentials, e.g. the screened Coulomb potential considered in the work of Nielsen and Ninomiya [39], or higher-order Born approximation, more transitions would be allowed and the transition probabilities would approach the semiclassical limit. However, the focus of this section is on the ultraquantum limit in which only the chiral modes are occupied. Here, the δ -impurity approximation is applicable and predicts a B -independent charge conductivity, which was also observed experimentally in Na₃Bi in the limit of high magnetic fields [170].

5.3. Semiclassical limit

In the limit of small magnetic fields and relatively large Fermi energies, the Landau levels are dense in energy. The system can be considered semiclassically, which was done first by Son and Spivak for a pair of isotropic Weyl cones [41, 176] described by two copies of the Weyl Hamiltonian (3.31). The following derivation of the chiral anomaly is not restricted to the isotropic Weyl Hamiltonian but holds for any Hamiltonian for one or more pairs of Weyl points.

In the semiclassical approach, the influence of the magnetic field on the electronic ground states is neglected, the band structure and related properties are unaffected by \mathbf{B} . Using the semiclassical equations of motion (2.29a) and (2.29b) in the Boltzmann equation (2.33) yields

$$\begin{aligned} \frac{\partial f_{\mathbf{k}}(\mathbf{r}, t)}{\partial t} + \left(1 + \frac{e}{\hbar} \mathbf{B} \cdot \mathbf{\Omega}_{\mathbf{k}}\right)^{-1} \left[\frac{1}{\hbar} \left(-e\mathbf{E} - e\mathbf{v}_{\mathbf{k}} \times \mathbf{B} + \frac{e^2}{\hbar} (\mathbf{E} \cdot \mathbf{B}) \mathbf{\Omega}_{\mathbf{k}}\right) \frac{\partial f_{\mathbf{k}}(\mathbf{r}, t)}{\partial \mathbf{k}} \right. \\ \left. + \left(\mathbf{v}_{\mathbf{k}} + \frac{e}{\hbar} \mathbf{E} \times \mathbf{\Omega}_{\mathbf{k}} + \frac{e}{\hbar} (\mathbf{\Omega}_{\mathbf{k}} \cdot \mathbf{v}_{\mathbf{k}}) \mathbf{B}\right) \frac{\partial f_{\mathbf{k}}(\mathbf{r}, t)}{\partial \mathbf{r}} \right] = \left(\frac{\partial f_{\mathbf{k}}(\mathbf{r}, t)}{\partial t}\right)_{\text{scatt}}. \end{aligned} \quad (5.27)$$

In order to calculate the cone-dependent distribution function, which does not depend on \mathbf{k} but on the energy and the chirality of the Weyl cone, Eq. (5.27) is averaged on an iso-energy surface of a Weyl cone with chirality χ ,

$$\frac{\partial f^{\chi}(\mathcal{E})}{\partial t} + \frac{1}{\mathcal{N}(\mathcal{E})} \left(\frac{e^2 \chi (\mathbf{E} \cdot \mathbf{B})}{4\pi^2 \hbar^2} \frac{\partial f(\mathcal{E})}{\partial \mathcal{E}} + \frac{\partial \mathbf{j}^{\chi}(\mathcal{E})}{\partial \mathbf{r}} \right) = \left(\frac{\partial f_{\mathbf{k}}(\mathcal{E})}{\partial t}\right)_{\text{scatt}}. \quad (5.28)$$

Here, $\frac{\partial f_{\mathbf{k}}(\mathbf{r}, t)}{\partial \mathbf{k}} = \hbar \mathbf{v}_{\mathbf{k}} \frac{\partial f(\mathcal{E})}{\partial \mathcal{E}}$ was approximated neglecting the \mathbf{k} -dependence of the distribution function in each cone. The particle current density $\mathbf{j}^{\chi}(\mathcal{E})$ of states with chirality χ is

$$\mathbf{j}^{\chi}(\mathcal{E}) = \frac{1}{V} \sum_{\mathbf{k} \in \chi} \left(1 + \frac{e}{\hbar} \mathbf{B} \cdot \mathbf{\Omega}_{\mathbf{k}}\right)^{-1} \left(\mathbf{v}_{\mathbf{k}} + \frac{e}{\hbar} \mathbf{E} \times \mathbf{\Omega}_{\mathbf{k}} + \frac{e}{\hbar} (\mathbf{\Omega}_{\mathbf{k}} \cdot \mathbf{v}_{\mathbf{k}}) \mathbf{B}\right) f_{\mathbf{k}}(\mathbf{r}, t) \delta(\mathcal{E}_{\mathbf{k}} - \mathcal{E}). \quad (5.29)$$

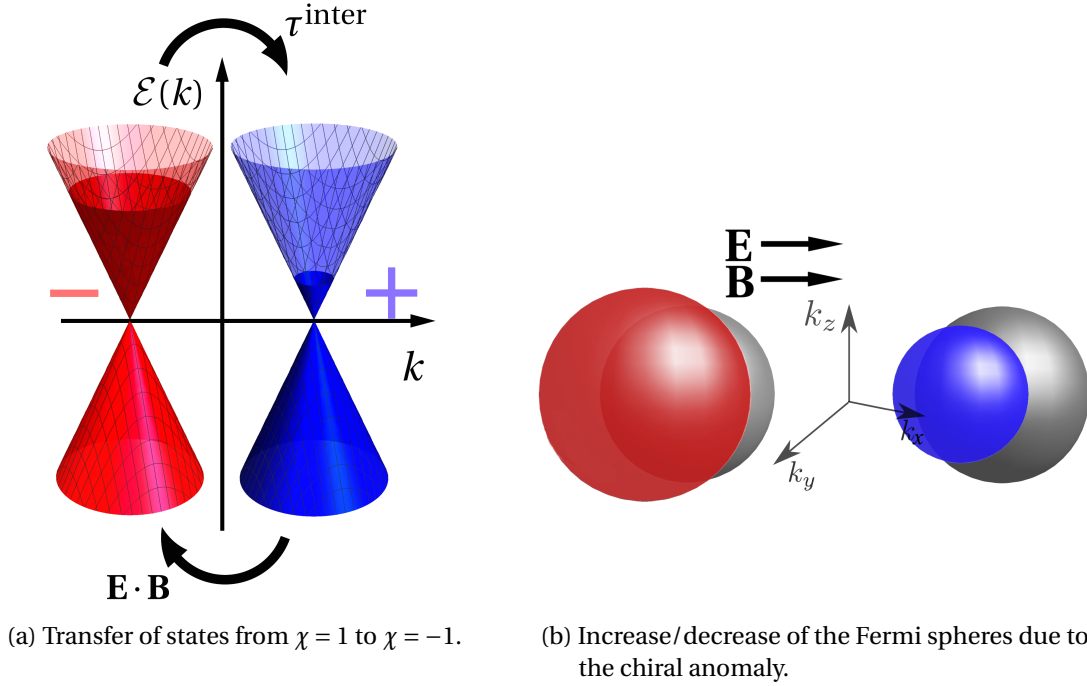


Figure 5.7.: Chiral anomaly in the semiclassical limit. The number of states in each Weyl cone is not conserved, states are transferred from one cone to the other (a). Thus, the chiral charge of the system is not conserved. In addition, scattering occurs between the Weyl cones. The chiral anomaly can be interpreted as a cone-dependent shift of the Fermi level or a change of size of the Fermi spheres (b).

Integrating over the energy and using a relaxation time approximation yields the continuity equation

$$\frac{\partial N^\chi}{\partial t} + \frac{\partial \mathbf{j}^\chi}{\partial \mathbf{r}} = -\chi \frac{e^2}{4\pi^2 \hbar^2} (\mathbf{E} \cdot \mathbf{B}) - \frac{\delta N^\chi}{\tau^{\text{inter}}}. \quad (5.30)$$

Here, N^χ is the particle density in the Weyl cone χ . The scattering term $\frac{\delta N^\chi}{\tau^{\text{inter}}}$ includes scattering processes between the Weyl cones, τ^{inter} is the averaged inter-cone scattering time. For $\chi \neq 0$ and nonorthogonal electric and magnetic fields, the continuity equation contains an additional source term $-\chi \frac{e^2}{4\pi^2 \hbar^2} (\mathbf{E} \cdot \mathbf{B})$, thus Eq. (5.30) expresses the chiral anomaly in the semiclassical limit and is equivalent to Eq. (5.21) in the quantum limit. By summation over all Weyl cones the source term vanishes. The total charge of the system is conserved but the chiral charge is not. Fig. 5.7(a) visualizes the transfer of states from one chirality to the other due to the chiral anomaly.

For the calculation of the experimentally accessible additional contribution to the longitudinal charge conductivity, the linearized Boltzmann equation (2.40) is solved. In a first approximation, the Lorentz force term is neglected and a relaxation time approximation with the momentum relaxation time is used. Neglecting the Lorentz term and the scattering-in terms, which is usually done when the chiral anomaly is discussed in the semiclassical Boltzmann theory [41, 176–179], is sufficient as long as only the longitudinal charge conductivity is calculated. For the calculation of transversal transport properties, including the Lorentz force is crucial, which will be demonstrated in section 5.5. Within this approximation, the Boltzmann equation can be solved analytically and the distribution function reads

$$f_{\mathbf{k}} = f_{\mathbf{k}}^0 + \frac{\partial f_{\mathbf{k}}^0}{\partial \mathcal{E}} e \Lambda_{\mathbf{k}} \cdot \mathbf{E} = f_{\mathbf{k}}^0 + \frac{\partial f_{\mathbf{k}}^0}{\partial \mathcal{E}} e \tau_{\mathbf{k}} \left(1 + \frac{e}{\hbar} \mathbf{B} \cdot \boldsymbol{\Omega}_{\mathbf{k}} \right)^{-1} \left[\mathbf{v}_{\mathbf{k}} + \frac{e}{\hbar} (\boldsymbol{\Omega}_{\mathbf{k}} \cdot \mathbf{v}_{\mathbf{k}}) \mathbf{B} \right] \cdot \mathbf{E}. \quad (5.31)$$

The term $\propto \mathbf{v}_{\mathbf{k}}$ on the right-hand side can be interpreted as a shift of the Fermi surfaces in \mathbf{k} -space,

5. Chiral anomaly in Weyl semimetals

the term $\propto (\mathbf{\Omega}_{\mathbf{k}} \cdot \mathbf{v}_{\mathbf{k}}) \mathbf{B}$ is interpreted as an increase ($\chi = -1$) or a decrease ($\chi = +1$) of the Fermi spheres, as visualized in Fig. 5.7(b). The electric charge current density is

$$\begin{aligned} \mathbf{j}^c &= -\frac{e}{V} \sum_{\mathbf{k}} \mathbf{r}_{\mathbf{k}} f_{\mathbf{k}} \\ &= -\frac{e}{V} \sum_{\mathbf{k}} \frac{[\mathbf{v}_{\mathbf{k}} + \frac{e}{\hbar} \mathbf{E} \times \mathbf{\Omega}_{\mathbf{k}} + \frac{e}{\hbar} (\mathbf{\Omega}_{\mathbf{k}} \cdot \mathbf{v}_{\mathbf{k}}) \mathbf{B}]}{(1 + \frac{e}{\hbar} \mathbf{B} \cdot \mathbf{\Omega}_{\mathbf{k}})} \left\{ f_{\mathbf{k}}^0 - e\tau_{\mathbf{k}} \frac{[\mathbf{v}_{\mathbf{k}} \cdot \mathbf{E} + \frac{e}{\hbar} (\mathbf{\Omega}_{\mathbf{k}} \cdot \mathbf{v}_{\mathbf{k}}) \mathbf{B} \cdot \mathbf{E}]}{(1 + \frac{e}{\hbar} \mathbf{B} \cdot \mathbf{\Omega}_{\mathbf{k}})} \delta(\mathcal{E}_{\mathbf{k}} - \mathcal{E}_{\text{F}}) \right\}. \end{aligned} \quad (5.32)$$

This expression is split into several contributions,

$$\mathbf{j}_{\text{eq}}^c = -\frac{e}{V} \sum_{\mathbf{k}} \left(1 + \frac{e}{\hbar} \mathbf{B} \cdot \mathbf{\Omega}_{\mathbf{k}}\right)^{-1} \mathbf{v}_{\mathbf{k}} f_{\mathbf{k}}^0, \quad (5.33a)$$

$$\mathbf{j}_{\text{AHE}}^c = -\frac{e^2}{\hbar V} \sum_{\mathbf{k}} \left(1 + \frac{e}{\hbar} \mathbf{B} \cdot \mathbf{\Omega}_{\mathbf{k}}\right)^{-1} \mathbf{E} \times \mathbf{\Omega}_{\mathbf{k}} f_{\mathbf{k}}^0, \quad (5.33b)$$

$$\mathbf{j}_{\text{CME}}^c = -\frac{e^2}{\hbar V} \sum_{\mathbf{k}} \left(1 + \frac{e}{\hbar} \mathbf{B} \cdot \mathbf{\Omega}_{\mathbf{k}}\right)^{-1} (\mathbf{\Omega}_{\mathbf{k}} \cdot \mathbf{v}_{\mathbf{k}}) \mathbf{B} f_{\mathbf{k}}^0, \quad (5.33c)$$

$$\mathbf{j}_{\text{cl}}^c = \frac{e^2}{V} \sum_{\mathbf{k}} \left(1 + \frac{e}{\hbar} \mathbf{B} \cdot \mathbf{\Omega}_{\mathbf{k}}\right)^{-2} \tau_{\mathbf{k}} \mathbf{v}_{\mathbf{k}} (\mathbf{v}_{\mathbf{k}} \cdot \mathbf{E}) \delta(\mathcal{E}_{\mathbf{k}} - \mathcal{E}_{\text{F}}), \quad (5.33d)$$

$$\mathbf{j}_{\text{linI}}^c = \frac{e^3}{\hbar V} \sum_{\mathbf{k}} \left(1 + \frac{e}{\hbar} \mathbf{B} \cdot \mathbf{\Omega}_{\mathbf{k}}\right)^{-2} \tau_{\mathbf{k}} \mathbf{v}_{\mathbf{k}} (\mathbf{\Omega}_{\mathbf{k}} \cdot \mathbf{v}_{\mathbf{k}}) (\mathbf{B} \cdot \mathbf{E}) \delta(\mathcal{E}_{\mathbf{k}} - \mathcal{E}_{\text{F}}), \quad (5.33e)$$

$$\mathbf{j}_{\text{2nda}}^c = \frac{e^3}{\hbar V} \sum_{\mathbf{k}} \left(1 + \frac{e}{\hbar} \mathbf{B} \cdot \mathbf{\Omega}_{\mathbf{k}}\right)^{-2} \tau_{\mathbf{k}} (\mathbf{E} \times \mathbf{\Omega}_{\mathbf{k}}) (\mathbf{v}_{\mathbf{k}} \cdot \mathbf{E}) \delta(\mathcal{E}_{\mathbf{k}} - \mathcal{E}_{\text{F}}), \quad (5.33f)$$

$$\mathbf{j}_{\text{linII}}^c = \frac{e^3}{\hbar V} \sum_{\mathbf{k}} \left(1 + \frac{e}{\hbar} \mathbf{B} \cdot \mathbf{\Omega}_{\mathbf{k}}\right)^{-2} \tau_{\mathbf{k}} (\mathbf{\Omega}_{\mathbf{k}} \cdot \mathbf{v}_{\mathbf{k}}) (\mathbf{v}_{\mathbf{k}} \cdot \mathbf{E}) \mathbf{B} \delta(\mathcal{E}_{\mathbf{k}} - \mathcal{E}_{\text{F}}), \quad (5.33g)$$

$$\mathbf{j}_{\text{2ndb}}^c = \frac{e^4}{\hbar^2 V} \sum_{\mathbf{k}} \left(1 + \frac{e}{\hbar} \mathbf{B} \cdot \mathbf{\Omega}_{\mathbf{k}}\right)^{-2} \tau_{\mathbf{k}} (\mathbf{E} \times \mathbf{\Omega}_{\mathbf{k}}) (\mathbf{\Omega}_{\mathbf{k}} \cdot \mathbf{v}_{\mathbf{k}}) (\mathbf{E} \cdot \mathbf{B}) \delta(\mathcal{E}_{\mathbf{k}} - \mathcal{E}_{\text{F}}), \quad (5.33h)$$

$$\mathbf{j}_{\text{CA}}^c = \frac{e^4}{\hbar^2 V} \sum_{\mathbf{k}} \left(1 + \frac{e}{\hbar} \mathbf{B} \cdot \mathbf{\Omega}_{\mathbf{k}}\right)^{-2} \tau_{\mathbf{k}} (\mathbf{\Omega}_{\mathbf{k}} \cdot \mathbf{v}_{\mathbf{k}})^2 (\mathbf{E} \cdot \mathbf{B}) \mathbf{B} \delta(\mathcal{E}_{\mathbf{k}} - \mathcal{E}_{\text{F}}). \quad (5.33i)$$

Eq. (5.33a) is an equilibrium contribution and vanishes for symmetry reasons. Eq. (5.33b) corresponds to the anomalous Hall effect. It vanishes for systems with time-reversal symmetry and for the isotropic model Hamiltonian. The third term, Eq. (5.33c), corresponds to a charge current parallel to a magnetic field which exists even in the absence of an electric field, called equilibrium chiral magnetic effect. It vanishes in systems with inversion or time-reversal symmetry but could formally exist when both symmetries are broken. The existence of this equilibrium current is controversially discussed [96, 180–183], although it has been shown that it is forbidden by gauge symmetry [184, 185]. The conventional charge current is expressed by Eq. (5.33d), called *classical* in the following. Eqs. (5.33e) and (5.33g) scale approximately linearly with B and exist only in systems with nonzero Berry curvature. They have also been discussed in Refs. [177–179] for systems with broken time-reversal symmetry. They seem to vanish for time-reversal invariant systems and the isotropic model Hamiltonian, but due to the phase-space correction factor, a finite contribution is possible also in time-reversal symmetric systems as well as the isotropic system. Eqs. (5.33f) and (5.33h) are of second order in \mathbf{E} and will not be discussed in this linear approach. The term usually related to as the chiral anomaly contribution to the charge current is Eq. (5.33i). It scales with B^2 , in contrast to the ultraquantum limit, in which the additional charge conductivity increases with B . Since $\mathbf{\Omega}_{\mathbf{k}} \cdot \mathbf{v}_{\mathbf{k}}$ enters Eq. (5.33i) quadratically, even systems with $\chi = 0$ at the Fermi surface could give a finite contribution, as long as they provide a nonzero Berry curvature.

Approximating $(1 + \frac{e}{\hbar} \mathbf{B} \cdot \mathbf{\Omega}_{\mathbf{k}}) \approx 1$ and assuming $\mathbf{B} \parallel z$, the charge conductivity for a pair of isotropic

Weyl cones with $\chi = \pm 1$ is

$$\sigma_{ij}^{\text{sc}} = \sigma_{ij}^{\text{cl}} + \sigma_{ij}^{\text{sc,CA}} = \frac{e^2 \tau_0(\mathcal{E}_F) \mathcal{E}_F^2}{3\pi^2 \hbar^3 v_0} \delta_{ij} + \frac{e^4 v_0^3 B^2 \tau_0(\mathcal{E}_F)}{4\pi^2 \hbar \mathcal{E}_F^2} \delta_{ij} \delta_{iz}. \quad (5.34)$$

The momentum relaxation time τ_0 is isotropic but energy dependent, (2.73),

$$\tau_0(\mathcal{E}) = \frac{\pi \hbar^4 v_0^3}{|U|^2 c_i V_0 \mathcal{E}^2}. \quad (5.35)$$

Thus, within the isotropic Weyl model, the longitudinal classical charge conductivity is constant in energy. The reduced DOS near the Weyl points is compensated by an enhanced momentum relaxation time due to the reduced phase space for scattering. The chiral-anomaly-related contribution scales with \mathcal{E}_F^{-4} , in contrast to the \mathcal{E}_F^{-2} -dependence usually discussed in literature [26, 41] due to the energy dependence of τ_0 . Including the phase-space correction factor would induce anisotropies of the momentum relaxation time and therefore modify the results for σ_{ii}^{cl} and σ_{zz}^{CA} as well as allow nonzero terms $\hat{\sigma}^{\text{linI}}$ and $\hat{\sigma}^{\text{linII}}$.

In the isotropic model, the direction of the magnetic field with respect to the Weyl point separation direction in \mathbf{k} -space is not relevant. The diagonal element of the charge conductivity tensor parallel to the direction of \mathbf{B} is constant when \mathbf{B} is rotated.

The Lorentz force, which was neglected in the previous discussion, forces the electrons to move on cyclotron orbits on the Fermi surface [186]. Therefore, including the Lorentz force term would drastically influence the transversal elements of the conductivity tensor and diagonal elements corresponding to a charge current not aligned with \mathbf{B} . In addition, it also can influence the components in the direction of the magnetic field (σ_{zz}) because the longitudinal mean free path of the electrons is reduced by the transversal Lorentz force. It turns out that for the isotropic model Hamiltonian, the influence of the Lorentz force on the longitudinal charge conductivity component σ_{zz} is negligible for symmetry reasons.

The longitudinal magnetoresistance resulting from the additional contribution to the charge conductivity in Eq. (5.34) reads

$$\text{MR}_{\parallel} = -\frac{3e^2 v_0^4 \hbar^2 B^2}{4\mathcal{E}_F^4 + 3e^2 v_0^4 B^2 \hbar^2}. \quad (5.36)$$

Although the energy dependence of the charge conductivity is strongly influenced by the \mathcal{E} -dependent momentum relaxation time, the longitudinal magnetoresistance is independent of τ since in the isotropic model the classical as well as chiral conductivity are affected equally by τ . Therefore, MR_{\parallel} is an appropriate quantity for comparing the results of different approximations as well as experimental data. The longitudinal magnetoresistance as a function of the magnetic field and the Fermi level is shown in Fig. 5.5 on page 84. In the semiclassical limit, it is always negative with its absolute value strongly increasing with B and decreasing \mathcal{E} .

5.4. Experimental evidence of the chiral anomaly

Although the chiral anomaly itself is not directly observable, its influence on the transport properties, which becomes manifest as a negative longitudinal magnetoresistance, is very promising, especially from an experimental point of view, since it provides the opportunity of identifying Weyl semimetal candidates by resistivity measurements. NLMR signals were detected in various Weyl and Dirac semimetal materials.

The first experimental observation of a NLMR related to the chiral anomaly was reported by Kim *et al.* [187] for $\text{Bi}_{1-x}\text{Sb}_x$ near the topological phase transition between topological and band insulator. At the transition, Dirac points exist which are split into two Weyl points of opposite

5. Chiral anomaly in Weyl semimetals

chirality by an external magnetic field. Subsequently, evidence of a NLMR in the Dirac semimetals Cd_3As_2 [171, 188, 189], Na_3Bi [170] and ZrTe_5 [190, 191] was found. The external magnetic field breaks time-reversal symmetry and splits a twofold degenerate Dirac cone into two Weyl cones. Further, a NLMR was detected in the Weyl semimetal TaAs [26] as well as in the half-Heusler compound GdPtBi [192]. In the latter system the equilibrium band structure contains twofold degenerate touching quadratic bands. A magnetic field creates four Weyl points around this crossing by lifting the spin degeneracy.

A challenging experimental task is to clearly prove that the NLMR signal is a signature of the chiral anomaly and does not originate from different phenomena [26, 172]. Other reasons for detecting a NLMR can be magnetism [193], effects related to the size or geometry of the sample, like the current-jetting effect [194, 195] or anisotropies [196]. In the ultraquantum limit, even materials with topologically trivial character can exhibit a NLMR [195, 197].

The experiments were performed and interpreted in the semiclassical [26, 170, 171, 187, 189, 190, 192] as well as the quantum regime [170–172, 188, 192]. For low magnetic fields (semiclassical limit) often an initial positive longitudinal magnetoresistance (PLMR) was observed before the signal merges to a NLMR. This feature is attributed to weak antilocalization effects [26, 187, 190, 198] and the Zeeman splitting due to the magnetic field [170], respectively.

5.5. Chiral anomaly within a Fermi surface harmonics approach

In this section, the transport properties of Weyl semimetals are considered more elaborately by calculating the full conductivity tensor and discussing in particular the influence of external magnetic fields. Including the Lorentz term in the Boltzmann equation (2.40) is essential because it considerably affects the transversal as well as those diagonal charge conductivity tensor elements corresponding to charge transport perpendicular to the magnetic field. In addition, the scattering term includes scattering-out as well as scattering-in terms. Thus, the mean free path $\Lambda_{\mathbf{k}}$ is not mandatory aligned with the semiclassical velocity [Eq. (2.29b)] but can sustain additional components due to the Lorentz force as well as scattering-out processes.

In order to solve the more complex Boltzmann equation, the method of Fermi surface harmonics [58–60], introduced in particular for systems with nontrivial topology in section 2.3.3, is employed, using the disjoint representation [58]. It provides an efficient way of solving the linearized Boltzmann equation and is at the same time comprehensible, allowing a straight analysis of the results. The main part of this section is from [J6].

5.5.1. Transport properties

As derived in section 2.3.3, the solution of the linearized Boltzmann equation (2.54) in the Fermi-surface-Harmonics approach is

$$\Lambda_{\mathbf{k}}(\mathbf{B}) = \sum_{M, M'} [(\mathcal{B} + \mathcal{C})^{-1}]_{MM'} \mathbf{D}_{M'} \Psi_M(\mathbf{k}) = \sum_{M, M'} [(\mathcal{B} + \mathcal{C})^{-1}]_{MM'} (\mathbf{D}_{M'}^I + \mathbf{D}_{M'}^{II}) \Psi_M(\mathbf{k}). \quad (5.37)$$

The matrices \mathcal{B} and \mathcal{C} correspond to the Lorentz force term and the scattering term, respectively, and are defined in Eqs. (2.56) and (2.57). The vector \mathbf{D} is defined in Eq. (2.58) and decomposed into two components,

$$\mathbf{D}_M^I = \mathcal{N}(\mathcal{E}_F)^{-1} \sum_{\mathbf{k}} \delta(\mathcal{E}_{\mathbf{k}} - \mathcal{E}_F) \Psi_M(\mathbf{k}) \tau_{\mathbf{k}} \left(1 + \frac{e}{\hbar} \mathbf{B} \cdot \boldsymbol{\Omega}_{\mathbf{k}}\right)^{-1} \mathbf{v}_{\mathbf{k}}, \quad (5.38a)$$

$$\mathbf{D}_M^{II} = \mathcal{N}(\mathcal{E}_F)^{-1} \sum_{\mathbf{k}} \delta(\mathcal{E}_{\mathbf{k}} - \mathcal{E}_F) \Psi_M(\mathbf{k}) \tau_{\mathbf{k}} \left(1 + \frac{e}{\hbar} \mathbf{B} \cdot \boldsymbol{\Omega}_{\mathbf{k}}\right)^{-1} \frac{e}{\hbar} (\boldsymbol{\Omega}_{\mathbf{k}} \cdot \mathbf{v}_{\mathbf{k}}) \cdot \mathbf{B}. \quad (5.38b)$$

5.5. Chiral anomaly within a Fermi surface harmonics approach

Hence, the mean free path is also formally split into two parts, $\Lambda_{\mathbf{k}}(\mathbf{B}) = \Lambda_{\mathbf{k}}^{\text{I}}(\mathbf{B}) + \Lambda_{\mathbf{k}}^{\text{II}}(\mathbf{B})$, which are defined by Eq. (5.37), in which $\mathbf{D}_{M'}$ is replaced by $\mathbf{D}_{M'}^{\text{I}}$ and $\mathbf{D}_{M'}^{\text{II}}$, respectively.

Combining Eqs. (2.29) and (5.37), the electric charge current density reads

$$\mathbf{j}^{\text{c}} = -\frac{e}{V} \sum_{\mathbf{k}} \left(1 + \frac{e}{\hbar} \mathbf{B} \cdot \boldsymbol{\Omega}_{\mathbf{k}}\right)^{-1} \left[\mathbf{v}_{\mathbf{k}} + \frac{e}{\hbar} \mathbf{E} \times \boldsymbol{\Omega}_{\mathbf{k}} + \frac{e}{\hbar} (\boldsymbol{\Omega}_{\mathbf{k}} \cdot \mathbf{v}_{\mathbf{k}}) \mathbf{B} \right] \left(f_0 + \frac{\partial f_0}{\partial \mathcal{E}} e \Lambda_{\mathbf{k}}(\mathbf{B}) \cdot \mathbf{E} \right). \quad (5.39)$$

The splitting of $\Lambda_{\mathbf{k}}$ allows to distinguish nine individual contributions to the charge current and to clearly identify the terms related to the chiral anomaly, as in section 5.3:

$$\mathbf{j}_{\text{eq}}^{\text{c}} = -\frac{e}{V} \sum_{\mathbf{k}} \left(1 + \frac{e}{\hbar} \mathbf{B} \cdot \boldsymbol{\Omega}_{\mathbf{k}}\right)^{-1} \mathbf{v}_{\mathbf{k}} f_{\mathbf{k}}^0, \quad (5.40a)$$

$$\mathbf{j}_{\text{AHE}}^{\text{c}} = -\frac{e^2}{V\hbar} \sum_{\mathbf{k}} \left(1 + \frac{e}{\hbar} \mathbf{B} \cdot \boldsymbol{\Omega}_{\mathbf{k}}\right)^{-1} \mathbf{E} \times \boldsymbol{\Omega}_{\mathbf{k}} f_{\mathbf{k}}^0, \quad (5.40b)$$

$$\mathbf{j}_{\text{CME}}^{\text{c}} = -\frac{e^2}{V\hbar} \sum_{\mathbf{k}} \left(1 + \frac{e}{\hbar} \mathbf{B} \cdot \boldsymbol{\Omega}_{\mathbf{k}}\right)^{-1} (\boldsymbol{\Omega}_{\mathbf{k}} \cdot \mathbf{v}_{\mathbf{k}}) \mathbf{B} f_{\mathbf{k}}^0, \quad (5.40c)$$

$$\mathbf{j}_{\text{cl}}^{\text{c}} = -\frac{e^2}{V} \sum_{\mathbf{k}} \left(1 + \frac{e}{\hbar} \mathbf{B} \cdot \boldsymbol{\Omega}_{\mathbf{k}}\right)^{-1} \mathbf{v}_{\mathbf{k}} \frac{\partial f_0}{\partial \mathcal{E}} [\Lambda_{\mathbf{k}}^{\text{I}}(\mathbf{B}) \cdot \mathbf{E}], \quad (5.40d)$$

$$\mathbf{j}_{\text{linI}}^{\text{c}} = -\frac{e^3}{V\hbar} \sum_{\mathbf{k}} \left(1 + \frac{e}{\hbar} \mathbf{B} \cdot \boldsymbol{\Omega}_{\mathbf{k}}\right)^{-1} (\boldsymbol{\Omega}_{\mathbf{k}} \cdot \mathbf{v}_{\mathbf{k}}) \mathbf{B} \frac{\partial f_0}{\partial \mathcal{E}} [\Lambda_{\mathbf{k}}^{\text{I}}(\mathbf{B}) \cdot \mathbf{E}], \quad (5.40e)$$

$$\mathbf{j}_{\text{2nda}}^{\text{c}} = -\frac{e^3}{V\hbar} \sum_{\mathbf{k}} \left(1 + \frac{e}{\hbar} \mathbf{B} \cdot \boldsymbol{\Omega}_{\mathbf{k}}\right)^{-1} (\mathbf{E} \times \boldsymbol{\Omega}_{\mathbf{k}}) \frac{\partial f_0}{\partial \mathcal{E}} [\Lambda_{\mathbf{k}}^{\text{I}}(\mathbf{B}) \cdot \mathbf{E}], \quad (5.40f)$$

$$\mathbf{j}_{\text{linII}}^{\text{c}} = -\frac{e^2}{V} \sum_{\mathbf{k}} \left(1 + \frac{e}{\hbar} \mathbf{B} \cdot \boldsymbol{\Omega}_{\mathbf{k}}\right)^{-1} \mathbf{v}_{\mathbf{k}} \frac{\partial f_0}{\partial \mathcal{E}} [\Lambda_{\mathbf{k}}^{\text{II}}(\mathbf{B}) \cdot \mathbf{E}], \quad (5.40g)$$

$$\mathbf{j}_{\text{2ndb}}^{\text{c}} = -\frac{e^3}{V\hbar} \sum_{\mathbf{k}} \left(1 + \frac{e}{\hbar} \mathbf{B} \cdot \boldsymbol{\Omega}_{\mathbf{k}}\right)^{-1} (\mathbf{E} \times \boldsymbol{\Omega}_{\mathbf{k}}) \frac{\partial f_0}{\partial \mathcal{E}} [\Lambda_{\mathbf{k}}^{\text{II}}(\mathbf{B}) \cdot \mathbf{E}], \quad (5.40h)$$

$$\mathbf{j}_{\text{CA}}^{\text{c}} = -\frac{e^3}{V\hbar} \sum_{\mathbf{k}} \left(1 + \frac{e}{\hbar} \mathbf{B} \cdot \boldsymbol{\Omega}_{\mathbf{k}}\right)^{-1} (\boldsymbol{\Omega}_{\mathbf{k}} \cdot \mathbf{v}_{\mathbf{k}}) \mathbf{B} \frac{\partial f_0}{\partial \mathcal{E}} [\Lambda_{\mathbf{k}}^{\text{II}}(\mathbf{B}) \cdot \mathbf{E}]. \quad (5.40i)$$

These terms correspond to the expressions (5.33a)–(5.33i). Indeed, the equilibrium terms (a)–(c) of Eqs. (5.33) and (5.40) are identical. As above, the second-order terms (5.40f) and (5.40h) are not considered in this linear approach. In the following, the terms (5.40d), (5.40e), (5.40g) and (5.40i) are discussed. Berry-curvature-related effects enter all terms via the phase-space correction factor $(1 + \frac{e}{\hbar} \mathbf{B} \cdot \boldsymbol{\Omega}_{\mathbf{k}})$ in $\mathcal{B} + \mathcal{C}$. However, the direct influence of the factor $(1 + \frac{e}{\hbar} \mathbf{B} \cdot \boldsymbol{\Omega}_{\mathbf{k}})^{-1}$ in Eq. (5.40) is compensated by the modified density of states when the integration in \mathbf{k} -space is performed. Further, $\Lambda_{\mathbf{k}}^{\text{II}}$, which is part of $\mathbf{j}_{\text{linII}}^{\text{c}}$ and $\mathbf{j}_{\text{CA}}^{\text{c}}$, is Berry-curvature-related. Finally, the Berry curvature directly enters the expressions for $\mathbf{j}_{\text{linI}}^{\text{c}}$ and $\mathbf{j}_{\text{CA}}^{\text{c}}$. Thus, the transport properties of a topologically nontrivial material are expected to differ from those of a topologically trivial material.

The Lorentz force as well as the scattering-in terms enter all nonequilibrium charge current expressions via $\mathcal{B} + \mathcal{C}$. Therefore, qualitative differences between Eqs. (5.33) and (5.40) are expected, especially for the transversal tensor elements of the charge conductivity and the diagonal elements not aligned with the magnetic field. Due to the inclusion of the Lorentz force, the planar Hall effect, which is large in Weyl semimetals due to the chiral anomaly [199, 200], is also contained in $\mathbf{j}_{\text{CA}}^{\text{c}}$.

In this section, the charge conductivity tensors related to the nonequilibrium charge current contributions $\mathbf{j}_{\text{cl}}^{\text{c}}$, $\mathbf{j}_{\text{linI}}^{\text{c}}$, $\mathbf{j}_{\text{linII}}^{\text{c}}$, and $\mathbf{j}_{\text{CA}}^{\text{c}}$ are considered for various Weyl systems. In their seminal paper on the chiral anomaly in the semiclassical limit [41], Son and Spivak considered a pair of Weyl points modeled by two copies of the isotropic Weyl Hamiltonian (3.31). In this section, the Weyl pairs are described by the anisotropic Hamiltonian (3.35) which provides a more realistic band

5. Chiral anomaly in Weyl semimetals

structure connecting the two Weyl cones at energies above the Weyl points and therefore containing anisotropies. This intrinsic anisotropy gives rise to additional contributions to the charge current, \mathbf{j}^{linI} and $\mathbf{j}^{\text{linII}}$, which do not exist for the isotropic Weyl Hamiltonian (if the phase-space correction is neglected). These additional contributions can modify the longitudinal magnetoresistance quantitatively as well as qualitatively; they even allow for a sign change [177–179].

In addition, the scattering properties are calculated energy- and \mathbf{k} -dependently, including scattering-out as well as scattering-in terms which strongly affects the energy dependence of the transport coefficients, as already shown above for the isotropic Weyl Hamiltonian (Eqs. (5.34) and (5.35)).

Whereas the chiral anomaly is often discussed for systems of two or four Weyl points [41, 176–179], here the number of Weyl points is systematically increased considering systems of two, four and 24 Weyl points, respectively, the latter system simulating the realistic Weyl semimetal TaAs. Thus, the influence of inversion and time-reversal symmetry, respectively, as well as the effect of an increased number of Weyl points on the transport properties can be analyzed.

Experiments often show a positive longitudinal magnetoresistance (PLMR) for small magnetic fields [26, 170, 171, 187, 190], which is usually attributed to weak antilocalization effects [198]. At medium scale magnetic fields, a negative LMR signal is observed, which is in good agreement with the semiclassical theory. These findings call to find other reasons leading to a PLMR in the semiclassical limit. Therefore, this section also aims at identifying such mechanisms. More precisely, in anisotropic systems with broken time-reversal symmetry additional contributions $\propto B$ to the charge conductivity (Refs. [177–179]), which appear in addition to the conventional terms $\propto B^2$ (Ref. [41]), can change the sign of the LMR. Further, considering transport transversal to the magnetic field can also modify the LMR. In particular, slightly misaligned magnetic fields with respect to the symmetry axes of the crystal give rise to qualitative deviations from the LMR that has been discussed in Ref. [41]; furthermore, such misalignment may even result in a sign change.

Very recently, a paper considering the influence of Lorentz force and chiral anomaly on isotropic Weyl systems using a Fourier harmonics approach for solving the Boltzmann equation was published [201]. However, this work provides additional insights since here the momentum relaxation time is calculated \mathbf{k} - and \mathbf{E} -dependently, scattering-in processes as well as anisotropies of the system are included and with TaAs a realistic Weyl semimetal is considered.

5.5.2. Inversion symmetric system: two Weyl points

The minimal number of Weyl points in a system with inversion symmetry and broken time-reversal symmetry is two. Here, a system of two Weyl points described by the model Hamiltonian (3.35) is considered in order to demonstrate general and inversion-symmetry-related features of the transport properties.

The chosen model parameters ($\gamma_W = 130 \text{ eV}\text{\AA}^2$, $m_0 = 1.73 \cdot 10^{-4} \text{ \AA}^{-2}$, $v_y = v_z = 2.2 \cdot 10^5 \text{ m/s}$) correspond approximately to those of a W1 point in TaAs (introduced in section 4.8.2 and discussed below). The Weyl cones and Fermi surfaces are symmetric with respect to the k_y - and k_z -direction, but asymmetries occur along k_x , that is the direction of Weyl points separation. The Fermi energy is set to $\mathcal{E}_F = 20 \text{ meV}$, which is approximately the Fermi level of the TaAs W1 points, and lies below \mathcal{E}_S .

For the calculation of the momentum relaxation time, the scattering potential is set constant to an arbitrary value of $U = 1 \text{ eV}$, the impurity concentration is assumed 1 at%, and the volume of the unit cell is set to $6 \times 6 \times 11 \text{ \AA}^3$. These parameters enter the results as constant factors and are therefore qualitatively irrelevant for the results. The \mathbf{k} -points on the Fermi surface are calculated using an adaptive tetrahedral method, which is briefly sketched in appendix E.2. It turned out that only Fermi surface harmonics up to $N = 3$ are sufficient for solving the linearized Boltzmann equation since contributions from higher order FSHs are negligibly small.

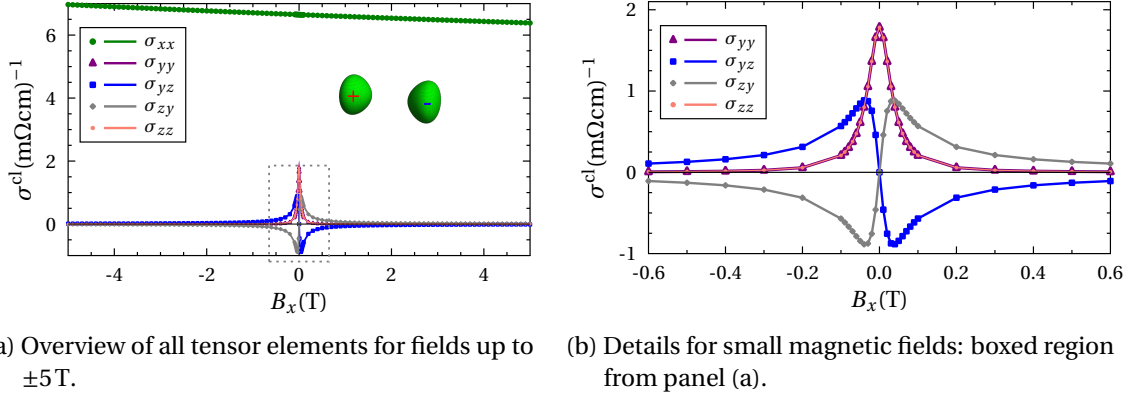


Figure 5.8.: Classical charge conductivity for a system of two Weyl points versus magnetic field applied in x -direction, which is the direction of the Weyl dipole orientation (sketched by the green Fermi sheets). The figures are adapted from [J6].

Classical charge conductivity

Fig. 5.8 shows the classical charge conductivity $\hat{\sigma}^{cl}$ (defined by Eq. (5.40d)) for an external magnetic field $\mathbf{B} = (B_x, 0, 0)$ pointing in the direction of anisotropies in \mathbf{k} -space. For $B_x = 0$, the conductivity tensor is diagonal. The tensor elements $\sigma_{yy}^{cl} = \sigma_{zz}^{cl}$ are not equivalent to σ_{xx}^{cl} because of the anisotropic Fermi surface. With increasing B_x , the influence of the Lorentz force becomes pronounced. As expected from analytical model calculations [186], the conductivity components not aligned with \mathbf{B} , that are σ_{yy}^{cl} and σ_{zz}^{cl} decrease with $-B_x^2$ for small fields because in this region scattering is dominant. For higher fields forcing the electrons to move on cyclotron orbits, these tensor elements decrease with B_x^{-2} .

The xx -component (green curve, only visible in Fig. 5.8(a)) provides an unconventional asymmetry with respect to B_x . For the highly symmetric system discussed here, it is expected constant in B_x . However, the asymmetry of the phase-space correction factor $(1 + \frac{e}{\hbar} \mathbf{B} \cdot \mathbf{\Omega}_{\mathbf{k}})$ with respect to $\mathbf{B} \leftrightarrow -\mathbf{B}$ for systems with broken time-reversal symmetry makes the momentum relaxation time also asymmetric in \mathbf{B} . Inversion symmetry dictates that $\tau_{\mathbf{k}}(\mathbf{B}) = \tau(k_x^2, \mathcal{E}, B_x)$. Although the magnetic field does not break this symmetry, it influences the momentum relaxation time by coupling to the Berry curvature. Its influence on $\tau_{\mathbf{k}}$ is asymmetric with respect to $\mathbf{B} \leftrightarrow -\mathbf{B}$ which leads to asymmetries in the transport properties. A more detailed discussion of the momentum relaxation time is given in section 5.5.5.

The transversal (off-diagonal) components $\sigma_{yz}^{cl} = -\sigma_{zy}^{cl}$ represent the Hall effect. As expected from analytics [186], $\sigma_{yz}^{cl} \sim B_x$ for small fields (scattering is dominant), and $\sigma_{yz}^{cl} \sim B_x^{-1}$ for larger fields (electrons move on cyclotron orbits).

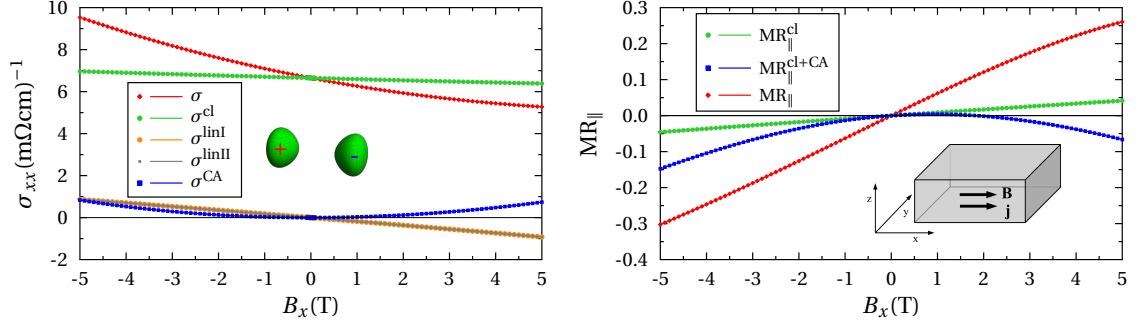
Berry-curvature-related charge conductivity

For the considered pair of Weyl points, the contributions $\hat{\sigma}^{linI}$, $\hat{\sigma}^{linII}$, and $\hat{\sigma}^{CA}$ to the charge conductivity that are related to the Berry curvature (defined in section 5.5.1) have only nonzero xx -components (depicted in Fig. 5.9(a)).

The contributions σ_{xx}^{linI} and σ_{xx}^{linII} are identical for $\mathbf{B} = (B_x, 0, 0)$. For this system with broken time-reversal symmetry and the considered B_x range ($|B_x| \leq 5T$), they can be of the same order as σ_{xx}^{CA} , which scales with B_x^2 . From Fig. 5.9(a) it seems that σ_{xx}^{linI} and σ_{xx}^{linII} depend approximately linearly on the magnetic field. However, they also have a small symmetric contribution (approximately 3% of the antisymmetric one) due to the phase-space correction.

Eqs (5.39) and (5.40) tell that the contributions $\hat{\sigma}^{linI}$, $\hat{\sigma}^{linII}$, and $\hat{\sigma}^{CA}$ are not a direct consequence of the nonzero chirality but result from the non-vanishing Berry curvature of the states at the

5. Chiral anomaly in Weyl semimetals



(a) Charge conductivity σ_{xx} . The total charge conductivity as well as the individual contributions are shown. $\hat{\sigma}^{\text{cl}}$, $\hat{\sigma}^{\text{linI}}$, $\hat{\sigma}^{\text{linII}}$, and $\hat{\sigma}^{\text{CA}}$, are defined in section 5.5.1.

(b) Longitudinal magnetoresistance MR_{\parallel} . The magnetoresistance considering only the classical charge conductivity (green) as well as the MR including $\hat{\sigma}^{\text{cl}}$ and $\hat{\sigma}^{\text{CA}}$ (blue) are shown. The LMR which takes into account all contributions to the charge conductivity is given in red. The inset sketches the sample with the directions of the magnetic field and the charge current.

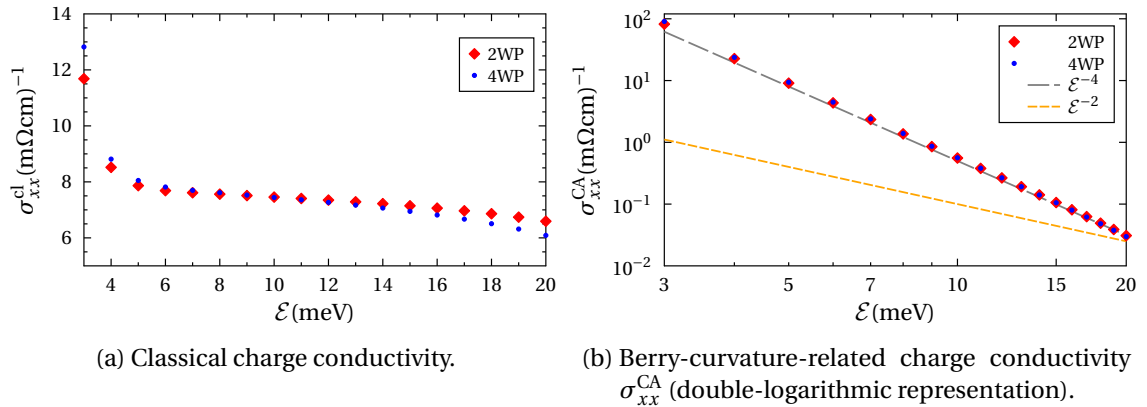
Figure 5.9.: Longitudinal transport properties for a system of two Weyl points separated in k_x -direction for magnetic field applied in x -direction. The figures are adapted from [J6].

Fermi level. Therefore, these terms contribute also in energy regions in which the Weyl points' Fermi surfaces are connected (there: $\chi = 0$). However, these are comparably small since the Berry curvature scales approximately with \mathcal{E}^{-2} .

The energy-dependent charge conductivity for an anisotropic system of two Weyl points is shown in Fig. 5.10. As in the isotropic Weyl model discussed in section 5.3, σ_{xx}^{cl} is approximately constant with respect to \mathcal{E} . The increase near the Weyl points originates from the enhanced phase-space correction factor. The Berry-curvature-related contribution σ_{xx}^{CA} scales with $\approx \mathcal{E}^{-4}$, as in the isotropic model.

Longitudinal magnetoresistance

To demonstrate the influence of $\hat{\sigma}^{\text{linI}}$ and $\hat{\sigma}^{\text{linII}}$, the LMR is decomposed as shown in Fig. 5.9(b). First, only the classical charge conductivity is considered (green curve). Because of the phase-space



(a) Classical charge conductivity.

(b) Berry-curvature-related charge conductivity σ_{xx}^{CA} (double-logarithmic representation).

Figure 5.10.: Longitudinal charge conductivity versus energy for systems with two and four Weyl points, respectively. The Weyl point energy is at $\mathcal{E} = 0$, the magnetic field reads $\mathbf{B} = (1 \text{ T}, 0, 0)$. The figures are adapted from [J6].

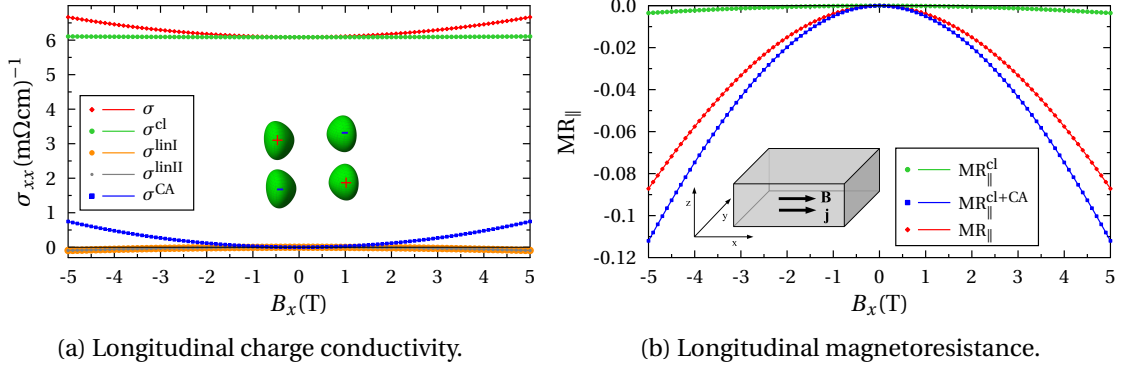


Figure 5.11.: Longitudinal transport properties of a system with four Weyl points (see sketch of the Fermi surfaces), as Fig. 5.9. The figures are adapted from [J6].

correction factor $(1 + \frac{e}{\hbar} \mathbf{B} \cdot \mathbf{\Omega}_{\mathbf{k}})$, the MR is not symmetric with respect to B_x , as discussed above. The second (blue) curve represents the LMR for which σ_{xx}^{cl} as well as σ_{xx}^{CA} are taken into account. The LMR is dominated by σ_{xx}^{CA} which increases with B_x^2 and leads to a NLMR, as discussed in literature [41]. The third (red) curve includes all contributions. Due to the nearly linear B_x -dependences of σ_{xx}^{linI} and σ_{xx}^{linII} , the LMR is asymmetric with respect to B_x . The additional contributions σ_{xx}^{linI} and σ_{xx}^{linII} can induce a sign change. However, for fields larger than those considered in Fig. 5.9, the quadratic contribution σ_{xx}^{CA} dominates and the LMR becomes negative.

By exchanging the positions of the Weyl points in \mathbf{k} -space, that is a reversal of the Weyl dipole moment, the sign of the Berry curvature is reversed at each \mathbf{k} . Since the magnetic field couples to the Berry curvature, this exchange has the same effect on the longitudinal transport properties as a reversal of the magnetic field.

5.5.3. Four anisotropic Weyl points

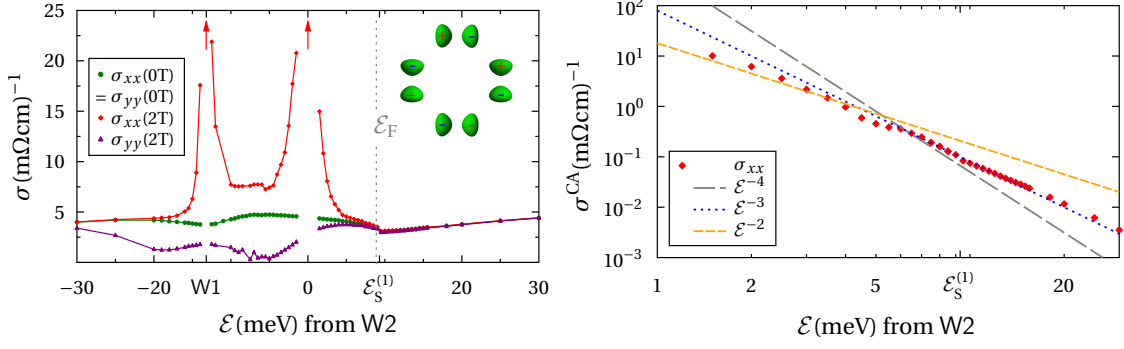
A minimal time-reversal symmetric system of four Weyl points is discussed in this section with the same model parameters as before. The classical charge conductivity (not shown here) exhibits the same qualitative B_x -dependence as for two Weyl points. The only difference is that for four Weyl points the longitudinal charge conductivity σ_{xx}^{cl} is symmetric with respect to $\mathbf{B} \leftrightarrow -\mathbf{B}$ and increases slightly with $|B_x|$. As before, this B_x -dependence originates from the phase-space correction which is now invariant under $(\mathbf{B} \leftrightarrow -\mathbf{B}) \wedge (\mathbf{k} \leftrightarrow -\mathbf{k})$.

The B_x -dependence of the longitudinal charge conductivity is shown in Fig. 5.11(a). The slight increase with $|B_x|$ of the classical contribution is insignificant, σ_{xx}^{CA} scales with B_x^2 . Without the phase-space correction factor, σ_{xx}^{linI} and σ_{xx}^{linII} would vanish because of time-reversal symmetry. However, since the applied magnetic field breaks this symmetry and couples to the Berry curvature, these terms can be nonzero. This feature is illustrated by means of the \mathbf{k} -dependent momentum relaxation time in section 5.5.5. For $\mathbf{B} = 0$, the momentum relaxation time is constant on an iso-energy surface. If time-reversal symmetry is broken by the magnetic field, the momentum relaxation time becomes anisotropic, $\tau_{\mathbf{k}} \neq \tau_{-\mathbf{k}}$, which allows finite contributions σ_{xx}^{linI} and σ_{xx}^{linII} . For the chosen parameters these contributions are negative, and scale approximately as $-B_x^2$. Their absolute value is up to 20% of σ_{xx}^{CA} . Thus, they compensate partially the (positive) contribution σ_{xx}^{CA} but do not induce a sign change of the LMR. In general σ_{xx}^{linI} and σ_{xx}^{linII} can be positive, depending on the specific model parameters.

As a result, the LMR is negative, as shown in Fig. 5.11(b), and its B_x -dependence agrees with that derived in Ref. [41]. It is thus evident that the additional terms modify the magnitude of the NLMR but do not change its qualitative B_x -dependence.

The energy dependencies of the conductivity contributions σ_{xx}^{cl} and σ_{xx}^{CA} are identical to those of the two Weyl points system, shown in Fig. 5.10. Further, even the numerical values for the system of

5. Chiral anomaly in Weyl semimetals



(a) Charge conductivities σ_{xx} and σ_{yy} of TaAs versus energy without ($B = 0$) and with ($B_x = 2\text{T}$) magnetic field, respectively. The gray dashed line marks the position of the Fermi level. The inset sketches the eight W1 points that lie in the ($k_z = 0$)-plane.

(b) Energy dependence of the Berry-curvature-related contribution σ_{xx}^{CA} for $B_x = 1\text{T}$ for energies above the W2 energy. The double logarithmic plot shows that σ_{xx}^{CA} scales approximately with \mathcal{E}^{-3} (dashed blue line). The figures are adapted from [J6].

Figure 5.12.: Energy dependence of the charge conductivity in TaAs. The positions of W1 and W2 as well as the associated saddle point $\mathcal{E}_S^{(1)}$ are indicated. $\mathcal{E}_S^{(2)}$ is not within the depicted energy range.

two and four Weyl points are close to each other. Although a larger number of states (phase space) contributes to the transport properties in the system with four Weyl points, this is compensated by a smaller momentum relaxation time due to the enhanced phase space for scattering.

5.5.4. TaAs (24 Weyl points)

The theory, until now applied to systems with two or four Weyl points, is extended to a more realistic system: the type-I time-reversal symmetric Weyl semimetal TaAs [100–103, 160–163], which hosts 24 Weyl points near the Fermi level, (see section 4.8.2). The band structure in the vicinity of these points is approximated by the model Hamiltonian (3.35) using the parameters derived from Ref. [162] and shown in Table 4.5.

The Weyl points, separated into 8 Weyl points labeled W1 and 16 Weyl points labeled W2, are arranged in groups of eight in three planes parallel to the ($k_z = 0$)-plane in the first Brillouin zone, as shown in Fig. 4.21(a). One of these planes is sketched in the inset of Fig. 5.12(a). The Cartesian axes x , y , and z are parallel to the [100], the [010], and the [001]-directions, respectively. The Fermi surface is invariant with respect to fourfold rotations about the z -axis.

Energy dependence of the charge conductivity

Since the B_x -dependence of the contributions to the charge conductivity is qualitatively equivalent to those for four Weyl points, it is not shown explicitly here. Thus, the focus is on the energy dependence of the transport coefficients. Due to the more complicated arrangement of Weyl points in energy, this dependence is not as simple as for the examples of two or four Weyl points.

Fig. 5.12(a) depicts the longitudinal charge conductivity (σ_{xx} and σ_{yy}) without and with magnetic field, respectively, as a function of energy. For $\mathbf{B} = 0$, σ_{xx} and σ_{yy} are equivalent for symmetry reasons. They are almost constant because the energy dependencies of the DOS and the momentum relaxation time approximately compensate, as discussed in section 5.3 for the isotropic model. Due to the Lifshitz transition, at $\mathcal{E}_S^{(1)}$ (saddle point of W1) a discontinuity occurs.

The presence of a magnetic field in x -direction ($B_x = 2\text{T}$) leads to a decrease of σ_{yy} because of the Lorentz force. The amount of reduction depends strongly on the energy. At energies near the Weyl points, the scattering rates are low, the electrons move along the iso-energy orbits almost unperturbed by scattering. Thus, the influence of the Lorentz force is pronounced (limit of strong

magnetic fields). At higher energies, scattering is dominant and the influence of the magnetic field on the electrons is less distinct (limit of weak magnetic fields).

The most noticeable effect of the magnetic field is the strong increase of the longitudinal charge conductivity σ_{xx} due to the chiral anomaly. The additional contributions are maximum around the W1 and W2 points.

The energy dependence of the Berry-curvature-related σ_{xx}^{CA} is examined in more detail by a double logarithmic representation for energies above the W2 energy, shown in Fig. 5.12(b). In general, the data points follow an \mathcal{E}^{-3} -dependence. Closer to the Weyl points, an \mathcal{E}^{-2} -dependence seems as well reasonable, which would support the data observed by Zhang *et al.* [26] for TaAs samples with different Fermi levels. The \mathcal{E}^{-4} -dependence calculated for Weyl points at a single energy (Fig. 5.10(b)) is not reproduced for the TaAs system because the different energies of the W1 and W2 points result in a complicated scattering behavior. A similar energy dependence is found for energies below W1 (not shown here). In between the energies of W1 and W2, the Berry-curvature-related charge conductivity σ_{xx}^{CA} is nearly constant because of the overlap of the Weyl cones in energy.

The energy dependence of the terms $\sigma_{xx}^{\text{linI}}$ and $\sigma_{xx}^{\text{linII}}$ (not shown here) reminds to that of σ_{xx}^{CA} . At \mathcal{E}_F , the contributions $\sigma_{xx}^{\text{linI}}$ and $\sigma_{xx}^{\text{linII}}$ are $\approx 4.5\%$ of σ_{xx}^{CA} . Here, the large number of Weyl points and the fourfold rotational symmetry of the Fermi surface reduce these anisotropy-related terms, as discussed in section 5.5.5.

The semiclassical approach is not appropriate for energies closer to the Weyl points than about 1meV because of interband contributions and lifetime broadening which are not taken into account. Within this narrow energy region, a Kubo approach is appropriate. In addition, the phase-space correction term diverges at the Weyl points, thereby increasing numerical errors. The energy range around the Weyl points in which the semiclassical Boltzmann method cannot be safely applied is estimated to ± 1 meV for W1 and ± 2.5 meV for W2, respectively. Within this energy range, the phase-space correction factor is < 100 for magnetic fields of up to 10T.

Angular dependence of the LMR

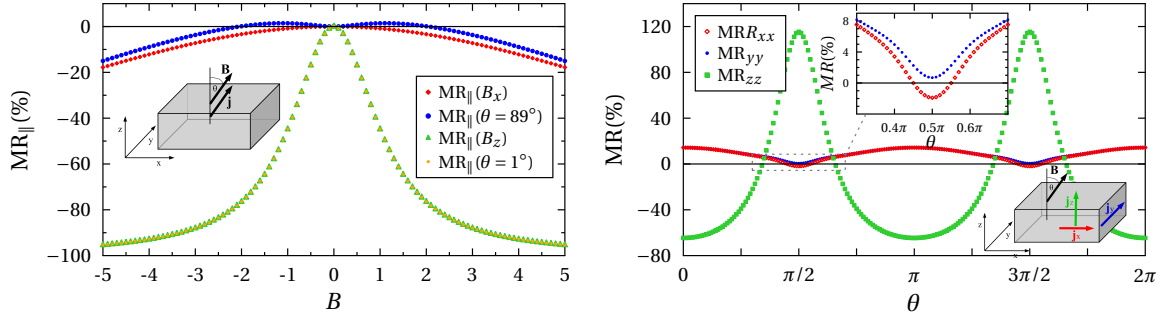
The Fermi level in TaAs given in Ref. [162] and used in this work (Table 4.5) is not very close to the Weyl points. Therefore, the chiral-anomaly-related charge conductivity, which was shown to scale with $\approx \mathcal{E}^{-3}$ (Fig. 5.12(b)), is not extraordinary large. However, due to the B^2 -dependence of this term, a clear NLMR signal is calculated at the Fermi level.

Fig. 5.13(a) shows the longitudinal magnetoresistance in TaAs for various directions of \mathbf{B} . Here, *longitudinal* always means the resistance related to a charge current parallel to the magnetic field. For \mathbf{B} in the direction of one of the Cartesian axes of the system, the LMR is negative because the chiral-anomaly terms dominate the B -dependence of the charge conductivity. Different amplitudes of the LMR are caused by the nonequivalence of the x - and z -directions. However, if \mathbf{B} is tilted off the x -axis by 1° ($\theta = 89^\circ$), a PLMR is observed for fields less than 2T. This B -dependence resembles the data measured in various experiments [26, 170, 171, 187, 190] for which the PLMR at small fields is usually explained by weak antilocalization [198]. Interestingly, the PLMR calculated here occurs only if \mathbf{B} is nearly parallel to the x -axis, but not if \mathbf{B} is slightly tilted off the z -axis.

In order to understand the PLMR for misaligned \mathbf{B} , the magnetoresistance corresponding to a current parallel to the crystal axes — MR_{xx} , MR_{yy} , and MR_{zz} — is examined as a function of the \mathbf{B} -direction, shown in Fig. 5.13(b). The magnetic field is set to $B = 1.5\text{T}$ and is rotated within the xz -plane. Here, θ is the angle between \mathbf{B} and the z -axis, as shown in the inset of Fig. 5.13(a). In the following discussion, the labels *longitudinal* and *transversal* refer to the orientation of the charge current with respect to the (tilted) magnetic field.

MR_{yy} is always transversal and positive, the latter explained by the fact that only the classical charge conductivity contributes, which is strongly influenced by the Lorentz force, and the chiral-anomaly-related terms vanish. The oscillations with θ originate from the anisotropy of the Fermi

5. Chiral anomaly in Weyl semimetals



(a) Longitudinal MR. The magnetic field is applied in the x - (B_x) and z -direction (B_z), respectively. In addition, it is slightly tilted by 1° of the crystal axes within the xz -plane (inset). The current for detecting the LMR is always parallel to the magnetic field.

(b) MR along the three crystal axes x , y , and z as a function of the angle θ of the magnetic field \mathbf{B} . The field is rotated in the xz -plane, with $\theta = 0$ corresponds to $\mathbf{B} \parallel z$ and $\theta = \pi/2$ corresponds to $\mathbf{B} \parallel x$ (see sketch). The absolute value of \mathbf{B} is 1.5T. The inset depicts details around $\theta = \pi/2$.

Figure 5.13.: Magnetoresistance (MR) in TaAs for various configurations of magnetic field and charge current for detecting the magnetoresistance. The figures are adapted from [J6].

surfaces.

MR_{xx} and MR_{zz} have both longitudinal as well as transversal components, depending on the direction of \mathbf{B} . If $\mathbf{B} \parallel z$, both terms are equivalent for symmetry reasons, $MR_{xx} = MR_{yy}$. For $B_x \neq 0$, the chiral anomaly produces a negative contribution to MR_{xx} . If θ near $\pi/2$, the contributions from the chiral anomaly dominate the classical term, and MR_{xx} becomes negative. For the same reason, MR_{zz} is negative for θ near 0 and positive around $\theta = \pi/2$. However, the amplitude of MR_{zz} is larger than those of MR_{xx} and MR_{yy} because of the anisotropy of the Fermi surfaces. The latter are elongated in the x - and y -directions, but are clinched in z -direction which leads to a small σ_{zz} , a large resistivity, and a large magnetoresistance. For the same reason of anisotropy the angular region with $MR_{zz} < 0$ is larger than the region with $MR_{xx} < 0$.

The LMR, which is associated with the direction of the magnetic field, is the projection of the magnetoresistivity onto the direction of \mathbf{B} and therefore contains components of MR_{xx} as well as MR_{zz} ,

$$MR_{||}(\mathbf{B}) = \frac{MR_{xx}(\mathbf{B})\rho_{xx}^0 \sin^2 \theta + MR_{zz}(\mathbf{B})\rho_{zz}^0 \cos^2 \theta + 2\rho_{xz}(\mathbf{B}) \sin \theta \cos \theta}{\rho_{xx}^0 \sin^2 \theta + \rho_{zz}^0 \cos^2 \theta}, \quad (5.41)$$

with ρ_{xx} and ρ_{zz} are diagonal elements of the resistivity tensor $\hat{\rho}$. The superscript 0 refers to $\hat{\rho}(\mathbf{B} = 0)$. The influence of the nondiagonal elements of $\rho(\mathbf{B})$ is less important here and will be neglected in the qualitative discussion.

For \mathbf{B} approximately in $\pm z$ -direction ($\theta \approx 0$ or $\approx \pi$), the negative contribution from MR_{zz} originating from the chiral anomaly dominates the classical positive contribution from MR_{xx} in a wide angular range. Thus, even if the magnetic field is tilted by 10° from the z -direction, the LMR would be negative for $B = 1.5\text{T}$. Around $\theta = \pi/2$ or $3\pi/2$, (\mathbf{B} approximately in $\pm x$ -direction) the positive MR_{zz} -component dominates over the negative MR_{xx} -component already for a tilt angle of 1° , leading to a PLMR. Only if \mathbf{B} is perfectly aligned in x -direction, the negative contribution due to the CA is dominant. For a larger magnetic field or Fermi levels closer to the Weyl point energies, the tilt angle under which the PLMR passes into a NLMR is reduced because the negative CA-related MR_{xx} increases stronger than the positive classical MR_{zz} , as discussed above in terms of the charge conductivity.

In other words, due to the Lorentz force, the charge current is not aligned with the electric field. Since the current direction is fixed to be parallel to \mathbf{B} per definition of the longitudinal MR, \mathbf{E} and

\mathbf{B} are not parallel, which reduces the transfer of states between the Weyl cones and consequently also the chiral-anomaly-related charge conductivity. Thus, the classical PLMR contribution can dominate the total LMR for small magnetic fields, whereas for larger fields the chiral anomaly contribution is sufficiently large to induce a total negative LMR signal. Hence, the PLMR for small tilt angles is a consequence of including the Lorentz force term in the Boltzmann equation. Revealing this feature is one of the main advantages of using the Fermi surface harmonics approach.

In Ref. [26], Zhang *et al.* report measurements of the LMR of five different TaAs samples with various Fermi levels. The magnetic field is applied in x - and z -direction, respectively, and the LMR is detected via a charge current parallel to the magnetic field. For both experimental geometries ($\mathbf{B} \parallel x$ and $\mathbf{B} \parallel z$), the characteristic curves show a PLMR for small fields and a NLMR for larger fields attributed to weak antilocalization and the chiral anomaly, respectively.

A slight tilt of the magnetic field and the charge current off the crystal symmetry axes could also give rise to LMR curves similar to the characteristic signals measured in Ref. [26]. However, as the previous calculations show, these features occur in the TaAs system only if \mathbf{B} is slightly tilted off the x -direction, but not if \mathbf{B} is almost parallel to z . Further, all transport properties depend strongly on the Fermi level since the DOS of a Weyl pair vanishes at the Weyl point energy, leading to a diverging momentum relaxation time. The Fermi levels observed for the samples of Ref. [26] are almost all closer than 5meV to the W2 points. For these energies, the model calculations do not show a pronounced PLMR for tilt angles up to 5° . Therefore, it is concluded that a slight tilt of the sample cannot be the origin of the observed PLMR, what supports the argument of the weak antilocalization.

5.5.5. Momentum relaxation time in the presence of a magnetic field

Due to the modified phase-space volume, the magnetic field influences the momentum relaxation time. In a pristine time-reversal invariant system, the magnetic field breaks time-reversal symmetry, which leads to $\tau_{\mathbf{k}} \neq \tau_{-\mathbf{k}}$. As a consequence, the additional contributions to the charge conductivity, $\hat{\sigma}^{\text{linI}}$ and $\hat{\sigma}^{\text{linII}}$, which are forbidden by time-reversal symmetry, do not vanish. This section demonstrates the influence of the magnetic field on the momentum relaxation time for systems with two Weyl points (broken time-reversal symmetry), four Weyl points (broken inversion symmetry) and 24 Weyl points (TaAs, broken inversion symmetry), respectively.

The momentum relaxation time $\tau_{\mathbf{k}}$ is calculated from Eq. (2.41) within the scattering theory introduced in section 2.5. Its values on the Fermi surfaces are depicted in Fig. 5.14 for systems hosting two and four Weyl points as well as TaAs (24 Weyl points). In general, the relaxation time decreases with increasing number of Weyl points due to the enhanced phase space for scattering.

For $\mathbf{B} = 0$ the momentum relaxation time is isotropic for time-reversal symmetric systems, which are the four Weyl points system (e) and TaAs (h), according to the symmetries of the Hamiltonian and its eigenstates. When time-reversal symmetry is broken, as for a system of two Weyl points (b), anisotropies along the k_x -direction show up, that is along the direction of the Weyl point separation, which is the direction of the Weyl pair dipole moment.

The magnetic field enters the momentum relaxation time via the phase-space correction factor when the integration in \mathbf{k} -space is performed, as shown in Eq. (2.32). Therefore, the momentum relaxation time becomes \mathbf{B} -dependent. Symmetry dictates that only the component of the magnetic field in the direction of the Weyl point separation (Weyl dipole direction) has influence on the momentum relaxation time. Further, $\tau_{\mathbf{k}}$ varies only in the Weyl dipole direction and is constant on planes perpendicular to this direction. This finding is a special property of the model Hamiltonian.

In the inversion symmetric system of two Weyl points, the momentum relaxation time is slightly changed by the magnetic field (top row of Fig. 5.14). If the magnetic field is pointing in the direction of the Weyl dipole [pointing from $\chi = -1$ to $\chi = 1$, (a)], the anisotropy of the momentum relaxation time is in general less pronounced, whereas it is more distinct when \mathbf{B} is antiparallel to the Weyl dipole moment (c). This asymmetry of the momentum relaxation time with respect to B_x explains

5. Chiral anomaly in Weyl semimetals

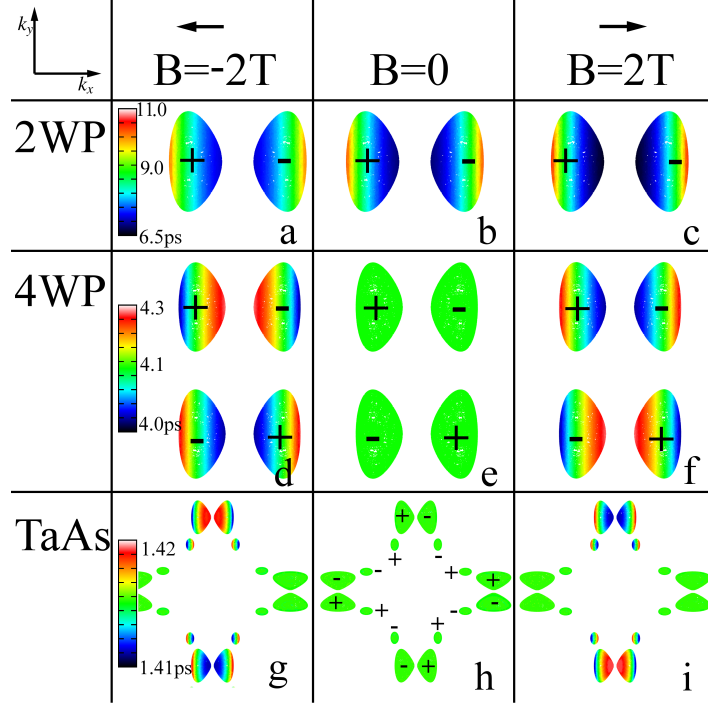


Figure 5.14.: Momentum relaxation time (color scale) for a system of two Weyl points [(a)–(c)], four Weyl points [(d)–(f)] and TaAs [(g)–(i)]. The relaxation time is calculated on the iso-energy surfaces and projected onto the $k_x k_y$ -plane. Therefore, for TaAs 16 of the 24 Weyl points are visible. The magnetic field of $\pm 2T$ is assumed in $\pm x$ -direction, respectively. The color scale differs for each row but rows share a common color scale. Adapted from [J6].

the asymmetric behavior of the transport properties discussed in section 5.5.2.

In the systems with four Weyl points (center row) and in TaAs (bottom row), the time-reversal symmetry is broken by the magnetic field. Therefore, $\tau_{\mathbf{k}} \neq \tau_{-\mathbf{k}}$. This symmetry breaking is the reason for nonzero additional contributions $\sigma_{xx}^{\text{linI}}$ and $\sigma_{xx}^{\text{linII}}$ to the charge conductivity, which vanish in the presence of time-reversal symmetry. The influence of the magnetic field on $\tau_{\mathbf{k}}$ depends on the orientation of \mathbf{B} with respect to each Weyl pair's dipole moment, as shown in (d), (f), (g), and (i), respectively.

For TaAs, whose 24 Weyl points are arranged symmetrically with respect to the x and y axes, it becomes evident [(g) and (i)] that the magnetic field affects only the momentum relaxation time of the Weyl point pairs separated in the direction of the magnetic field (x). The influence of the magnetic field becomes less pronounced here because of the fourfold rotational symmetry of the Fermi surface. The phase space for scattering and the number of scattering processes that are not affected by the phase-space correction are enhanced. Thus, the anisotropy-related charge conductivity contributions $\hat{\sigma}^{\text{linI}}$ and $\hat{\sigma}^{\text{linII}}$ are reduced.

6. Conclusion

In this thesis, the Edelstein effect and the chiral anomaly, which are transport effects driven by spin-orbit coupling, are discussed within a semiclassical Boltzmann approach. Both effects are associated with the interconversion of electric and magnetic properties and provide the opportunity of unconventionally manipulating a macroscopic observable: Due to the Edelstein effect, a spin density or magnetic moment can be induced purely electrically, whereas the chiral anomaly corresponds to a transfer of chiral electronic states in the presence of magnetic and electric fields, accompanied by an enhancement of charge conductivity.

The Edelstein effect is the generation of a homogeneous spin density by an external electric field and originates from broken inversion symmetry leading to Rashba spin splitting and spin-momentum locking. It can be utilized to create spin polarization in pristine nonmagnetic materials, as well as to induce a spin-orbit torque in ferromagnetic materials and thereby manipulate their magnetization.

In this work, a complete semiclassical framework for treating the Edelstein effect in two- as well as three-dimensional model systems is presented, solving the Boltzmann equation with a relaxation time ansatz including an energy- and momentum-dependent transport lifetime. The paradigm system providing the Edelstein effect is the isotropic Rashba model with its Fermi level above the degeneracy point. In this system, the magnitude of the current-induced spin density scales linearly with the Rashba parameter, which is a measure of the spin-orbit coupling strength, and is constant with respect to the Fermi level. Considering the energy region in between the band edge and the degeneracy point reveals a linear energy dependence of the charge-to-spin conversion efficiency. The highest Edelstein efficiency is calculated for the ordered Bi/Ag (111) surface alloy, which provides a giant Rashba splitting.

In addition to the conventionally examined isotropic Rashba system, this thesis covers the Edelstein effect in a large variety of materials including anisotropic Rashba and Dresselhaus systems, ferromagnetic Rashba systems, topological insulators and Weyl semimetals.

The Edelstein effect is commonly defined as *current-induced in-plane spin polarization perpendicular to the electric field*. However, deviations occur in Rashba systems with reduced symmetry, such as the (110) and (111) surfaces of fcc lattices, in the presence of magnetic impurities and due to additional Dresselhaus SOC accounting for a broken bulk inversion symmetry. Depending on the direction of the applied electric field, the induced spin density is not mandatory perpendicular to this field and can contain even an out-of-plane component. Further, in highly anisotropic systems, also the magnitude of the Edelstein effect strongly depends on the orientation of the field, which allows a geometry-based optimization of the effect. At the Au(110) surface, the induced spin density is modified by a factor of more than 2 by an in-plane rotation of the electric field. In these anisotropic systems, saddle points occur in the energy dispersion, corresponding to Lifshitz transitions and accompanied by vanishing spin densities.

External magnetic fields as well as a finite intrinsic magnetization break time-reversal symmetry of a Rashba system and thereby lead to intrinsic Edelstein contributions, calculated using a Kubo formula. These intrinsic contributions are perpendicular to the extrinsic as well as the equilibrium spin polarization and are comparably small. However, the intrinsic Edelstein effect brings about promising transport properties such as a spin-polarized current with spin moments aligned in the current direction.

The surface states of 3D topological insulators exhibit a comparably large Edelstein effect since they host a single Fermi circle. Thus, no compensation from Fermi lines with opposite spin texture occurs. The chirality of the surface states determines the sign of the current-induced spin density and can therefore be directly measured via the Edelstein effect. Topological insulators are a promising material class for a potential technological application of the Edelstein effect, because

6. Conclusion

not only the surface states themselves are protected against symmetry-preserving perturbations, but also the Edelstein response is constant with respect to energy.

Combining the findings on the enhancement of the Edelstein effect by geometry and lack of compensation for single Fermi lines, a notably efficient charge-to-spin conversion is expected in systems with strongly spin-polarized surface states whose Fermi contours are elongated single lines. These features are provided by the topological surface states of Weyl semimetals, which are identified as promising materials for an efficient charge-to spin conversion. The calculated Edelstein efficiency in the type-I Weyl semimetal TaAs is enhanced by at least one order of magnitude in comparison to Rashba systems and topological insulators. This enormous enlargement mainly originates from the large momentum relaxation times of the surface states due to their localization and the low, but nonzero, bulk density of states, in addition to the favorable Fermi surface geometry and the lack of compensation. Weyl semimetals provide a strongly energy-dependent Edelstein effect due to the bulk density of states varying in energy.

In addition to the extraordinarily large Edelstein effect, Weyl semimetals exhibit the chiral anomaly, originally established in the field of high energy physics, and the related observable transport signatures. In the presence of nonorthogonal electric and magnetic fields, the number of particles of a distinct chirality is not conserved, which leads to a negative longitudinal magnetoresistance.

In this work, the chiral anomaly and the associated transport properties, in particular the charge conductivity and the magnetoresistance, are discussed in the ultraquantum limit, in which only one chiral Landau level intersects the Fermi level, as well as the case of many Landau levels at the Fermi energy. However, the focus of the presented results is on the semiclassical limit, neglecting Landau quantization. Using a Fermi surface harmonics formalism extended for systems with non-vanishing Berry curvature, the Boltzmann equation is solved in an comprehensible way, including the Lorentz force, scattering-in terms, and phase-space corrections. In contrast to the common literature on the chiral anomaly, which discusses only the charge current parallel to the magnetic field, in this work the full conductivity tensor is calculated which allows the discussion of the magnetic field's influence on longitudinal as well as transversal transport properties.

In the semiclassical limit, the chiral-anomaly-related charge conductivity typically increases quadratically with the magnetic field, attended by a negative longitudinal magnetoresistance. However, in anisotropic Weyl systems, additional contributions scaling linearly with the magnetic field can occur and even change the sign of the longitudinal magnetoresistance in systems with broken time-reversal symmetry, as demonstrated in this work.

Analyzing the transport properties of TaAs, it is found that a slight tilt of the magnetic field with respect to the crystal axes can lead to a positive longitudinal magnetoresistance. Due to anisotropies of the Fermi surface, the reduction of conductivity by the Lorentz force dominates the chiral-anomaly induced positive contributions and determines the sign of the magnetoresistance for small magnetic fields.

Calculating the momentum relaxation time as a function of energy modifies the energy-dependence of the chiral-anomaly-related charge conductivity qualitatively from \mathcal{E}^{-2} to \mathcal{E}^{-4} in isotropic systems, whereas this dependence is less pronounced for the considered TaAs hosting Weyl points at various energies.

Although the presented Boltzmann approach based on model Hamiltonians is less accurate in comparison to *ab initio* methods, does not fully include inter-band transitions and is therefore not applicable for small-gap systems, it is a transparent and insightful method for calculating diverse transport properties. The results presented in this thesis provide deeper understanding of the Edelstein effect and the origin of the negative as well as the positive magnetoresistance in Weyl semimetals. Additional insights, especially in the energy regions in which the Boltzmann equation is not applicable, could be obtained from a Kubo approach.

In particular the Fermi surface harmonics formalism is a promising method for efficiently solving the Boltzmann equation in an intelligible and comprehensive way. The method can be applied to various systems and physical problems, notably to systems with nontrivial topology. In future

works, the Fermi surface harmonics formalism could be useful especially for phenomena which cannot be described in the relaxation time approximation, e.g. the extrinsic spin Hall effect in time-reversal invariant systems. One possible further project is a generalization of the approach in order to describe bulk as well as surface states. Considering more realistic scattering potentials as well as the influence of finite temperatures could improve the accuracy and reveal further insights.

A. Scattering at magnetic impurities

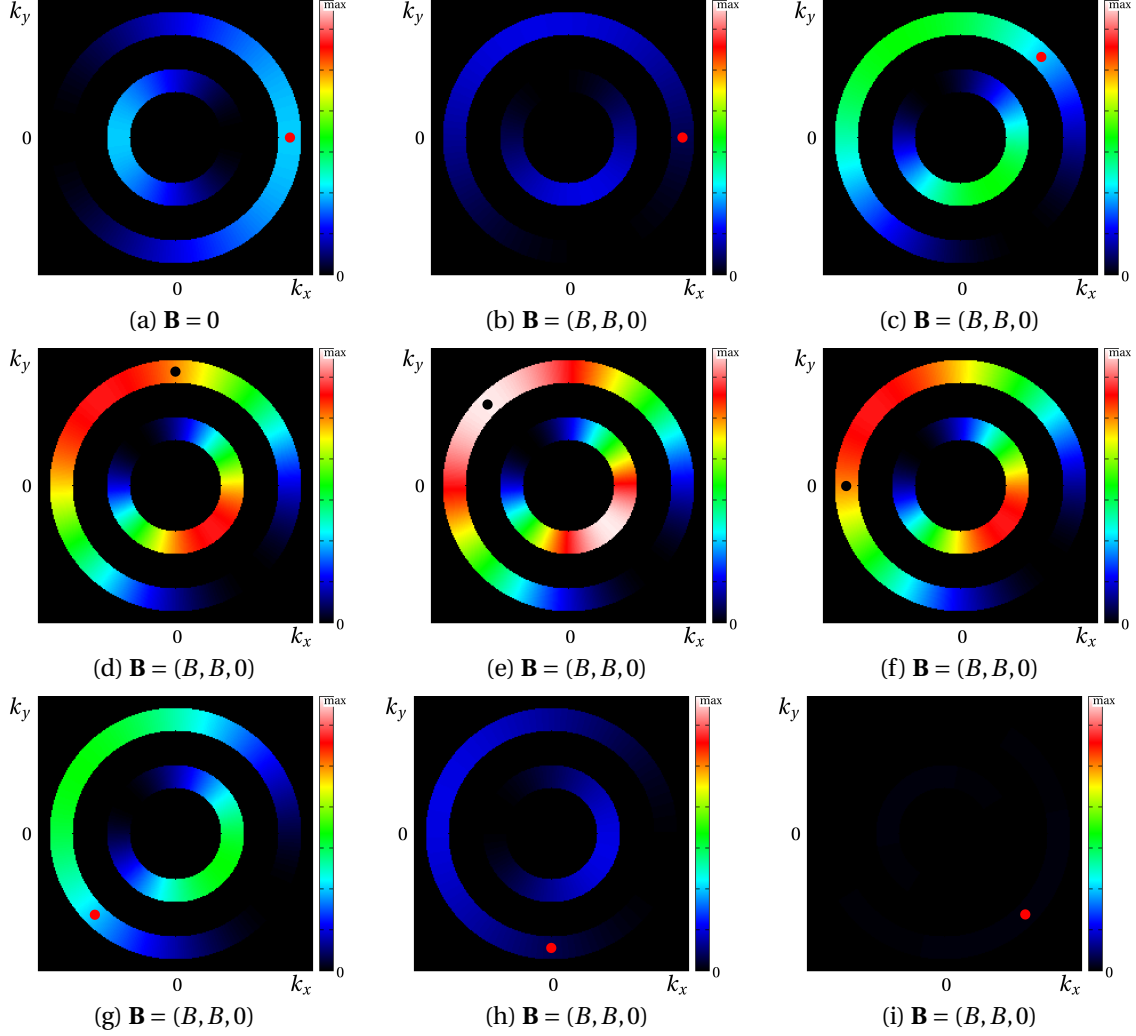


Figure A.1.: Microscopic transition probabilities of an isotropic Rashba system, $\mathcal{E}_F > 0$, with magnetic impurities. The initial state \mathbf{k} is on the outer Fermi circle and marked by a red and black dot, respectively. The color scale corresponds to the microscopic transition probability for elastic scattering from the initial state to another state on the Fermi circle. In panel (a) the transition probability is shown for nonmagnetic impurities. Here, $P_{\mathbf{k}' \rightarrow \mathbf{k}}$ depends only on the angle between initial and final state. The momentum relaxation time and transport lifetime are isotropic. Magnetic impurities break time-reversal symmetry. Panels (b)-(i) shows the microscopic transition probability for impurities inducing a local magnetic field $\mathbf{B} = (B, B, 0)$ for different directions of the initial state. The local magnetic field modifies the overlap of final and initial states. Therefore, the phase space for scattering out of the state $\mathbf{k} \parallel (-1, 1, 0)$ on the outer circle (panel (e)) is in general enhanced since the spin of this state is parallel to \mathbf{B} . Consequently, the momentum relaxation time is reduced in comparison to a system with nonmagnetic impurities. The state $\mathbf{k} \parallel (1, -1, 0)$ on the outer circle (panel (i)) has a spin polarization antiparallel to the magnetic field. Thus, the phase space for scattering is reduced leading to an enhanced momentum relaxation and transport lifetime, as shown in Fig. 4.9(b).

B. Fermi lines for a Rashba system with in-plane magnetic field

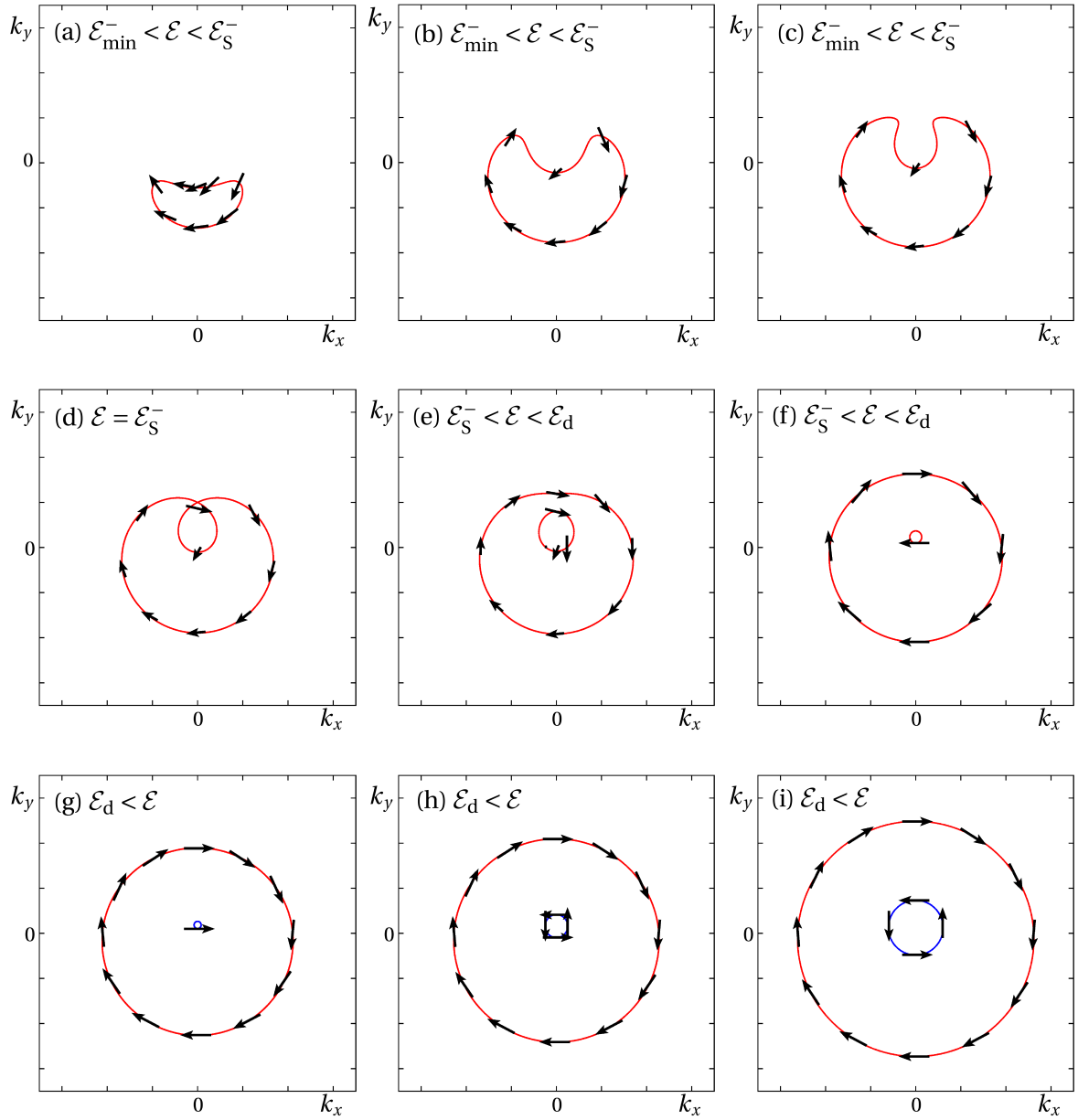


Figure B.1.: Lines of constant energy for a Rashba system with magnetic field in x -direction. The arrows indicate the in-plane spin expectation values. At \mathcal{E}_S^- the system goes through a Lifshitz transition.

C. Rashba system with Zeeman splitting, $\mathbf{B} = B(1, 0, 1)$

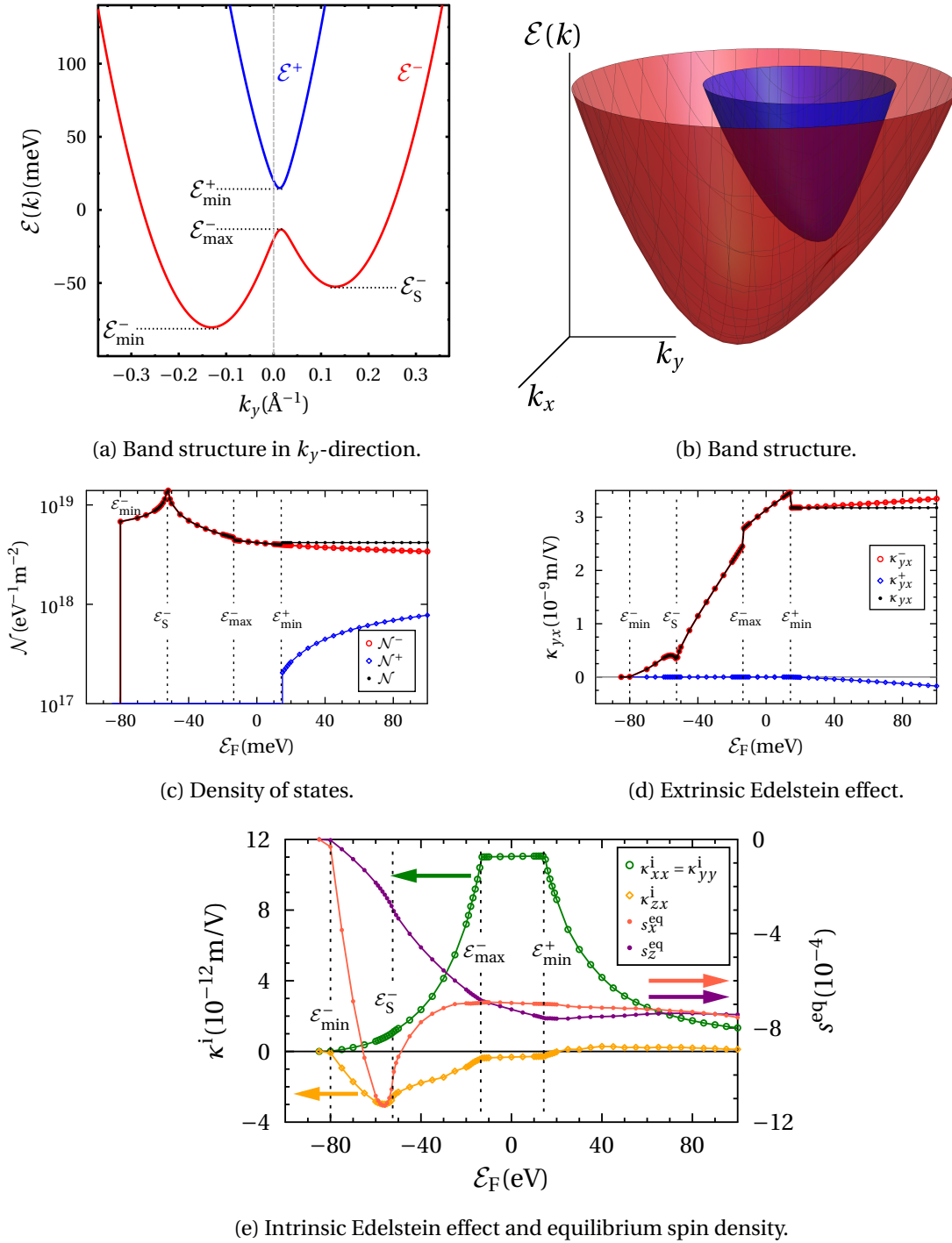


Figure C.1.: Band structure, density of states and Edelstein effect in a Rashba system with Zeeman splitting from a magnetic field applied in $(1, 0, 1)$ -direction. Here, features from the cases $\mathbf{B} \parallel z$ and $\mathbf{B} \parallel x$, discussed in the main text (section 4.5.4) arise. The degeneracy at the diabolic point is lifted and the spectrum is asymmetric with respect to the k_y -direction.

D. Band structure and Fermi lines in systems with Rashba and Dresselhaus SOC

D.1. (001) surface

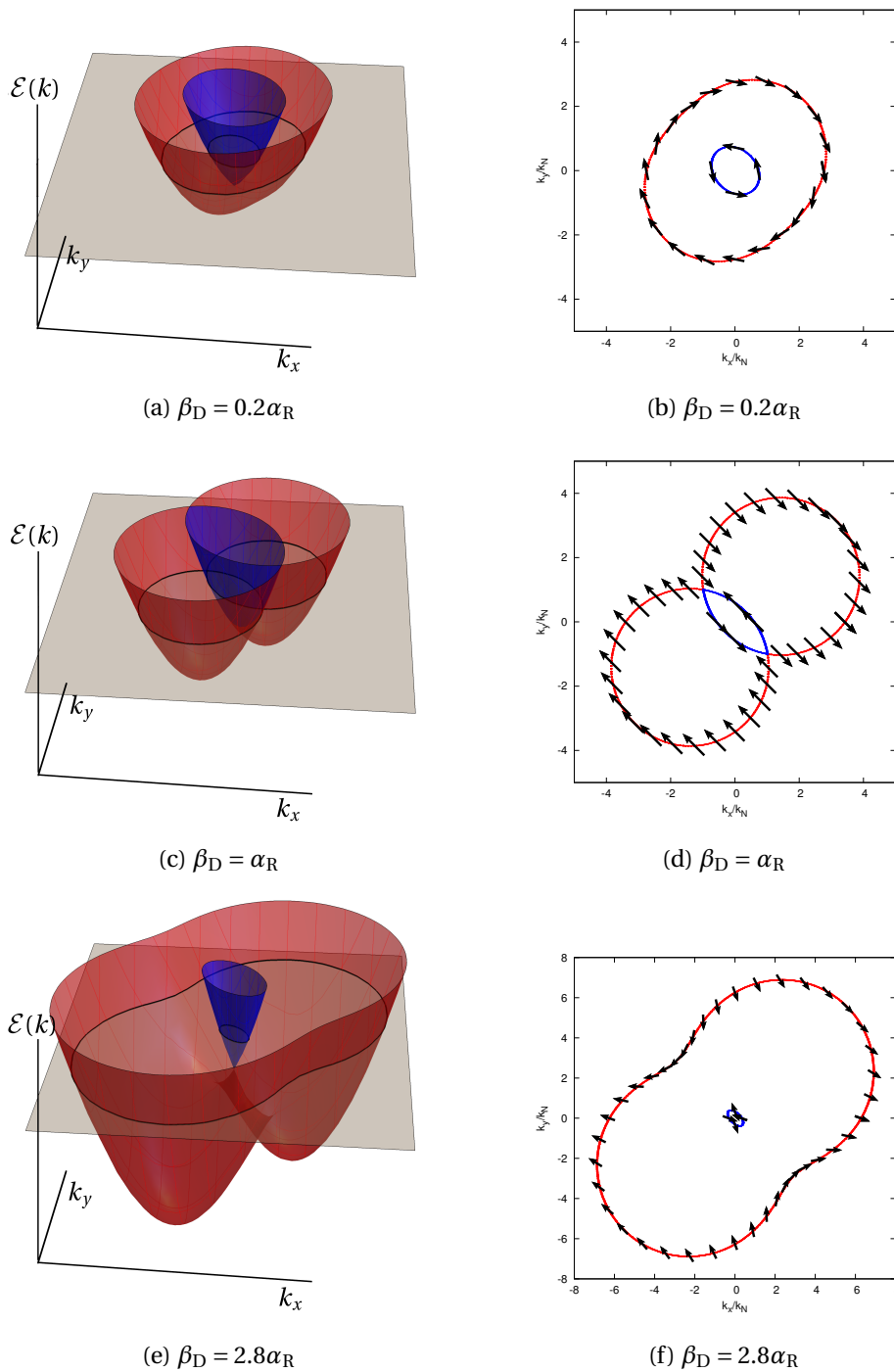


Figure D.1.: Band structure and Fermi lines with spin texture for a (001) zincblende surface with Rashba and linear Dresselhaus SOC for various ratios β_D/α_R .

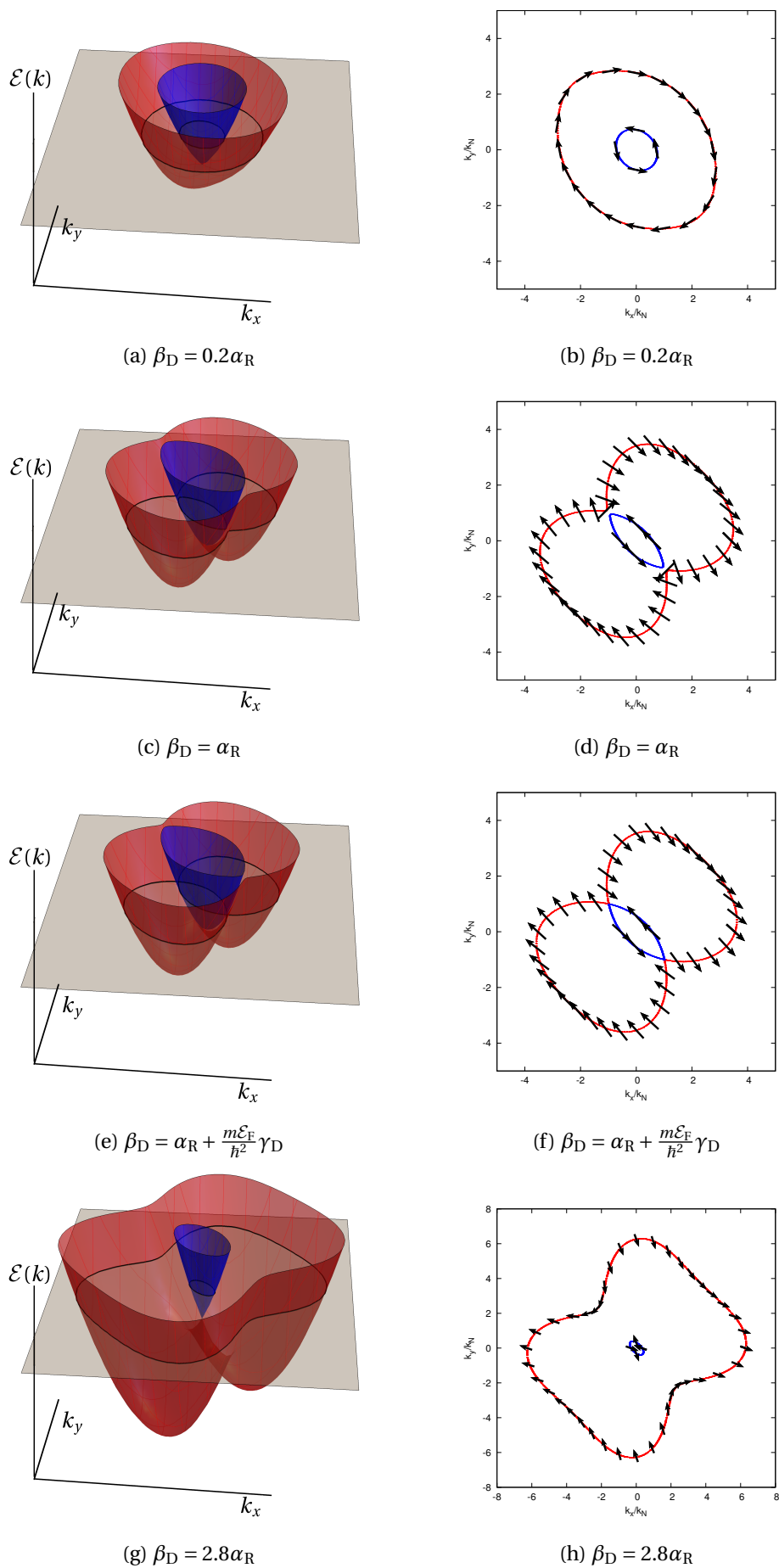


Figure D.2.: Band structure and Fermi lines with spin texture for a (001) zincblende surface with Rashba, linear and cubic Dresselhaus SOC for $\gamma_D = 0.1 \text{ \AA}^2 \alpha_R$ and various ratios β_D/α_R .

D.2. (110) surface

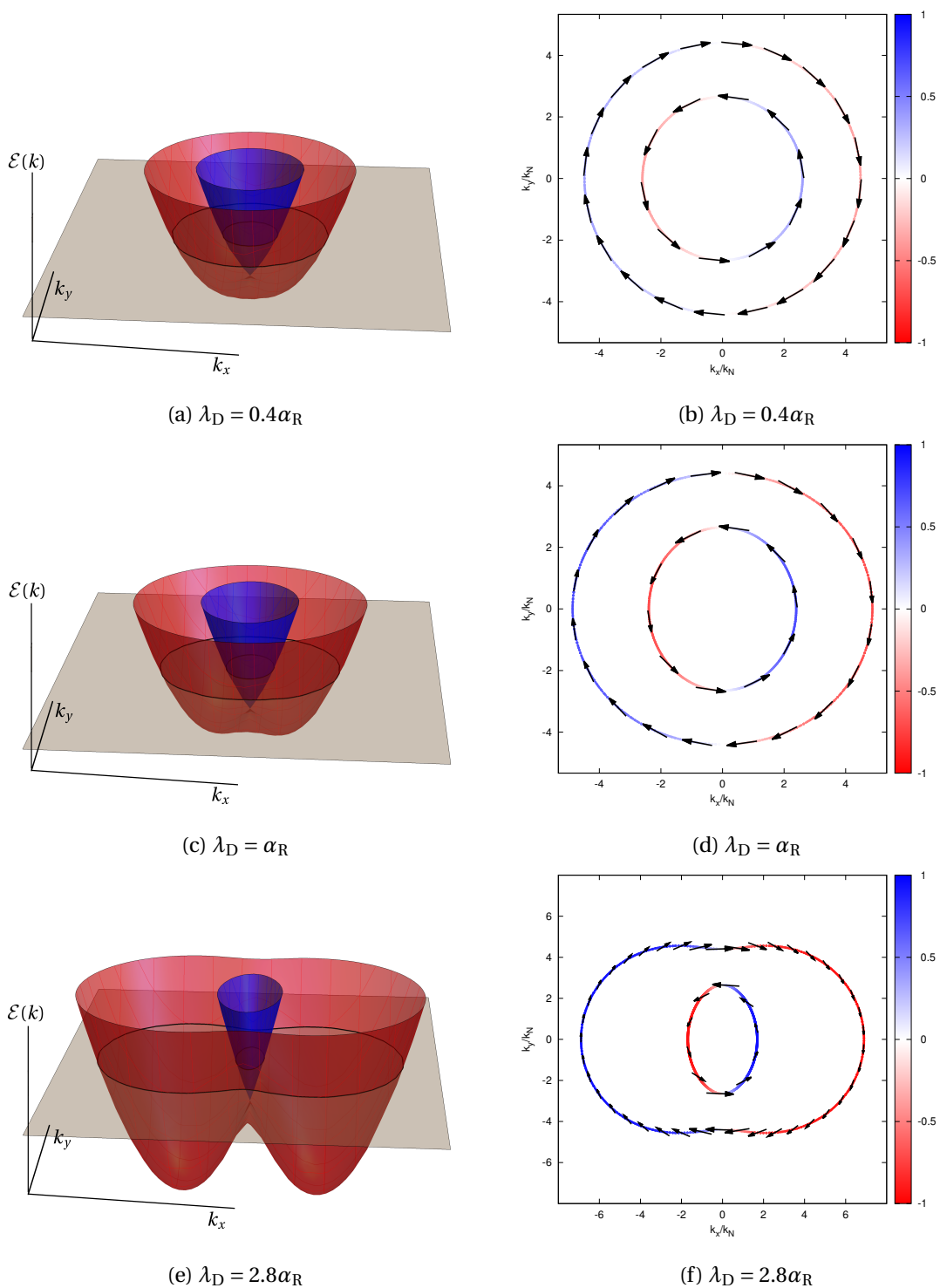


Figure D.3.: Band structure and Fermi lines with spin texture for a (110) zincblende surface with Rashba and linear Dresselhaus SOC for various ratios λ_D/α_R . The arrows correspond to the in-plane spin expectation values, the color scale represents the out-of-plane component.

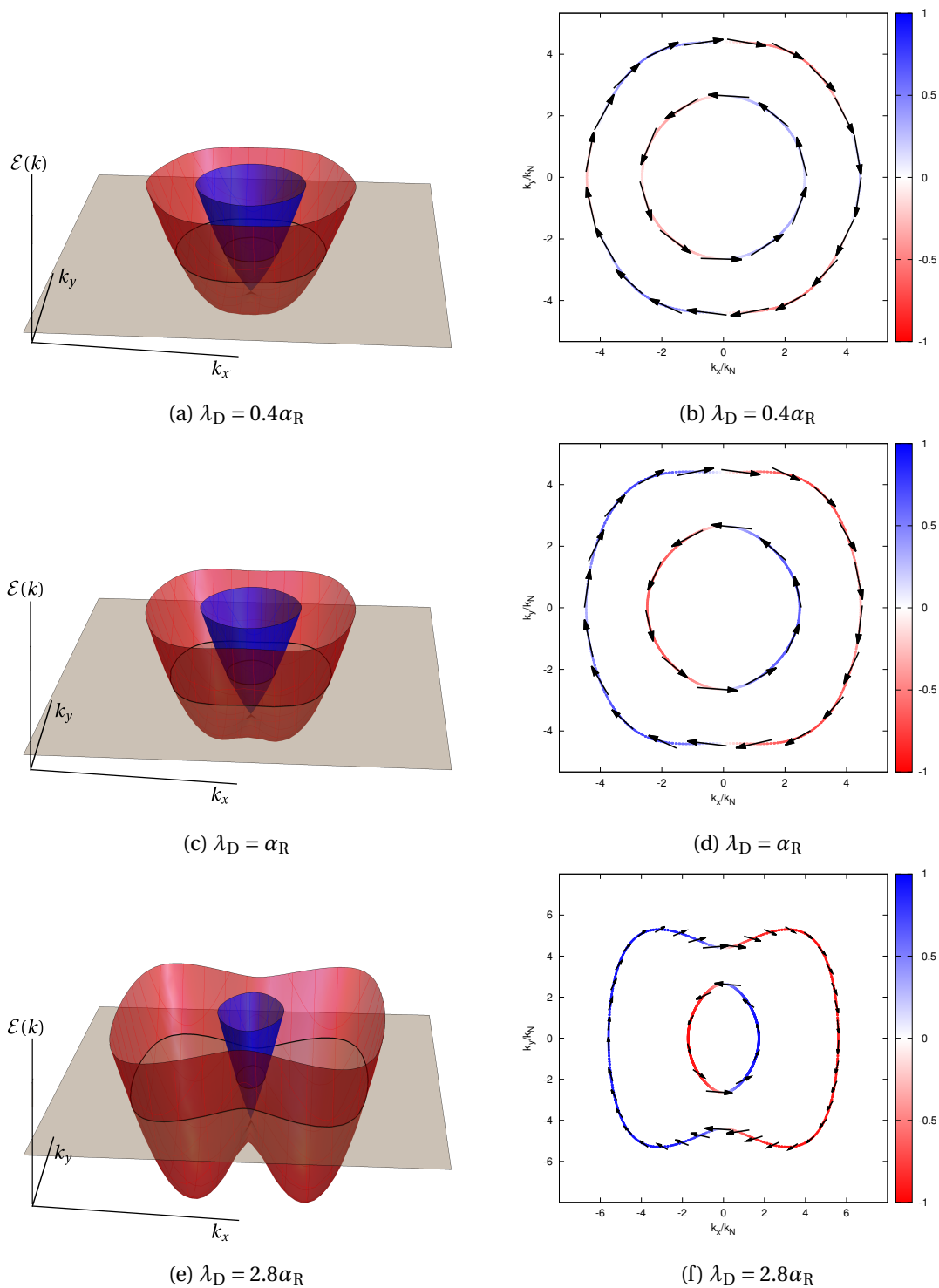


Figure D.4.: Band structure and Fermi lines with spin texture for a (110) zincblende surface with Rashba, linear and cubic Dresselhaus SOC for $\gamma_D = 0.1\text{\AA}^2\alpha_R$ and various ratios λ_D/α_R . The arrows correspond to the in-plane spin expectation values, the color scale represents the out-of-plane component.

E. Fermi surface determination and integration

In anisotropic systems whose Fermi surfaces cannot be approximated as spheres, circles or ellipsoids, an analytical integration over the Fermi surface is usually not possible. Therefore, numerical methods are used for determining the \mathbf{k} -points at the Fermi surface, for which the Boltzmann equation is solved in order to calculate transport properties by a Fermi surface integration.

To determine the Fermi surfaces of two- and three-dimensional systems, an adaptive triangular and tetrahedral method, respectively, is used [202, 203]. Basically, both procedures are similar and differ mainly with respect to the dimension of the considered system. In the following the two-dimensional triangular as well as the three-dimensional tetrahedral method are sketched.

E.1. Two-dimensional triangular method

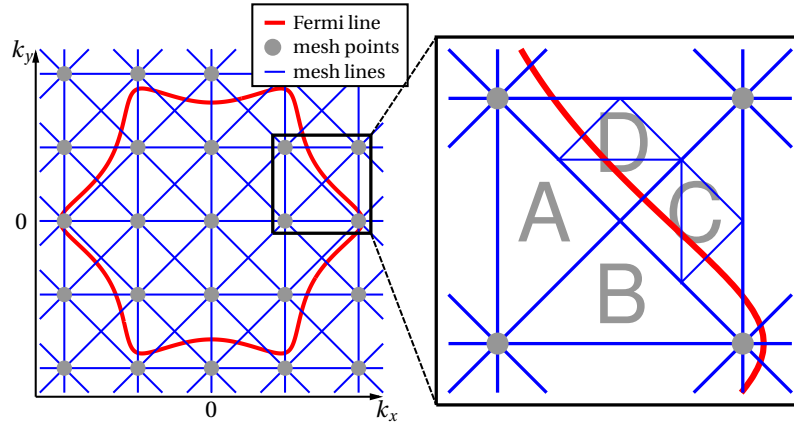


Figure E.1.: Adaptive triangle method for the determination of the Fermi lines (red) in 2D \mathbf{k} -space. Left panel: The \mathbf{k} -space is divided by a rectangular mesh (gray dots). The grid points are connected in such a way that triangles are generated (blue lines). Right panel: Detail (boxed region in the left panel). The triangles A and B are not intersected by the Fermi line, therefore they are excluded from further consideration. The Fermi line passes through the triangles C and D, they are divided iteratively into smaller triangles until the required precision is attained. Adapted from [J6].

In order to identify states which are approximately at the Fermi line, the 2D \mathbf{k} -space is sectioned by a rectangular grid, sketched in Fig. E.1. Each rectangle is divided into four triangles by straight lines, as depicted. Thus, the mesh points as well as the center of four mesh points form the triangular points. The energy value $\mathcal{E}_{\mathbf{k}}^n$ of the corresponding band is calculated at each triangular point. If the function $\mathcal{E}_{\mathbf{k}}^n - \mathcal{E}_F$ changes sign in between two triangular points, then the Fermi line passes in between these points.

Provided that the starting grid was chosen appropriately, triangles whose edges are not intersected by the Fermi line do not have to be considered further. For closed Fermi contours, a triangle lying at the Fermi line is intersected exactly twice. It is divided into four smaller triangles with the centers of the edges as new corners, as shown in the right panel of Fig. E.1. This procedure is repeated until the desired precision is reached. The “final” \mathbf{k} -points of the Fermi line are calculated by linear interpolation. This adaptive method requires a dense mesh only in the regions near the Fermi lines whereas the initial sampling is less precise.

The integration of a function $F(\mathbf{k})$ along the Fermi line is performed according to the trapezoidal

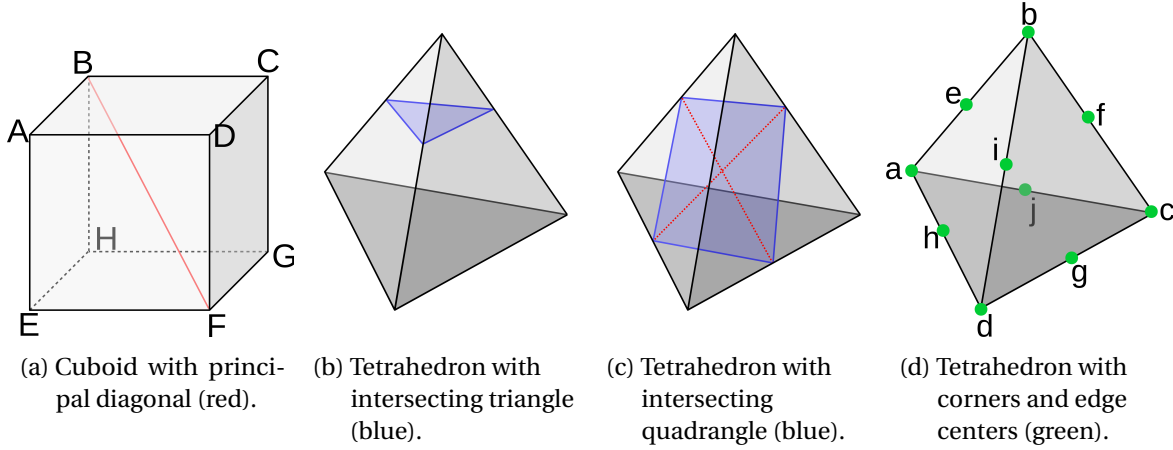


Figure E.2.: Tetrahedral method: The 3D \mathbf{k} -space is divided into cuboids. Each cuboid is divided into eight edge-sharing tetrahedra

rule,

$$\int_{\mathcal{E}_{\mathbf{k}}=\mathcal{E}_F} F(\mathbf{k}) dk_{\parallel} \approx \sum_{j=1}^{N_k} \frac{1}{2} [F(\mathbf{k}_j) + F(\mathbf{k}_{j+1})] |\mathbf{k}_j - \mathbf{k}_{j+1}|, \quad (\text{E.1})$$

where N_k is the number of \mathbf{k} -points which approximate the Fermi line.

E.2. Three-dimensional tetrahedral method

The procedure for finding Fermi surfaces in 3D \mathbf{k} -space is similar to the 2D method. The 3D Brillouin zone is divided by a 3D grid into cuboids, of which one is shown in Fig. E.2(a). Each cuboid is then fragmented into six tetrahedra of equal volume, which share one common principal diagonal, as proposed in [203]. In Fig. E.2(a), the shared edge is the BF line and the tetrahedra are (BFCD), (BFCG), (BFAD), (BFAE), (BFHG), (BFHE). For each tetrahedron, the number of edges intersecting the Fermi surface is determined, as described above for the triangular method. The number of intersection points of a tetrahedron with the Fermi surface can be 0 (tetrahedron is discarded), 3 (approximately triangular intersection with the Fermi surface), or 4 (approximately quadrangular intersection). If the required accuracy of Fermi surface points is not reached yet, the tetrahedron is divided into eight smaller tetrahedra built from the original tetrahedron corners and the centers of the edges (points a-j in Fig. E.2(d)) and the procedure is repeated iteratively until the desired precision is attained. The final intersecting triangles and quadrangles are then used as \mathbf{k} -points of the Fermi surface. In order to build the whole Fermi surface out of triangles, the quadrangles are divided into four triangles, as shown in Fig. E.2(b). To avoid systematic errors, the whole procedure is repeated three times starting with the other principal diagonals for the initial segmentation of the cuboid (Fig. E.2(a)). The integration over the Fermi surface is performed according to

$$\int_{\mathcal{E}_{\mathbf{k}}=\mathcal{E}_F} F(\mathbf{k}) d^2 k_{\parallel} \approx \sum_{j=1}^{N_k} F(\mathbf{k}_j^c) A_j, \quad (\text{E.2})$$

with \mathbf{k}_j^c the center of the triangle, slightly corrected by linear interpolation, and A_j the area of the triangle.

Bibliography

- [1] **S. A. Wolf, D. D. Awschalom, R. A. Buhrman, J. M. Daughton, S. von Molnár, M. L. Roukes, A. Y. Chtchelkanova, and D. M. Treger**, *Spintronics: A Spin-Based Electronics Vision for the Future*. Science **294**, 1488 (2001).
- [2] **M. N. Baibich, J. M. Broto, A. Fert, F. N. Van Dau, F. Petroff, P. Etienne, G. Creuzet, A. Friederich, and J. Chazelas**, *Giant Magnetoresistance of (001)Fe/(001)Cr Magnetic Superlattices*. Phys. Rev. Lett. **61**, 2472 (1988).
- [3] **G. Binasch, P. Grünberg, F. Saurenbach, and W. Zinn**, *Enhanced magnetoresistance in layered magnetic structures with antiferromagnetic interlayer exchange*. Phys. Rev. B **39**, 4828 (1989).
- [4] *The Nobel Prize in Physics 2007*. NobelPrize.org. Nobel Media AB 2018. <https://www.nobelprize.org/prizes/physics/2007/summary/>, [Online; 15. Nov 2018].
- [5] **S. S. P. Parkin, N. More, and K. P. Roche**, *Oscillations in exchange coupling and magnetoresistance in metallic superlattice structures: Co/Ru, Co/Cr, and Fe/Cr*. Phys. Rev. Lett. **64**, 2304 (1990).
- [6] *IBM 100 – the Application of Spintronics*. <http://www-03.ibm.com/ibm/history/ibm100/us/en/icons/spintronics/>, [Online; 16. Nov 2018].
- [7] **S. Datta and B. Das**, *Electronic analog of the electro-optic modulator*. Appl. Phys. Lett. **56**, 665 (1990).
- [8] **S. S. P. Parkin, M. Hayashi, and L. Thomas**, *Magnetic Domain-Wall Racetrack Memory*. Science **320**, 190 (2008).
- [9] **G. Schmidt**, *Concepts for spin injection into semiconductors—a review*. J. Phys. D **38**, R107 (2005).
- [10] **N. F. Mott and H. S. W. Massey**, *Theory of Atomic Collisions*. Oxford University Press, Oxford (1965).
- [11] **L. D. Landau and E. M. Lifshitz**, *Quantum Mechanics: Non-Relativistic Theory*. Pergamon Press, Oxford (1965).
- [12] **M. Dyakonov and V. Perel**, *Current-induced spin orientation of electrons in semiconductors*. Phys. Lett. A **35**, 459 (1971).
- [13] **J. E. Hirsch**, *Spin Hall Effect*. Phys. Rev. Lett. **83**, 1834 (1999).
- [14] **Y. K. Kato, R. C. Myers, A. C. Gossard, and D. D. Awschalom**, *Observation of the Spin Hall Effect in Semiconductors*. Science **306**, 1910 (2004).
- [15] **J. Sinova, S. O. Valenzuela, J. Wunderlich, C. H. Back, and T. Jungwirth**, *Spin Hall effects*. Rev. Mod. Phys. **87**, 1213 (2015).
- [16] **A. G. Aronov and Y. B. Lyanda-Geller**, *Nuclear electric resonance and orientation of carrier spins by an electric field*. JETP Lett. **50**, 431 (1989).
- [17] **V. M. Edelstein**, *Spin polarization of conduction electrons induced by electric current in two-dimensional asymmetric electron systems*. Solid State Commun. **73**, 233 (1990).

- [18] **P. M. Haney, H.-W. Lee, K.-J. Lee, A. Manchon, and M. D. Stiles**, *Current induced torques and interfacial spin-orbit coupling: Semiclassical modeling*. Phys. Rev. B **87**, 174411 (2013).
- [19] **D. Culcer, E. H. Hwang, T. D. Stanescu, and S. Das Sarma**, *Two-dimensional surface charge transport in topological insulators*. Phys. Rev. B **82**, 155457 (2010).
- [20] **A. R. Mellnik, J. S. Lee, A. Richardella, J. L. Grab, P. J. Mintun, M. H. Fischer, A. Vaezi, A. Manchon, E.-A. Kim, N. Samarth, and D. C. Ralph**, *Spin-transfer torque generated by a topological insulator*. Nature **511**, 449 (2010).
- [21] **D. Pesin and A. H. MacDonald**, *Spintronics and pseudospintronics in graphene and topological insulators*. Nat. Mater. **11**, 409 (2012).
- [22] **Y. Ando, T. Hamasaki, T. Kurokawa, K. Ichiba, F. Yang, M. Novak, S. Sasaki, K. Segawa, Y. Ando, and M. Shiraishi**, *Electrical Detection of the Spin Polarization Due to Charge Flow in the Surface State of the Topological Insulator $\text{Bi}_{1.5}\text{Sb}_{0.5}\text{Te}_{1.7}\text{Se}_{1.3}$* . Nano Lett. **14**, 6226 (2014).
- [23] **C. H. Li, O. M. J. van 't Erve, J. T. Robinson, Y. Liu, L. Li, and B. T. Jonker**, *Electrical detection of charge-current-induced spin polarization due to spin-momentum locking in Bi_2Se_3* . Nat. Nanotech. **9**, 218 (2014).
- [24] **J. Tian, I. Miotkowski, S. Hong, and Y. P. Chen**, *Electrical injection and detection of spin-polarized currents in topological insulator $\text{Bi}_2\text{Te}_2\text{Se}$* . Sci. Rep. **5**, 14293 (2015).
- [25] **J.-C. Rojas-Sánchez, S. Oyarzún, Y. Fu, A. Marty, C. Vergnaud, S. Gambarelli, L. Vila, M. Jamet, Y. Ohtsubo, A. Taleb-Ibrahimi, P. Le Fèvre, F. Bertran, N. Reyren, J.-M. George, and A. Fert**, *Spin to Charge Conversion at Room Temperature by Spin Pumping into a New Type of Topological Insulator: α -Sn Films*. Phys. Rev. Lett. **116**, 096602 (2016).
- [26] **C.-L. Zhang, S.-Y. Xu, I. Belopolski, Z. Yuan, Z. Lin, B. Tong, G. Bian, N. Alidoust, C.-C. Lee, S.-M. Huang, T.-R. Chang, G. Chang, C.-H. Hsu, H.-T. Jeng, M. Neupane, D. S. Sanchez, H. Zheng, J. Wang, H. Lin, C. Zhang, H.-Z. Lu, S.-Q. Shen, T. Neupert, M. Zahid Hasan, and S. Jia**, *Signatures of the Adler-Bell-Jackiw chiral anomaly in a Weyl fermion semimetal*. Nat. Commun. **7**, 10735 (2016).
- [27] **M. Rodriguez-Vega, G. Schwiete, J. Sinova, and E. Rossi**, *Giant Edelstein effect in topological-insulator-graphene heterostructures*. Phys. Rev. B **96**, 235419 (2017).
- [28] **E. Lesne, Y. Fu, S. Oyarzun, J. C. Rojas-Sánchez, D. C. Vaz, H. Naganuma, G. Sicoli, J.-P. Attané, M. Jamet, E. Jacquet, J.-M. George, A. Barthélémy, H. Jaffrès, A. Fert, M. Bibes, and L. Vila**, *Highly efficient and tunable spin-to-charge conversion through Rashba coupling at oxide interfaces*. Nat. Mater. **15**, 1261 (2016).
- [29] **G. Seibold, S. Caprara, M. Grilli, and R. Raimondi**, *Theory of the Spin Galvanic Effect at Oxide Interfaces*. Phys. Rev. Lett. **119**, 256801 (2017).
- [30] **Q. Song, H. Zhang, T. Su, W. Yuan, Y. Chen, W. Xing, J. Shi, J. Sun, and W. Han**, *Observation of inverse Edelstein effect in Rashba-split 2DEG between SrTiO_3 and LaAlO_3 at room temperature*. Sci. Adv. **3**, 1602312 (2017).
- [31] **S. Murakami**, *Phase transition between the quantum spin Hall and insulator phases in 3D: emergence of a topological gapless phase*. New J. Phys. **9**, 356 (2007).
- [32] **X. Wan, A. M. Turner, A. Vishwanath, and S. Y. Savrasov**, *Topological semimetal and Fermi-arc surface states in the electronic structure of pyrochlore iridates*. Phys. Rev. B **83**, 205101 (2011).

BIBLIOGRAPHY

- [33] **K.-Y. Yang, Y.-M. Lu, and Y. Ran**, *Quantum Hall effects in a Weyl semimetal: Possible application in pyrochlore iridates*. Phys. Rev. B **84**, 075129 (2011).
- [34] **A. A. Burkov and L. Balents**, *Weyl Semimetal in a Topological Insulator Multilayer*. Phys. Rev. Lett. **107**, 127205 (2011).
- [35] **S.-Y. Xu, I. Belopolski, N. Alidoust, M. Neupane, G. Bian, C. Zhang, R. Sankar, G. Chang, Z. Yuan, C.-C. Lee, S.-M. Huang, H. Zheng, J. Ma, D. S. Sanchez, B. Wang, A. Bansil, F. Chou, P. P. Shibayev, H. Lin, S. Jia, and M. Z. Hasan**, *Discovery of a Weyl fermion semimetal and topological Fermi arcs*. Science **349**, 613 (2015).
- [36] **H. Weyl**, *Elektron und Gravitation. I*. Zeitschrift für Physik **56**, 330 (1929).
- [37] **S. L. Adler**, *Axial-Vector Vertex in Spinor Electrodynamics*. Phys. Rev. **177**, 2426 (1969).
- [38] **J. S. Bell and R. Jackiw**, *A PCAC puzzle: $\pi^0 \rightarrow \gamma\gamma$ in the σ -model*. Il Nuovo Cimento A **60**, 47 (1969).
- [39] **H. Nielsen and M. Ninomiya**, *The Adler-Bell-Jackiw anomaly and Weyl fermions in a crystal*. Phys. Lett. B **130**, 389 (1983).
- [40] **V. Aji**, *Adler-Bell-Jackiw anomaly in Weyl semimetals: Application to pyrochlore iridates*. Phys. Rev. B **85**, 241101 (2012).
- [41] **D. T. Son and B. Z. Spivak**, *Chiral anomaly and classical negative magnetoresistance of Weyl metals*. Phys. Rev. B **88**, 104412 (2013).
- [42] **N. Ashcroft and N. Mermin**, *Festkörperphysik*. Oldenbourg Wissenschaftsverlag GmbH, München (2013).
- [43] **M. V. Berry**, *Quantal phase factors accompanying adiabatic changes*. Proc. Royal Soc. London A **392**, 45 (1984).
- [44] **D. Xiao, M.-C. Chang, and Q. Niu**, *Berry phase effects on electronic properties*. Rev. Mod. Phys. **82**, 1959 (2010).
- [45] **B. Bernevig and T. Hughes**, *Topological Insulators and Topological Superconductors*. Princeton University Press, Princeton and Oxford (2013).
- [46] **T. Kato**, *On the Adiabatic Theorem of Quantum Mechanics*. J. Phys. Soc. Jpn. **5**, 435 (1950).
- [47] **Y. Mokrousov**, *Berry phase in quantum mechanics*, volume 139 of *Schriften des Forschungszentrums Jülich Reihe Schlüsseltechnologien / Key Technologies*, A6. Forschungszentrum Jülich GmbH, Jülich (2017).
- [48] **R. Gross and A. Marx**, *Festkörperphysik*. De Gruyter Studium, De Gruyter, Berlin, Boston (2014).
- [49] **P. Kramer and M. Saraceno**, *Geometry of the time-dependent variational principle in quantum mechanics*. Lecture notes in physics, Springer-Verlag, Berlin Heidelberg (1981).
- [50] **G. Sundaram and Q. Niu**, *Wave-packet dynamics in slowly perturbed crystals: Gradient corrections and Berry-phase effects*. Phys. Rev. B **59**, 14915 (1999).
- [51] **D. Xiao, J. Shi, and Q. Niu**, *Berry Phase Correction to Electron Density of States in Solids*. Phys. Rev. Lett. **95**, 137204 (2005).
- [52] **R. Peierls**, *Zur Theorie des Diamagnetismus von Leitungselektronen*. Z. Phys. **80**, 763 (1933).

- [53] **J. C. Slater**, *Electrons in Perturbed Periodic Lattices*. Phys. Rev. **76**, 1592 (1949).
- [54] **J. M. Luttinger**, *The Effect of a Magnetic Field on Electrons in a Periodic Potential*. Phys. Rev. **84**, 814 (1951).
- [55] **M.-C. Chang** and **Q. Niu**, *Berry phase, hyperorbits, and the Hofstadter spectrum: Semiclassical dynamics in magnetic Bloch bands*. Phys. Rev. B **53**, 7010 (1996).
- [56] **J. Ziman**, *Prinzipien der Festkörpertheorie*. Harri Deutsch, Thun, Frankfurt am Main, (1999).
- [57] **Y. Kagan** and **V. Flerov**, *Theory of the resistivity and magnetoresistance of metals at low temperatures*. JETP **39**, 673 (1974).
- [58] **P. B. Allen**, *Fermi-surface harmonics: A general method for nonspherical problems. Application to Boltzmann and Eliashberg equations*. Phys. Rev. B **13**, 1416 (1976).
- [59] **I. Mertig** and **E. Mrosan**, *Magnetoresistivity of metals. I. Solution of the linearised Boltzmann equation using Fermi surface harmonics*. J. of Phys. F **12**, 3031 (1982).
- [60] **I. Mertig**, **E. Mrosan**, and **P. Ziesche**, *Multiple Scattering Theory of Point Defects in Metals: Electronic Properties*. Teubner-Texte zur Physik, Teubner Verlagsgesellschaft, Leipzig (1986).
- [61] **M. Trushin**, **J. Kailasvuori**, **J. Schliemann**, and **A. H. MacDonald**, *Finite conductivity minimum in bilayer graphene without charge inhomogeneities*. Phys. Rev. B **82**, 155308 (2010).
- [62] **R. Kubo**, *Statistical-Mechanical Theory of Irreversible Processes. I. General Theory and Simple Applications to Magnetic and Conduction Problems*. J. Phys. Soc. Jpn. **12**, 570 (1957).
- [63] **G. Giuliani** and **G. Vignale**, *Quantum Theory of the Electron Liquid*. Cambridge University Press, Cambridge (2005).
- [64] **F. Freimuth**, **S. Blügel**, and **Y. Mokrousov**, *Spin-orbit torques in Co/Pt(111) and Mn/W(001) magnetic bilayers from first principles*. Phys. Rev. B **90**, 174423 (2014).
- [65] **J. Železný**, **Y. Zhang**, **C. Felser**, and **B. Yan**, *Spin-Polarized Current in Noncollinear Antiferromagnets*. Phys. Rev. Lett. **119**, 187204 (2017).
- [66] **P. Strange**, *Relativistic Quantum Mechanics: With Applications in Condensed Matter and Atomic Physics*. Cambridge University Press, Cambridge (1998).
- [67] **S. Stepanow**, *Relativistische Quantentheorie: Für Bachelor: Mit Einführung in die Quantentheorie der Vielteilchensysteme*. Springer-Lehrbuch, Springer-Verlag, Berlin Heidelberg (2010).
- [68] **P. A. M. Dirac**, *The quantum theory of the electron*. Proc. Royal Soc. London A **117**, 610 (1928).
- [69] **P. A. M. Dirac**, *The quantum theory of the Electron. Part II*. Proc. Royal Soc. London A **118**, 351 (1928).
- [70] **T. M. McCormick**, **I. Kimchi**, and **N. Trivedi**, *Minimal models for topological Weyl semimetals*. Phys. Rev. B **95**, 075133 (2017).
- [71] **E. Simon**, **A. Szilva**, **B. Ujfalussy**, **B. Lazarovits**, **G. Zarand**, and **L. Szunyogh**, *Anisotropic Rashba splitting of surface states from the admixture of bulk states: Relativistic ab initio calculations and $k \cdot p$ perturbation theory*. Phys. Rev. B **81**, 235438 (2010).

BIBLIOGRAPHY

- [72] **J. D. Koralek, C. P. Weber, J. Orenstein, B. A. Bernevig, S.-C. Zhang, S. Mack, and D. D. Awschalom**, *Emergence of the persistent spin helix in semiconductor quantum wells*. *Nature* **458**, 610 (2009).
- [73] **J. Nitta, T. Akazaki, H. Takayanagi, and T. Enoki**, *Gate Control of Spin-Orbit Interaction in an Inverted $\text{In}_{0.53}\text{Ga}_{0.47}\text{As}/\text{In}_{0.52}\text{Al}_{0.48}\text{As}$ Heterostructure*. *Phys. Rev. Lett.* **78**, 1335 (1997).
- [74] **D. VanGennep, S. Maiti, D. Graf, S. W. Tozer, C. Martin, H. Berger, D. L. Maslov, and J. J. Hamlin**, *Pressure tuning the Fermi level through the Dirac point of giant Rashba semiconductor BiTeI* . *J. Phys. Condens. Matter* **26**, 342202 (2014).
- [75] **M. V. Berry and M. Wilkinson**, *Diabolical points in the spectra of triangles*. *Proc. Royal Soc. London A* **392**, 15 (1984).
- [76] **G. Dresselhaus**, *Spin-Orbit Coupling Effects in Zinc Blende Structures*. *Phys. Rev.* **100**, 580 (1955).
- [77] **S. Döhrmann, D. Hägele, J. Rudolph, M. Bichler, D. Schuh, and M. Oestreich**, *Anomalous Spin Dephasing in (110) GaAs Quantum Wells: Anisotropy and Intersubband Effects*. *Phys. Rev. Lett.* **93**, 147405 (2004).
- [78] **A. N. Chantis, M. van Schilfgaarde, and T. Kotani**, *Ab Initio Prediction of Conduction Band Spin Splitting in Zinc Blende Semiconductors*. *Phys. Rev. Lett.* **96**, 086405 (2006).
- [79] **J. J. Krich and B. I. Halperin**, *Cubic Dresselhaus Spin-Orbit Coupling in 2D Electron Quantum Dots*. *Phys. Rev. Lett.* **98**, 226802 (2007).
- [80] **S. Zhang**, *Topological insulators*. *Scholarpedia* **10**, 30275 (2015).
- [81] **D. J. Thouless, M. Kohmoto, M. P. Nightingale, and M. den Nijs**, *Quantized Hall Conductance in a Two-Dimensional Periodic Potential*. *Phys. Rev. Lett.* **49**, 405 (1982).
- [82] **M. Z. Hasan and C. L. Kane**, *Colloquium: Topological insulators*. *Rev. Mod. Phys.* **82**, 3045 (2010).
- [83] **F. D. M. Haldane**, *Model for a Quantum Hall Effect without Landau Levels: Condensed-Matter Realization of the "Parity Anomaly"*. *Phys. Rev. Lett.* **61**, 2015 (1988).
- [84] **C. L. Kane and E. J. Mele**, *Z_2 Topological Order and the Quantum Spin Hall Effect*. *Phys. Rev. Lett.* **95**, 146802 (2005).
- [85] **R. Roy**, *Z_2 classification of quantum spin Hall systems: An approach using time-reversal invariance*. *Phys. Rev. B* **79**, 195321 (2009).
- [86] **M. Sato and Y. Ando**, *Topological superconductors: a review*. *Rep. Prog. Phys.* **80**, 076501 (2017).
- [87] **B. A. Bernevig and S.-C. Zhang**, *Quantum Spin Hall Effect*. *Phys. Rev. Lett.* **96**, 106802 (2006).
- [88] **M. König, S. Wiedmann, C. Brüne, A. Roth, H. Buhmann, L. W. Molenkamp, X.-L. Qi, and S.-C. Zhang**, *Quantum Spin Hall Insulator State in HgTe Quantum Wells*. *Science* **318**, 766 (2007).
- [89] **R. Roy**, *Characterization of three-dimensional topological insulators by two-dimensional invariants*. *New J. Phys.* **12**, 065009 (2010).
- [90] **H. Zhang, C.-X. Liu, X.-L. Qi, X. Dai, Z. Fang, and S.-C. Zhang**, *Topological insulators in Bi_2Se_3 , Bi_2Te_3 and Sb_2Te_3 with a single Dirac cone on the surface*. *Nat. Phys.* **5**, 438 (2009).

- [91] **S.-Q. Shen, W.-Y. Shan, and H.-Z. Lu**, *Topological insulator and the Dirac equation*. SPIN **01**, 33 (2011).
- [92] **H. Nielsen and M. Ninomiya**, *A no-go theorem for regularizing chiral fermions*. Phys. Lett. B **105**, 219 (1981).
- [93] **H. Nielsen and M. Ninomiya**, *Absence of neutrinos on a lattice*. Nucl. Phys. B **185**, 20 (1981).
- [94] **H. Nielsen and M. Ninomiya**, *Absence of neutrinos on a lattice*. Nucl. Phys. B **193**, 173 (1981).
- [95] **P. Hosur and X. Qi**, *Recent developments in transport phenomena in Weyl semimetals*. C. R. Phys. **14**, 857 (2013).
- [96] **A. A. Burkov**, *Chiral Anomaly and Diffusive Magnetotransport in Weyl Metals*. Phys. Rev. Lett. **113**, 247203 (2014).
- [97] **S. Murakami and S.-i. Kuga**, *Universal phase diagrams for the quantum spin Hall systems*. Phys. Rev. B **78**, 165313 (2008).
- [98] **R. Okugawa and S. Murakami**, *Dispersion of Fermi arcs in Weyl semimetals and their evolutions to Dirac cones*. Phys. Rev. B **89**, 235315 (2014).
- [99] **H. Rostami and M. Polini**, *Nonlinear anomalous photocurrents in Weyl semimetals*. Phys. Rev. B **97**, 195151 (2018).
- [100] **Y. Sun, S.-C. Wu, and B. Yan**, *Topological surface states and Fermi arcs of the noncentrosymmetric Weyl semimetals TaAs, TaP, NbAs, and NbP*. Phys. Rev. B **92**, 115428 (2015).
- [101] **S.-Y. Xu, I. Belopolski, D. S. Sanchez, M. Neupane, G. Chang, K. Yaji, Z. Yuan, C. Zhang, K. Kuroda, G. Bian, C. Guo, H. Lu, T.-R. Chang, N. Alidoust, H. Zheng, C.-C. Lee, S.-M. Huang, C.-H. Hsu, H.-T. Jeng, A. Bansil, T. Neupert, F. Komori, T. Kondo, S. Shin, H. Lin, S. Jia, and M. Z. Hasan**, *Spin Polarization and Texture of the Fermi Arcs in the Weyl Fermion Semimetal TaAs*. Phys. Rev. Lett. **116**, 096801 (2016).
- [102] **H. Weng, C. Fang, Z. Fang, B. A. Bernevig, and X. Dai**, *Weyl Semimetal Phase in Noncentrosymmetric Transition-Metal Monophosphides*. Phys. Rev. X **5**, 011029 (2015).
- [103] **S.-M. Huang, S.-Y. Xu, I. Belopolski, C.-C. Lee, G. Chang, B. Wang, N. Alidoust, G. Bian, M. Neupane, C. Zhang, S. Jia, A. Bansil, H. Lin, and M. Z. Hasan**, *A Weyl Fermion semimetal with surface Fermi arcs in the transition metal monophosphide TaAs class*. Nat. Commun. **6**, 7373 (2015).
- [104] **A. A. Soluyanov, D. Gresch, Z. Wang, Q. Wu, M. Troyer, X. Dai, and B. A. Bernevig**, *Type-II Weyl semimetals*. Nature **527**, 495 (2015).
- [105] **Y. Sun, S.-C. Wu, M. N. Ali, C. Felser, and B. Yan**, *Prediction of Weyl semimetal in orthorhombic MoTe₂*. Phys. Rev. B **92**, 161107 (2015).
- [106] **J. C. Rojas Sánchez, L. Vila, G. Desfonds, S. Gambarelli, J. P. Attané, J. M. De Teresa, C. Magén, and A. Fert**, *Spin-to-charge conversion using Rashba coupling at the interface between non-magnetic materials*. Nat. Commun. **4**, 2944 (2013).
- [107] **P. Gambardella and I. M. Miron**, *Current-induced spin-orbit torques*. Philos. Trans. Royal Soc. A **369**, 3175 (2011).
- [108] **E. Rashba**, *Properties of semiconductors with an extremum loop. 1. Cyclotron and combination resonance in a magnetic field perpendicular to the plane of the loop*. Sov. Phys. Solid State **2**, 1109 (1960).

BIBLIOGRAPHY

- [109] **Y. Bychkov** and **E. Rashba**, *Properties of a 2D electron gas with lifted spectral degeneracy*. JETP **39**, 78 (1984).
- [110] **Y. A. Bychkov** and **E. I. Rashba**, *Oscillatory effects and the magnetic susceptibility of carriers in inversion layers*. J. of Phys. C **17**, 6039 (1984).
- [111] **R. H. Silsbee**, *Theory of the detection of current-induced spin polarization in a two-dimensional electron gas*. Phys. Rev. B **63**, 155305 (2001).
- [112] **R. H. Silsbee**, *Spin-orbit induced coupling of charge current and spin polarization*. J. Phys. Condens. Matter **16**, R179 (2004).
- [113] **J.-i. Inoue**, **G. E. W. Bauer**, and **L. W. Molenkamp**, *Diffuse transport and spin accumulation in a Rashba two-dimensional electron gas*. Phys. Rev. B **67**, 033104 (2003).
- [114] **K. Shen**, **G. Vignale**, and **R. Raimondi**, *Microscopic Theory of the Inverse Edelstein Effect*. Phys. Rev. Lett. **112**, 096601 (2014).
- [115] **D. S. Smirnov** and **L. E. Golub**, *Electrical Spin Orientation, Spin-Galvanic, and Spin-Hall Effects in Disordered Two-Dimensional Systems*. Phys. Rev. Lett. **118**, 116801 (2017).
- [116] **C. Gorini**, **A. Maleki Sheikhabadi**, **K. Shen**, **I. V. Tokatly**, **G. Vignale**, and **R. Raimondi**, *Theory of current-induced spin polarization in an electron gas*. Phys. Rev. B **95**, 205424 (2017).
- [117] **Y. K. Kato**, **R. C. Myers**, **A. C. Gossard**, and **D. D. Awschalom**, *Current-Induced Spin Polarization in Strained Semiconductors*. Phys. Rev. Lett. **93**, 176601 (2004).
- [118] **Y. K. Kato**, **R. C. Myers**, **A. C. Gossard**, and **D. D. Awschalom**, *Coherent spin manipulation without magnetic fields in strained semiconductors*. Nature **427**, 50 (2004).
- [119] **V. Sih**, **R. C. Myers**, **Y. K. Kato**, **W. H. Lau**, **A. C. Gossard**, and **D. D. Awschalom**, *Spatial imaging of the spin Hall effect and current-induced polarization in two-dimensional electron gases*. Nat. Phys. **1**, 31 (2005).
- [120] **A. Y. Silov**, **P. A. Blajnov**, **J. H. Wolter**, **R. Hey**, **K. H. Ploog**, and **N. S. Averkiev**, *Current-induced spin polarization at a single heterojunction*. Appl. Phys. Lett. **85**, 5929 (2004).
- [121] **H. J. Zhang**, **S. Yamamoto**, **B. Gu**, **H. Li**, **M. Maekawa**, **Y. Fukaya**, and **A. Kawasuso**, *Charge-to-Spin Conversion and Spin Diffusion in Bi/Ag Bilayers Observed by Spin-Polarized Positron Beam*. Phys. Rev. Lett. **114**, 166602 (2015).
- [122] **S. Sangiao**, **J. M. De Teresa**, **L. Morellon**, **I. Lucas**, **M. C. Martínez-Velarte**, and **M. Viret**, *Control of the spin to charge conversion using the inverse Rashba-Edelstein effect*. Appl. Phys. Lett. **106**, 172403 (2015).
- [123] **M. Isasa**, **M. C. Martínez-Velarte**, **E. Villamor**, **C. Magén**, **L. Morellón**, **J. M. De Teresa**, **M. R. Ibarra**, **G. Vignale**, **E. V. Chulkov**, **E. E. Krasovskii**, **L. E. Hueso**, and **F. Casanova**, *Origin of inverse Rashba-Edelstein effect detected at the Cu/Bi interface using lateral spin valves*. Phys. Rev. B **93**, 014420 (2016).
- [124] **N. F. Mott**, *The Electrical Conductivity of Transition Metals*. Proc. Royal Soc. London A **153**, 699 (1936).
- [125] **M. I. Dyakonov**, *Magnetoresistance due to Edge Spin Accumulation*. Phys. Rev. Lett. **99**, 126601 (2007).

- [126] **S. Zhang** and **A. Fert**, *Conversion between spin and charge currents with topological insulators*. Phys. Rev. B **94**, 184423 (2016).
- [127] **R. Dey**, **N. Prasad**, **L. F. Register**, and **S. K. Banerjee**, *Conversion of spin current into charge current in a topological insulator: Role of the interface*. Phys. Rev. B **97**, 174406 (2018).
- [128] **M. Johnson**, *Theory of spin-dependent transport in ferromagnet-semiconductor heterostructures*. Phys. Rev. B **58**, 9635 (1998).
- [129] **P. R. Hammar** and **M. Johnson**, *Potentiometric measurements of the spin-split subbands in a two-dimensional electron gas*. Phys. Rev. B **61**, 7207 (2000).
- [130] **Y. Tserkovnyak**, **A. Brataas**, and **G. E. W. Bauer**, *Enhanced Gilbert Damping in Thin Ferromagnetic Films*. Phys. Rev. Lett. **88**, 117601 (2002).
- [131] **L. Liu**, **T. Moriyama**, **D. C. Ralph**, and **R. A. Buhrman**, *Spin-Torque Ferromagnetic Resonance Induced by the Spin Hall Effect*. Phys. Rev. Lett. **106**, 036601 (2011).
- [132] **K. Kondou**, **R. Yoshimi**, **A. Tsukazaki**, **Y. Fukuma**, **J. Matsuno**, **K. S. Takahashi**, **M. Kawasaki**, **Y. Tokura**, and **Y. Otani**, *Fermi-level-dependent charge-to-spin current conversion by Dirac surface states of topological insulators*. Nat. Phys. **12**, 1027 (2016).
- [133] **E. E. Krasovskii**, *Microscopic origin of the relativistic splitting of surface states*. Phys. Rev. B **90**, 115434 (2014).
- [134] **S. LaShell**, **B. A. McDougall**, and **E. Jensen**, *Spin Splitting of an Au(111) Surface State Band Observed with Angle Resolved Photoelectron Spectroscopy*. Phys. Rev. Lett. **77**, 3419 (1996).
- [135] **H. Cercellier**, **C. Didiot**, **Y. Fagot-Revurat**, **B. Kierren**, **L. Moreau**, **D. Malterre**, and **F. Reinert**, *Interplay between structural, chemical, and spectroscopic properties of Ag/Au(111) epitaxial ultrathin films: A way to tune the Rashba coupling*. Phys. Rev. B **73**, 195413 (2006).
- [136] **D. Popović**, **F. Reinert**, **S. Hufner**, **V. G. Grigoryan**, **M. Springborg**, **H. Cercellier**, **Y. Fagot-Revurat**, **B. Kierren**, and **D. Malterre**, *High-resolution photoemission on Ag/Au(111): Spin-orbit splitting and electronic localization of the surface state*. Phys. Rev. B **72**, 045419 (2005).
- [137] **C. R. Ast**, **J. Henk**, **A. Ernst**, **L. Moreschini**, **M. C. Falub**, **D. Pacilé**, **P. Bruno**, **K. Kern**, and **M. Grioni**, *Giant Spin Splitting through Surface Alloying*. Phys. Rev. Lett. **98**, 186807 (2007).
- [138] **M. Hoesch**, **M. Muntwiler**, **V. N. Petrov**, **M. Hengsberger**, **L. Patthey**, **M. Shi**, **M. Falub**, **T. Greber**, and **J. Osterwalder**, *Spin structure of the Shockley surface state on Au(111)*. Phys. Rev. B **69**, 241401 (2004).
- [139] **T. Oguchi** and **T. Shishidou**, *The surface Rashba effect: a $k \cdot p$ perturbation approach*. J. Phys. Condens. Matter **21**, 092001 (2009).
- [140] **L. Van Hove**, *The Occurrence of Singularities in the Elastic Frequency Distribution of a Crystal*. Phys. Rev. **89**, 1189 (1953).
- [141] **T. Nakamura**, **Y. Ohtsubo**, **Y. Yamashita**, **S.-i. Ideta**, **K. Tanaka**, **K. Yaji**, **A. Harasawa**, **S. Shin**, **F. Komori**, **R. Yukawa**, **K. Horiba**, **H. Kumigashira**, and **S.-i. Kimura**, *Giant Rashba splitting of quasi-one-dimensional surface states on Bi/InAs(110)-(2 × 1)*. Phys. Rev. B **98**, 075431 (2018).
- [142] **J. Prempfer**, **M. Trautmann**, **J. Henk**, and **P. Bruno**, *Spin-orbit splitting in an anisotropic two-dimensional electron gas*. Phys. Rev. B **76**, 073310 (2007).

BIBLIOGRAPHY

- [143] **L. Fu**, *Hexagonal Warping Effects in the Surface States of the Topological Insulator Bi₂Te₃*. Phys. Rev. Lett. **103**, 266801 (2009).
- [144] **E. Frantzeskakis** and **M. Gioni**, *Anisotropy effects on Rashba and topological insulator spin-polarized surface states: A unified phenomenological description*. Phys. Rev. B **84**, 155453 (2011).
- [145] **H. Bentmann**, **F. Forster**, **G. Bihlmayer**, **E. V. Chulkov**, **L. Moreschini**, **M. Gioni**, and **F. Reinert**, *Origin and manipulation of the Rashba splitting in surface alloys*. Europhys. Lett. **87**, 37003 (2009).
- [146] **L. Moreschini**, **A. Bendounan**, **H. Bentmann**, **M. Assig**, **K. Kern**, **F. Reinert**, **J. Henk**, **C. R. Ast**, and **M. Gioni**, *Influence of the substrate on the spin-orbit splitting in surface alloys on (111) noble-metal surfaces*. Phys. Rev. B **80**, 035438 (2009).
- [147] **F. Meier**, **H. Dil**, **J. Lobo-Checa**, **L. Patthey**, and **J. Osterwalder**, *Quantitative vectorial spin analysis in angle-resolved photoemission: Bi/Ag(111) and Pb/Ag(111)*. Phys. Rev. B **77**, 165431 (2008).
- [148] **A. Manchon** and **S. Zhang**, *Theory of spin torque due to spin-orbit coupling*. Phys. Rev. B **79**, 094422 (2009).
- [149] **J. Krempaský**, **S. Muff**, **F. Bisti**, **M. Fanciulli**, **H. Volfová**, **A. P. Weber**, **N. Pilet**, **P. Warnicke**, **H. Ebert**, **J. Braun**, **F. Bertran**, **V. V. Volobuev**, **J. Minár**, **G. Springholz**, **J. H. Dil**, and **V. N. Strocov**, *Entanglement and manipulation of the magnetic and spin-orbit order in multiferroic Rashba semiconductors*. Nat. Commun. **7**, 13071 (2016).
- [150] **D. Di Sante**, **P. Barone**, **R. Bertacco**, and **S. Picozzi**, *Electric Control of the Giant Rashba Effect in Bulk GeTe*. Advanced Materials **25**, 509 (2013).
- [151] **S. Picozzi**, *Ferroelectric Rashba semiconductors as a novel class of multifunctional materials*. Frontiers in Physics **2**, 10 (2014).
- [152] **M. Trushin** and **J. Schliemann**, *Anisotropic current-induced spin accumulation in the two-dimensional electron gas with spin-orbit coupling*. Phys. Rev. B **75**, 155323 (2007).
- [153] **I. Tokatly** and **E. Sherman**, *Gauge theory approach for diffusive and precessional spin dynamics in a two-dimensional electron gas*. Annals of Physics **325**, 1104 (2010).
- [154] **X. Cartoixà**, **L.-W. Wang**, **D.-Y. Ting**, and **Y.-C. Chang**, *Higher-order contributions to Rashba and Dresselhaus effects*. Phys. Rev. B **73**, 205341 (2006).
- [155] **R. Eppenga** and **M. F. H. Schuurmans**, *Effect of bulk inversion asymmetry on [001], [110], and [111] GaAs/AlAs quantum wells*. Phys. Rev. B **37**, 10923 (1988).
- [156] **E. A. de Andrada e Silva**, *Conduction-subband anisotropic spin splitting in III-V semiconductor heterojunctions*. Phys. Rev. B **46**, 1921 (1992).
- [157] **B. A. Bernevig**, **J. Orenstein**, and **S.-C. Zhang**, *Exact SU(2) Symmetry and Persistent Spin Helix in a Spin-Orbit Coupled System*. Phys. Rev. Lett. **97**, 236601 (2006).
- [158] **A. Matos-Abiague** and **R. L. Rodríguez-Suárez**, *Spin-orbit coupling mediated spin torque in a single ferromagnetic layer*. Phys. Rev. B **80**, 094424 (2009).
- [159] **I. Mertig**, *Transport properties of dilute alloys*. Rep. Prog. Phys. **62**, 237 (1999).

- [160] **L. X. Yang, Z. K. Liu, Y. Sun, H. Peng, H. F. Yang, T. Zhang, B. Zhou, Y. Zhang, Y. F. Guo, M. Rahn, D. Prabhakaran, Z. Hussain, S.-K. Mo, C. Felser, B. Yan, and Y. L. Chen**, *Weyl semimetal phase in the non-centrosymmetric compound TaAs*. Nat. Phys. **11**, 728 (2015).
- [161] **F. Arnold, M. Naumann, S.-C. Wu, Y. Sun, M. Schmidt, H. Borrmann, C. Felser, B. Yan, and E. Hassinger**, *Chiral Weyl Pockets and Fermi Surface Topology of the Weyl Semimetal TaAs*. Phys. Rev. Lett. **117**, 146401 (2016).
- [162] **C.-C. Lee, S.-Y. Xu, S.-M. Huang, D. S. Sanchez, I. Belopolski, G. Chang, G. Bian, N. Alidoust, H. Zheng, M. Neupane, B. Wang, A. Bansil, M. Z. Hasan, and H. Lin**, *Fermi surface interconnectivity and topology in Weyl fermion semimetals TaAs, TaP, NbAs, and NbP*. Phys. Rev. B **92**, 235104 (2015).
- [163] **B. Q. Lv, H. M. Weng, B. B. Fu, X. P. Wang, H. Miao, J. Ma, P. Richard, X. C. Huang, L. X. Zhao, G. F. Chen, Z. Fang, X. Dai, T. Qian, and H. Ding**, *Experimental Discovery of Weyl Semimetal TaAs*. Phys. Rev. X **5**, 031013 (2015).
- [164] **J. Buckeridge, D. Jevdokimovs, C. R. A. Catlow, and A. A. Sokol**, *Bulk electronic, elastic, structural, and dielectric properties of the Weyl semimetal TaAs*. Phys. Rev. B **93**, 125205 (2016).
- [165] **A. Hubert and G. Traeger**, *Magneto-optical sensitivity functions of thin-film systems*. J. Magn. Magn. Mater. **124**, 185 (1993).
- [166] **C. You and S. Shin**, *Derivation of simplified analytic formulae for magneto-optical Kerr effects*. Appl. Phys. Lett. **69**, 1315 (1996).
- [167] **Z. Q. Qiu and S. D. Bader**, *Surface magneto-optic Kerr effect*. Rev. Sci. Instrum. **71**, 1243 (2000).
- [168] **E. V. Gorbar, V. A. Miransky, I. A. Shovkovy, and P. O. Sukhachov**, *Origin of dissipative Fermi arc transport in Weyl semimetals*. Phys. Rev. B **93**, 235127 (2016).
- [169] **R. W. Jackiw**, *Quantum Symmetry Anomalies*. Int. J. Mod. Phys. A **25**, 659 (2010).
- [170] **J. Xiong, S. K. Kushwaha, T. Liang, J. W. Krizan, M. Hirschberger, W. Wang, R. J. Cava, and N. P. Ong**, *Evidence for the chiral anomaly in the Dirac semimetal Na₃Bi*. Science **350**, 413 (2015).
- [171] **C. Z. Li, L. X. Wang, H. Liu, J. Wang, Z. M. Liao, and D. P. Yu**, *Giant negative magnetoresistance induced by the chiral anomaly in individual Cd₃As₂nanowires*. Nat. Commun. **6**, 10137 (2015).
- [172] **S. Liang, J. Lin, S. Kushwaha, J. Xing, N. Ni, R. J. Cava, and N. P. Ong**, *Experimental Tests of the Chiral Anomaly Magnetoresistance in the Dirac-Weyl Semimetals Na₃Bi and GdPtBi*. Phys. Rev. X **8**, 031002 (2018).
- [173] **S. Adler**, *Anomalies*. In **J.-P. François, G. L. Naber, and T. S. Tsun** (Eds.), *Encyclopedia of Mathematical Physics*, 205, Academic Press, Oxford (2006).
- [174] **E. Noether**, *Invariante Variationsprobleme*. Gött. Nachr. **1918**, 235 (1918).
- [175] **J. E. Sipe and A. I. Shkrebtii**, *Second-order optical response in semiconductors*. Phys. Rev. B **61**, 5337 (2000).
- [176] **B. Z. Spivak and A. V. Andreev**, *Magnetotransport phenomena related to the chiral anomaly in Weyl semimetals*. Phys. Rev. B **93**, 085107 (2016).
- [177] **G. Sharma, P. Goswami, and S. Tewari**, *Chiral anomaly and longitudinal magnetotransport in type-II Weyl semimetals*. Phys. Rev. B **96**, 045112 (2017).

BIBLIOGRAPHY

- [178] **V. A. Zyuzin**, *Magnetotransport of Weyl semimetals due to the chiral anomaly*. Phys. Rev. B **95**, 245128 (2017).
- [179] **A. Cortijo**, *Linear magnetochiral effect in Weyl semimetals*. Phys. Rev. B **94**, 241105 (2016).
- [180] **A. A. Zyuzin** and **A. A. Burkov**, *Topological response in Weyl semimetals and the chiral anomaly*. Phys. Rev. B **86**, 115133 (2012).
- [181] **A. A. Zyuzin**, **S. Wu**, and **A. A. Burkov**, *Weyl semimetal with broken time reversal and inversion symmetries*. Phys. Rev. B **85**, 165110 (2012).
- [182] **A. Cortijo**, **D. Kharzeev**, **K. Landsteiner**, and **M. A. H. Vozmediano**, *Strain-induced chiral magnetic effect in Weyl semimetals*. Phys. Rev. B **94**, 241405 (2016).
- [183] **A. A. Burkov**, *Negative longitudinal magnetoresistance in Dirac and Weyl metals*. Phys. Rev. B **91**, 245157 (2015).
- [184] **Y. V. Nazarov**, *Instability due to magnetically induced currents*. JETP **64**, 193 (1986).
- [185] **M. A. Zubkov**, *Absence of equilibrium chiral magnetic effect*. Phys. Rev. D **93**, 105036 (2016).
- [186] **W. Brauer**, *Einführung in die Elektronentheorie der Metalle*. Akademische Verlagsgesellschaft Geest & Portig K.-G., Leipzig (1972).
- [187] **H.-J. Kim**, **K.-S. Kim**, **J.-F. Wang**, **M. Sasaki**, **N. Satoh**, **A. Ohnishi**, **M. Kitaura**, **M. Yang**, and **L. Li**, *Dirac versus Weyl Fermions in Topological Insulators: Adler-Bell-Jackiw Anomaly in Transport Phenomena*. Phys. Rev. Lett. **111**, 246603 (2013).
- [188] **T. Liang**, **Q. Gibson**, **M. N. Ali**, **M. Liu**, **R. J. Cava**, and **N. P. Ong**, *Ultrahigh mobility and giant magnetoresistance in the Dirac semimetal Cd₃As₂*. Nat. Mater. **14**, 280 (2015).
- [189] **C. Zhang**, **E. Zhang**, **W. Wang**, **Y. Liu**, **Z.-G. Chen**, **S. Lu**, **S. Liang**, **J. Cao**, **X. Yuan**, **L. Tang**, **Q. Li**, **C. Zhou**, **T. Gu**, **Y. Wu**, **J. Zou**, and **F. Xiu**, *Room-temperature chiral charge pumping in Dirac semimetals*. Nat. Commun. **8**, 13741 (2017).
- [190] **Q. Li** and **D. E. Kharzeev**, *Chiral magnetic effect in condensed matter systems*. Nucl. Phys. A **956**, 107 (2016).
- [191] **T. Liang**, **J. Lin**, **Q. Gibson**, **S. Kushwaha**, **M. Liu**, **W. Wang**, **H. Xiong**, **J. A. Sobota**, **M. Hashimoto**, **P. S. Kirchmann**, **Z.-X. Shen**, **R. J. Cava**, and **N. P. Ong**, *Anomalous Hall effect in ZrTe₅*. Nat. Phys. **14**, 451 (2018).
- [192] **M. Hirschberger**, **S. Kushwaha**, **Z. Wang**, **Q. Gibson**, **S. Liang**, **C. A. Belvin**, **B. A. Bernevig**, **R. J. Cava**, and **N. P. Ong**, *The chiral anomaly and thermopower of Weyl fermions in the half-Heusler GdPtBi*. Nat. Mater. **15**, 1161 (2016).
- [193] **L. Ritchie**, **G. Xiao**, **Y. Ji**, **T. Y. Chen**, **C. L. Chien**, **M. Zhang**, **J. Chen**, **Z. Liu**, **G. Wu**, and **X. X. Zhang**, *Magnetic, structural, and transport properties of the Heusler alloys Co₂MnSi and NiMnSb*. Phys. Rev. B **68**, 104430 (2003).
- [194] **A. Pippard**, *Magnetoresistance in Metals*. Cambridge Studies in Low Temperature Physics, Cambridge University Press, Cambridge (1989).
- [195] **J. Hu**, **T. F. Rosenbaum**, and **J. B. Betts**, *Current Jets, Disorder, and Linear Magnetoresistance in the Silver Chalcogenides*. Phys. Rev. Lett. **95**, 186603 (2005).

- [196] **N. Kikugawa, P. Goswami, A. Kiswandhi, E. S. Choi, D. Graf, R. E. Baumbach, J. S. Brooks, K. Sugii, Y. Iida, M. Nishio, S. Uji, T. Terashima, P. Rourke, N. E. Hussey, H. Takatsu, S. Yonezawa, Y. Maeno, and L. Balicas**, *Interplanar coupling-dependent magnetoresistivity in high-purity layered metals*. Nat. Commun. **7**, 10903 (2016).
- [197] **P. N. Argyres and E. N. Adams**, *Longitudinal Magnetoresistance in the Quantum Limit*. Phys. Rev. **104**, 900 (1956).
- [198] **H.-Z. Lu and S.-Q. Shen**, *Weak antilocalization and localization in disordered and interacting Weyl semimetals*. Phys. Rev. B **92**, 035203 (2015).
- [199] **S. Nandy, G. Sharma, A. Taraphder, and S. Tewari**, *Chiral Anomaly as the Origin of the Planar Hall Effect in Weyl Semimetals*. Phys. Rev. Lett. **119**, 176804 (2017).
- [200] **A. A. Burkov**, *Giant planar Hall effect in topological metals*. Phys. Rev. B **96**, 041110 (2017).
- [201] **M. Imran and S. Hershfield**, *Berry curvature force and Lorentz force comparison in the magnetotransport of Weyl semimetals*. Phys. Rev. B **98**, 205139 (2018).
- [202] **J. Henk**, *Integration over two-dimensional Brillouin zones by adaptive mesh refinement*. Phys. Rev. B **64**, 035412 (2001).
- [203] **P. E. Blöchl, O. Jepsen, and O. K. Andersen**, *Improved tetrahedron method for Brillouin-zone integrations*. Phys. Rev. B **49**, 16223 (1994).

List of Publications

- [J1] **D. Fedorov, C. Herschbach, A. Johansson, S. Ostanin, I. Mertig, M. Gradhand, K. Chadova, D. Ködderitzsch, and H. Ebert**, *Analysis of the giant spin Hall effect in Cu(Bi) alloys*. Phys. Rev. B **88**, 085116 (2013).
- [J2] **A. Johansson, C. Herschbach, D. Fedorov, M. Gradhand, and I. Mertig**, *Validity of the relativistic phase shift model for the extrinsic spin Hall effect in dilute metal alloys*. J. Phys.: Condens. Matter **26**, 27420 (2014).
- [J3] **A. Johansson, C. Herschbach, D. Fedorov, J. Henk, and I. Mertig**, *Spin Hall effect in two-dimensional systems within the relativistic phase shift model*. Phys. Rev. B **92**, 184401 (2015).
- [J4] **A. Johansson, J. Henk, and I. Mertig**, *Theoretical aspects of the Edelstein effect for anisotropic two-dimensional electron gas and topological insulators*. Phys. Rev. B **93**, 195440 (2016).
- [J5] **A. Johansson, J. Henk, and I. Mertig**, *Edelstein effect in Weyl semimetals*. Phys. Rev. B **97**, 085417 (2018).
- [J6] **A. Johansson, J. Henk, and I. Mertig**, *Chiral anomaly in type-I Weyl semimetals: Comprehensive analysis within a semiclassical Fermi surface harmonics approach*. Submitted to Phys. Rev. B (2018).

Curriculum vitae

Personal data

Name Annika Johansson
Date and place of birth February 2, 1992, Heidelberg
Address Jakobsstraße 36
06618 Naumburg (Saale)

Education

since 07/2018 Member of the International Max Planck Research School
for Science and Technology of Nano-Systems (IMPRS-STNS)
since 12/2015 PhD studies, Martin Luther University Halle-Wittenberg (MLU)
10/2013-11/2015 Master degree (M.Sc.) course “Medical physics”, MLU, final grade 1.0
Master thesis: Theoretische Betrachtungen zum Edelstein-Effekt
(Theoretical considerations of the Edelstein effect)
10/2010-09/2013 Bachelor degree (B.Sc.) course “Medical physics”, MLU, final grade 1.1
Bachelor thesis: Sphärisches Bandmodell und Spin-Hall-Effekt
(Spherical band model and spin Hall effect)
08/2002-03/2010 Grammar school, Maria Ward-Gymnasium Mainz, final grade (Abitur): 1.0
09/1998-08/2002 Elementary school, Grundschule Nieder-Olm

Academic work experience

11/2017 Internship at Princeton University with B. A. Bernevig
since 12/2015 Research assistant, Max Planck Institute of Microstructure Physics,
Fellow Group Ingrid Mertig
10/2013-11/2015 Student assistant, Institute of Physics, MLU,
SFB 762: Functionality of Oxide Interfaces
10/2011-12/2012 Student assistant, Institute of Mathematics, MLU

Scholarships and awards

10/2013 Gustav Mie Bachelor award of the Institute of Physics, MLU
02/2011-11/2015 Scholarship of Studienstiftung des deutschen Volkes
(German Academic Scholarship Foundation)

Halle, 29.11.2018 Annika Johansson

Acknowledgments

Writing and in particular finishing this thesis would not have been possible without many people who accompanied and supported me during the last three years.

First of all, I would like to thank Prof. Ingrid Mertig for providing me the opportunity to work in her group, sharing her knowledge with me and guiding me to interesting physical problems. Since my first day as a Bachelor student I felt very welcome and really enjoyed our motivating and encouraging discussions. I am also very grateful that I could discuss with many visiting scientists and present my work at conferences.

Furthermore, I would like to express my gratitude to PD Dr. Jürgen Henk, without whom this work would not have been possible. He always found time to discuss my questions and results and produced new ideas by asking the right questions. He introduced me into scientific work in a straightforward, patient way.

Further, I would like to thank all my colleagues from the group *Quantum theory of the Solid State* at the Martin Luther University Halle-Wittenberg for the excellent working atmosphere and many discussions about physics as well as “real” life. Even in stressful times I was always looking forward to coming to the office.

In addition, my friends contributed indirectly by enriching my life beyond physics. Further, they helped me to manage the commuting situation by hosting me whenever the train was canceled.

I am very thankful to my family who accompanied me on the long way to this thesis. They shared many good and challenging moments with me during my PhD time. However, I am glad that we are still able to talk about topics apart from physics.

Finally, I would like to thank Lars, who had probably the most difficult part in the whole PhD process. Without his support and encouragement this thesis would not have been finished.

Eidesstattliche Erklärung

Ich erkläre, dass ich die vorliegende Arbeit

Spin-orbit driven transport: Edelstein effect and chiral anomaly

selbstständig und ohne fremde Hilfe verfasst habe. Es wurden keine anderen als die angegebenen Quellen und Hilfsmittel benutzt. Die den benutzten Werken wörtlich oder inhaltlich entnommenen Stellen habe ich als solche kenntlich gemacht.

Ich erkläre, alle Angaben wahrheitsgemäß gemacht zu haben und keine vergeblichen Promotionsversuche unternommen zu haben. Diese Arbeit wurde in der gegenwärtigen oder einer anderen Fassung keiner anderen wissenschaftlichen Einrichtung zur Erlangung eines akademischen Grades vorgelegt.

Ich bin weder vorbestraft noch sind gegen mich Ermittlungsverfahren anhängig.

Halle, 29.11.2018

Annika Johansson

